Univerzita Karlova

Přírodovědecká fakulta

Studijní program: Fyzická geografie a geoekologie

Mgr. Robert Minařík

Detekce disturbance lesa pomocí UAV multispektrální fotogrammetrie

Detection of the forest disturbance using UAV multispectral photogrammetry

Disertační práce

Školitel: prof. RNDr. Jakub Langhammer, Ph.D.

Praha, 2022

Prohlašuji, že jsem předloženou závěrečnou práci zpracoval samostatně a že jsem uvedl všechny použité informační zdroje a literaturu. Tato práce ani její podstatná část nebyly předloženy k získání jiného nebo stejného akademického titulu.

V Olomouci, 14. 04. 2022

…….

Poděkování

Na tomto místě chci poděkovat prof. Jakubu Langhammerovi za pomoc při směřování výzkumu, cenné rady a komentáře při řešení disertace, odborné diskuse a spolupráci v terénu. Mé kolegyni Theodoře Lendzioch děkuji za nepostradatelnou pomoc v terénu. Na závěr děkuji své rodině, že jste se mnou vydrželi až do konce.

Výzkum byl podpořen z projektů: GAUK č. 824217; EU COST Action 1306 LD15130; EU COST Action CA16219 LTC 19024; MHMP DOT/54/12/ 013649/2018; GAČR 19-05011S.

Abstrakt

V současné době nejvíce negativně ovlivňují vývoj smíšených a boreálních lesů Evropy epidemické (kalamitní) přemnožení kůrovců *(Scolytinae Latreille, 1804)* vlivem klimatické změny a nevhodné skladby dřevin, která mohou výrazně narušit zdravotní stav lesů a způsobit ekonomické ztráty. Proto je nezbytné použít vhodné metody pro včasnou detekci kůrovcové disturbance. Metody multispektrálního dálkového průzkumu země (DPZ) pomocí bezpilotních leteckých systémů (UAS) představují novou možnost bezkontaktního monitoringu krajiny poskytující kvantitativní informaci o zdravotním stavu vegetace s vysokým časoprostorovým rozlišením, proto se jeví jako vhodné i pro včasnou detekci disturbance. Disertační práce se zaměřila na ověření využití metod UAS multispektrální fotogrammetrie a klasifikace obrazu pro detekci disturbance lesa způsobené lýkožroutem smrkovým (*Ips typographus Linnaeus, 1758)* na úrovni jednotlivých stromů s rozlišením jednotlivých fází napadení pro studium dynamiky disturbance. V disertační práci byly rozpracovány všechny důležité aspekty detekce: analýza vhodnosti spektrálních pásem pro detekci disturbance, radiometrická kalibrace multispektrálních kamer, automatizovaná segmentace jednotlivých korun z fotogrammetrického mračna bodů (PPC) a klasifikace fází disturbance na úrovni jednotlivých stromů pomocí konvolučních neuronových sítí (CNN) z multispektrálního ortofota. Nejlépe je vegetační stres způsobený napadením stromu lýkožroutem smrkovým rozpoznatelný ve spektrálních pásmech reagující na změnu obsahu chlorofylu z důvodu narušení vodivých pletiv odpovídající červené (650 nm), red-edge (700 nm) a NIR (800 nm) části spektra a pomocí vegetačních indexů vypočítaných z těchto pásem. V případě použití klasifikátorů CNN se doporučuje použití základních pásem RGB, red-edge, případně NIR bez vegetačních indexů. Automatické metody segmentace korun z PPC mohou být náhradou za časově náročnou manuální segmentaci korun z ortofota pro klasifikaci fáze napadení jednotlivých stromů při zachování ideální hustoty bodů (~20–60 bodů/m^2, minimálně 10 bodů/m^2). Nižší nebo vyšší hustota mračna bodů vede ke snížení přesnosti segmentace. Nejlepší klasifikační CNN modely byly schopny detekovat jednotlivé fáze disturbance s přesností okolo 80 % včetně rané fáze napadení stromu lýkožroutem bez použití časové řady snímků. Metody UAS multispektrální fotogrammetrie ve spojení s CNN klasifikátorem jsou tedy plně použitelné pro detekci disturbance lesa a její dynamiky a vyplňují měřítkovou mezeru mezi pozemním průzkumem a leteckým DPZ, kdy po shromáždění referenční množiny umožnují automatizovanou detekci fází disturbance větších lesních celků na úrovni jednotlivých stromů. Proto lze tyto metody využít nejen pro základní identifikaci napadených stromů a včasnou asanaci, ale také pro sledování dynamiky vývoje kůrovcové disturbance, detekci hotspotů, predikci šíření a pochopení nedávných změn režimů disturbance v důsledku klimatické změny.

Klíčová slova: disturbance lesa; Ips typographus; multispektrální fotogrammetrie; bezpilotní letecké systémy; objektová klasifikace jednotlivých stromů; konvoluční neuronové sítě

Abstract

Epidemic (calamitous) overpopulations of bark beetles *(Scolytinae Latreille, 1804)* caused by climate change and inappropriate tree species composition currently have the most negative impacts on the development of Europe's mixed and boreal forests. Epidemic overpopulations can significantly undermine forest health and cause economic losses. It is therefore essential to use appropriate methods for early detection of bark beetle disturbance. Multispectral remote sensing (RS) methods using unmanned aerial systems (UAS) represent a new option for contactless landscape monitoring providing quantitative information on vegetation health with high spatiotemporal resolution and therefore appear to be suitable for early detection of disturbance. The thesis focused on the validation of the use of UAS multispectral photogrammetry and image classification methods for the detection of individual forest disturbance stages caused by the spruce bark beetle *(Ips typographus Linnaeus, 1758)* at the level of individual trees for the study of disturbance dynamics. In this dissertation, all important aspects of detection were elaborated: analysis of the suitability of spectral bands for disturbance detection, radiometric calibration of multispectral cameras, automated segmentation of individual canopies from photogrammetric point cloud (PPC) and classification of disturbance stages at individual tree level using convolutional neural networks (CNN) from the multispectral orthophoto. Vegetation stress caused by spruce bark beetle is best detected in spectral bands reflecting changes in chlorophyll content due to disruption of the vascular bundles. This corresponds to the red (650 nm), red-edge (700 nm) and NIR (800 nm) part of the spectrum of the multispectral cameras and vegetation indices calculated from these bands. In case of using CNN classifiers, it is recommended to use RGB, red-edge or NIR bands without vegetation indices. Automatic methods of canopy segmentation from PPC can be a substitute for time-consuming manual canopy segmentation from the orthophoto for infestation stage classification of individual trees while maintaining an ideal point density (~20–60 points/m^2, minimum 10 points/m^2). Lower or higher point cloud densities lead to reduced segmentation accuracy. The best CNN classification models were able to detect individual disturbance phases including the green attack stage resulting in the accuracy around 80% without using time series imagery. The UAS multispectral photogrammetry methods featuring the CNN classifiers are therefore fully applicable to the detection of forest disturbance and its dynamics, filling the scaling gap between field surveys and aerial RS, because once a reference set has been collected, they allow automated detection of disturbance phases of larger forest units at the individual tree level. Therefore, these methods can be used not only for basic identification of infested trees and early elimination, but also for monitoring the dynamics of bark beetle disturbance, detecting hotspots, predicting spread, and understanding recent changes in disturbance regimes due to climate change.

Keywords: forest disturbance; Ips typographus; multispectral photogrammetry; unmanned aerial systems; individual tree-based classification; convolutional neural networks

Obsah

1. Úvod 7
2. Současný stav poznání 12
   2.1. Bezpilotní letecké systémy 12
   2.2. Spektrální pásma a UAS senzory pro detekci kůrovcové disturbance 12
   2.3. Fotogrammetrické zpracování a klasifikace obrazu 14
3. Materiál a metodika 16
   3.1. Použité UAS systémy 16
   3.2. Zájmové území 17
   3.3. Metodika detekce jednotlivých fází disturbance 19
      3.3.1. Radiometrická kalibrace 20
      3.3.2. Segmentace jednotlivých korun 21
      3.3.3. Klasifikace jednotlivých fází disturbance 22
4. Výsledky 23
   4.1. Článek I 23
   4.2. Článek II 24
   4.3. Článek III 25
   4.4. Článek IV 26
   4.5. Článek V 27
5. Diskuze 29
   5.1. Výběr spektrálních pásem pro detekci disturbance 29
   5.2. Radiometrická kalibrace multispektrální kamery 30
   5.3. Faktory ovlivňující přesnost segmentace a klasifikace jednotlivých korun stromů 31
   5.4. Klasifikace fází disturbance na úrovni jednotlivých stromů pomocí CNN 32
6. Závěry 35
7. Použitá literatura 36
8. Publikované články 47

1. Úvod

Disturbance lesa je přirozenou součástí procesu strukturálního vývoje lesů mírného pásma a tajgy (Frelich, 2002). Disturbance ovlivňuje související procesy v krajině, od změn mikroklimatu a dynamiky odtoku, až po změnu půdního pokryvu a erozi půdy (Borrelli et al., 2016; Franklin et al., 2002; Langhammer et al., 2015). Disturbanci lesa způsobují různé faktory jako je znečištění ovzduší nebo neregulovaná těžba, ale nejvíce za posledních třicet let negativně ovlivňují vývoj lesních porostů ve střední Evropě epidemické (kalamitní) přemnožení kůrovců rodu *Ips*, zejména druhu *Ips typographus (Linnaeus, 1758)*, Lýkožrout smrkový, vlivem klimatické změny (Hlásny et al., 2021; Kautz et al., 2017; Lindner et al., 2010; Morris et al., 2017; Schuldt et al., 2020; Seidl et al., 2014, 2017; Senf et al., 2018, 2021). V současné době jsou epidemické stavy hrozbou, která může významně narušit zdravotní stav lesů a způsobit ekonomické ztráty (Aukema et al., 2011), proto je nezbytné použít vhodné metody pro detekci kůrovcové disturbance.

Tradiční a základní metodou pro detekci napadených stromů lýkožrouty je pozemní průzkum, kdy jsou hledány symptomy napadení na kmeni (závrtové otvory, drtinky u paty kmene), opad světle zeleného jehličí nebo barevné změny jehličí (Göthlin et al., 2000). Napadený strom prochází třemi fázemi (Coulson et al., 1985; Sprintsin, 2011; Wermelinger, 2004). V první zelené fázi (green attack) se neprojevují zřetelné příznaky změny barvy jehličí viditelné lidským okem, a proto není snadné napadení v tomto stadiu odhalit (Niemann et al., 2005; Wermelinger, 2004). Avšak, praktickou výhodou detekce napadení stromu lýkožroutem v zelené fázi je, že nová generace brouků ještě nevyletěla a je tedy možné strom skácet ještě před vyrojením (Wermelinger, 2004; Wulder et al., 2009). V druhé fázi reznutí (red attack) jehličí postupně žloutne, rezne, opadává kůra stromu a strom se stává kůrovcovou souší. Ve třetí fázi souše (grey attack) jehličí a kůra zcela opadá a zůstane jen mrtvá souš. Poslední dvě fáze napadení jsou již dobře rozpoznatelné pozemním průzkumem, ale již došlo k vyrojení brouků (Göthlin et al., 2000; Niemann et al., 2005). Kromě omezeného rozpoznání počátečního stádia disturbance je nevýhodou terénního průzkumu i jeho finanční a časová náročnost, takže tento přístup je vhodný pouze v lokálním měřítku. Pomocí dálkového průzkumu Země (DPZ) je ale možné odhalit napadení v již zelené fázi v úzkých pásmech viditelného a blízkého infračerveného spektra, kvůli změnám odrazivosti napadeného stromu způsobené úbytkem chlorofylu v důsledku narušení proudění vody a živin ve vodivých pletivech (Abdullah et al., 2018; Niemann et al., 2005; Sprintsin, 2011; Yamaoka et al., 2011). Zároveň je detekovatelný rozdíl v obsahu vody jehlic i u čerstvě napadených stromů ve vlnových délkách krátkovlnného a termálního infračerveného spektra (Berni, Zarco-Tejada, Suárez, & Fereres, 2009; Foster et al., 2017). Multispektrální nebo hyperspektrální DPZ se proto začal hojně využívat k neinvazivní detekci a mapovaní disturbance lesa ve větším než lokálním měřítku a nahradil původní metodu leteckého průzkumu, kdy byly poškozené části lesa zakreslovány do mapy pozorovatelem (Hall et al., 2016).

Historicky i v současné době jsou pro detekci a mapování disturbance lesa nejčastěji používána multispektrální družicová data středního rozlišení družic Landsat (DeRose et al., 2011; Hais et al., 2009, 2016; Havašová et al., 2015; Meddens et al., 2013; Meddens & Hicke, 2014; Senf et al., 2015), SPOT (Latifi et al., 2014) a Sentinel-2 (Abdullah et al., 2019a; Bárta et al., 2021; Fernandez-Carrillo et al., 2020), protože jsou snadno dostupná a existují časové řady pro analýzu vývoje disturbance nejčastěji v ročním kroku (Senf et al., 2017). Nasazení multispektrálního družicového DPZ pro detekci disturbance způsobené lýkožrouty má však své limity v prostorovém rozlišení, které je důležitým faktorem úspěšné detekce disturbance obecně a je klíčovým faktorem umožňujícím detekci jednotlivých napadených stromů (Hall et al., 2016; Senf et al., 2017). Prostorové rozlišení satelitních snímků nad 10 m včetně je vhodnější pro mapování disturbancí v měřítku epidemické populace pouze pomocí plošného (per-pixel) přístupu, kdy mapovací jednotkou je pixel (Hall et al., 2016). Jejich prostorové rozlišení není vhodné pro detekci jednotlivých napadených stromů, protože je velikost pixelu větší než informační (mapovaná) jednotka – koruna stromu. Méně často jsou využívány letecké hyperspektrální (Fassnacht et al., 2014; Lausch et al., 2013; Näsi et al., 2018) a satelitní multispektrální snímky (Immitzer & Atzberger, 2014; Ortiz et al., 2013) s rozlišením 1–9 m, které jsou používány zejména pro detekci a mapování zelené fáze napadení prostorově rozptýlených malých skupin stromů per-pixel přístupem v regionálním a vyšším měřítku z důvodu vysokých nákladů na pořízení snímků a nízké operativnosti, kvůli vysokým nárokům na počasí a plánovaní kampaně (Hall et al., 2016). Vysoká pořizovací cena snímků je problematická na úrovni obecních, městských lesů a soukromých vlastníků. Nízká operativnost a per-pixel přístup jsou nevhodné pro management disturbancí způsobených lýkožroutem, které vyžadují časté snímkování v aktivní sezóně lýkožrouta a rychlé zpracování z důvodu včasné identifikace jednotlivých napadených stromů a jejich asanace (Meigs et al., 2015; Senf et al., 2017). Pro cílenou asanaci jednotlivých napadených stromů je nezbytné použít snímky se submetrovým (<1 m) prostorovým rozlišením a klasifikaci automaticky nebo manuálně vymezených jednotlivých korun stromů (individual tree crown delineation – ITCD) , aby byl nahrazen tradiční terénní průzkum (Bater et al., 2010; Hall et al., 2016; Näsi et al., 2018; Wulder et al., 2012), proto se jeví jako ideální snímkování pomocí bezpilotních leteckých systémů (UAS).

UAS vybavené miniaturními multispektrálními nebo hyperspektrálními senzory jsou hojně používány pro nedestruktivní monitorování životního prostředí v mnoha oblastech, jako je precizní zemědělství, ochrana přírody a také lesnictví (Candiago et al., 2015; Pádua et al., 2017; Salamí et al., 2014; Torresan et al., 2017). V porovnání s družicovými multispektrálními senzory se bezpilotní senzory vyznačují podstatně vyšším prostorovým rozlišením, časovým rozlišením, zejména v oblastech s častou oblačností, flexibilitu v návrhu letecké kampaně a výměnu senzorů (Zhang & Kovacs, 2012). Ve srovnání s leteckým snímkováním mají senzory UAV nižší provozní náklady a lepší prostorové rozlišení, což umožňuje podrobnější analýzy studovaných lokalit (Näsi et al., 2015). Vysoká úroveň prostorových detailů, kterou umožňují nízké výšky snímkování, je však kompenzována omezeným prostorovým pokrytím kampaní, které vyplývá z krátké doby letu většiny bezpilotních snímkovacích

platforem. Kromě ultra vysokého prostorového rozlišení v řádu centimetrů jsou hlavními výhodami využití UAS pro detekci jednotlivých napadených stromů lýkožrouty relativně nízká pořizovací cena a možnost provádět opakovaná snímkování po období rojení, jakmile začnou být detekovatelné spektrální změny.

Historicky podmínku submetrového rozlišení splňovaly hlavně letecké senzory, ale bez dat o vertikální struktuře porostu bylo donedávna i tak obtížné provést segmentaci jednotlivých korun (Ke & Quackenbush, 2011; Senf et al., 2017). První metody segmentace korun z leteckých snímků pracovaly pouze s jasem snímků vysokého rozlišení ve 2D (Ke & Quackenbush, 2011). V současné době jsou však k dispozici moderní technologie laserového skenování nebo nové metody fotogrammetrie (structure from motion) poskytující i 3D informaci o struktuře porostu ve formě mračna bodů využitelnou pro segmentaci jednotlivých korun (Næsset, 2007; White et al., 2016). Tyto metody jsou použitelné nejen pro letecké snímky, ale i UAS snímky včetně multispektrálních (Guimarães et al., 2020; Hastings et al., 2020). Současné UAS multispektrální senzory používají spektrální pásma z viditelné a infračervené části spektra, která se v laboratorních studiích ukázala jako citlivá na změnu chlorofylu, takže jsou tyto UAS senzory vhodné pro monitoring zdravotního stavu vegetace (Adão et al., 2017; Assmann et al., 2018) a po aplikaci radiometrických korekcí i pro UAS spektroskopii (Aasen et al., 2018). To umožňuje získat z jedné sady UAS dat informace o spektrální charakteristice indikující napadení stromu lýkožroutem na úrovni jednotlivých stromů.

Ačkoli se může zdát velmi vysoké rozlišení UAS snímků v řádu centimetrů jako nejlepší, obrazová jednotka (pixel) je už tak malá v porovnání s mapovanou jednotkou, že to ztěžuje interpretaci klasifikované mapy v terénu. Proto nedávné studie zaměřené na detekci disturbance lesa způsobené lýkožroutem smrkovým ze snímků s ultra vysokým rozlišením (letecká nebo UAS data) použily klasifikaci zdravotního stavu stromů založenou na ITCD přístupu s manuálním (Dash et al., 2017; Kampen et al., 2019; Ortiz et al., 2013) nebo automatickým vymezením korun (Klouček et al., 2019; Näsi et al., 2015). Ve všech výše uvedených studiích byly použity standardní algoritmy strojového učení. Tyto algoritmy obvykle vyžadují heuristický výběr vhodných transformací obrazu a ručně vytvořené latentní proměnné, jako jsou vegetační indexy (Guimarães et al., 2020) a texturní metriky (Haralick, 1979), vytvořené z dat před modelováním (Kattenborn et al., 2021; Safonova et al., 2019). Výběr nejlepších prediktorů proto vyžaduje znalosti o interakcích mezi biochemickými vlastnostmi stromů různého zdravotního stavu a spektrální odezvou detekovanou senzorem (Kattenborn et al., 2021). Požadavek uživatelské znalosti je potenciální nevýhodou pro použití klasifikátorů strojového učení v lesnické praxi. Tuto nevýhodu však řeší algoritmy hlubokého učení, zejména konvoluční neuronové sítě (CNN), které nevyžadují transformaci obrazu a výpočet latentních proměnných (Chollet, 2017; Zhu et al., 2017). CNN se samy učí nejvhodnější obrazové transformace iterativně přímo v procesu trénování z předložených vzorů (Hoeser & Kuenzer, 2020; Kattenborn et al., 2021; Reichstein et al., 2019; Zhu et al., 2017). Díky této výhodě jsou CNN klasifikátory považovány za současnou metodu obrazové klasifikace dat (Hoeser & Kuenzer, 2020;

Kattenborn et al., 2021; Reichstein et al., 2019). Studie na detekci disturbance lesa způsobené škůdci na úrovni jednotlivých stromů pomocí CNN však stále nejsou běžné.

V současné době existuje pouze několik relativně nových studií na disturbance lesa způsobené škůdci a identifikaci jednotlivých napadených stromů z RGB snímků pomocí CNN, ale všechny se pouze zabývají základní klasifikaci na „zdravý“ bez změny barvy jehlic (bez rozlišení stromů nenapadených a ve fázi green attack), napadený se změnou barvy jehlic a mrtvý strom. Safonova et al. (2019) klasifikovali napadené skupiny (ne jednotlivé stromy) stromů *Abies sibirica Ledeb.* kůrovcem *Polygraphus proximus Blandf.* v boreálních lesích Sibiře pomocí CNN a RGB snímků. Nguyen et al. (2021) identifikovali jednotlivé napadené stromy *Abies mariesii Mast*. různými škůdci v Japonsku pomocí snímků RGB a algoritmu hlubokého učení natrénovaného na velkém souboru dat. Qin et al. (2021) identifikovali napadení jednotlivých borovic škůdcem *Bursaphelenchus xylophilus (Steiner & Buhrer, 1934) Nickle (1970)* v Číně opět pomocí RGB snímků a CNN klasifikátoru. Navíc žádná ze studií se nevěnovala klasifikaci zdravotního stavu lesa na úrovni jednotlivých stromů z multispektrálních či hyperspektrálních snímků pomocí CNN kvůli jejich nižšímu rozlišení. Existuje pouze několik studií zaměřených na klasifikaci druhové skladby lesa na úrovni jednotlivých korun pomocí CNN z UAS hyperspektrálních snímků, které potvrzují vysokou úspěšnost CNN klasifikátorů (Miyoshi et al., 2020; Nezami et al., 2020; Sothe, De Almeida, Schimalski, La Rosa, et al., 2020).

Závažnost, rozsah posledních kalamit a předpokládaný nárůst disturbancí vlivem klimatické změny zvýšil zájem vědců o pochopení mechanismů a faktorů spouštějících kalamitní přemnožení lýkožroutů a vývoj nových, relativně rychlých a vysoce automatizovaných postupů včasné detekce disturbance lesa a monitoring její dynamiky na úrovni jednotlivých stromů (Abdullah et al., 2018; Hall et al., 2016; Holopainen et al., 2014; Näsi et al., 2018). Porozumění je nedávných změn režimů disturbance vlivem klimatické změny je důležité pro vývoj nových strategií hospodaření jako je například hospodaření orientované na odolnost (Senf & Seidl, 2021). Předchozí výzkumy vyvolaly otázku, zda je možné detekovat nejen jednotlivé napadené stromy, ale i rozlišit, v jaké fázi napadení lýkožroutem se strom nachází se zaměřením na rozpoznání rané fáze, aby bylo možné skácet strom ještě před vyrojením další generace. Jako vhodné pro tento účel se jeví použití UAS multispektrálních snímků pro zachování vysokého rozlišení jako nutné podmínky pro klasifikaci na úrovni jednotlivých stromů (individual tree based classification – ITBC) přístupu a multispektrální data v kombinaci s nasazením pokročilých klasifikátorů hlubokého učení, což je předmětem předkládané disertační práce.

Cílem práce je ověřit využití metod UAS multispektrálního snímkování, fotogrammetrie a klasifikace obrazu pro studium dynamiky změn zdravotního stavu a disturbance lesa způsobené lýkožroutem smrkovým na úrovni jednotlivých stromů. Práce se zaměřuje na využití zcela nového typu miniaturizovaného multispektrálního senzoru v kombinaci s UAS nosičem a současných metod hlubokého učení pro ITBC klasifikaci obrazu. Základní hypotézou je, že tyto nové technologie pořizování přesné prostorové a kvalitativní informace umožní detekovat nejen napadené stromy, ale i jednotlivé fáze disturbance včetně rané fáze napadení (green attack) na úrovni jednotlivých stromů

bez retrospektivy pro získání nových poznatků o dynamice disturbance lesa v důsledku kůrovcové kalamity a lesního managementu. Mezi dílčí cíle disertační práce patří:

- Ověření, zda jsou jednotlivé fáze disturbance detekovatelné dostupnými UAS multispektrálními senzory.
- Navržení vhodné radiometrické kalibrace UAS multispektrálních senzorů proveditelné i v terénu pro získání senzorem a atmosférou nezkreslených hodnot odrazivosti objektů na snímku.
- Výběr vhodné metody identifikace a segmentace jednotlivých korun (ITCD) *Picea abies (L.) H. Karst* – smrků ztepilých ve smíšeném lese s využitím multispektrálních UAS snímků a fotogrammetrického mračna bodů.
- Návrh a ověření vhodné klasifikace fáze napadení jednotlivých stromů pomocí metod hlubokého učení na úrovni jednotlivých korun s využitím multispektrálních UAS snímků.

2. Současný stav poznání

2.1. Bezpilotní letecké systémy

Bezpilotní letecký systém (UAS) je definován jako celý systém, který zahrnuje bezpilotní letadlo (dron, unnmaned aerial vehicle – UAV) včetně veškerého technického a personálního vybavení potřebného k jeho řízení (Santamaria et al., 2012). UAV platformy se obvykle dělí do dvou skupin: pevná křídla (fixed-wing) a multikoptéry – rotary-wing (Toth & Jóźków, 2016). Oba typy jsou omezeny různými podmínkami plynoucí z jejich konstrukce (Anderson & Gaston, 2013). Letadla typu křídlo potřebují pro vzlet a přistání volný koridor v řádu desítek metrů, ale díky vyšší cestovní rychlosti, výšce letu a plachtění jsou schopny nasnímkovat větší území s rozlišením v řádu jednotek centimetrů. Multikoptéry startují a přistávají kolmo, mohou stát na místě nebo letět velmi nízkou rychlostí ve výšce pouze několika metrů nad povrchem, proto jsou vhodnější pro pokrytí menších území se subcentimetrovým prostorovým rozlišením. Při plánování výzkumu jen nutné zvolit vhodný typ UAV podle cíle výzkumu, ale vzhledem ke kolmému startu a lepší manévrovatelnosti se v lesnictví více používají (71 %) multikoptérové UAS (Guimarães et al., 2020).

Dálkový průzkum lesů pomocí UAS představuje současný výzkumný směr v lesnictví, protože UAS mají mnoho výhod oproti satelitnímu nebo družicovému DPZ. UAS mají nízké pořizovací a provozní náklady, umožňují operativní intenzivní sběr dat a flexibilní výměnu senzorů podle potřeb výzkumu (Zhang & Kovacs, 2012). Snímkovací let může být proveden v čase podle potřeb výzkumu (specifické fenologické fáze vegetace, období rojení a vysoké aktivity škůdců, požár, škody po vichřici), a také umožňují uživateli optimalizovat přesný čas letu, aby se vyhnul např. oblačnosti (Tang & Shao, 2015). V neposlední řadě bezpilotní letouny umožňují sběr dat s vysokým prostorovým rozlišením, což je v trvale udržitelném lesním hospodářství kritický aspekt na úrovni porostů (Pádua et al., 2017). Jediným limitem je velikost snímaného území, která závisí na výšce, letu a výdrži baterie v závislosti na zatížení UAS (Matese et al., 2015), ale při výměně baterií s mezipřistáním během mise dosahuje pokrytí řádu stovek hektarů až jednotek kilometrů čtverečních v závislosti na typu platformy (Guimarães et al., 2020; Pádua et al., 2017).

2.2. Spektrální pásma a UAS senzory pro detekci kůrovcové disturbance

Obecně platí, že schopnost detekovat vegetační stres z dat DPZ závisí na spektrálním, prostorovém, časovém a radiometrickém rozlišení senzorů (Chen & Meentemeyer, 2016; Wulder et al., 2009). Vegetační stres projevující se postupnou degradací rostlinných pigmentů chlorofylů, karotenoidů a antokyanů vlivem narušení vodivých pletiv kůrovci (změna barvy koruny) lze detekovat v pásmech viditelného (400–700 nm) a zejména red-edge (okolo 700 nm) spektra, které je u druhu *Picea abies (L.) H. Karst* (dále smrk nebo smrk ztepilý) nejcitlivější ke stresu a pomáhá pro detekci rané fáze napadení (Abdullah et al., 2018; Adamczyk & Osberger, 2015; Eitel et al., 2011; Masaitis et al., 2013). Kromě red-edge pásma pomáhá pro dřívější detekci disturbance také infračervené spektrum, a to zejména pásma blízkého, krátkovlnného a termálního infračerveného

spektra (Abdullah et al., 2018), kde jsou detekovatelné změny v absorpci vody napadených stromů mezi 1318 až 1322 nm (Cheng et al., 2010) a nárůst teploty koruny (Sprintsin, 2011). Vzhledem k spektrálním projevům kůrovcové disturbance se jeví jako ideální použití multispektrálních nebo hyperspektrálních senzorů. I přes nižší spektrální rozlišení jsou pro detekci disturbance lesa více používány multispektrální družicové senzory středního a vysokého rozlišení než hyperspektrální senzory z důvodu volně dostupných archivů umožňující i analýzu časových řad (Abdullah et al., 2019a, 2019b; Bárta et al., 2021; Fernandez-Carrillo et al., 2020; Hall et al., 2016; Hladky et al., 2020; Lausch et al., 2017; Senf et al., 2017; Stych et al., 2019). Nicméně i letecké hyperspektrální senzory byly v menší míře, kvůli vyšší náročnosti pořízení dat a zpracování, úspěšně použity pro detekci disturbance lesa (Campbell et al., 2004; Fassnacht et al., 2014; Lausch et al., 2013; Mišurec et al., 2016; Windrim et al., 2020). Současný technologický pokrok umožnil miniaturizaci multispektrálních a hyperspektrálních senzorů, takže je možné je zavěsit i na UAS.

Obecně se UAS senzory pro kvantitativní DPZ dělí na bodové spektrometry, pushbroom (řádkové) spektrometry a senzory s plošným (maticovým čipem) jako mají digitální fotoaparáty (Aasen et al., 2018). V lesnictví a agrolesnictví se používají téměř výhradně senzory s plošným čipem, které produkují snímky zpracovatelné fotogrammetrickými metodami do podoby klasického ortofota i 3D mračna bodů, aby bylo možné získat informace o strukturálních i fyziologických stavech porostu (Guimarães et al., 2020; Iglhaut et al., 2019; Pádua et al., 2017; Torresan et al., 2017). Ojediněle byly použity i pushbroom spektrometry, ale pouze ve fúzi s multispektrální kamerou nebo s lidarovými daty umožňující extrakci 3D modelu (Calderón et al., 2013; Lin et al., 2019).

Podle počtu pásem je možné dále senzory s plošným čipem rozdělit na klasické RGB, color-infrared (CIR), multispektrální kamery s více objektivy a hyperspektrální kamery (Aasen et al., 2018). Klasické RGB nebo CIR kamery umožňují pouze limitovanou detekci rané zelené fáze kůrovcové disturbance, protože operují pouze s RGB pásmy a filtrem neusměrněným blízkým infračerveným pásmem, až do maximální vlnové délky detekované čipem (Abdullah et al., 2018; Klouček et al., 2019). Výhodou RGB a CIR kamer je však vysoké rozlišení snímku (cca 3000 x 4000 pixelů) umožňující tvorbu podrobných 3D modelů korun pro segmentaci jednotlivých korun a vyšší výkon klasifikace sofistikovaných algoritmů hlubokého učení (Nguyen et al., 2021; Safonova et al., 2019). Naopak nejčastěji používané sekvenční hyperspektrální kamery, které snímají jednotlivá pásma obrazu postupně velmi malými časovými prodlevami, poskytují až sto úzkých spektrálních pásem ideálních pro detekci vegetačního stresu, ale bez doplňkové palubní navigační jednotky není možné snímky fotogrammetricky zpracovat (Adão et al., 2017). Pro detekci disturbance lesa byly UAS hyperspektrální sekvenční senzory použity zřídka (Honkavaara et al., 2020; Näsi et al., 2015, 2018). Dále existují hyperspektrální senzory skenující všechna pásma najednou (tzv. snapshot), kdy jsou jednotlivá pásma uložena střídavě v pixelech (mosaic filter-on-chip) nebo v řádcích (spatiospectral filter-on-chip) čtvercových segmentů pixelové matice. Tyto senzory zatím nebyly využity pro detekci disturbance lesa (Aasen et al., 2015, 2018).

Nejvíce se v současné době používají pro detekci disturbance lesa UAS multispektrální senzory s více objektivy vybavenými sadou multispektrálních filtrů s úzkým intervalem propouštěných vlnových délek umístěnou za objektivy (Guimarães et al., 2020; Torresan et al., 2017). Tyto senzory představují z pohledu detekce disturbance lesa ideální kompromis mezi CIR a hyperspektrálními senzory. Disponující prostorovým rozlišením cca 1280 x 960 pixelů umožňující bezproblémové fotogrammetrické zpracování. Zároveň kromě RGB pásem operují také v pásmu red-edge a úzké části infračerveného spektra, které jsou více citlivé na detekci zelené fáze napadení stromu. Nejnovější generace víceobjektivových senzorů disponuje také termální kamerou, která je schopna rozlišit změny teploty koruny vlivem napadení stromu kůrovcem v rané fázi (Smigaj et al., 2015).

2.3. Fotogrammetrické zpracování a klasifikace obrazu

V současné době je v lesnictví standardem použití nových fotogrammetrických metod structure from motion (SfM) umožňující extrakci 3D digitálního modelu korun ve formě mračna bodů ve fotogrammetrickém softwaru ze sekvence UAS snímků postupně pořízených během letu dronu, což umožňuje bezkontaktně získat informace i o struktuře stromového patra a je základem pro automatickou segmentaci korun ze snímku (Guimarães et al., 2020; Iglhaut et al., 2019). Techniky SfM poskytují mračna bodů založená na shodě prvků v překrývajících se snímcích (Fritz et al., 2013). Interpolací vytvořených hustých mračen bodů lze získat několik rastrových výstupů jako je digitální model povrchu nebo terénu, které mohou být použity pro ortogonalizaci MS snímků nebo pro přímé analýzy (Puliti et al., 2015). Na rozdíl od laserového skenování, signál nepronikne korunou a nelze získat informace o nižších patrech, ale to není limitující pro detekci disturbance lesa podle symptomů koruny (Kattenborn et al., 2021). Na druhou stranu lze fotogrammetrické mračno bodů získat z jakékoliv RGB nebo multispektrální kamery s běžným fotografickým snímačem (Aasen et al., 2018). Fotogrammetrické mračno bodů tak představuje levnější alternativu k mračnu z laserového skenování srovnatelné nebo lepší geometrické přesnosti pro ITCD (Iglhaut et al., 2019; Lisein et al., 2015; Puliti et al., 2015). V současné době se segmentace jednotlivých korun (ITCD přístup) z UAS dat používá zejména pro odvození základních inventarizačních parametrů jednotlivých stromů jako je výška, průměr koruny a druhovou klasifikaci jednotlivých stromů, ale studie zaměřené na detekci jednotlivých napadených stromů škůdci jsou stále v menšině (Guimarães et al., 2020; Iglhaut et al., 2019).

Dosavadní studie zaměřené na detekci kůrovcové disturbance lesa na úrovni jednotlivých stromů lze rozdělit do několika skupin podle postupu segmentace korun. Základním přístupem je manuální vektorizace korun nad multispektrálními snímky, vyčtení spektrálních hodnot a následná klasifikace korun, např. random forest modelem, generalizovanými lineárními modely nebo entropickými modely (Dash et al., 2017; Kampen et al., 2019). Manuální segmentace korun a zařazení do informační třídy disturbance je však časově náročná pro praktické využití v lesnictví. Jiné studie aplikují na multispektrální snímky klasickou objektovou klasifikaci (OBIA) implementovanou např. v eCognition, kdy jsou koruny tvořeny více segmenty složené z pixelů na základě spektrálních hodnot

a prostorového kontextu. (Adamczyk & Osberger, 2015; Brovkina et al., 2018; Heurich et al., 2010). Nejpokročilejší přístup kombinuje automatické vymezení jednotlivých korun stromů z fotogrammetrického mračna s následnou klasifikací korun jako jednotlivých objektů (ITBC). Tento přístup je nový a bylo publikováno pouze několik studií, které ale použily zjednodušenou reprezentaci jednotlivých korun stromů formou vrcholového bufferu (Klouček et al., 2019) nebo nejjasnějších vrcholových pixelů (Näsi et al., 2015). Navíc, tyto studie použily standardní klasifikátory strojového učení místo přirozeně nejvhodnějších CNN.

CNN jsou navrženy tak, aby se z předložených obrazových vzorů cílových tříd objektů (zde obrázky jednotlivých korun různých fází disturbance) naučily rozpoznávat typické rysy, textury nebo abstraktnější tvary, které nejlépe popisují cílovou třídu. (Hoeser & Kuenzer, 2020; Reichstein et al., 2019; Zhu et al., 2017). CNN se skládá z řetězce tzv. konvolučních a pooling vrstev zakončených klasifikační částí složenou z jedné nebo více plně zapojených vrstev – jednoduchý nebo mnohovrstvý perceptron (Chollet, 2017; Chollet & Allaire, 2018). V konvoluční vrstvě se zvýrazňují typické rysy objektů dané kategorie (zde koruny v různých stádiích disturbance) postupnými transformacemi obrazu prostřednictvím konvolučních operací v různých prostorových měřítcích prostřednictvím pooling operací z originálních spektrálních pásem senzoru (Hoeser & Kuenzer, 2020; Kattenborn et al., 2021; Zhu et al., 2017). Výsledkem řetězce konvolučních a pooling operací jsou dominantní rysy jednotlivých tříd transformované do vektoru hodnot, které vstupují do plně zapojených vrstev klasifikátoru.

Výhodou CNN oproti klasické OBIA pro ITBC je, že je obrazový segment (koruna) je předložen klasifikátoru jako celek a jsou hledány klíčové rysy celku (Kattenborn et al., 2021). U klasické OBIA jsou segmenty tvořeny automaticky podle spektrálních a prostorových kontextových informací (Blaschke, 2010). To nezaručuje, že koruny budou tvořeny pouze jedním segmentem (H. Huang et al., 2020; Onishi & Ise, 2021). Na rozdíl od ostatních metod strojového učení výhodou CNN pro klasifikaci značně spektrálně a kontextově heterogenní vegetace je, že transformace obrazu a identifikaci klíčových rozpoznávacích rysů jednotlivých tříd z předložených vzorů provádí síť sama prostřednictvím konvolučních a pooling operací a není potřeba provádět transformace obrazu (např. vegetační indexy) uživatelsky (Kattenborn et al., 2021). Nasazení CNN se stává současným standardem v příbuzných úlohách segmentace jednotlivých korun (Braga et al., 2020; Weinstein et al., 2019) nebo druhové klasifikace jednotlivých stromů (dos Santos et al., 2019; Onishi & Ise, 2021; Schiefer et al., 2020; Sothe, De Almeida, Schimalski, La Rosa, et al., 2020; Sothe, De Almeida, Schimalski, Liesenberg, et al., 2020), ale pro detekci disturbance lesa je nasazení CNN stále pionýrské (Kattenborn et al., 2021).

3. Materiál a metodika

3.1. Použité UAS systémy

V rámci disertační práce byly testovány dva bezpilotní letecké systémy. První systém tvořila multispektrální kamera Tetracam μ-MCA Snap 6 nesená oktokoptérou ARF MicroKopter OktoXL. Platforma je univerzální, vybavená dvouosým stabilizačním gimbalem s možností zavěsit jednu nebo více kamer až do hmotnosti 2500 g. Kamera Tetracam je vybavena šesti čipy typu global shutter s rozlišením 1280 x 1024 pixelů v kombinaci s objektivy s pevným ohniskem 9,6 mm a výměnnými spektrálními filtry (Tabulka 1).

Pásma byla vybrána pro detekci stresu vegetace způsobeného napadením lýkožroutem smrkovým pokrývající viditelnou, blízkou infračervenou (NIR) a red-edge část spektra podle rešerše literatury (Adamczyk & Osberger, 2015; Eitel et al., 2011; Fassnacht et al., 2014). Kamera byla dodána bez radiometrické kalibrace pro výpočet odrazivosti povrchu, kterou by bylo možné použít ve fotogrammetrickém programu. Nicméně, vhodná radiometrická kalibrace obecně použitelná pro multispektrální senzory byla navržena v rámci disertační práce (článek II a III). V dalším textu jsou také kanály označovány jako pásma 1-6.

Tabulka 1. Spektrální rozlišení kamery Tetracam μ-MCA Snap 6.

Číslo pásma	Filtry	Centrální vlnová délka (nm)	FWHM * (nm)
1	Green	550	20
2	Red	650	20
3	Red edge	700	20
4	Near infrared I (NIR)	800	20
5	Near infrared II (NIR)	850	20
6	Near infrared III (NIR)	900	20

* FWHM: full width at half maximum.

Druhý UAS se skládá z kvadrokoptéry DJI Matrice 210 RTK a multispektrální kamery MicaSense RedEdge-M. Kamera MicaSense RedEdge-M je vybavena pěti kanály se senzory typu global shutter (1280 × 980 pixelů), objektivy s pevnou ohniskovou vzdáleností 5,4 mm a pevnými spektrálními filtry (Tabulka 2). Ke kameře je připojen snímač dopadajícího světla (DLS) na těle dronu směrem vzhůru, který zaznamenává dopadající světlo ve stejných vlnových délkách jako kamera a ukládá je do metadat snímku. Tato metainformace automaticky koriguje surové snímky o změny osvětlení při fotogrammetrickém zpracování. Výhodou UAS je přesná navigace dronu pomocí real time kinematic metody určení pozice bez nutnosti zaměřování vlícovacích bodů a výrobcem definovaná absolutní radiometrická kalibrace kamery, která je součástí fotogrammetrického software. Nevýhodou UAS je uzavřenost systému, kdy na dron mohou být zavěšeny pouze kamery s DJI bajonetem, což není případ kamery Tetracam. Kamera MicaSense byla použita v článcích IV a V.

Tabulka 2. Spektrální rozlišení kamery MicaSense RedEdge-M.

Číslo pásma	Filtry	Centrální vlnová délka (nm)	FWHM * (nm)
1	Blue	475	20
2	Green	560	20
3	Red	668	10
4	Red edge	717	10
5	Near infrared (NIR)	840	40

* FWHM: full width at half maximum.

3.2. Zájmové území

V disertační práci byla vybrána dvě zájmová území reprezentující dva typy lesa: horský smrkový les s přirozeným výskytem disturbancí a hospodářský smíšený les v městské aglomeraci postižený disturbancí z důvodu zvýšení četnosti klimatických extrémů a nevhodné skladby dřevin. Tyto dva typy lesa byly vybrány záměrně, aby byly metody multispektrální UAS fotogrammetrie a klasifikace obrazu testovány na typech lesa s odlišnou dynamikou disturbance. V horském smrkovém lese jsou kůrovcové disturbance přirozenou součástí obnovy porostu a dosahují nižší dynamiky vlivem kratší aktivní sezóny lýkožrouta než v nepůvodních porostech v nížinách díky horskému klimatu (Kulakowski & Bebi, 2004). Na druhé straně hospodářský les v nížině vykazuje vysokou dynamiku disturbance z důvodu dlouhé aktivní sezóny lýkožrouta a vývoji několika generací ročně díky teplejšímu klimatu a suchu (Näsi et al., 2018). Navíc městské klima se zvýšeným obsahem oxidu uhličitého v ovzduší působí jako aditivní stresový faktor ještě více oslabující obranyschopnost stromů a zvyšuje dynamiku disturbance (Alvey, 2006; Tubby & Webber, 2010).

Lokalita přirozeného horského smrkového lesa byla vybrána tak, aby zde probíhala aktivní disturbance a byly zde zastoupeny plochy v rozdílném stádiu disturbance a zároveň procesy nebyly narušeny zásahem člověka. Lokalita se nacházela na okraji bezzásahové I. Zóny Národního parku Šumava v povodí Hamerského potoka. Po větrných smrštích na bavorské straně pohoří došlo v polovině 80. let 20. století k masivnímu napadení lýkožroutem smrkovým což mělo za následek rozsáhlé narušení a rozpad lesa. Napadení bylo dále urychleno po větrných smrštích v letech 2007 a 2008 a co do rozsahu a intenzity bylo významné v evropském měřítku (Borrelli et al., 2016). V důsledku toho bylo zájmové území tvořené komplexní strukturou dospělých smrků, souší, rozpadlých kmenů a obnovujícího se mladého lesa (Obr. 1). Cílem bylo ověřit, zda jsou metody UAS fotogrammetrie vhodné pro detekci disturbance v takto komplexních přirozeného lesa s rozlišením základních fází disturbance a obnovy lesa (článek I).

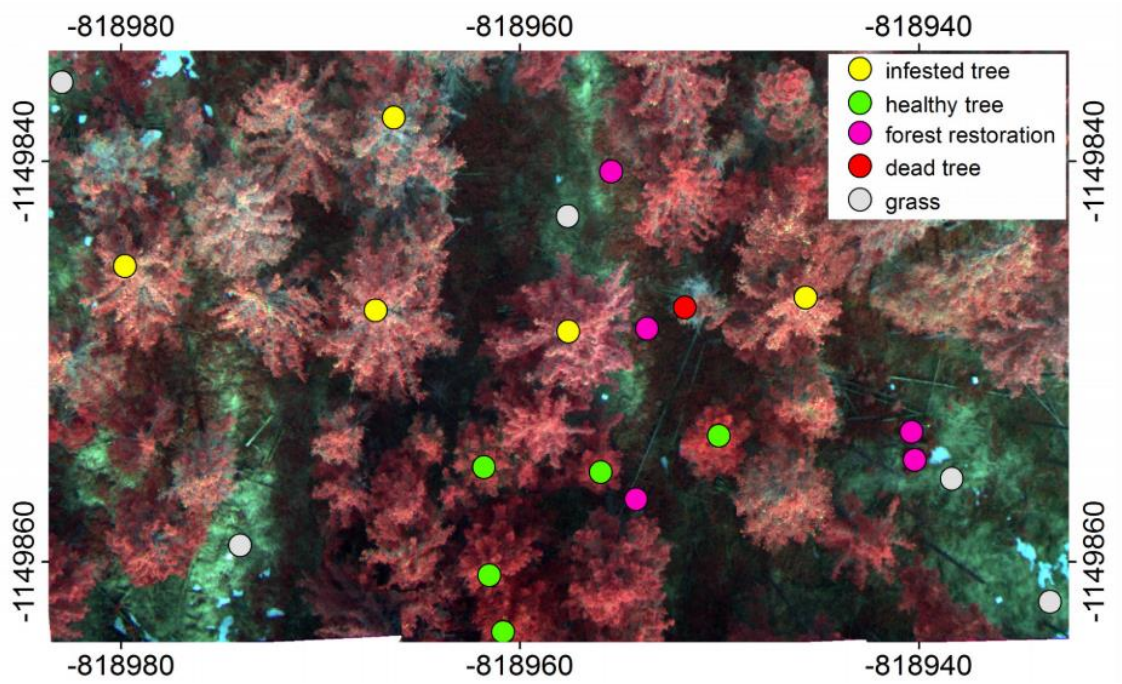

Obr. 1. Detailní UAS ortofoto v nepravých barvách pokusné lokality přirozeného horského smrkového lesa na Šumavě.

Reprezentativní lokalita hospodářského lesa byla vybrána v Klánovickém lese. Klánovický les představuje největší komplex příměstských lesů v pražské metropolitní oblasti. Od roku 1982 je téměř celý lesní komplex chráněn jako přírodní rezervace s několika cennými částmi, které mají vyšší status ochrany v rámci soustavy Natura 2000. V současné době má Klánovický les rozlohu 1030 ha a vyznačuje se smíšenou strukturou listnatých a jehličnatých dřevin s převahou dubu 33 %, borovice 31 %, břízy 11 % a smrku ztepilého 6 % (MHMP., 2020). Od roku 2015 byl Klánovický les zasažen opakovanými disturbancemi z důvodu přemnožení lýkožrouta smrkového a vichřicemi (Hujslova & Simandl, 2018). Rychlý postup disturbance umocnilo pětileté období sucha, které vedlo ke snížení přirozené obranyschopnosti stromů před lýkožroutem a vývoji čtyř generací brouků za rok (Hlásny et al., 2019). Cílem experimentů na této lokalitě (Obr. 2) bylo ověřit vhodnost metod UAS fotogrammetrie pro detekci jednotlivých fází disturbance pro získání poznatků o její dynamice na úrovni jednotlivých stromů v heterogenních podmínkách smíšeného lesa (článek IV a V).

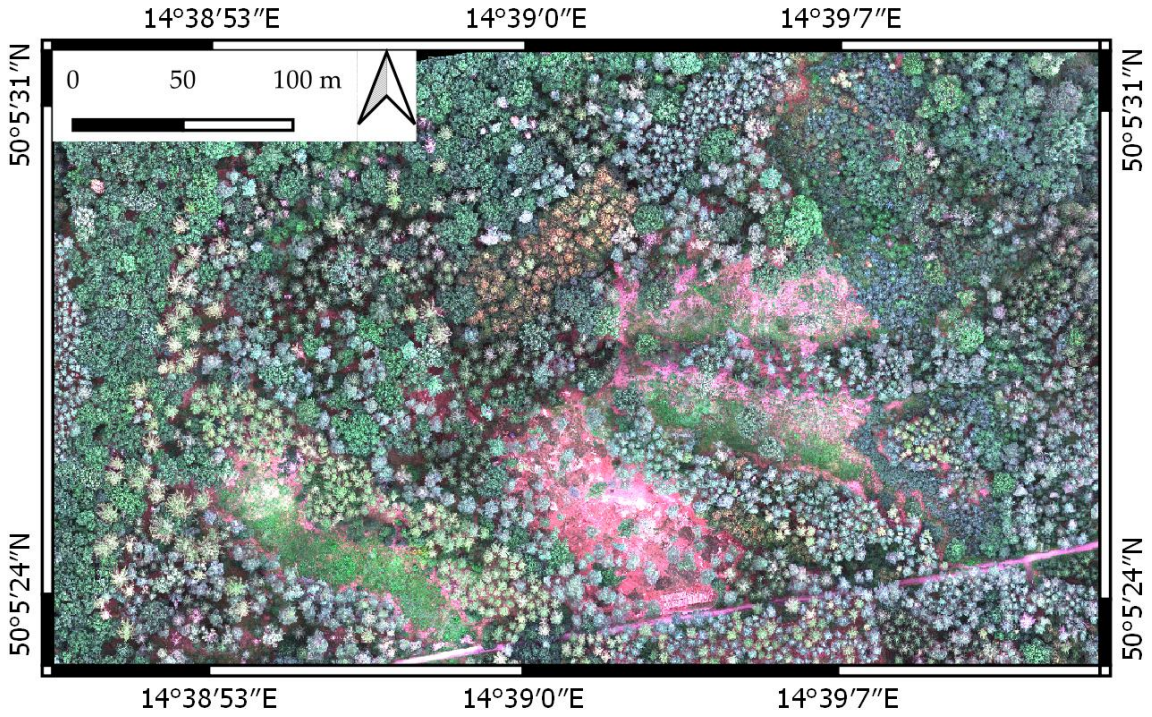

Obr. 2. Detailní UAS ortofoto v pravých barvách pokusné lokality hospodářského smíšeného lesa v Klánovickém

3.3. Metodika detekce jednotlivých fází disturbance

Pilotní studie (článek I) se zaměřila na testování detekce základních fází disturbance a obnovy lesa v přirozených podmínkách smrkové monokultury pomocí UAS multispektrální fotogrammetrie a ověření vhodnosti vybraných pásem multispektrální kamery Tetracam μ-MCA Snap 6 pro tento účel. Podle výsledků pilotní studie byla vypracována současná metodika.

První částí bylo navržení obecné radiometrické kalibrace multispektrální kamery s více objektivy na příkladu Tetracam μ-MCA Snap 6 (článek II a III). Navržená metodika zahrnuje obě fáze radiometrické kalibrace DPZ senzorů pro každý kanál kamery. Metodika zahrnuje jak radiometrické (senzorové) korekce pro normalizaci DN hodnot pixelů, tak atmosférické korekce pro výpočet odrazivosti z normalizovaných DN hodnot (Aspinall et al., 2002).

Druhou částí bylo navržení a otestování metodiky automatické segmentace celých korun jehličnatých dřevin ve smíšeném lese z fotogrammetrického mračna bodů (PPC) a radiometricky kalibrovaného ortofota za účelem extrakce a srovnání specifických příznaků jednotlivých fází napadení (článek IV). Bylo zkoumáno, jak ovlivňuje hustota bodů PPC přesnost jednotlivých metod segmentace, zda je jejich přesnost natolik vysoká, že se extrahované spektrální a výškové příznaky (charakteristiky) jednotlivých kategorií disturbance z automaticky vymezených korun statisticky významně neliší od charakteristik extrahovaných z referenčních manuálně vymezených korun a je tedy možné stále rozlišit jednotlivé kategorie. Referenční stromy byly mapovány pozemním geodetickým průzkumem a byly

zatřízeny do čtyř kategorií: borovice a tři třídy smrku podle stádia napadení sbbd (přechod mezi fázemi napadení green attack a red attack, kdy jehlice žloutnou), sbbg (smrky ve fázi napadení green attack) a sh (nenapadené stromy). Borovice byly zařazeny, protože jejich spektrální chování bylo podobné kategorii sbbd.

V návaznosti na automatickou segmentaci korun byla navržena a testována klasifikace fází disturbance na úrovni celých korun využívající CNN (článek V). Byly porovnány tři architektury CNN pro klasifikaci jednotlivých korun stromů do stejných čtyř kategorií: borovice, sbbd, sbbg, sh. Vzhledem k zamýšlenému fotogrammetrickému zpracování (využití 3D mračna bodů pro segmentaci) a klasifikaci celých korun pomocí CNN nebylo uvažováno o vyzkoušení hyperspektrálního senzoru z důvodů nízkého prostorového rozlišení a problematické koregistraci pásem. Fotogrammetrické zpracování všech leteckých kampaní proběhlo metodou SfM v programu Agisoft Metashape. V následujících podkapitolách jsou stručně popsány metody a experimenty disertační práce.

3.3.1. Radiometrická kalibrace

Senzorové korekce byly založeny na laboratorních metodách redukce šumu senzoru, vinětace objektivu a nestejné kvantové účinnosti světločivných buněk snímače jako hlavních zdrojů chyb (Kelcey & Lucieer, 2012; Mansouri et al., 2005; Olsen et al., 2010). Pro potlačení šumu byla zvolena obrazová metoda dark offset subtraction (Kelcey & Lucieer, 2012; Mullikin et al., 1994). Metoda je založena na vybudování databáze průměrných temných snímků pro běžně používané expoziční časy snímkování, kdy je signál generován hlavně zahříváním snímače. Efekty vinětace a nevyrovnané kvantové účinnosti světločivných buněk snímače byly potlačeny obrazovou metodou look-up-table (Yu, 2004). Metoda je založena na výpočtu průměrného korekčního faktoru vinětace ze sady snímků spektrálně homogenní plochy nasvícené uniformním světlem (tzv. flat field) pro běžně používané expoziční časy snímkování. Korekční faktor je spočítán pro každý pixel jako poměr maximální hodnoty jasu (DN) ze všech pixelů průměrného snímku a aktuální hodnoty DN každého pixelu. Z různých metodik atmosférické korekce byla zvolena in-situ kalibrace založená na metodě empirické linie (Teillet, 1986), která se používá i pro snímkování bezpilotními letouny a může být relativně snadno použita ve fotogrammetrickém software (Berni, Zarco-Tejada, Suárez, González-Dugo, et al., 2009; Yang et al., 2017). Principem metody je kvantifikace lineárního vztahu mezi DN hodnotami a referenční odrazivosti kalibračních terčů. Tato metoda výrazně omezuje vliv atmosférické vlivy, převádí DN na odrazivost a umožňuje tak porovnávat soubory dat, které byly pořízeny v různých ročních obdobích a za různých světelných podmínek (Smith & Milton, 1999). Pro získání databáze korekčních temných a flat field snímků byl proveden experiment v kalibrační laboratoři Ústavu výzkumu globální změny AV ČR, v. v. i. (CzechGlobe). Nastavení experimentů simulovalo běžné podmínky a časy expozice používané při snímkování, aby vzniklá databáze korekčních snímků mohla sloužit pro korekci snímků z terénu.

Účinnost radiometrické kalibrace byla hodnocena na kalibračních terčích se známou hodnotou odrazivosti. Pro hodnocení účinnosti radiometrické kalibrace byl vybrán multispektrální snímek z terénní kampaně. Dva terče byly umístěny uprostřed pro konstrukci empirické linie. Tři validační terče byly umístěny v rozích snímku, kde lze předpokládat silný vliv vinětace. V rámci kalibrace byl nejprve odečten průměrný temný snímek pro stejný expoziční čas. Poté byl každý snímek vynásoben korekčním snímkem flat field pro potlačení vinětace, nevyrovnané kvantové účinnosti a byla provedena atmosférická korekce. Pak byla porovnána průměrná hodnota odrazivosti pixelů validačních terčů surového snímku a plně kalibrovaného snímku.

3.3.2. Segmentace jednotlivých korun

Navržená automatizovaná segmentace korun je založena na maskování cílových dřevin na začátku procesu díky vhodného načasování snímkování, kdy jsou zelené jen jehličnany. Nejprve jsou odvozeny masky jehličnanů vypočítané z multispektrálního ortofota. Základní vegetační maska oddělující zelené jehličnany od pozadí byla vypočítána prahováním excess green indexu (ExG) (Torres-Sánchez et al., 2015). Prahová hodnota byla získána pomocí neřízené klasifikace k-means do dvou tříd a vizuální interpretace tříd (Cardil et al., 2019). Pro lepší odfiltrování falešně pozitivních vrcholů korun tvořených zastíněnými hlavními větvemi byla vypočítána stejným postupem dodatečná maska stínů z NIR pásma (Ke & Quackenbush, 2011), která je aplikována pouze ve fázi identifikace vrcholů korun. Vegetační masky jsou aplikovány přímo na PPC nebo z něho odvozený výškový model korun (canopy height model – CHM). Poté jsou aplikovány vybrané metody automatické segmentace jednotlivých korun stromů na maskované PPC nebo CHM.

Bylo provedeno srovnání tří současných metod segmentace korun používané v leteckém laserovém skenování (Roussel et al., 2020), které jsou nyní aplikovány na PPC. Byly vybrány metody Dalponte2016 (Dalponte & Coomes, 2016), marker-controlled watershed segmentation (MCWS) (Meyer & Beucher, 1990) a Li2012 (Li et al., 2012), protože byly vysoce hodnoceny v předchozích srovnávacích studiích Xiao et al. (2019) a Hastings et al. (2020). Kromě pokročilých metod segmentace byla testována také základní metoda Bufferu okolo identifikovaného vrcholu koruny. Vrcholy korun použité v algoritmech Dalponte2016, MCWS a Bufferu byly nalezeny pomocí filtru lokálního maxima (lmf) s proměnlivou velikostí vyhledávacího okna podle výšky stromu (Popescu & Wynne, 2004). Navíc byl zkoumán vliv hustoty PPC na přesnost segmentace, protože se originální PPC ultra vysoké kvality (701 bodů/m^2) ukázalo jako příliš husté. PPC bylo decimováno různými gridy o velikosti 0,1–1 m. V rámci gridu byl zachován pouze nejvyšší bod.

Vybrané spektrální a výškové příznaky korun (vegetační indexy NDVI, ENDVI, NDRE, plocha koruny a kvartily výšky 3D bodů tvořících korunu) extrahované z multispektrálního ortofota a PPC z automaticky segmentovaných korun jednotlivých metod byly porovnány se statistikami korun referenčních stromů jednotlivých tříd disturbance. Geometrická shodnost byla kvantifikována

metrikami „detection accuracy score“ (DA) (Yin & Wang, 2016) a „quality rate“ (QR) index (Weidner, 2008).

3.3.3. Klasifikace jednotlivých fází disturbance

Pro účely klasifikace a zachování relativní jednoduchosti klasifikace byla použita segmentace metodou Buffer a byla použita pouze originální pásma multispektrálního ortofota, protože předchozí studie potvrzují, že pro CNN klasifikátor jsou tyto základní vstupy dostatečné (Geng et al., 2017; Hartling et al., 2019). Automatická identifikace korun proběhla ověřenou metodou lmf (Popescu & Wynne, 2004). Poté byl automaticky vytvořen okolo vrcholového bodu čtvercový buffer rozdílných velikostí podle kvartilů výšky stromů z PPC. Vytvořený buffer sloužil pro extrakci odrazivosti jednotlivých korun stromů z ortofota pro účely analýzy spektrálních odlišností a klasifikaci jednotlivých fází disturbance na úrovni celých korun. Analýza spektrálních odlišností sloužila pro výběr informačně nejhodnotnějších pásem pro klasifikaci.

Pro účely klasifikace jednotlivých fází disturbance byly testovány tři architektury CNN vhodné pro malé datasety. Jako první byla použita modifikovaná relativně jednoduchá síť ze studie Nezami et al. (2020), označená jako Nez. Pro rychlý pokles ztrátové funkce (loss function) a optimální rychlost učení se dávky (batches) trénovacích vzorů skládaly pouze z jednoho snímku. Tento postup byl teoreticky navržen autory Chollet & Allaire (2018), ale prakticky nevyzkoušen. Síť Nez byla trénována přímo (from scratch) a bez data augmentation. Jako druhá byla navržena vlastní složitější CNN inspirovaná studií Safonova et al. (2019), ale upravená na multispektrální data. Tato síť byla rovněž trénována přímo (from scratch) ve dvou verzích označovaných jako Saf bez data augmentation a Safaugu zahrnující data augmentation. Jako poslední byla vyzkoušena metoda transfer learning sítě DenseNet 169 (G. Huang et al., 2017) s předtrénovanými vahami z datasetu ImageNet, protože dosáhla vysoké přesnosti v předchozích studiích (Natesan et al., 2020; Safonova et al., 2019). Ze sítě DenseNet 169 byla implementována celá konvoluční báze a byl napsán pouze klasifikátor na výstupu.

Pro trénování všech CNN modelů byla použita ztrátová funkce cross-entropy a optimizátor adaptive moment estimation optimizer – Adam (Kingma & Ba, 2014). Celkově bylo k dispozici 672 referenčních stromů s automaticky segmentovanými korunami, které byly náhodně rozděleny na trénovací, validační a testovací dataset v poměru 70:10:20. Relativní četnost jednotlivých kategorií byla zachována ve všech datasetech. Pro srovnání přínosu CNN pro klasifikaci jednotlivých fází disturbance bylo provedeno srovnání s výsledky klasifikace běžně používaným modelem random forest (Breiman, 2001). Chybová matice byla vypočítána na základě porovnání predikovaných a referenčních tříd disturbance. Z chybové matice byla pro každý model a každou informační třídu vypočítána přesnost klasifikace. Porovnání přesnosti klasifikace mezi třídami bylo prostřednictvím metrik uživatelské přesnosti (precision – p) (p), zpracovatelské přesnosti (recall – r) a F-score (Kattenborn et al., 2021). Celková výkonnost modelů byla hodnocena pomocí průměrného F-score a Cohenova kappa indexu (Congalton, 1991).

4. Výsledky

V kapitole jsou shrnuty výsledky pěti článků disertační práce. Tři články byly publikovány v impaktovaném časopise *Remote sensing* (IF_{2020} = 4.848) a dva články v recenzovaných sbornících *The International Archives of the Photogrammetry, Remote Sensing and Spatial Information Sciences* indexovaných na Web of Science.

4.1. Článek I

Minařík, R., & Langhammer, J. (2016). Use of a multispectral UAV photogrammetry for detection and tracking of forest disturbance dynamics. In L. Halounova (Ed.), *International Archives of the Photogrammetry, Remote Sensing and Spatial Information Sciences: Vols. XLI-B8* (pp. 711–718). Copernicus GmbH. https://doi.org/10.5194/isprsarchives-XLI-B8-711-2016

Studie se zaměřuje na ověření schopnosti detekovat základní fáze disturbance a obnovy lesa v přirozeném prostředí horského smrkového lesa pomocí UAS systému s multispektrální kamerou Tetracam μ-MCA Snap 6. Pro ověření základní metodiky byla zahájena snímkovací kampaň na experimentální lokalitě s různými fázemi narušení a obnovy lesa. Spektrální křivky jednotlivých kategorií byly extrahovány ze surových DN hodnot z vrcholového bufferu. Dále byly vypočítány vybrané vegetační indexy umožňující detekci vegetačního stresu. Snímky s vysokým prostorovým a spektrálním rozlišením umožnily na základě různé spektrální odezvy ze snímků detekovat jednotlivé základní fáze disturbance: zdravé – nenapadené, napadené a mrtvé smrky, semenáčky stromů přirozené obnovy a trávu.

Ve srovnání se zdravými stromy jsou celkově hodnoty DN napadených stromů významně vyšší ve viditelných vlnových délkách a významně nižší v NIR vlnových délkách. Hodnoty DN odumřelých stromů jsou od napadených stromů signifikantně oddělitelné pouze v červené a red-edge části spektra. Nejlépe je vegetační stres způsobený napadením stromu lýkožroutem smrkovým rozpoznatelný v pásmech kamery odpovídající červené (650 nm), red-edge (700 nm) a NIR (800 nm) části spektra.

Byly identifikovány pouze tři indexy, které se jsou schopny rozpoznat různé kategorie disturbance lesa ve komplexních podmínkách. Z testovaných indexů se nejlepší schopnost oddělit různé kategorie projevila u klasického indexu NDVI. Mezi analyzovanými indexy to byl jediný index, u kterého se mezikvartilové rozpětí hodnot (IRQ) mezi danými kategoriemi nepřekrývalo. Index NDVI se projevil jako citlivější ve vyšších hodnotách, kterých dosahují zdravé a krátce napadené stromy. Jednoduchý poměrový index pásem 800/650 umožnil rozlišit zdravé, napadené stromy a obnovující se patro od přízemní vegetace. Poměrový index 800/650 se projevil jako citlivější k nižším hodnotám silně narušených a mrtvých stromů. Třetím vhodným indexem byl NDRE (obdoba NDVI, ale červené pásmo je nahrazeno red-edge), který rozlišil základní fáze disturbance (zdravé, napadené, mrtvé).

Prvotní studie prokázala dobrou odlišitelnost základních fází disturbance ze surových multispektrálních snímků a nasměrovala další výzkum. Pro porovnání multispektrálních ortofot z různých kamer nebo analýzu časových změn bylo nutné navrhnout radiometrickou kalibraci

snímků. Vysoké rozlišení snímků v řádu centimetrů schopné rozlišit neolistěné části větví přineslo novou výzvu pro návrh metod klasifikace korun jako celku, protože jedna koruna vytvořila heterogenní směs pixelů s vysokou variabilitou hodnot.

4.2. Článek II

Minařík, R., Langhammer, J., & Hanuš, J. (2019). Radiometric and Atmospheric Corrections of Multispectral μMCA Camera for UAV Spectroscopy. *Remote Sensing*, *11*(20), 2428. https://doi.org/10.3390/rs11202428

Tato studie představuje komplexní radiometrickou kalibrační metodu založenou na obrazových metodách korekce pro víceobjektivové multispektrální kamery na příkladu kalibrace Tetracam μMCA. Laboratorním experimentem byla zjištěna statisticky významná závislost šumu jak na teplotě okolí, tak na expozičním čase. Silnější závislost šumu na teplotě okolí byla odhalena v červené, red-edge, NIR II a III (850 a 900 nm) části spektra. Silnější závislost šumu na expozičním čase byla odhalena v zeleném a NIR I (800 nm) pásmu. Pozitivní interakce faktorů teploty okolí a expozičního času se projevila v zeleném, červeném, red-edge, NIR II a NIR III pásmu. V těchto pásmech došlo k rychlému nárůstu šumu v měřeních od 19 ° do 27 °C při delších dobách expozice (500 a 1000 μS). Výsledky laboratorního experimentu také odhalily závislost hodnoty korekčního koeficientu vinětace na expozičním čase a intenzitě dopadajícího záření. Nejsilnější efekt vinětace a nejvyšší hodnoty korekčního koeficientu byly v pásmech 1 a 4, následovaných pásmy 6, 5, 2 a 3. Jasně se prokázalo, že průměrný korekční koeficient klesá s prodlužující se dobou expozice a silnějším osvětlením u všech pásem. Průměrná hodnota korekčního koeficientu se lišila pro každé pásmo při stejných hodnotách expozičního času a intenzitě osvětlení z důvodu relativních posunů snímače a ohniska. Celkově výsledky laboratorního experimentu ukázaly nutnost sestavit databázi korekčních snímků šumu a vinětace každého kanálu zvlášť pro různé kombinace expozičních časů v různých ročních obdobích (definované okolní teplotou a intenzitou záření) z důvodu jejich odlišného chování popsaného výše.

Účinek navrženého senzorových korekcí byl nejprve zkoumány pomocí náhodně vybraného diagonálního profilu v písku porovnáním normalizovaných a surových DN hodnot a jejich variability. Na rozdíl od surového profilu, normalizovaný profil vykazoval žádný nebo minimální pokles DN hodnot směrem k okrajům. Dále došlo ke statisticky významnému poklesu variačního koeficientu (CV) o 50–70 % u normalizovaných hodnot v porovnání se surovými daty. Účinnost radiometrické kalibrace byla hodnocena na kalibračních terčích se známou hodnotou odrazivosti. Aplikace atmosférické korekce metodou empirické linie na normalizované DN vedla k významně přesnějšímu určení odrazivosti tří validačních terčů ve srovnání s nezpracovanými daty. Normalizovaná odmocnina střední kvadratické chyby (NRMSE) určení odrazivosti každého terče klesla dvakrát až desetkrát u kalibrovaného snímku ve srovnání se surovým. U kalibrovaného snímku byla NRMSE všech pásem v intervalu 0,24 až 2,10 %. K největšímu zlepšení došlo podle očekávání u terčů nejvíce postižených efektem vinětace.

Celkově výsledky studie potvrdily obecný předpoklad, že největší dopad na celkovou přesnost měla redukce efektu vinětace pomocí metody LUT, která vedla k významnému snížení rozptylu diagonálního profilu a přesnému výpočtu odrazivosti kontrolních terčů. Výsledky studie prokázaly, že navržená radiometrická kalibrace vedla k získání (obnově) senzorem a atmosférou nezkreslených hodnot odrazivosti testovacích terčů velmi blízké jejich skutečné hodnotě, což je klíčové pro porovnání odrazivosti objektů zemského povrchu ze snímků pořízených za různých světelných podmínek např. pro analýzu časových změn. Současně byla prokázána jeho praktická použitelnost v podmínkách terénních kampaní a kalibrace je aplikovatelná i na další vícekanálové multispektrální kamery, které jsou vybaveny CCD/CMOS senzory typu global shutter.

4.3. Článek III

Minařík, R., & Langhammer, J. (2019). Rapid Radiometric calibration of multiple camera array using in-situ data for UAV multispectral photogrammetry. *The International Archives of the Photogrammetry, Remote Sensing and Spatial Information Sciences*, *XLII-2/W17*, 209–215. https://doi.org/10.5194/isprs-archives-XLII-2-W17-209-2019

Tato studie porovnává dva možné přístupy radiometrické kalibrace multispektrální kamery Tetracam μMCA Snap pomocí metody redukce šumu dark offset subtraction, metody redukce vinětace LUT a atmosférické korekce empirickou linií. Laboratorní kalibrace s použitím korekčních snímků pořízených v kontrolovaných podmínkách byla porovnána s rychlou in-situ kalibrací s použitím korekčních snímků pořízených během terénní kampaně. Předpokládalo se, že přesnost kalibrace in-situ by mohla být srovnatelná s laboratorní kalibrací, mohla by ji nahradit a zjednodušit proces radiometrické kalibrace.

Experiment byl proveden pro univerzální expoziční čas 500μS. Snímky pro dark offset subtraction byly pořízeny in-situ v černém přepravním kufru kamery. Jako flat field plocha pro výpočet korekčního koeficientu metodou LUT byl použit světlý kalibrační terč připravený v místě vzletu. Přesnost kalibračních přístupů byla posouzena porovnáním hodnot odrazivosti tří validačních terčů extrahovaných z kalibrovaných snímků na základě laboratorního nebo in-situ postupu s referenčním spektroskopickým měřením. Významnost rozdílů mezi kalibračními postupy byla hodnocena Mann-Whitneyho U testem.

U obou způsobů kalibrace byla také dosaženo podobné zlepšení přesnosti výsledných hodnot odrazivosti kalibračních terčů, ale u laboratorního postupu byly dosaženy mírně nižší hodnoty NRMSE naznačující menší zbytkový rozptyl (laboratorní NRMSE 0,24 až 2,10 %; in-situ NRMSE 0,24 až 3,40 %). Výsledné p-hodnoty potvrzují ve většině případů významně nižší hodnoty NRMSE laboratorní kalibrace, ale zlepšení přesnosti kvantifikované pomocí NRMSE je při použití obou kalibračních přístupů ve srovnání s nezpracovanými daty dvakrát až desetkrát vyšší než rozdíly NRMSE mezi nimi, proto lze obě metody považovat za vysoce použitelné pro UAS snímkování.

4.4. Článek IV

Minařík, R., Langhammer, J., & Lendzioch, T. (2020). Automatic Tree Crown Extraction from UAS Multispectral Imagery for the Detection of Bark Beetle Disturbance in Mixed Forests. *Remote Sensing*, *12*(24), 4081. https://doi.org/10.3390/rs12244081

V této studii byla navržena metodika vymezení jednotlivých korun stromů (ITCD) pro detekci disturbance lesa ve smíšeném lese pomocí fotogrammetrického mračna bodů (PPC) a multispektrálního ortofota za účelem extrakce specifických příznaků napadených stromů. Použití masky zelené vegetace mělo vysoce pozitivní vliv na odfiltrování nezeleného pozadí a nežádoucích druhů dřevin, takže byly detekovány a segmentovány pouze koruny cílových smrků v různém stádiu disturbance a borovic pro odlišení od pokročile napadených smrků sbbd. Kromě ušetření výpočetního času segmentace a redukci falešných vrcholů, mělo maskování i vysoce pozitivní efekt na přesnost segmentace automatických korun v porovnání s referenčními korunami, protože byly částečně potlačeny mixely spodních větví a pozadí mezi korunami.

Výsledky odhalily silný vliv hustoty PPC na detekci vrcholů a segmentaci korun. Originální PPC s extrémní hustotou 701 bodů/m^2 se ukázalo jako naprosto nevhodné a dosáhlo F-score detekce vrcholů korun pouze 0,61-0,67 kvůli vysokému počtu falešně pozitivních detekcí tvořených multi-vrcholy, které vedly ke vzniku duplicitních segmentů korun, ale decimace mračna v pravidelném gridu vedla k eliminaci tohoto efektu. Výsledky prokázaly pozitivní efekt mírné a střední redukce hustoty PPC na 10–85 bodů/m^2 (odpovídá decimačnímu gridu 0,3 – 0,1m). Nižší nebo vyšší hustota bodů měla negativní vliv na přesnost detekce vrcholů. Výsledné F-score bylo srovnatelné v rozmezí 0,95–0,96 u všech datasetů. Statistické testy neprokázaly významný rozdíl mezi přesností segmentace metod Dalponte2016, MCWS a Li2012 provedené na mračnech s hustotou bodů 10–85 bodů/m^2. V případě PPC s nízkou testovanou hustotou 1 a 4 body/m^2 došlo ke snížení přesnosti segmentace a byly významné rozdíly mezi metodami. Nejlepší přesnosti bylo dosažené metodou MCWS. Metoda Buffer dosáhla vždy nižšího výkonu z důvodu zjednodušení interpretace koruny.

Srovnání spektrálních a výškových příznaků automaticky vymezených korun s referenčními bylo provedeno pouze pro mračna s hustotou 22 bodů/m^2 (dále las02) a 1bod/m^2 (dále las1) jako optimální a nedostatečná varianta. V případě mračna las02 nebyly zjištěny statisticky významné rozdíly spektrálních a výškových příznaků korun stromů v rámci jednotlivých kategorií disturbance mezi referenčními a automatickými korunami jednotlivých metod segmentace. Mračno las1 bylo příliš řídké pro přesnou segmentaci korun, což se projevilo i ve statisticky významných rozdílech příznaků automatických a referenčních korun jednotlivých metod.

Celkově výsledky prokázaly, že větší vliv na přesnost segmentace a extrakci specifických příznaků napadených stromů měla hustota bodového mračna než zvolená metoda segmentace. Nejpřesnější a robustní metodou vůči hustotě bodů byla metoda MCWS. Spektrální příznaky byly robustnější vůči variabilitě přesnosti segmentace jednotlivých metod i při nižší hustotě PPC, protože významné rozdíly mezi referenčními a segmentovanými korunami byly méně časté než u výškových

příznaků. Indexy NDVI a ENDVI dokázaly oddělit všechna stadia napadení kůrovcem (sbbd, sbbg, sh), což je činí vhodnějšími pro detekci kůrovcových disturbancí. Tyto indexy však nejsou schopny oddělit borovice od pokročile napadených smrků (sbbd), na rozdíl od NDRE. Proto je nejvhodnější použít více indexů. Závěrem studie je, že navržená automatická segmentace korun může představovat náhradu za časově náročnou manuální segmentaci korun pro detekci jednotlivých stromů napadených kůrovcem z multispektrálního fotogrammetrického mračna nebo CHM s vysokou hustotou ~20–60 bodů/m^2, minimálně 10 bodů/m^2. Nižší nebo vyšší hustota mračna bodů vede ke snížení přesnosti segmentace, protože nejmodernější algoritmy jsou primárně určeny pro lidarová mračna s přibližně 50 body/m^2 (Yan et al., 2020).

4.5. Článek V

Minařík, R., Langhammer, J., & Lendzioch, T. (2021). Detection of Bark Beetle Disturbance at Tree Level Using UAS Multispectral Imagery and Deep Learning. *Remote Sensing*, *13*(23), 4768. https://doi.org/10.3390/rs13234768

Cílem této studie bylo ověřit potenciál konvolučních neuronových sítí (CNN) pro detekci jednotlivých stromů napadených kůrovcem včetně aktuální fáze napadení z multispektrálních UAS snímků. V širším kontextu bylo cílem navrhnout relativně jednoduchou, poloautomatizovanou a efektivní metodiku pro detekci napadených jednotlivých stromů, který by mohl být použit v lesnické praxi s využitím poznatků ze všech předchozích článků.

Vrcholy korun stromů pro tvorbu bufferů reprezentující koruny stromů byly detekovány s vysokou přesností (F-score 0,92) srovnatelnou s výsledky článku IV. Analýza spektrálních odlišností vybrala nejvhodnější pásma pro klasifikaci, ve kterých byly jasně spektrálně odlišitelné jednotlivé fáze disturbance. Nejlepší spektrální odlišnost fází disturbance byla v modrém a červeném pásmu, kde byly nalezeny statisticky významné rozdíly mezi odrazivostí tříd sbbd, sbbg a sh. Tyto třídy byly rovněž oddělitelné v zelené a red-edge části spektra s významnými rozdíly hodnot odrazivosti. Kategorie však nebyly v NIR pásmu spektrálně oddělitelné, proto bylo NIR pásmo vynecháno pro klasifikaci.

Na základě výsledků bylo rozhodnuto provést klasifikaci se dvěma sadami snímků složenými z pásem 1–4 (4b) a 1–3 (3b) a prozkoumat vliv výběru pásma na výsledky klasifikace. Porovnání průměrných F-score klasifikace pro jednotlivé třídy ukázalo silnou souvislost se spektrální odlišností tříd. Nejvyššího průměrného F-score bylo dosaženo u třídy borovic bez ohledu na verzi modelu, protože byla jasně spektrálně i texturně odlišná od smrků bez ohledu na stupeň napadení. Třídy napadení smrků dosahovaly nižších průměrných F-score, a to kvůli jejich vzájemně podobnějším spektrálním a texturním odezvám, což vedlo k částečně chybné klasifikaci stromů těchto tříd.

Výsledky ukázaly, že CNN modely používající pouze tři RGB pásma (4c3b) byly lepší než modely se čtyřmi pásmy (4c4b). Nejlepšího klasifikačního výkonu bylo dosaženo při použití CNN Nez4c3b (F-score tříd sbbd, sbbg, sh: 0.79, 0.83, 0.78; průměrné F-score 0.84; kappa 0.80) a Safaugu4c3b (F-score tříd sbbd, sbbg, sh: 0.78, 0.77, 0.75; průměrné F-score 0.81; kappa 0,76).

Výkonnost obou modelů je srovnatelná, ale model NEZ má pro tuto úlohu vyšší learning rate. Hlavní chybné klasifikace byly mezi sbbd a sbbg kvůli podobným spektrálním křivkám. Nejlepší klasifikační modely měly chybovost mezi těmito dvěma třídami do 20 %. U nejlepších modelů DenseNet169 a RF byla větší chybovost 30–37 %.

Po sloučení tříd sbbd a sbbg do obecnější třídy napadených stromů sbb se výběr typu modelu pro klasifikaci stal méně důležitým. Všechny testované typy modelů, včetně RF, byly schopny klasifikovat a detekovat napadené stromy s F-score třídy vyšším než 0,90. Nejlepší celkové metriky dosáhl opět model Safaugu3c3b (F-score napadených stromů 0.96; průměrné F-score 0.92; kappa 0,92) a model Nez3cb (F-score napadených stromů 0.94; průměrné F-score 0.91; kappa 0,87) klasifikující pouze RGB snímky.

Závěrem studie bylo, že modely Nez a Safaugu CNN jsou lepší než modely RF a modely transfer learning pro identifikaci napadených stromů a pro rozlišování různých stádií napadení. Výkonnost modelů Neze a Safaugu je srovnatelná s předchozími pracemi využívajícími klasifikátory strojového učení a některými studiemi hlubokého učení, a to i v případě, že je použita hrubší klasifikace stavu napadení stromů do kategorií zdravé/napadené bez rozlišení stadia napadení. Proto lze tyto modely využít nejen pro základní identifikaci napadených stromů, ale také pro sledování dynamiky vývoje kůrovcové disturbance.

5. Diskuse

5.1. Výběr spektrálních pásem pro detekci disturbance

Výsledky pilotní studie (článek I) potvrzují schopnost MS kamery zachytit spektrální změny odrážející změnu obsahu chlorofylu způsobenou napadením stromu lýkožrouty v červené, red-edge, NIR a omezeně v zelené části spektra. Výsledky analýzy spektrální odezvy jsou v souladu s předchozími pracemi, i když byly použity radiometricky nekalibrované DN hodnoty. Větší citlivost pásma red-edge na změnu obsahu chlorofylu vlivem vegetačního stresu byla potvrzena v experimentálních studiích (Datt, 1998, 1999; le Maire et al., 2004). Abdullah et al. (2018) vyhodnocuje jako nejvhodnější zelenou a red-edge část spektra (536–559 nm a 732–790 nm) pro rozlišení green attack. Gitelson et al. (2006) vyhodnotili red-edge a NIR pásma jako nejvhodnější pro hodnocení zdravotního stavu lesa. Podle laboratorní studie Masaitis et al. (2013) je red-edge pásmo (701,0–715,7) nejcitlivější pro detekci stresu a pro spektrální oddělení jehlic odebraných ze zdravých smrků a stromů pod vegetačním stresem. Rozdílná citlivost spektrálních pásem se promítla i do srovnání účinnosti spektrálních indexů pro rozlišení tříd. Nejlepších výsledků rozlišení tříd bylo dosaženo indexy NDVI, poměrového indexu 800/650 nm a NDRE obsahující v různých kombinacích zelené, červené, red-edge a NIR pásmo. Podobných výsledků bylo dosaženo i v článku IV, kdy jako nevhodnější pro rozlišení jednotlivých fází disturbance včetně green attack segmentovaných korun jeví indexy NDVI a ENDVI využívající viditelnou (RGB) a NIR část spektra. Silnější úloha viditelné části spektra pro detekci jednotlivých fází disturbance na úrovni jednotlivých stromů se projevila v článku V u CNN klasifikace celých korun stromů. Bylo zjištěno, že modely CNN využívající pouze pásma RGB byly lepší než modely využívající RGB + red-edge, protože pásmo red-edge mělo vyšší spektrální překryvy tříd disturbance, což vedlo k nižším metrikám přesnosti klasifikace. Naopak vyšší přesnosti random forest (RF) modelů dosahovaly verze RGB + red-edge a nejhoršího výkonu bylo dosaženo při použití RF RGB modelu, protože RF algoritmus a obecně „shallow learning“ algoritmy těží z více prediktorů a latentních proměnných (Kattenborn et al., 2021; Kuhn & Johnson, 2013).

Provedenou analýzu spektrálních odlišností v článku V lze chápat v širším kontextu jako redukci dimenze příznakového prostoru (výběr vhodných pásem) klasifikace. Avšak, výběru vhodných pásem pro CNN klasifikaci není věnována přílišná pozornost, protože síť sama provádí transformace obrazu a většinou se používají pouze RGB snímky (Kattenborn et al., 2021). Základním přístupem je výběr všech pásem MS obrazu nebo vybraných kombinací a zpětné testování vlivu pásem na přesnost klasifikace stromu (Nezami et al., 2020; Sothe, De Almeida, Schimalski, La Rosa, et al., 2020). Tento přístup však vyžaduje vícenásobné provedení klasifikace, což je výpočetně a časově náročné. Alternativou je provést analýzu spektrálních odlišností předem, jak je navrženo v článku V nebo pro začátek použít jen RGB pásma. Výsledky jsou v souladu s předchozími studiemi zaměřenými na klasifikaci jehličnatých dřevin pomocí hyperspektrálních dat (Miyoshi et al., 2020; Nezami et al., 2020), které rovněž nepotvrdily vyšší přesnost klasifikace modelů využívající více pásem než RGB.

5.2. Radiometrická kalibrace multispektrální kamery

Výsledky experimentu kalibrace kamery (článek II) potvrdily předpoklad, že největší vliv na celkovou přesnost kalibrace má redukce efektu vinětace, což je v souladu se závěry (Lebourgeois et al., 2008). Korekce vinětace pomocí metody LUT, která je ve srovnání s metodou optického modelování přesnější (Yu, 2004), výrazně snížila rozptyl vybraného diagonálního profilu. Variační koeficient se ve všech pásmech snížil na polovinu a DN se vyrovnaly obdobně jako v studii (Olsen et al., 2010). V případě kalibračních terčů na okrajích snímku postižených silným efektem vinětace NRMSE klesla čtyřikrát až desetkrát. Hodnoty NRMSE se po aplikovaní radiometrické kalibrace pohybovaly v rozmezí 0,24 až 2,10 %, což je srovnatelné s výsledky Pozo et al. (2014) (2 %), Aasen et al. (2015) (1 %) a Yang et al. (2017) (5 %).

Výhodou navržené radiometrické kalibrace založené na výpočtu korekcí ze snímků je, že může být aplikována na jakoukoli vícekanálovou multispektrální kameru s monochromatickými senzory a spektrálními filtry (např. systémy Parrot Sequoia a MicaSense Red-Edge). Laboratorním experimentem bylo zjištěno, že se hodnoty šumu a korekčního faktoru vinětace významně liší nejen pro každý kanál kamery, ale i v závislosti na teplotě okolí, expozičním čase a intenzitě dopadajícího záření. Tato závislost činí obrazově založené metody senzorových korekcí mírně nepraktickými, protože je nutné vybudovat rozsáhlou databázi korekčních snímků šumu a vinětace pro všechny běžné podmínky snímkování v terénu. Alternativou k tomuto přístupu by bylo pořídit soubor korekčních snímků v terénu podle aktuálních podmínek. Avšak, touto problematikou se zabývalo jen několik autorů pro jiné typy kamer (Aasen et al., 2015; Crusiol et al., 2017; Yang et al., 2017). Proto byla rozpracována v článku III. Ačkoli statistické testování odhalilo mírně lepší shodu laboratorně kalibrované odrazivosti s referenčními daty, přesnost in-situ kalibrovaného přístupu je dostatečná a může být použita jako alternativa ke klasickému laboratornímu přístupu, protože výsledné hodnoty NRMSE jsou významně nižší (0,2–3,4 %) při použití obou kalibračních přístupů ve srovnání s nezpracovanými daty (0,7–17,6 %). Richter & Schläpfer (2002) považují hodnoty NRMSE pod 2 % za velmi dobrou shodu s referenčními údaji a hodnoty NRMSE pod 5 % za dostatečnou shodu v letecké obrazové spektroskopii. Chyba do 5 % je také srovnatelná s předchozími studiemi na in-situ kalibraci hyperspektrálních senzorů (Aasen et al., 2015; Crusiol et al., 2017; Yang et al., 2017).

Díky těmto zjištěním je navrhovaný in-situ přístup použitelný pro různé environmentální studie využívající multispektrální UAS fotogrammetrii. Hlavní výhodou navrhované metody kalibrace in-situ je, že není třeba investovat do dalšího vybavení, jako je integrační koule a vytváření a udržování databáze snímků s redukcí šumu a vinětace, což je základní princip metod dark offset subtraction a LUT. Kalibrační snímky se pořizují během podaného experimentu za stejných povětrnostních podmínek a databázi lze vytvářet "za pochodu".

5.3. Faktory ovlivňující přesnost segmentace a klasifikace jednotlivých korun stromů

Prostorové rozlišení snímků má vliv na přesnost segmentace a klasifikace obrazu (Hall et al., 2016; Schiefer et al., 2020; Senf et al., 2017). Družice se středním rozlišením, zejména data Landsat využívající subpixelovou analýzu nebo data Sentinel-2, jsou mnohem častěji používány pro detekci disturbance než senzory s hrubším rozlišením, tj. MODIS nebo AVHRR (Senf et al., 2017). Abdullah et al. (2019) dosáhli celkové přesnosti detekce green attack 65 % ze snímku Sentinel-2 a 36 % ze snímku Landsat-8, což rovněž potvrzuje, že prostorové rozlišení je pro mapování kůrovcové disturbance klíčové. U snímků s rozlišením v řádu metrů a výše má smysl pouze per-pixel klasifikace disturbance lesa, protože je velikost pixelu srovnatelná nebo větší než mapovaná jednotka – koruna stromu (Hall et al., 2016; Meddens et al., 2011). U submetrových UAS snímků s rozlišením v řádu centimetrů je naopak per-pixel přístup problematický, protože je velikost pixelu mnohem nižší než mapovaná jednotka (koruna stromu) (Wulder et al., 2012). Holé větve a jejich stíny způsobují silné změny odrazivosti na úrovni jednotlivých pixelů, ovlivňují rozdělení hodnot celé koruny a narušují jasně odlišitelnou hranici mezi korunou a pozadím. Tyto problémy mohou omezit interpretaci klasifikovaného snímků pomocí pixelového přístupu, protože okraje korun mohou splývat s pozadím (Ke & Quackenbush, 2011).

Kromě prostorového rozlišení se také ukázala závislost přesnosti segmentace na hustotě PPC. Zkoumání vlivu hustoty fotogrammetrického mračna se doposud věnovalo velmi málo studií, ale závěry článku IV jsou v souladu s výsledky předchozích studií zaměřených na analýzu mračna bodů z leteckého laserového skenování. Kandare et al. (2016) zjistili, že hustota PPC od 6 do 50 bodů/m^2 nezlepšila přesnost ITCD, ale použití nižší hustoty mračna (<6 bodů/m^2) bylo při použití stejné metody segmentace výrazně méně přesné. Wallace et al. (2014) uvádějí, že zvýšení hustoty bodů z 5 na 50 bodů/m^2 vedlo k významnému zlepšení chyby z opomenutí (omission error). Výsledky článku IV ukázaly, že hustota bodového mračna má významnější vliv na přesnost segmentace než zvolená metoda segmentace. Toto zjištění je v souladu se zjištěním Wallace et al. (2014), kteří ukázali, že zvýšení hustoty bodů z 5 na 50 bodů/m^2 bylo významnější než použitý algoritmus ITCD. To je však v rozporu s předchozími zjištěními Kaartinen et al. (2012) a Reitberger et al. (2009), kdy se použitý algoritmus ukázal jako významný. Je to proto, že tyto studie porovnávaly pouze relativně řídké PPC s hustotou 2–5 bodů/m^2, kdy i relativně malé zvýšení hustoty mělo významný vliv. Pokud není hustota bodového mračna extrémně nízká pod 10 bodů/m^2, poskytují pokročilé algoritmy segmentace výsledky srovnatelné přesnosti.

Ve smíšeném lese navíc mohou ostatní druhy dřevin vykazovat podobnou spektrální odezvu jako napadené stromy, takže jsou per-pixel neodlišitelné, ale mohou být rozlišeny podle kontextu. Například v článku IV byla odhalena spektrální podobnost mezi borovicemi a déle napadenými smrky se světle zelenými nebo nažloutlými jehlicemi (kategorie sbbd) u indexů NDVI a ENDVI, ale kategorie

byly odlišitelné pomocí indexu NDRE. Jedním ze způsobů, jak tento problém překonat, je tedy testování více vegetačních indexů pro rozlišení tříd disturbance (Abdullah et al., 2018; Adamczyk & Osberger, 2015). Další možností je použití objektové analýzy multispektrálního obrazu (OBIA) pro detekci disturbance lesa škůdci (Brovkina et al., 2018; Lehmann et al., 2015; Otsu et al., 2019), případně v kombinaci s CHM (Hentz & Strager, 2017). Tento přístup však stále nezahrnuje přesné vymezení jednotlivých korun a ztěžuje interpretaci klasifikace. Koruny stromů jsou obvykle tvořeny více segmenty, protože generované segmenty jsou vymezeny pomocí spektrálních, prostorových kontextových informací (Blaschke, 2010). Nicméně, pro oddělení dalších druhů dřevin, které vykazují podobné spektrální reakce jako napadené stromy a intuitivní interpretaci výsledků klasifikace, je nejlepší použít přístup založený na segmentaci celých korun z PPC s využitím spektrálních a výškových příznaků korun navržený v článku IV. Tato zjištění jsou v souladu s předchozí studií Kampen et al. (2019), kteří poprvé implementovali výškové metriky získané z CHM do objektové klasifikace stavu vitality smrku algoritmem random forest. Nejlepším přístupem je použití CNN, které samy detekují vhodné rozpoznávací rysy v kontextu celého předloženého obrazového vzoru a provádějí transformace obrazu prostřednictvím konvolučních a pooling vrstev (Kattenborn et al., 2021). Proto se použití spektrálních transformací (např. vegetační indexy), textury a výškových charakteristik se nedoporučuje u klasifikátorů CNN, protože nepřináší zlepšení a může dokonce přivodit ztrátu informace a snížit přesnost klasifikačního modelu (Nezami et al., 2020; Sothe, De Almeida, Schimalski, La Rosa, et al., 2020; Sothe, De Almeida, Schimalski, Liesenberg, et al., 2020).

5.4. Klasifikace fází disturbance na úrovni jednotlivých stromů pomocí CNN

Klasifikace napadených stromů do různých fází disturbance je stále málo používaná a méně přesná než základní rozlišení napadených stromů s rezavými jehlicemi od stromů se stále zelenými jehlicemi bez ohledu na napadení stromu lýkožroutem, protože je náročné oddělit stromy ve fázi green attack (Bárta et al., 2021; Safonova et al., 2019). Předchozí studie zaměřené na detekci disturbance pomocí UAS na úrovni jednotlivých stromů proto většinou použily jednodušší klasifikaci na nenapadené (se zelenými jehlicemi, bez rozlišení green attack) a napadené stromy se změnou barvy jehlic s přesností kappa 0,73 – 0,75 (Brovkina et al., 2018; Kampen et al., 2019; Nguyen et al., 2021).

Hodnotící metriky nejlepších CNN modelů z článku V klasifikujících do čtyř tříd jsou srovnatelné nebo mírně vyšší s předchozími studiemi na klasifikaci napadení jednotlivých stromů škůdci z UAS dat, i když byla použita podrobnější klasifikace. Nejlepšího výkonu v detekci tříd disturbance sbbd, sbbg a sh dosáhly CNN modely Nez (F-score 0,79, 0,83 a 0,78, celková kappa 0,80) a Safaugu (F-score 0.78, 0.77, 0.75, celková kappa 0,77) pouze s RGB pásmy. Sloučením tříd disturbance sbbd a sbbg do jedné třídy napadených stromů sbb se výběr modelu stal méně důležitým. Nejlepších výsledků bylo opět dosaženo modely Nez (průměrné F-score 0.91, kappa 0.87) a Safaugu (průměrné F-score 0.92, kappa 0.82). Studie Qin et al. (2021) a Safonova et al. (2019) dosáhli přesnosti klasifikace srovnatelné s CNN modely z článku V klasifikující do tří tříd, ale přístup navržený

v disertační práci dosáhl vyšších nebo srovnatelných metrik hodnocení modelů s použitím řádově menšího počtu vzorků. Navíc, stromy ve fázi green attack byly se zdravými v jedné kategorii na rozdíl od zde uvedeného přístupu, kdy byly stromy ve fázi green attack sloučeny s déle napadenými stromy a nenapadené stromy zůstaly v samostatné kategorii. To umožňuje lepší oddělení napadených stromů od nenapadených a jejich efektivní asanaci.

Hlavním problémem klasifikace bylo oddělení přechodné kategorie sbbg (stromy ve fázi green attack) od sbbd (déle napadené stromy, kdy jehličí žloutne) a okrajově sh (nenapadené stromy) kvůli podobným spektrálním vlastnostem. Běžným přístupem rozpoznání fáze green attack je detekce z časových řad multispektrálních snímků. Předchozí studie dosáhly klasifikace s hodnotou kappa 0,61–0,78 (Bárta et al., 2021; Dash et al., 2017; Immitzer & Atzberger, 2014). Klouček et al. (2019) detekovali ranou fázi napadení v přirozeném horském smrkovém lese z retrospektivní časové řady pomocí UAS. Stromy ve fázi green attack byly rozpoznány s výslednou hodnotou celkové přesností 0,78. V pozdějších fázích, kdy došlo ke změně barvy jehlic byla celková přesnost až 0,96. Pouze Ortiz et al. (2013) použili snímky RapidEye v kombinaci s daty TerraSAR-X jednoho data pro včasnou identifikaci stromů ve fázi green attack s přesností kappa 0,74, ale pouze plošným přístupem. Analýza časových řad však vyžaduje opakované lety během sezóny a napadení stromů škůdcem se zjišťuje zpětně, což je nevýhodou pro rychlé mapování aktuálního stavu kalamity s rozlišením fází napadení u jednotlivých stromů. Všechny studie navíc klasifikovaly stromy pouze do kategorií green attack/zdravý/(odumřelý) bez rozlišení dalších fází. V rámci disertační práce byla ale navržena klasifikace (článek V), která rozpozná jednotlivé fáze disturbance včetně green attack z aktuálních obrazových dat bez časových řad a tím poskytne současné informace o stavu a nepřímo i dynamice disturbance. Postup je založen na správném načasování snímkování po rojení a použití CNN klasifikátoru. Vegetační stres způsobený napadením kůrovci je možné detekovat z multispektrálních snímků po 14 dnech od napadení (Dash et al., 2017; Eitel et al., 2011), proto je možné pomocí vhodného načasování snímkování včas detekovat a eliminovat napadené stromy před vyrojením další generace. Tento přístup však vyžaduje znalost přibližných termínů rojení v dané oblasti během sezóny. To je potenciální omezení našeho přístupu. K překonání tohoto omezení je možné použít pozemní metody detekce rojení, jako jsou feromonové lapače (Wermelinger, 2004).

V případové studii článku V byl limitujícím faktorem výsledné přesnosti počet trénovacích vzorů korun stromů (672) Předpokládá se, že použití většího počtu trénovacích vzorků by zlepšilo přesnost klasifikace a snížilo chybné zatřízení mezi kategoriemi sbbd a sbbg podobně jako u klasifikace druhů stromů (Natesan et al., 2020). Kromě zvýšení počtu experimentálních lokalit je další možností získat více trénovacích vzorků z opakovaného snímkování více sezón případně dalších rojení v rámci jedné sezóny pro zvýšení generalizace specifických spektrálních příznaků jednotlivých tříd identifikovaných v procesu učení CNN klasifikátoru. Vysokou generalizaci vzorů specifických pro danou třídu zatím zaručuje samotná architektura CNN, která iterativně optimalizuje transformace prostoru příznaků během procesu trénování (Chollet & Allaire, 2018; Kattenborn et al., 2021). Přesnost

nejlepších použitých CNN klasifikačních modelů je ale srovnatelná nebo lepší než u předchozích prací zaměřených na detekci green attack, i když používaly klasifikaci do méně tříd a více trénovacích dat, takže je možné navrženou klasifikaci použít i k podrobnému monitorování dynamiky disturbance z časových řad. Proto pro navazující výzkum je plánováno zkombinovaní navrženého klasifikačního postupu s analýzou časových řad pro monitoring dynamiky disturbance umožňující pochopení nedávných změn režimů disturbance v důsledku klimatické změny.

6. Závěry

Hlavním přínosem disertační práce je ověření, že současné metody UAS multispektrální fotogrammetrie a klasifikace obrazu umožňují detekci jednotlivých fází napadení stromu lýkožroutem smrkovým i s rozlišením rané fáze (green attack) bez použití časových řad na úrovni jednotlivých stromů pro studium dynamiky disturbance v přirozeném i hospodářském lese.

Nejlépe je vegetační stres způsobený napadením stromu lýkožroutem smrkovým rozpoznatelný ve spektrálních pásmech reagující na změnu obsahu chlorofylu z důvodu narušení vodivých pletiv odpovídající červené (650 nm), red-edge (700 nm) a NIR (800 nm) části spektra a pomocí vegetačních indexů vypočítaných z těchto pásem. Případný nedostatek pásem se dá částečně nahradit sofistikovaným klasifikátorem CNN, který pracuje i s kontextuální informací. V případě použití klasifikátorů CNN se doporučuje použití základních pásem RGB, red-edge a případně NIR bez transformace obrazu.

Navržená radiometrická kalibrace kamery je univerzálně použitelná pro všechny multispektrální kamery s více objektivy a významně potlačuje negativní efekty kamery způsobené zahříváním elektroniky, vinětaci a vliv atmosféry s chybou kalibrace do 5 %. Radiometrickou kalibraci je možné provést předem v laboratoři nebo in-situ pouze se základním vybavením. Provedení radiometrické kalibrace kamery každého kanálu kamery je nutností pro srovnání ortofot z různých období nebo analýzu časových změn.

Automatické metody segmentace korun mohou být náhradou za časově náročnou manuální segmentaci korun z ortofota pro detekci fáze napadení jednotlivých stromů. Pro segmentaci jednotlivých korun jehličnatého nebo smíšeného lesa se doporučuje decimovat fotogrammetrické mračno bodů na úroveň lidarového mračna (~20–60 bodů/m^2, minimálně 10 bodů/m^2). Pokud je dodržena dostatečná hustota bodového mračna zaručující věrnou reprezentaci korun, může být zvolen jakýkoli pokročilý algoritmus.

Nejlepší klasifikační CNN modely byly schopny jednotlivé fáze disturbance detekovat s přesností okolo 80 % včetně rané fáze napadení stromu lýkožroutem bez retrospektivní časové řady. Proto lze tyto modely využít nejen pro základní identifikaci napadených stromů a včasnou asanaci, ale také pro sledování dynamiky vývoje kůrovcové disturbance. Přesnost klasifikace fází disturbance je srovnatelná nebo vyšší než předchozí přístupy, i při klasifikaci do více tříd disturbance najednou.

Metody UAS multispektrální fotogrammetrie ve spojení s CNN klasifikátorem jsou tedy plně použitelné pro detekci disturbance lesa a její dynamiky a vyplňují měřítkovou mezeru mezi pozemním průzkumem a leteckým snímkování, kdy po shromáždění referenční – trénovací množiny umožnují automatizovanou detekci fází disturbance větších lesních celků na úrovni jednotlivých stromů. Pro navazující výzkum je plánováno zkombinování navržené klasifikace s analýzou časových řad umožňující detekci hotspotů, predikci šíření a pochopení nedávných změn režimů disturbance v důsledku klimatické změny.

7. Použitá literatura

Aasen, H., Burkart, A., Bolten, A., & Bareth, G. (2015). Generating 3D hyperspectral information with lightweight UAV snapshot cameras for vegetation monitoring: From camera calibration to quality assurance. *ISPRS Journal of Photogrammetry and Remote Sensing*, *108*, 245–259. https://doi.org/10.1016/j.isprsjprs.2015.08.002

Aasen, H., Honkavaara, E., Lucieer, A., & Zarco-Tejada, P. J. (2018). Quantitative remote sensing at ultra-high resolution with UAV spectroscopy: A review of sensor technology, measurement procedures, and data correctionworkflows. In *Remote Sensing* (Vol. 10, Issue 7, p. 1091). Multidisciplinary Digital Publishing Institute. https://doi.org/10.3390/rs10071091

Abdullah, H., Darvishzadeh, R., Skidmore, A. K., Groen, T. A., & Heurich, M. (2018). European spruce bark beetle (Ips typographus, L.) green attack affects foliar reflectance and biochemical properties. *International Journal of Applied Earth Observation and Geoinformation*, *64*(October 2017), 199–209. https://doi.org/10.1016/j.jag.2017.09.009

Abdullah, H., Skidmore, A. K., Darvishzadeh, R., & Heurich, M. (2019a). Sentinel-2 accurately maps green-attack stage of European spruce bark beetle (*Ips typographus* , L.) compared with Landsat-8. *Remote Sensing in Ecology and Conservation*, *5*(1), 87–106. https://doi.org/10.1002/rse2.93

Abdullah, H., Skidmore, A. K., Darvishzadeh, R., & Heurich, M. (2019b). Timing of red-edge and shortwave infrared reflectance critical for early stress detection induced by bark beetle (Ips typographus, L.) attack. *International Journal of Applied Earth Observation and Geoinformation*, *82*, 101900. https://doi.org/10.1016/j.jag.2019.101900

Adamczyk, J., & Osberger, A. (2015). Red-edge vegetation indices for detecting and assessing disturbances in Norway spruce dominated mountain forests. *International Journal of Applied Earth Observation and Geoinformation*, *37*, 90–99. https://doi.org/10.1016/j.jag.2014.10.013

Adão, T., Hruška, J., Pádua, L., Bessa, J., Peres, E., Morais, R., & Sousa, J. J. (2017). Hyperspectral imaging: A review on UAV-based sensors, data processing and applications for agriculture and forestry. *Remote Sensing*, *9*(11). https://doi.org/10.3390/rs9111110

Alvey, A. A. (2006). Promoting and preserving biodiversity in the urban forest. *Urban Forestry and Urban Greening*, *5*(4), 195–201. https://doi.org/10.1016/j.ufug.2006.09.003

Anderson, K., & Gaston, K. J. (2013). Lightweight unmanned aerial vehicles will revolutionize spatial ecology. *Frontiers in Ecology and the Environment*, *11*(3), 138–146. https://doi.org/10.1890/120150

Aspinall, R. J., Marcus, W. A., & Boardman, J. W. (2002). Considerations in collecting, processing, and analysing high spatial resolution hyperspectral data for environmental investigations. In *Journal of Geographical Systems* (Vol. 4, Issue 1, pp. 15–29). https://doi.org/10.1007/s101090100071

Assmann, J. J., Kerby, J. T., Cunliffe, A. M., & Myers-Smith, I. H. (2018). Vegetation monitoring using multispectral sensors — best practices and lessons learned from high latitudes. *Journal of Unmanned Vehicle Systems*, *7*(1), 54–75. https://doi.org/10.1139/juvs-2018-0018

Aukema, J. E., Leung, B., Kovacs, K., Chivers, C., Britton, K. O., Englin, J., Frankel, S. J., Haight, R. G., Holmes, T. P., Liebhold, A. M., McCullough, D. G., & von Holle, B. (2011). Economic impacts of Non-Native forest insects in the continental United States. *PLoS ONE*, *6*(9), e24587. https://doi.org/10.1371/journal.pone.0024587

Bárta, V., Lukeš, P., & Homolová, L. (2021). Early detection of bark beetle infestation in Norway spruce forests of Central Europe using Sentinel-2. *International Journal of Applied Earth Observation and Geoinformation*, *100*(April), 102335. https://doi.org/10.1016/j.jag.2021.102335

Bater, C. W., Wulder, M. A., White, J. C., & Coops, N. C. (2010). Integration of LIDAR and Digital Aerial Imagery for Detailed Estimates of Lodgepole Pine (Pinus contorta) Volume Killed by Mountain Pine Beetle (Dendroctonus ponderosae). *Journal of Forestry*, *108*(3).

Berni, J. A. J., Zarco-Tejada, P. J., Suárez, L., & Fereres, E. (2009). Thermal and narrowband multispectral remote sensing for vegetation monitoring from an unmanned aerial vehicle. *IEEE Transactions on Geoscience and Remote Sensing*, *47*(3), 722–738. https://doi.org/10.1109/TGRS.2008.2010457

Berni, J. A. J., Zarco-Tejada, P. J., Suárez, L., González-Dugo, V., & Fereres, E. (2009). Remote sensing of vegetation from UAV platforms using lightweight multispectral and thermal imaging sensors. *Int. Arch. Photogramm. Remote Sens. Spatial Inform. Sci*, *38*, 6 pp. https://doi.org/10.1007/s11032-006-9022-5

Blaschke, T. (2010). Object based image analysis for remote sensing. *ISPRS Journal of Photogrammetry and Remote Sensing*, *65*(1), 2–16. https://doi.org/10.1016/j.isprsjprs.2009.06.004

Borrelli, P., Panagos, P., Langhammer, J., Apostol, B., & Schütt, B. (2016). Assessment of the cover changes and the soil loss potential in European forestland: First approach to derive indicators to capture the ecological impacts on soil-related forest ecosystems. *Ecological Indicators*, *60*, 1208–1220. https://doi.org/10.1016/j.ecolind.2015.08.053

Braga, J. R. G., Peripato, V., Dalagnol, R., Ferreira, M. P., Tarabalka, Y., Aragão, L. E. O. C., de Campos Velho, H. F., Shiguemori, E. H., & Wagner, F. H. (2020). Tree crown delineation algorithm based on a convolutional neural network. *Remote Sensing*, *12*(8). https://doi.org/10.3390/RS12081288

Breiman, L. (2001). Random forests. *Machine Learning*. https://doi.org/10.1023/A:1010933404324

Brovkina, O., Cienciala, E., Surový, P., & Janata, P. (2018). Unmanned aerial vehicles (UAV) for assessment of qualitative classification of Norway spruce in temperate forest stands. *Geo-Spatial Information Science*, *21*(1), 12–20. https://doi.org/10.1080/10095020.2017.1416994

Calderón, R., Navas-Cortés, J. A., Lucena, C., & Zarco-Tejada, P. J. (2013). High-resolution airborne hyperspectral and thermal imagery for early detection of Verticillium wilt of olive using fluorescence, temperature and narrow-band spectral indices. *Remote Sensing of Environment*, *139*, 231–245. https://doi.org/10.1016/j.rse.2013.07.031

Campbell, P. K. E., Rock, B. N., Martin, M. E., Neefus, C. D., Irons, J. R., Middleton, E. M., & Albrechtova, J. (2004). Detection of initial damage in Norway spruce canopies using hyperspectral airborne data. *International Journal of Remote Sensing*, *25*(24), 5557–5584. https://doi.org/10.1080/01431160410001726058

Candiago, S., Remondino, F., Giglio, M. De, Dubbini, M., & Gattelli, M. (2015). Evaluating Multispectral Images and Vegetation Indices for Precision Farming Applications from UAV Images. *Remote Sensing*, *7*(Vi), 4026–4047. https://doi.org/10.3390/rs70404026

Cardil, A., Otsu, K., Pla, M., Silva, C. A., & Brotons, L. (2019). Quantifying pine processionary moth defoliation in a pine-oak mixed forest using unmanned aerial systems and multispectral imagery. *PLoS ONE*, *14*(3), e0213027. https://doi.org/10.1371/journal.pone.0213027

Chen, G., & Meentemeyer, R. K. (2016). *Remote Sensing of Forest Damage by Diseases and Insects* (pp. 145–162). https://doi.org/10.1201/9781315371931-9

Cheng, T., Rivard, B., Sánchez-Azofeifa, G. A., Feng, J., & Calvo-Polanco, M. (2010). Continuous wavelet analysis for the detection of green attack damage due to mountain pine beetle infestation. *Remote Sensing of Environment*, *114*(4), 899–910. https://doi.org/10.1016/j.rse.2009.12.005

Chollet, F. (2017). Xception: Deep learning with depthwise separable convolutions. *Proceedings - 30th IEEE Conference on Computer Vision and Pattern Recognition, CVPR 2017*. https://doi.org/10.1109/CVPR.2017.195

Chollet, F., & Allaire, J. J. (2018). *Deep learning with R*.

Congalton, R. G. (1991). A review of assessing the accuracy of classifications of remotely sensed data. *Remote Sensing of Environment*, *37*(1), 35–46. https://doi.org/10.1016/0034-4257(91)90048-B

Coulson, R. N., Amman, G. D., Dahlsten, D. L., DeMars Jr, C. J., & Stephen, F. M. (1985). Forest-bark beetle interactions: bark beetle population dynamics. *Integrated Pest Management in Pine-Bark Beetle Ecosystems. John Wiley & Sons, New York*, 61–80.

Crusiol, L. G. T., Nanni, M. R., Silva, G. F. C., Furlanetto, R. H., da Silva Gualberto, A. A., Gasparotto, A. de C., & De Paula, M. N. (2017). Semi professional digital camera calibration techniques for Vis/NIR spectral data acquisition from an unmanned aerial vehicle. *International Journal of Remote Sensing*, *38*(8–10), 2717–2736. https://doi.org/10.1080/01431161.2016.1264032

Dalponte, M., & Coomes, D. A. (2016). Tree-centric mapping of forest carbon density from airborne laser scanning and hyperspectral data. *Methods in Ecology and Evolution*, *7*(10), 1236–1245. https://doi.org/10.1111/2041-210X.12575

Dash, J. P., Watt, M. S., Pearse, G. D., Heaphy, M., & Dungey, H. S. (2017). Assessing very high resolution UAV imagery for monitoring forest health during a simulated disease outbreak. *ISPRS Journal of Photogrammetry and Remote Sensing*, *131*(July), 1–14. https://doi.org/10.1016/j.isprsjprs.2017.07.007

Datt, B. (1998). Remote sensing of chlorophyll a, chlorophyll b, chlorophyll a+b, and total carotenoid content in eucalyptus leaves. *Remote Sensing of Environment*, *66*(2), 111–121. https://doi.org/10.1016/S0034-4257(98)00046-7

Datt, B. (1999). Visible/near infrared reflectance and chlorophyll content in Eucalyptus leaves. *International Journal of Remote Sensing*, *20*(14), 2741–2759. https://doi.org/10.1080/014311699211778

DeRose, R. J., Long, J. N., & Ramsey, R. D. (2011). Combining dendrochronological data and the disturbance index to assess Engelmann spruce mortality caused by a spruce beetle outbreak in southern Utah, USA. *Remote Sensing of Environment*, *115*(9), 2342–2349. https://doi.org/10.1016/j.rse.2011.04.034

dos Santos, A. A., Marcato Junior, J., Araújo, M. S., Di Martini, D. R., Tetila, E. C., Siqueira, H. L., Aoki, C., Eltner, A., Matsubara, E. T., Pistori, H., Feitosa, R. Q., Liesenberg, V., & Gonçalves, W. N. (2019). Assessment of CNN-based methods for individual tree detection on images captured by RGB cameras attached to UAVS. *Sensors (Switzerland)*, *19*(16), 3595. https://doi.org/10.3390/s19163595

Eitel, J. U. H., Vierling, L. A., Litvak, M. E., Long, D. S., Schulthess, U., Ager, A. A., Krofcheck, D. J., & Stoscheck, L. (2011). Broadband, red-edge information from satellites improves early stress detection in a New Mexico conifer woodland. *Remote Sensing of Environment*, *115*(12), 3640–3646. https://doi.org/10.1016/j.rse.2011.09.002

Fassnacht, F. E., Latifi, H., Ghosh, A., Joshi, P. K., & Koch, B. (2014). Assessing the potential of hyperspectral imagery to map bark beetle-induced tree mortality. *Remote Sensing of Environment*, *140*, 533–548. https://doi.org/10.1016/j.rse.2013.09.014

Fernandez-Carrillo, A., Patočka, Z., Dobrovolný, L., Franco-Nieto, A., & Revilla-Romero, B. (2020). Monitoring Bark Beetle Forest Damage in Central Europe. A Remote Sensing Approach Validated with Field Data. *Remote Sensing*, *12*(21), 3634. https://doi.org/10.3390/rs12213634

Foster, A. C., Walter, J. A., Shugart, H. H., Sibold, J., & Negron, J. (2017). Spectral evidence of early-stage spruce beetle infestation in Engelmann spruce. *Forest Ecology and Management*, *384*, 347–357. https://doi.org/10.1016/j.foreco.2016.11.004

Franklin, J. F., Spies, T. A., Pelt, R. Van, Carey, A. B., Thornburgh, D. A., Berg, D. R., Lindenmayer, D. B., Harmon, M. E., Keeton, W. S., Shaw, D. C., Bible, K., & Chen, J. (2002). Disturbances and structural development of natural forest ecosystems with silvicultural implications, using Douglas-fir forests as an example. *Forest Ecology and Management*, *155*(1–3), 399–423. https://doi.org/10.1016/S0378-1127(01)00575-8

Frelich, L. E. (2002). *Forest Dynamics and Disturbance Regimes*. Cambridge University Press. https://doi.org/10.1017/CBO9780511542046

Fritz, A., Kattenborn, T., & Koch, B. (2013). UAV-BASED PHOTOGRAMMETRIC POINT CLOUDS – TREE STEM MAPPING IN OPEN STANDS IN COMPARISON TO TERRESTRIAL LASER SCANNER POINT CLOUDS. *The International Archives of the Photogrammetry, Remote Sensing and Spatial Information Sciences*, *XL-1/W2*, 141–146. https://doi.org/10.5194/ISPRSARCHIVES-XL-1-W2-141-2013

Geng, J., Wang, H., Fan, J., & Ma, X. (2017). Deep Supervised and Contractive Neural Network for SAR Image Classification. *IEEE Transactions on Geoscience and Remote Sensing*, *55*(4). https://doi.org/10.1109/TGRS.2016.2645226

Gitelson, A. A., Keydan, G. P., & Merzlyak, M. N. (2006). Three-band model for noninvasive estimation of chlorophyll, carotenoids, and anthocyanin contents in higher plant leaves. *Geophysical Research Letters*, *33*(11). https://doi.org/10.1029/2006GL026457

Göthlin, E., Schroeder, L. M., & Lindelöw, A. (2000). Attacks by Ips typographus and Pityogenes chalcographus on Windthrown Spruces (Picea abies) During the Two Years Following a Storm Felling. *Scandinavian Journal of Forest Research*, *15*(5), 542–549. https://doi.org/10.1080/028275800750173492

Guimarães, N., Pádua, L., Marques, P., Silva, N., Peres, E., & Sousa, J. J. (2020). Forestry Remote Sensing from Unmanned Aerial Vehicles: A Review Focusing on the Data, Processing and Potentialities. *Remote Sensing*, *12*(6), 1046. https://doi.org/10.3390/rs12061046

Hais, M., Jonášová, M., Langhammer, J., & Kučera, T. (2009). Comparison of two types of forest disturbance using multitemporal Landsat TM/ETM+ imagery and field vegetation data. *Remote Sensing of Environment*, *113*(4), 835–845. https://doi.org/10.1016/j.rse.2008.12.012

Hais, M., Wild, J., Berec, L., Brůna, J., Kennedy, R., Braaten, J., & Brož, Z. (2016). Landsat Imagery Spectral Trajectories—Important Variables for Spatially Predicting the Risks of Bark Beetle Disturbance. *Remote Sensing*, *8*(8), 687. https://doi.org/10.3390/rs8080687

Hall, R. J., Castilla, G., White, J. C., Cooke, B. J., & Skakun, R. S. (2016). Remote sensing of forest pest damage: A review and lessons learned from a Canadian perspective ∗. *Canadian Entomologist*, *148*(S1), S296–S356. https://doi.org/10.4039/tce.2016.11

Haralick, R. M. (1979). Statistical and structural approaches to texture. *Proceedings of the IEEE*. https://doi.org/10.1109/PROC.1979.11328

Hartling, S., Sagan, V., Sidike, P., Maimaitijiang, M., & Carron, J. (2019). Urban tree species classification using a worldview-2/3 and liDAR data fusion approach and deep learning. *Sensors (Switzerland)*, *19*(6), 1284. https://doi.org/10.3390/s19061284

Hastings, J. H., Ollinger, S. V., Ouimette, A. P., Sanders-DeMott, R., Palace, M. W., Ducey, M. J., Sullivan, F. B., Basler, D., & Orwig, D. A. (2020). Tree species traits determine the success of LiDAR-based crown mapping in a mixed temperate forest. *Remote Sensing*, *12*(2), 309. https://doi.org/10.3390/rs12020309

Havašová, M., Bucha, T., Ferenčík, J., & Jakuš, R. (2015). Applicability of a vegetation indices-based method to map bark beetle outbreaks in the High Tatra Mountains. *Annals of Forest Research*, *58*(2), 295–310. https://doi.org/10.15287/afr.2015.388

Hentz, A. M. K., & Strager, M. P. (2017). Cicada damage detection based on UAV spectral and 3D data. *Silvilaser 2017*, *10*(1), 95–96.

Heurich, M., Ochs, T., Andresen, T., & Schneider, T. (2010). Object-orientated image analysis for the semi-automatic detection of dead trees following a spruce bark beetle (Ips typographus) outbreak. *European Journal of Forest Research*, *129*(3), 313–324. https://doi.org/10.1007/s10342-009-0331-1

Hladky, R., Lastovicka, J., Holman, L., & Stych, P. (2020). Evaluation of the influence of disturbances on forest vegetation using Landsat time series; a case study of the Low Tatras National Park. *Https://Doi.Org/10.1080/22797254.2020.1713704*, *53*(1), 40–66. https://doi.org/10.1080/22797254.2020.1713704

Hlásny, T., Krokene, P., Liebhold, A., Montagné-Huck, C., Müller, J., Qin, H., Raffa, K., Schelhaas, M., Seidl, R., Svoboda, M., & others. (2019). *Living with bark beetles: impacts, outlook and management options*.

Hlásny, T., Zimová, S., Merganičová, K., Štěpánek, P., Modlinger, R., & Turčáni, M. (2021). Devastating outbreak of bark beetles in the Czech Republic: Drivers, impacts, and management implications. *Forest Ecology and Management*, *490*, 119075. https://doi.org/10.1016/j.foreco.2021.119075

Hoeser, T., & Kuenzer, C. (2020). Object Detection and Image Segmentation with Deep Learning on Earth Observation Data: A Review-Part I: Evolution and Recent Trends. *Remote Sensing*, *12*(10), 1667. https://doi.org/10.3390/rs12101667

Holopainen, M., Vastaranta, M., & Hyyppä, J. (2014). Outlook for the Next Generation's Precision Forestry in Finland. *Forests 2014, Vol. 5, Pages 1682-1694*, *5*(7), 1682–1694. https://doi.org/10.3390/F5071682

Honkavaara, E., Näsi, R., Oliveira, R., Viljanen, N., Suomalainen, J., Khoramshahi, E., Hakala, T., Nevalainen, O., Markelin, L., Vuorinen, M., Kankaanhuhta, V., Lyytikäinen-Saarenmaa, P., & Haataja, L. (2020). Using multitemporal hyper-and multispectral UAV imaging for detecting bark beetle infestation on norway spruce. *International Archives of the Photogrammetry, Remote Sensing and Spatial Information Sciences - ISPRS Archives*, *43*(B3), 429–434. https://doi.org/10.5194/isprs-archives-XLIII-B3-2020-429-2020

Huang, G., Liu, Z., Van Der Maaten, L., & Weinberger, K. Q. (2017). Densely connected convolutional networks. *Proceedings - 30th IEEE Conference on Computer Vision and Pattern Recognition, CVPR 2017*, *2017-Janua*, 2261–2269. https://doi.org/10.1109/CVPR.2017.243

Huang, H., Lan, Y., Yang, A., Zhang, Y., Wen, S., & Deng, J. (2020). Deep learning versus Object-based Image Analysis (OBIA) in weed mapping of UAV imagery. *International Journal of Remote Sensing*, *41*(9), 3446–3479. https://doi.org/10.1080/01431161.2019.1706112

Hujslova, J., & Simandl, P. (2018). Windstorm Herwart in Czechia. *Meteorological Bulletin*, *72*, 61–63.

Iglhaut, J., Cabo, C., Puliti, S., Piermattei, L., O'Connor, J., & Rosette, J. (2019). Structure from Motion Photogrammetry in Forestry: a Review. *Current Forestry Reports*, *5*(3), 155–168. https://doi.org/10.1007/s40725-019-00094-3

Immitzer, M., & Atzberger, C. (2014). Early Detection of Bark Beetle Infestation in Norway Spruce (Picea abies, L.) using WorldView-2 Data. *Photogrammetrie Fernerkundung Geoinformation*, *5*, 351–367. https://doi.org/Doi 10.1127/1432-8364/2014/0229

Kaartinen, H., Hyyppä, J., Yu, X., Vastaranta, M., Hyyppä, H., Kukko, A., Holopainen, M., Heipke, C., Hirschmugl, M., Morsdorf, F., Næsset, E., Pitkänen, J., Popescu, S., Solberg, S., Wolf, B. M., & Wu, J. C. (2012). An international comparison of individual tree detection and extraction using airborne laser scanning. *Remote Sensing*, *4*(4), 950–974. https://doi.org/10.3390/rs4040950

Kampen, M., Ledebauer, S., Mund, J.-P., & Immitzer, M. (2019). UAV-Based Multispectral Data for Tree Species Classification and Tree Vitality UAV-Based Multispectral Data for Tree Species Classification and Tree Vitality Analysis. *Dreilandertagung Der DGPF, Der OVG Und Der SGPF in Wien, Osterreich – Publikationen Der DGPF, Band 28*, *January*, 623–639.

Kandare, K., Ørka, H. O., Chan, J. C. W., & Dalponte, M. (2016). Effects of forest structure and airborne laser scanning point cloud density on 3D delineation of individual tree crowns. *European Journal of Remote Sensing*, *49*, 337–359. https://doi.org/10.5721/EuJRS20164919

Kattenborn, T., Leitloff, J., Schiefer, F., & Hinz, S. (2021). Review on Convolutional Neural Networks (CNN) in vegetation remote sensing. *ISPRS Journal of Photogrammetry and Remote Sensing*, *173*, 24–49. https://doi.org/10.1016/j.isprsjprs.2020.12.010

Kautz, M., Meddens, A. J. H., Hall, R. J., & Arneth, A. (2017). Biotic disturbances in Northern Hemisphere forests - a synthesis of recent data, uncertainties and implications for forest monitoring and modelling. *Global Ecology and Biogeography*, *26*(5), 533–552. https://doi.org/10.1111/geb.12558

Ke, Y., & Quackenbush, L. J. (2011). A review of methods for automatic individual tree-crown detection and delineation from passive remote sensing. *International Journal of Remote Sensing*, *32*(17), 4725–4747. https://doi.org/10.1080/01431161.2010.494184

Kelcey, J., & Lucieer, A. (2012). Sensor correction of a 6-band multispectral imaging sensor for UAV remote sensing. *Remote Sensing*, *4*(5), 1462–1493. https://doi.org/10.3390/rs4051462

Kingma, D. P., & Ba, J. (2014). Adam: A Method for Stochastic Optimization. *3rd International Conference on Learning Representations, ICLR 2015 - Conference Track Proceedings*. https://arxiv.org/abs/1412.6980v9

Klouček, T., Komárek, J., Surový, P., Hrach, K., Janata, P., & Vašíček, B. (2019). The Use of UAV Mounted Sensors for Precise Detection of Bark Beetle Infestation. *Remote Sensing*, *11*(13), 1561. https://doi.org/10.3390/rs11131561

Kuhn, M., & Johnson, K. (2013). Applied Predictive Modeling with Applications in R. In *Springer*.

Kulakowski, D., & Bebi, P. (2004). Range of Variability of unmanaged subalpine forests. *Forum for Science 2004: Forest Protection and Natural Hazards*, 47–54. http://wsl.ch/dienstleistungen/publikationen/pdf/6207.pdf

Langhammer, J., Su, Y., & Bernsteinová, J. (2015). Runoff response to climate warming and forest disturbance in a mid-mountain basin. *Water (Switzerland)*, *7*(7), 3320–3342. https://doi.org/10.3390/w7073320

Latifi, H., Schumann, B., Kautz, M., & Dech, S. (2014). Spatial characterization of bark beetle infestations by a multidate synergy of SPOT and Landsat imagery. *Environmental Monitoring and Assessment*, *186*(1), 441–456. https://doi.org/10.1007/s10661-013-3389-7

Lausch, A., Erasmi, S., King, D. J., Magdon, P., & Heurich, M. (2017). Understanding forest health with Remote sensing-Part II-A review of approaches and data models. *Remote Sensing*, *9*(2). https://doi.org/10.3390/rs9020129

Lausch, A., Heurich, M., Gordalla, D., Dobner, H.-J., Gwillym-Margianto, S., & Salbach, C. (2013). Forecasting potential bark beetle outbreaks based on spruce forest vitality using hyperspectral remote-sensing techniques at different scales. *Forest Ecology and Management*, *308*, 76–89. https://doi.org/10.1016/j.foreco.2013.07.043

le Maire, G., François, C., & Dufrêne, E. (2004). Towards universal broad leaf chlorophyll indices using PROSPECT simulated database and hyperspectral reflectance measurements. *Remote Sensing of Environment*, *89*(1), 1–28. https://doi.org/10.1016/j.rse.2003.09.004

Lebourgeois, V., Bégué, A., Labbé, S., Mallavan, B., Prévot, L., & Roux, B. (2008). Can Commercial Digital Cameras Be Used as Multispectral Sensors? A Crop Monitoring Test. *Sensors*, *8*(11), 7300–7322. https://doi.org/10.3390/s8117300

Lehmann, J., Nieberding, F., Prinz, T., & Knoth, C. (2015). Analysis of Unmanned Aerial System-Based CIR Images in Forestry—A New Perspective to Monitor Pest Infestation Levels. *Forests*, *6*(3), 594–612. https://doi.org/10.3390/f6030594

Li, W., Guo, Q., Jakubowski, M. K., & Kelly, M. (2012). A New Method for Segmenting Individual Trees from the Lidar Point Cloud. *Photogrammetric Engineering & Remote Sensing*, *78*(1), 75–84. https://doi.org/10.14358/PERS.78.1.75

Lin, Q., Huang, H., Wang, J., Huang, K., & Liu, Y. (2019). Detection of pine shoot beetle (PSB) Stress on pine forests at individual tree level using UAV-based hyperspectral imagery and lidar. *Remote Sensing*, *11*(21). https://doi.org/10.3390/rs11212540

Lindner, M., Maroschek, M., Netherer, S., Kremer, A., Barbati, A., Garcia-Gonzalo, J., Seidl, R., Delzon, S., Corona, P., Kolström, M., Lexer, M. J., & Marchetti, M. (2010). Climate change impacts, adaptive capacity, and vulnerability of European forest ecosystems. *Forest Ecology and Management*, *259*(4), 698–709. https://doi.org/10.1016/j.foreco.2009.09.023

Lisein, J., Michez, A., Claessens, H., & Lejeune, P. (2015). Discrimination of deciduous tree species from time series of unmanned aerial system imagery. *PLoS ONE*, *10*(11), 1–20. https://doi.org/10.1371/journal.pone.0141006

Mansouri, a., Marzani, F. S., & Gouton, P. (2005). Development of a Protocol for CCD Calibration: Application to a Multispectral Imaging System. *International Journal of Robotics and Automation*, *20*(2). https://doi.org/10.2316/Journal.206.2005.2.206-2784

Masaitis, G., Mozgeris, G., & Augustaitis, A. (2013). Spectral reflectance properties of healthy and stressed coniferous trees. *IForest*, *6*(JANUARY 2013), 30–36. https://doi.org/10.3832/ifor0709-006

Matese, A., Toscano, P., Di Gennaro, S. F., Genesio, L., Vaccari, F. P., Primicerio, J., Belli, C., Zaldei, A., Bianconi, R., & Gioli, B. (2015). Intercomparison of UAV, aircraft and satellite remote sensing platforms for precision viticulture. *Remote Sensing*, *7*(3), 2971–2990. https://doi.org/10.3390/rs70302971

Meddens, A. J. H., & Hicke, J. A. (2014). Spatial and temporal patterns of Landsat-based detection of tree mortality caused by a mountain pine beetle outbreak in Colorado, USA. *Forest Ecology and Management*, *322*, 78–88. https://doi.org/10.1016/j.foreco.2014.02.037

Meddens, A. J. H., Hicke, J. A., & Vierling, L. A. (2011). Evaluating the potential of multispectral imagery to map multiple stages of tree mortality. *Remote Sensing of Environment*, *115*(7), 1632–1642. https://doi.org/10.1016/j.rse.2011.02.018

Meddens, A. J. H., Hicke, J. A., Vierling, L. A., & Hudak, A. T. (2013). Evaluating methods to detect bark beetle-caused tree mortality using single-date and multi-date Landsat imagery. *Remote Sensing of Environment*, *132*, 49–58. https://doi.org/10.1016/j.rse.2013.01.002

Meigs, G. W., Kennedy, R. E., Gray, A. N., & Gregory, M. J. (2015). Spatiotemporal dynamics of recent mountain pine beetle and western spruce budworm outbreaks across the Pacific Northwest Region, USA. *Forest Ecology and Management*, *339*(1), 71–86. https://doi.org/10.1016/j.foreco.2014.11.030

Meyer, F., & Beucher, S. (1990). Morphological segmentation. *Journal of Visual Communication and Image Representation*, *1*(1), 21–46. https://doi.org/10.1016/1047-3203(90)90014-M

Mišurec, J., Kopačková, V., Lhotáková, Z., Campbell, P., & Albrechtová, J. (2016). Detection of spatio-temporal changes of Norway spruce forest stands in ore mountains using landsat time series and airborne hyperspectral imagery. *Remote Sensing*, *8*(2), 92. https://doi.org/10.3390/rs8020092

Miyoshi, G. T., Arruda, M. dos S., Osco, L. P., Junior, J. M., Gonçalves, D. N., Imai, N. N., Tommaselli, A. M. G., Honkavaara, E., & Gonçalves, W. N. (2020). A novel deep learning method to identify single tree species in UAV-based hyperspectral images. *Remote Sensing*, *12*(8), 1294. https://doi.org/10.3390/RS12081294

Morris, J. L., Cottrell, S., Fettig, C. J., Hansen, W. D., Sherriff, R. L., Carter, V. A., Clear, J. L., Clement, J., DeRose, R. J., Hicke, J. A., Higuera, P. E., Mattor, K. M., Seddon, A. W. R., Seppä, H. T., Stednick, J. D., & Seybold, S. J. (2017). Managing bark beetle impacts on ecosystems and society: priority questions to motivate future research. *Journal of Applied Ecology*, *54*(3), 750–760. https://doi.org/10.1111/1365-2664.12782

Mullikin, J. C., van Vliet, L. J., Netten, H., Boddeke, F. R., van der Feltz, G., & Young, I. T. (1994). Methods for CCD Camera Characterization. In H. C. Titus & A. Waks (Eds.), *Image Acquisition and Scientific Imaging Systems* (Vol. 2173, Issue 1994, pp. 73–84). International Society for Optics and Photonics. https://doi.org/10.1117/12.175165

Næsset, E. (2007). Airborne laser scanning as a method in operational forest inventory: Status of accuracy assessments accomplished in Scandinavia. *Scandinavian Journal of Forest Research*, *22*(5), 433–442. https://doi.org/10.1080/02827580701672147

Näsi, R., Honkavaara, E., Blomqvist, M., Lyytikäinen-Saarenmaa, P., Hakala, T., Viljanen, N., Kantola, T., & Holopainen, M. (2018). Remote sensing of bark beetle damage in urban forests at individual tree level using a novel hyperspectral camera from UAV and aircraft. *Urban Forestry and Urban Greening*, *30*(January), 72–83. https://doi.org/10.1016/j.ufug.2018.01.010

Näsi, R., Honkavaara, E., Lyytikäinen-Saarenmaa, P., Blomqvist, M., Litkey, P., Hakala, T., Viljanen, N., Kantola, T., Tanhuanpää, T., & Holopainen, M. (2015). Using UAV-based photogrammetry and hyperspectral imaging for mapping bark beetle damage at tree-level. *Remote Sensing*, *7*(11), 15467–15493. https://doi.org/10.3390/rs71115467

Natesan, S., Armenakis, C., & Vepakomma, U. (2020). Individual tree species identification using dense convolutional network (Densenet) on multitemporal RGB images from UAV. *Journal of Unmanned Vehicle Systems*, *8*(4), 310–333. https://doi.org/10.1139/juvs-2020-0014

Nezami, S., Khoramshahi, E., Nevalainen, O., Pölönen, I., & Honkavaara, E. (2020). Tree species classification of drone hyperspectral and RGB imagery with deep learning convolutional neural networks. *Remote Sensing*, *12*(7), 1070. https://doi.org/10.3390/rs12071070

Nguyen, H. T., Caceres, M. L. L., Moritake, K., Kentsch, S., Shu, H., & Diez, Y. (2021). Individual sick fir tree (Abies mariesii) identification in insect infested forests by means of UAV images and deep learning. *Remote Sensing*, *13*(2), 1–24. https://doi.org/10.3390/rs13020260

Niemann, K. O., Visintini, F., & others. (2005). *Assessment of potential for remote sensing detection of bark beetle-infested areas during green attack*.

Olsen, D., Dou, C., Zhang, X., Hu, L., Kim, H., & Hildum, E. (2010). Radiometric calibration for AgCam. *Remote Sensing*, *2*(2), 464–477. https://doi.org/10.3390/rs2020464

Onishi, M., & Ise, T. (2021). Explainable identification and mapping of trees using UAV RGB image and deep learning. *Scientific Reports*, *11*(1), 903. https://doi.org/10.1038/s41598-020-79653-9

Ortiz, S. M., Breidenbach, J., & Kändler, G. (2013). Early detection of bark beetle green attack using terraSAR-X and rapideye data. *Remote Sensing*, *5*(4), 1912–1931. https://doi.org/10.3390/rs5041912

Otsu, K., Pla, M., Duane, A., Cardil, A., & Brotons, L. (2019). Estimating the Threshold of Detection on Tree Crown Defoliation Using Vegetation Indices from UAS Multispectral Imagery. *Drones*, *3*(4), 80. https://doi.org/10.3390/drones3040080

Pádua, L., Vanko, J., Hruška, J., Adão, T., Sousa, J. J., Peres, E., & Morais, R. (2017). UAS, sensors, and data processing in agroforestry: a review towards practical applications. *International Journal of Remote Sensing*, *38*(8–10), 2349–2391. https://doi.org/10.1080/01431161.2017.1297548

Popescu, S. C., & Wynne, R. H. (2004). Seeing the Trees in the Forest. *Photogrammetric Engineering & Remote Sensing*, *70*(5), 589–604. https://doi.org/10.14358/PERS.70.5.589

Pozo, S. Del, Rodríguez-Gonzálvez, P., Hernández-López, D., & Felipe-García, B. (2014). Vicarious radiometric calibration of a multispectral camera on board an unmanned aerial system. *Remote Sensing*, *6*(3), 1918–1937. https://doi.org/10.3390/rs6031918

Puliti, S., Ørka, H. O., Gobakken, T., & Næsset, E. (2015). Inventory of small forest areas using an unmanned aerial system. *Remote Sensing*, *7*(8). https://doi.org/10.3390/rs70809632

Qin, J., Wang, B., Wu, Y., Lu, Q., & Zhu, H. (2021). Identifying pine wood nematode disease using uav images and deep learning algorithms. *Remote Sensing*, *13*(2), 1–14. https://doi.org/10.3390/rs13020162

Reichstein, M., Camps-Valls, G., Stevens, B., Jung, M., Denzler, J., Carvalhais, N., & Prabhat. (2019). Deep learning and process understanding for data-driven Earth system science. *Nature*. https://doi.org/10.1038/s41586-019-0912-1

Reitberger, J., Schnörr, C., Krzystek, P., & Stilla, U. (2009). 3D segmentation of single trees exploiting full waveform LIDAR data. *ISPRS Journal of Photogrammetry and Remote Sensing*, *64*(6), 561–574. https://doi.org/10.1016/j.isprsjprs.2009.04.002

Richter, R., & Schläpfer, D. (2002). Geo-atmospheric processing of airborne imaging spectrometry data. Part 2: Atmospheric/topographic correction. *International Journal of Remote Sensing*, *23*(13), 2631–2649. https://doi.org/10.1080/01431160110115834

Roussel, J. R., Auty, D., Coops, N. C., Tompalski, P., Goodbody, T. R. H., Meador, A. S., Bourdon, J. F., de Boissieu, F., & Achim, A. (2020). lidR: An R package for analysis of Airborne Laser Scanning (ALS) data. In *Remote Sensing of Environment* (Vol. 251, p. 112061). Elsevier Inc. https://doi.org/10.1016/j.rse.2020.112061

Safonova, A., Tabik, S., Alcaraz-Segura, D., Rubtsov, A., Maglinets, Y., & Herrera, F. (2019). Detection of Fir Trees (Abies sibirica) Damaged by the Bark Beetle in Unmanned Aerial Vehicle Images with Deep Learning. *Remote Sensing*, *11*(6), 643. https://doi.org/10.3390/rs11060643

Salamí, E., Barrado, C., & Pastor, E. (2014). UAV flight experiments applied to the remote sensing of vegetated areas. *Remote Sensing*, *6*(11), 11051–11081. https://doi.org/10.3390/rs61111051

Santamaria, E., Barrado, C., Pastor, E., Royo, P., & Salami, E. (2012). Reconfigurable automated behavior for UAS applications. *Aerospace Science and Technology*, *23*(1), 372–386. https://doi.org/10.1016/j.ast.2011.09.005

Schiefer, F., Kattenborn, T., Frick, A., Frey, J., Schall, P., Koch, B., & Schmidtlein, S. (2020). Mapping forest tree species in high resolution UAV-based RGB-imagery by means of convolutional neural networks. *ISPRS Journal of Photogrammetry and Remote Sensing*, *170*(December), 205–215. https://doi.org/10.1016/j.isprsjprs.2020.10.015

Schuldt, B., Buras, A., Arend, M., Vitasse, Y., Beierkuhnlein, C., Damm, A., Gharun, M., Grams, T. E. E., Hauck, M., Hajek, P., Hartmann, H., Hiltbrunner, E., Hoch, G., Holloway-Phillips, M., Körner, C., Larysch, E., Lübbe, T., Nelson, D. B., Rammig, A., … Kahmen, A. (2020). A first assessment of the impact of the extreme 2018 summer drought on Central European forests. *Basic and Applied Ecology*, *45*, 86–103. https://doi.org/10.1016/j.baae.2020.04.003

Seidl, R., Schelhaas, M.-J., Rammer, W., & Verkerk, P. J. (2014). Increasing forest disturbances in Europe and their impact on carbon storage. *Nature Climate Change*, *4*(9), 806–810. https://doi.org/10.1038/nclimate2318

Seidl, R., Thom, D., Kautz, M., Martin-Benito, D., Peltoniemi, M., Vacchiano, G., Wild, J., Ascoli, D., Petr, M., Honkaniemi, J., Lexer, M. J., Trotsiuk, V., Mairota, P., Svoboda, M., Fabrika, M., Nagel, T. A., & Reyer, C. P. O. (2017). Forest disturbances under climate change. *Nature Climate Change*, *7*(6), 395–402. https://doi.org/10.1038/nclimate3303

Senf, C., Pflugmacher, D., Wulder, M. A., & Hostert, P. (2015). Characterizing spectral-temporal patterns of defoliator and bark beetle disturbances using Landsat time series. *Remote Sensing of Environment*. https://doi.org/10.1016/j.rse.2015.09.019

Senf, C., Pflugmacher, D., Zhiqiang, Y., Sebald, J., Knorn, J., Neumann, M., Hostert, P., & Seidl, R. (2018). Canopy mortality has doubled in Europe's temperate forests over the last three decades. *Nature Communications*, *9*(1), 4978. https://doi.org/10.1038/s41467-018-07539-6

Senf, C., Sebald, J., & Seidl, R. (2021). Increasing canopy mortality affects the future demographic structure of Europe's forests. *One Earth*, *4*(5), 749–755. https://doi.org/10.1016/j.oneear.2021.04.008

Senf, C., & Seidl, R. (2021). Mapping the forest disturbance regimes of Europe. *Nature Sustainability*, *4*(1), 63–70. https://doi.org/10.1038/s41893-020-00609-y

Senf, C., Seidl, R., & Hostert, P. (2017). Remote sensing of forest insect disturbances: Current state and future directions. *International Journal of Applied Earth Observation and Geoinformation*, *60*(April), 49–60. https://doi.org/10.1016/j.jag.2017.04.004

Smigaj, M., Gaulton, R., Barr, S. L., & Suárez, J. C. (2015). UAV-Borne thermal imaging for forest health monitoring: Detection Of disease-induced canopy temperature increase. *International Archives of the Photogrammetry, Remote Sensing and Spatial Information Sciences - ISPRS Archives*, *40*(3W3), 349–354. https://doi.org/10.5194/isprsarchives-XL-3-W3-349-2015

Smith, G. M., & Milton, E. J. (1999). The use of the empirical line method to calibrate remotely sensed data to reflectance. *International Journal of Remote Sensing*, *20*(13), 2653–2662. https://doi.org/10.1080/014311699211994

Sothe, C., De Almeida, C. M., Schimalski, M. B., La Rosa, L. E. C., Castro, J. D. B., Feitosa, R. Q., Dalponte, M., Lima, C. L., Liesenberg, V., Miyoshi, G. T., & Tommaselli, A. M. G. (2020). Comparative performance of convolutional neural network, weighted and conventional support vector machine and random forest for classifying tree species using hyperspectral and photogrammetric data. *GIScience and Remote Sensing*, *57*(3), 369–394. https://doi.org/10.1080/15481603.2020.1712102

Sothe, C., De Almeida, C. M., Schimalski, M. B., Liesenberg, V., La Rosa, L. E. C., Castro, J. D. B., & Feitosa, R. Q. (2020). A comparison of machine and deep-learning algorithms applied to multisource data for a subtropical forest area classification. *International Journal of Remote Sensing*, *41*(5), 1943–1969. https://doi.org/10.1080/01431161.2019.1681600

Sprintsin, M. (2011). Combining land surface temperature and shortwave infrared reflectance for early detection of mountain pine beetle infestations in western Canada. *Journal of Applied Remote Sensing*, *5*(1), 053566. https://doi.org/10.1117/1.3662866

Stych, P., Jerabkova, B., Lastovicka, J., Riedl, M., & Paluba, D. (2019). A Comparison of WorldView-2 and Landsat 8 Images for the Classification of Forests Affected by Bark Beetle Outbreaks Using a Support Vector Machine and a Neural Network: A Case Study in the Sumava Mountains. *Geosciences 2019, Vol. 9, Page 396*, *9*(9), 396. https://doi.org/10.3390/GEOSCIENCES9090396

Tang, L., & Shao, G. (2015). Drone remote sensing for forestry research and practices. *Journal of Forestry Research*, *26*(4), 791–797. https://doi.org/10.1007/s11676-015-0088-y

Teillet, P. M. (1986). Image correction for radiometric effects in remote sensing. *International Journal of Remote Sensing*, *7*(12), 1637–1651. https://doi.org/10.1080/01431168608948958

Torres-Sánchez, J., López-Granados, F., & Peña, J. M. (2015). An automatic object-based method for optimal thresholding in UAV images: Application for vegetation detection in herbaceous crops. *Computers and Electronics in Agriculture*, *114*, 43–52. https://doi.org/10.1016/j.compag.2015.03.019

Torresan, C., Berton, A., Carotenuto, F., Di Gennaro, S. F., Gioli, B., Matese, A., Miglietta, F., Vagnoli, C., Zaldei, A., & Wallace, L. (2017). Forestry applications of UAVs in Europe: a review. *International Journal of Remote Sensing*, *38*(8–10), 2427–2447. https://doi.org/10.1080/01431161.2016.1252477

Toth, C., & Jóźków, G. (2016). Remote sensing platforms and sensors: A survey. *ISPRS Journal of Photogrammetry and Remote Sensing*, *115*, 22–36. https://doi.org/10.1016/j.isprsjprs.2015.10.004

Tubby, K. V., & Webber, J. F. (2010). Pests and diseases threatening urban trees under a changing climate. *Forestry*, *83*(4), 451–459. https://doi.org/10.1093/forestry/cpq027

Wallace, L., Lucieer, A., & Watson, C. S. (2014). Evaluating tree detection and segmentation routines on very high resolution UAV LiDAR ata. *IEEE Transactions on Geoscience and Remote Sensing*, *52*(12), 7619–7628. https://doi.org/10.1109/TGRS.2014.2315649

Weidner, U. (2008). Contribution to the assessment of segmentation quality for remote sensing applications. *International Archives of Photogrammetry, Remote Sensing and Spatial Information Sciences*, *37*(B7), 479–484.

Weinstein, B. G., Marconi, S., Bohlman, S., Zare, A., & White, E. (2019). Individual tree-crown detection in rgb imagery using semi-supervised deep learning neural networks. *Remote Sensing*, *11*(11). https://doi.org/10.3390/rs11111309

Wermelinger, B. (2004). Ecology and management of the spruce bark beetle Ips typographus—a review of recent research. *Forest Ecology and Management*, *202*(1–3), 67–82. https://doi.org/10.1016/j.foreco.2004.07.018

White, J. C., Coops, N. C., Wulder, M. A., Vastaranta, M., Hilker, T., & Tompalski, P. (2016). Remote Sensing Technologies for Enhancing Forest Inventories: A Review. In *Canadian Journal of Remote Sensing* (Vol. 42, Issue 5, pp. 619–641). Taylor and Francis Inc. https://doi.org/10.1080/07038992.2016.1207484

Windrim, L., Carnegie, A. J., Webster, M., & Bryson, M. (2020). Tree Detection and Health Monitoring in Multi-Spectral Aerial Imagery and Photogrammetric Pointclouds using Machine Learning. *IEEE Journal of Selected Topics in Applied Earth Observations and Remote Sensing*, 1–1. https://doi.org/10.1109/jstars.2020.2995391

Wulder, M. A., White, J. C., Carroll, A. L., & Coops, N. C. (2009). Challenges for the operational detection of mountain pine beetle green attack with remote sensing. *Forestry Chronicle*, *85*(1), 32–38. https://doi.org/10.5558/tfc85032-1

Wulder, M. A., White, J. C., Ortlepp, S. M., Mora, B., Coggins, S., Coops, N. C., & Heath, J. (2012). Digital high spatial resolution aerial imagery to support forest health monitoring: the mountain pine beetle context. *Journal of Applied Remote Sensing*, *6*(1), 062527. https://doi.org/10.1117/1.jrs.6.062527

Xiao, W., Zaforemska, A., Smigaj, M., Wang, Y., & Gaulton, R. (2019). Mean shift segmentation assessment for individual forest tree delineation from airborne lidar data. *Remote Sensing*, *11*(11), 1263. https://doi.org/10.3390/rs11111263

Yamaoka, Y., Swanson, R. H., & Hiratsuka, Y. (2011). Inoculation of lodgepole pine with four blue-stain fungi associated with mountain pine beetle, monitored by a heat pulse velocity (HPV) instrument. *Https://Doi.Org/10.1139/X90-005*, *20*(1), 31–36. https://doi.org/10.1139/X90-005

Yan, W., Guan, H., Cao, L., Yu, Y., Li, C., & Lu, J. Y. (2020). A self-adaptive mean shift tree-segmentation method using UAV LiDAR data. *Remote Sensing*, *12*(3), 515. https://doi.org/10.3390/rs12030515

Yang, G., Li, C., Wang, Y., Yuan, H., Feng, H., Xu, B., & Yang, X. (2017). The DOM generation and precise radiometric calibration of a UAV-mounted miniature snapshot hyperspectral imager. *Remote Sensing*, *9*(7), 642. https://doi.org/10.3390/rs9070642

Yin, D., & Wang, L. (2016). How to assess the accuracy of the individual tree-based forest inventory derived from remotely sensed data: a review. In *International Journal of Remote Sensing* (Vol. 37, Issue 19, pp. 4521–4553). Taylor and Francis Ltd. https://doi.org/10.1080/01431161.2016.1214302

Yu, W. (2004). Practical anti-vignetting methods for digital cameras. *IEEE Transactions on Consumer Electronics*, *50*(4), 975–983. https://doi.org/10.1109/TCE.2004.1362487

Zhang, C., & Kovacs, J. M. (2012). The application of small unmanned aerial systems for precision agriculture: A review. In *Precision Agriculture* (Vol. 13, Issue 6, pp. 693–712). https://doi.org/10.1007/s11119-012-9274-5

Zhu, X. X., Tuia, D., Mou, L., Xia, G. S., Zhang, L., Xu, F., & Fraundorfer, F. (2017). Deep Learning in Remote Sensing: A Comprehensive Review and List of Resources. In *IEEE Geoscience and Remote Sensing Magazine*. https://doi.org/10.1109/MGRS.2017.2762307

8. Publikované články

Článek		**Autorský podíl**
Článek I	Minařík, R., & Langhammer, J. (2016). Use of a multispectral UAV photogrammetry for detection and tracking of forest disturbance dynamics. In L. Halounova (Ed.), *International Archives of the Photogrammetry, Remote Sensing and Spatial Information Sciences: Vols. XLI-B8* (pp. 711–718). Copernicus GmbH. https://doi.org/10.5194/isprsarchives-XLI-B8-711-2016	60 %
Článek II	Minařík, R., Langhammer, J., & Hanuš, J. (2019). Radiometric and Atmospheric Corrections of Multispectral μMCA Camera for UAV Spectroscopy. *Remote Sensing*, *11*(20), 2428. https://doi.org/10.3390/rs11202428	55 %
Článek III	Minařík, R., & Langhammer, J. (2019). Rapid Radiometric calibration of multiple camera array using in-situ data for UAV multispectral photogrammetry. *The International Archives of the Photogrammetry, Remote Sensing and Spatial Information Sciences*, *XLII-2/W17*, 209–215. https://doi.org/10.5194/isprs-archives-XLII-2-W17-209-2019	80 %
Článek IV	Minařík, R., Langhammer, J., & Lendzioch, T. (2020). Automatic Tree Crown Extraction from UAS Multispectral Imagery for the Detection of Bark Beetle Disturbance in Mixed Forests. *Remote Sensing*, *12*(24), 4081. https://doi.org/10.3390/rs12244081	60 %
Článek V	Minařík, R., Langhammer, J., & Lendzioch, T. (2021). Detection of Bark Beetle Disturbance at Tree Level Using UAS Multispectral Imagery and Deep Learning. *Remote Sensing*, *13*(23), 4768. https://doi.org/10.3390/rs13234768	80 %

Článek I

Minařík, R., & Langhammer, J. (2016). Use of a multispectral UAV photogrammetry for detection and tracking of forest disturbance dynamics. In L. Halounova (Ed.), *International Archives of the Photogrammetry, Remote Sensing and Spatial Information Sciences: Vols. XLI-B8* (pp. 711–718). Copernicus GmbH. https://doi.org/10.5194/isprsarchives-XLI-B8-711-2016

USE OF A MULTISPECTRAL UAV PHOTOGRAMMETRY FOR DETECTION AND TRACKING OF FOREST DISTURBANCE DYNAMICS

R. Minařík [a], J. Langhammer [a, *]

[a] Dept. of Physical Geography and Geoecology, Faculty of Science, Charles University in Prague, Albertov 6, Prague 2, 128 43, Czech Republic - (robert.minarik, jakub.langhammer)@natur.cuni.cz

Commission VIII, WG VIII/7

KEY WORDS: UAV, Photogrammetry, Multispectral Sensor, Forest Disturbance, Vegetation Indices, Change Detection

ABSTRACT:

This study presents a new methodological approach for assessment of spatial and qualitative aspects of forest disturbance based on the use of multispectral imaging camera with the UAV photogrammetry. We have used the miniaturized multispectral sensor Tetracam Micro Multiple Camera Array (μ-MCA) Snap 6 with the multirotor imaging platform to get multispectral imagery with high spatial resolution. The study area is located in the Sumava Mountains, Central Europe, heavily affected by windstorms, followed by extensive and repeated bark beetle (Ips typographus [L.]) outbreaks in the past 20 years. After two decades, there is apparent continuous spread of forest disturbance as well as rapid regeneration of forest vegetation, related with changes in species and their diversity. For testing of suggested methodology, we have launched imaging campaign in experimental site under various stages of forest disturbance and regeneration. The imagery of high spatial and spectral resolution enabled to analyse the inner structure and dynamics of the processes. The most informative bands for tree stress detection caused by bark beetle infestation are band 2 (650nm) and band 3 (700nm), followed by band 4 (800 nm) from the, red-edge and NIR part of the spectrum. We have identified only three indices, which seems to be able to correctly detect different forest disturbance categories in the complex conditions of mixture of categories. These are Normalized Difference Vegetation Index (NDVI), Simple 800/650 Ratio Pigment specific simple ratio B1 and Red-edge Index.

1. INTRODUCTION

Disturbance is the key control of the dynamics of forest ecosystems across various environments (Frelich, 2002). It has enormous effects on related landscape processes ranging from the changes in microclimate and runoff dynamics (Langhammer et al., 2015) to land cover changes and soil erosion (Borrelli et al., 2016). Various factors cause the disturbance such as air pollution, storms, unregulated harvesting and pest insect outbreak), but the most significant impacts that may affect the dynamics of mountain forests in Central and Western Europe are considered by windstorms and bark beetle outbreaks (Kulakowski and Bebi, 2004). In Central Europe, especially the Sumava Mountains has undergone a significant forest disturbance in the past two decades as a result of repeated windstorms and bark beetle infestation (Ips typographus [L.]) (Hais et al., 2009). Simultaneously, this area is experiencing significant increases in observed air temperatures (Langhammer et. al, 2015), which might cause a raise in the frequency of extreme weather events and promote forest diseases (Lindner et al., 2010).

Damage monitoring and risk assessment of bark beetles have traditionally been based on laborious and time-consuming field sampling methods, focusing on symptoms on the trunk and foliage (Göthlin et al., 2000; Lausch et al. 2013). In general, an invasion by bark beetle causes visible crown symptoms, i.e., discoloration and defoliation, before succumbing from the infestation (Näsi et al., 2015). The needles of Norway spruce first turn yellow (yellow attack), then to reddish brown (red attack), and finally grey (tree mortality) (Ortiz et al., 2013). Consequently, remote sensing technologies are widely applied for non-invasive mapping of forest disturbance by pest insects. Multi-temporal medium or low resolution satellite datasets like Landsat (TM/ETM+) and SPOT (Hais et al., 2009; Latifi et al., 2014), Colour-Infrared (CIR) images captured by manned aircraft (Heurich et al., 2010), TerraSAR-X and RapidEye data (Ortiz et al., 2013; Adamczyk and Osberger, 2015), or airborne pushbroom imagining radiometer (Campbell et al., 2004) have been used for monitoring of disturbances by bark beetle infestation. However, conventional remote sensing (RS) methods are not always appropriate for monitoring forest disturbance dynamics particularly in the case of rapid calamity mapping of small privately owned forest stands due to a high operating cost or limited spatial and temporal image data (Chambers et. al, 2007). These applications require low-cost but high-resolution RS data and acquisition on demand. By addressing the limitations of conventional remote sensing approaches in forestry, Unmanned Aerial Vehicle (UAV) equipped with a multi or hyperspectral camera may provide accurate means of monitoring pest infestation at the stand and even species level (Lehmann et al., 2015).

UAV has been widely applied for RS of the environment and vegetation areas. Compared to satellite-based RS applications, UAV-based applications have a much better resolution and greater flexibility in selecting suitable payloads and appropriate spatiotemporal resolution (Zhang and Kovacs, 2012). When comparing UAV-based applications with full-scale manned aircraft RS, UAV has lower operating costs and flight altitude

* Corresponding author

closer to treetops providing very detailed insight into forest dynamics (Näsi et al., 2015). The current review of UAV flight experiments applied to the RS of vegetated areas including taxonomy is presented in Salamí et al. (2014). Approximately 40 UAV experiments are introduced in the review, but only six studies are centred on forest mapping. In environment monitoring, Laliberte et al. (2011) employed multispectral sensor carried by UAV for rangeland vegetation classification. Turner et al. (2014) investigated the physiological state of Antarctic Moss ecosystems using UAV equipped with tree different (visible, multispectral and thermal) sensors.

Rapidly increasing pest-induced forest disturbances are a threat to forest health, therefore, accurate and cost-efficient detection of stand and tree conditions for timely forest management are needed, but studies employing UAV in forest health monitoring are rare and there is an open space for new projects (Näsi et. al., 2015).

Lehmann et al. (2015) were one of the first researches that used UAV for detection of pest infestation level in forest ecosystem Authors used multispectral imagery and object-based image analysis to detect an infestation in oak stands. The UAV was equipped with a calibrated consumer-grade digital camera with removed hot mirror filter to obtain modified colour infrared (CIR) images. Näsi et al. (2015) introduced the first study which investigated bark beetle damage at tree-level by means of UAV photogrammetry and hyperspectral imaging. In agriculture, tree health monitoring with multispectral, hyperspectral or thermal UAV- based data have been studied, e.g. vineyard (Turner et al., 2011) and peach orchard (Berni et al., 2009).

The aim of the study is to introduce a new methodological approach for assessment of spatial and qualitative aspects of forest disturbance at high spatial and spectral resolution. This study combines the use of multispectral imaging sensor Tetracam μ-MCA Snap 6 with the UAV Mikrokopter OctoXL platform. Using the photogrammetric tools there was derived seamless high-resolution multispectral imagery covering the study area. Based on the acquired seamless dataset there we have performed a qualitative analysis of the different categories of the disturbance and regeneration of Norway spruce forest.

2. MATERIAL AND METHODS

2.1 Study Site

The study site is situated in the Sumava mountains at the border between the Czech Republic and Germany (Figure 1a), formed by an elevated montane plain with moderate hillslopes. The Norway spruce (Picea abies) monoculture is the dominant tree species in the regions. After the windstorms in the Bavarian side of mountains in mid of 1980´s there occurred a massive bark beetle (Ips typographus [L.]) infestation, which resulted in extensive forest disturbance and decay. The infestation was accelerated after the windstorms in 2007 and 2008 and in terms of its extent and intensity is significant at European scale (Borrelli et al., 2016). While the area is protected as a National Park, the forest was left to the natural processes of forest disturbance, decay, and regeneration without human intervention. In result, the former forest monoculture is recently featuring mixed structure of the old forest, disturbed standing trees, decayed tree trunks and spots of the newly regenerating young forest.

We have selected the study site at headwaters of Hamerský brook near Kvilda village, with high recent dynamics of forest cover changes. In the study site, sized 150 x 100 meters (Figure 1b), where we have identified the research plot with an appropriate mosaic of forest disturbance categories (Figure 1c). Based on the field observation, there were chosen representative samples of the five classes (infested trees, healthy trees, dead trees, forest restoration, grass) to investigate their spectral response. For a selection of the test plot, we have aimed for particular samples, featuring (i) high level of heterogeneity in terms of forest disturbance categories and (ii) high level of homogeneity inside the selected category.

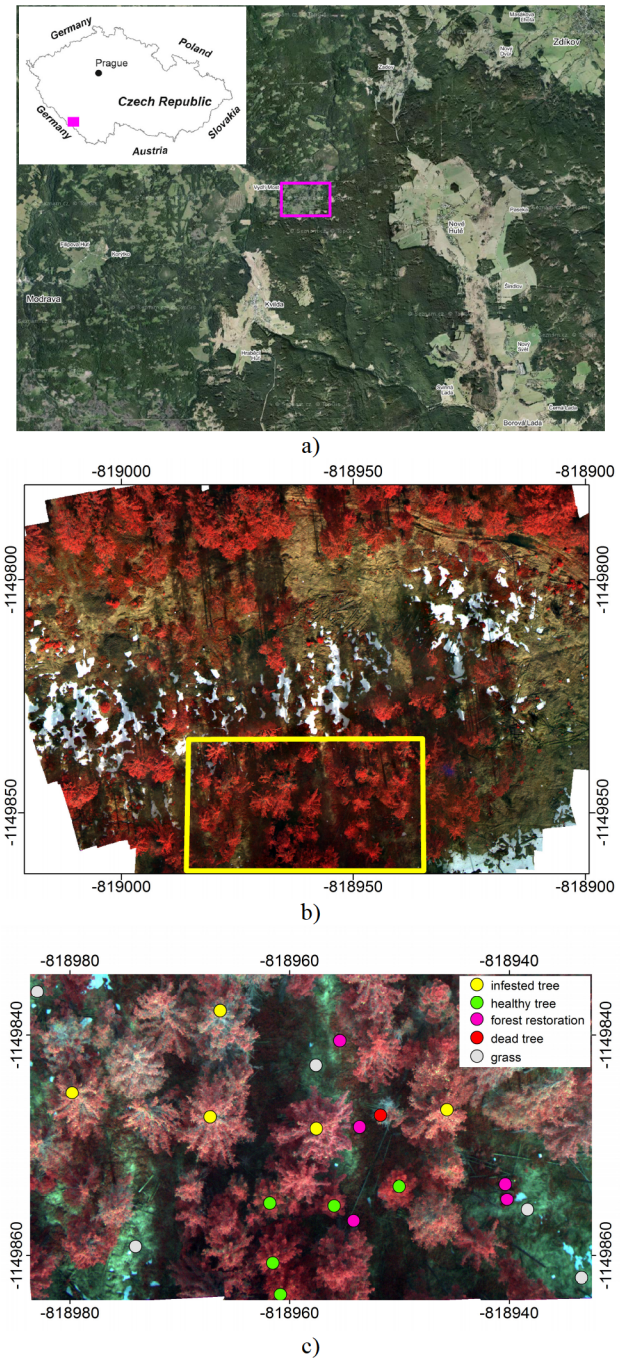

Figure 1. Study area. a) Study region with marked Forest Infrared Index, b) Study site, where UAV imaging was performed, c) Research plot, analysed in this study.

2.2 UAV and Sensor

In this study, we used a multi-rotor UAV, namely ARF MicroKopter OktoXL (Figure 2), developed by HiSystems GmbH, Moormerland, Germany. The OktoXL was equipped by active gimbal with stabilised camera mount to balance the pitch and roll of the helicopter during the survey. The typical flight duration was around 15 minutes having the multispectral camera and two batteries on board.

To collect multispectral images we used Tetracam µ-MCA Snap 6, capturing imagery in six independent channels. Each channel is acquired by an independent camera with fixed lens, 1.3 mega-pixels (1280 x 1024 pixels) Complementary Metal Oxide Semiconductor (CMOS) global shutter sensor and changeable band pass filter. Global shutter sensor µ-MCA Snap cameras was selected as preferred solution over the rolling shutter as it allows capturing imagery in conditions of faster and less stable UAV platforms (Tetracam, 2015). The key feature of the µ-MCA array is a possibility to customize the composition of wavelength pass filters at each lens according to the needs of the research task.

The applied µ-MCA Snap 6 array was equipped with a set of filters fitted to detection of vegetation stress resulting from the bark beetle infestation, covering also the red edge part of the spectrum. According to experimental laboratory study Masaitis et al. (2013), the red edge (701.0 – 715.7) is the most sensitive spectral zone for stress detection and for spectral separation between the needles taken from healthy Norway spruces and trees under stress. The data sets collected for this study had 550, 650, 700, 800, 850 and 900 nm optical filters fitted, with a Full-Width at Half Maximum (FWHM) of 20 nm.

Figure 2. ARF MicroKopter Okto XL equipped with multispectral camera µ-MCA Snap 6.

2.3 Data Acquisition

Multispectral image acquisition was carried out on 4 April 2016 around 1 p.m. Weather condition were the windless and almost clear sky. The flight was proceded at an altitude of 50 meters covering a regular grid of 150 x 100 meters resulting in 200 multispectral images with the spatial resolution 2.5 cm. Images were captured every second in continuous mode to keep at least 80% frontal and 60 % side overlap. A reference calibration image of Teflon tag was captured directly before the flight. The main purpose was to compensate for ambient atmospheric and sun angle influences vs. reference standard conditions at the time of factory calibration (Tetracam, 2015).

Prior to survey flight, there were equally distributed white papers in A4 format, which acted as Ground Control Points (GCPs). The coordinates of 21 GCPs were measured by geodetic Global Navigation Satellite System (GNSS) receiver Topcon Hiper SR with achieved horizontal accuracy of 1.8 cm and vertical accuracy of 2.5 cm.

2.4 Photogrammetric Processing

The Tetracam PixelWrench2 (PW2) was used for the raw images download via USB and data conversion to single page TIF file format which is readable for commonly used multispectral image analysis programs. The band-to-band registration step is automatically included in PW2 as part of the raw to multipage TIF format conversion based on camera´s alignment file.

The photogrammetric processing was performed using Agisoft Photoscan Professional 1.2.4 developed by AgiSoft LLC, St. Petersburg, Russia. PhotoScan allows to perform the 3D reconstruction of the scene from the imagery, employing the Structure from Motion and Semi-Global Matching algorithms. The reliable performance of the software in the feature detection, image matching, and in consequent deriving of the dense point cloud, 3D model and ortho imagery has been proven in previous studies, e.g. Verhoeven (2011).

All of the 200 multispectral images, acquired in the imaging campaign over the study area were included into orientation processing. The band 4 (800 nm) was set as a master channel for estimating image orientations. After initial photo alignment, GCPs were used as markers to optimize the sparse cloud and to transform image orientation into geodetic coordinate system S-JTSK Krovak East North (EPSG 5514). Seven GCPs served as checkpoints to evaluate the accuracy of alignment. The following steps in the workflow consisted in the dense cloud generation, automatic ground point classification. Based on these datasets, the Digital Terrain Model (DTM) and orthoimages were generated.

However, there is a limiting factor affecting the reliability of the data products, resulting from the photogrammetric workflow. In the Agisoft Photoscan, the orthoimage or even the single orthorectified images are resampled by the Bilinear Interpolation, which modifies the source Digital Number (DN) values of imagery. To avoid such modification and to retain the maximum possible reliability of the original DN values, the original images were used for qualitative analysis of the different categories of the forest disturbance and regeneration. The four selected original images were georeferenced in ArcGIS 10.3.1 using GCPs and distinctive terrain objects with Nearest Neighbourhood resampling method. Finally, the images were stitched ERDAS IMAGINE 2013.

2.5 Detection of forest disturbance

The spectral response for given categories of forest damage status was analyzed across the multispectral bands. Based on the set of selected samples for each category, we have identified the typical DN values and their variation for each spectral band (Figure 3). One sample of a dead tree with a complete loss of canopy was added as an extra category into the analysis for better comparison of different disturbance phases. The analysis was performed within one image only to inhibit even subtle changes of DN caused by slightly different light conditions between images capturing. Each sample was represented by a circle containing approximately 525 pixels.

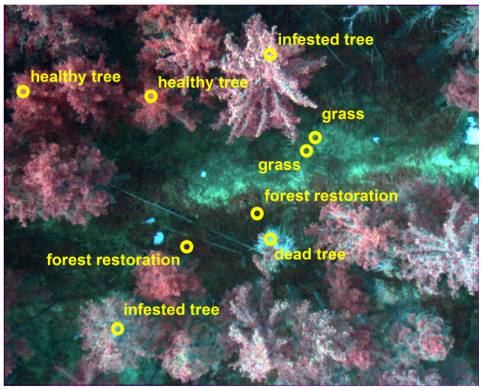

Figure 3. Selected appropriate samples for the spectral response analysis of different disturbance categories.

Index	Formula	Reference
Greenness Index	$\frac{green}{red}$	Le Maire et al. (2004)
Simple ratio (SR) 800/550	$\frac{NIR}{green}$	Le Maire et al. (2004)
Simple ratio 800/650 Pigment specific SR B1	$\frac{NIR}{red}$	Blackburn (1998)
Datt 2	$\frac{NIR}{red_edge}$	Datt (1999)
NDVI	$\frac{NIR-red}{NIR+red}$	Tucker (1979)
Green NDVI	$\frac{NIR-green}{NIR+green}$	Gitelson and Merzlyak (1997)
Red-edge index (NDRE)	$\frac{NIR-(red_edge)}{NIR+(red_edge)}$	Barnes et al. (2000)
Red-edge Green NDVI	$\frac{(red_edge)-green}{(red_edge)+green}$	Buschmann and Nagel (1993)
Red-edge NDVI	$\frac{(red_edge)-red}{(red_edge)+red}$	Ortiz et al. (2013)
Anthocyanin reflectance index 2 (ARI2)	$NIR\left[\left(\frac{1}{green}\right)-\left(\frac{1}{red_edge}\right)\right]$	Gitelson et al. (2002)

Table 1. Summary of selected vegetation indices used for tree stress detection caused by bark beetle infestation, where green is band 1 (550 nm), red is band 2 (650 nm), red_edge is band 3 (700nm) and NIR is band 4 (800 nm).

The signal of the stress or vitality of vegetation in the context of remote sensing techniques is reflected by the changes in biochemical and biophysical characteristics of the trees. The bark beetle infestation correlates, among others, with the changes in the greenness and leaf pigments concentration (Lausch et al., 2013). Based on the previous works (Tuominen et al., 2009; Ortiz et al., 2013; Adamczyk and Osberger, 2015), suitable vegetation indices have been selected to detect tree stress with respect to the spectral sensibility of the camera (Table 1).

Based on the set of selected spectral indices (Table 1), there was performed analysis of their values at given categories of forest disturbance. The aim was to analyse the informative value of different spectral indices to detect the different qualitative stages of vegetation based on µ-MCA Snap 6 sensor spectral bands. The assessed indicators are of three categories according to the principle of calculation – the simple ratio-like indices, the Normalized Difference Vegetation Indices (NDVI)-like indices and the Anthocyanin reflectance index 2 (ARI2).

Vegetation indices were extracted for all samples in every class within a buffer 25 cm around points. The number of samples was 5 for each class except dead trees category, in which was the only one (see Figure 1c). In the calculation process, the calibration values computed in PW2 were applied.

3. RESULTS AND DISCUSSION

3.1 Photogrammetric processing

The photogrammetric processing of multispectral images using Agisoft Photoscan resulted in a dataset with a re-projection error of 0.2 pixels. The root mean square error (RMSE) values of the seven checkpoints residuals were 0.07 m in horizontal (XY) plane and 0.14 in the Z direction. The resulting dataset represents the six-channel orthophoto with spatial resolution 2.5 cm (see Figure 1b). The photogrammetric processing accuracy is consistent with Turner et al. (2014) who state the accuracy of processing from 5.61 to 7.29 cm using former version (mini-MCA) of the camera.

The only but great disadvantage is that Agisoft Photoscan supplies only Bilinear interpolation resampling method which modifies original DN values. This is not acceptable for the analysis of forest damage status and in general for every vegetation health analysis by means of remote sensing. For this reason, the alternative workflow similar to Lehman et al. (2015) using georeferenced images stitched in ERDAS IMAGINE was used (see Figure 1c). The selected original images were georeferenced according to orthophoto with an accuracy of approximately 20 cm.

3.2 Spectral response of different disturbance categories

The spectral response analysis of different disturbance categories was performed (Figure 4). In comparison to the healthy trees, DN values of the infested trees are much higher in visible wavelengths and significantly lower in NIR wavelengths. Higher (radiance) DN values in the visible spectrum are an indicator of vegetation stress. The DN values of dead tree are separable only in the red and red-edge portion of the spectrum from infested trees. In the NIR wavelengths, there are no differences between DN values of dead and infested trees and also between categories forest restoration and grass. Results point to a greater sensitivity to variations of chlorophyll

in the red and red-edge than in NIR part of the spectrum. The most informative bands for tree stress detection caused by bark beetle infestation are band 2 (650nm) and band 3 (700nm), followed by band 4 (800 nm) from the red-edge and NIR part of the spectrum. The spectral response analysis is consistent with previous works. The greater sensitivity of red-edge band for assessing vegetation stress has been confirmed in experimental studies of Datt (1998) and Le Maire et al. (2004).

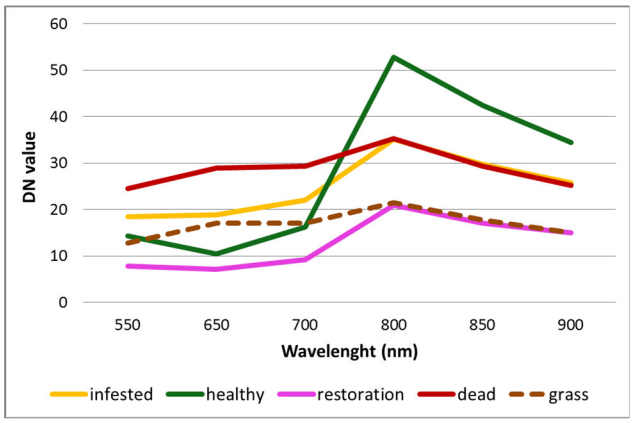

Figure 4. Average DN values of the established categories: infested trees, healthy trees, forest restoration, dead trees, and grass in the 550-900 nm spectral region.

3.3 Vegetation indices

The analysis of the variability of the values indicated the significant differences in sensitivity of the analysed indices to detect forest disturbance (Figure 5). Most of the assessed indicators are performing well in the detection of basic categories of a healthy forest, dead trees and the infested forest. These three categories are clearly separated while in particular the healthy forest and dead trees represent significantly unequivocal categories.

Most distinct separation of the basic categories with only marginal overlaps of values is apparent for Simple ratio 800/650 Pigment specific simple ratio B1 (Figure 5c), NDVI (Figure 5e) and the Red-edge index (Figure 5g). To the contrary, the fuzzy values even in these boundary categories are apparent in the Red-edge Green NDVI (Figure 5h) index and in the Anthocyanin reflectance index (Figure 5j), where the distinction of categories is almost impossible.

The key differences among the indices performance are apparent in their ability to distinguish the transition categories. In particular, it applies to the categories of the regenerating vegetation from the grass and infested trees. The distinction of the heterogeneous categories appeared to be complicated for most of the indicators. Despite the correct distinction at the level of mean values, the most common problem is the variability of values, resulting in significant overlaps.

We have identified only three indices, which seems to be able to correctly detect different forest disturbance categories in the complex conditions of a mixture of categories. From the tested indices, the best ability to separate the different categories was apparent in the classic NDVI index (Figure 5e). Among the analysed indices this was the only index where the interquartile range of values (IRQ) was without overlaps among the given categories. The Simple ratio 800/650 index (Figure 5c) is then able to distinctly separate the high forest from the understory vegetation and fair distinction between the infested and the regenerating forest categories. As the third well performing index, we can identify the Red-edge index (Figure 5g), which offers very narrow bands of IRQ variability suggesting good separability with only marginal overlaps among the categories. This confirms the statements by Datt (1999) and observations by Gitelson et al. (2006) concerning the use of red-edge and NIR reflectance as an indicator of forest health.

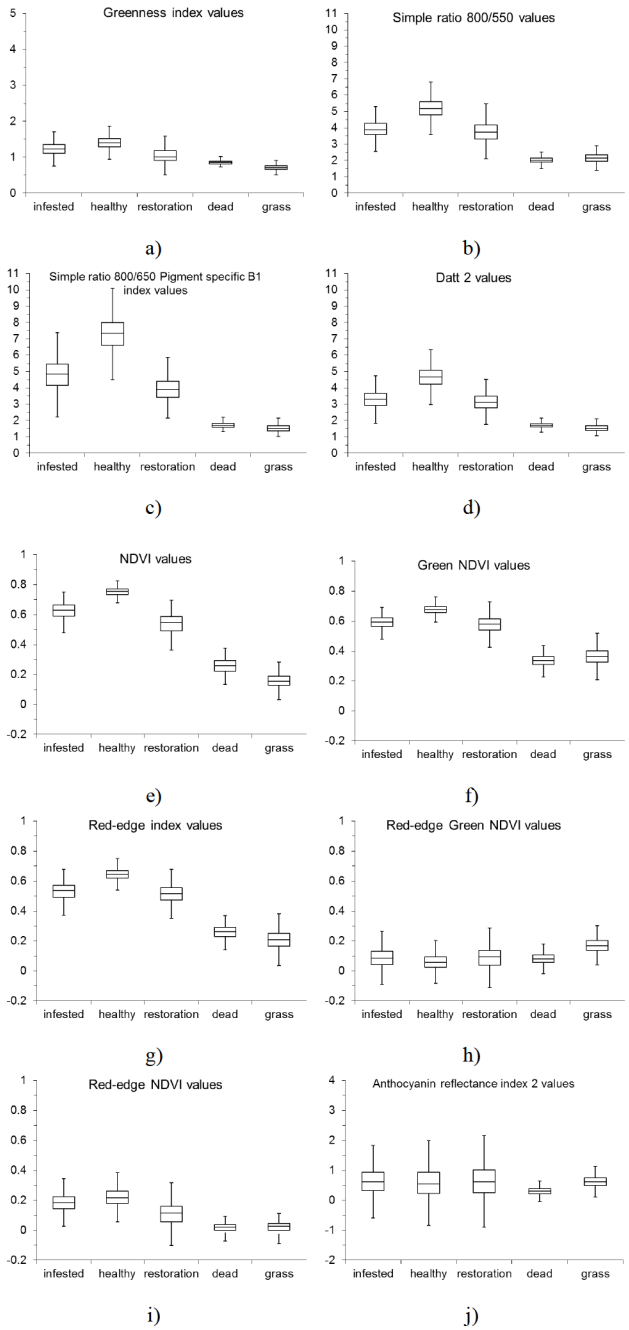

Figure 5. Distribution of values of the selected vegetation indices in tested categories of forest disturbance.

The differences in calculation among the three indices are apparent after their application to the study area (Figure 6). Every index has differently shaped histogram, tending in the case of NDVI to higher values (Figure 6a), for the NDRE to

mid-values (Figure 6b) and in the case of SR 800/650 index to the low values (Figure 6c). The diverging shape of histograms implies the different sensitivity of the three indices, calculated based on the μ-MCA Snap 6 data to the different stages of forest disturbance.

Histogram of the NDVI index is left-skewed towards the higher NDVI values. Such distribution suggests a better sensitivity of the index to healthy, regenerating and slightly disturbed forest cover. The distribution of NDRE index is most symmetric from the three indices with the slight left-skewed shape of the histogram, similar to the NDVI index. The NDRE index thus appears as most balanced, however, with potential overlaps in the zone of low values, i.e. the areas of damaged or low vegetation. To the contrary, the Simple ration 800/650 features a right-skewed distribution where the substantial part of the index values variability is covering the lower values. It suggests suitability for better separation of the categories with less dense canopy, open areas, heavily disturbed or dead trees.

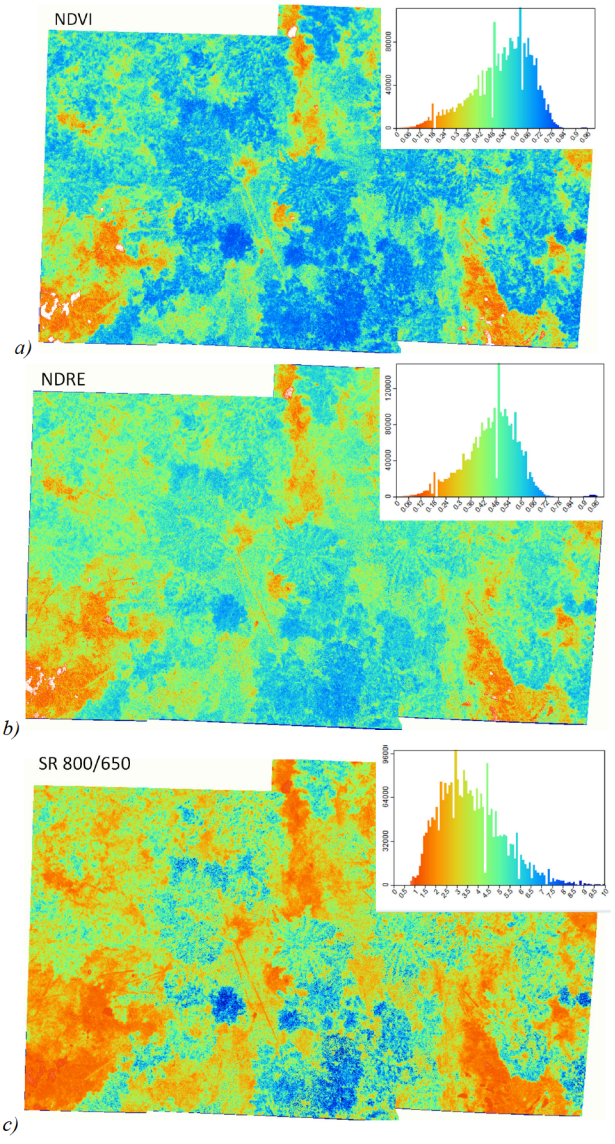

Figure 6. Spatial distribution of NDVI (a), SR 800/650 (b) and NDRE (c) indices over the study site.

4. CONCLUSIONS

In this paper, there are presented first results of the research study, aimed to employ the potential of the ultra-high resolution multispectral imagery for analysis of the signal of forest disturbance and regeneration in the montane spruce forest. The research was focused on a study site featuring the key stages of forest health status occurring in the area, including the healthy, disturbed and dead trees, the open areas, and newly regenerating vegetation.

The multirotor UAV equipped with the multispectral camera μ-MCA Snap 6 was first applied to test the applicability of the sensor for such analysis on the example of mid-latitude forest, attacked by the extensive bark beetle infestation. The spectral bands of the μ-MCA Snap 6 sensor were set to cover the reflectance in green, red, red edge and near infrared zone (550, 650, 700, 800, 850 and 900 nm) with a relatively narrow band width (20 nm). Based on the acquired imagery there was calculated a set of spectral indexes, applied in forest disturbance studies.

For the given indexes and there was tested the distribution of values in the test sites, reflecting the samples of the key categories of the forest status. Most of the tested indexes were able to correctly distinguish the boundary categories represented by the healthy and dead trees. The Anthocyanin reflectance index or Red-edge GNDVI were only two indexes unable to separate even such distinct categories of forest status and thus were excluded from the further analyses of the forest disturbance with the given data. The testing, however, proved that the distinct separation is difficult for the categories reflecting the transition of the status or featuring a mixture of categories like the slightly or heavily infested trees or the regenerating forest. There were identified only three indexes - NDVI, SR 800/650 Pigment Specific simple ratio B1 and NDRE, where the selected categories forest status are reflected by crisp ranges of values with distributions, not overlapping with the other categories.

For these best performing indicators there was tested the distribution of values their spatial variability and sensitivity to detect different stages of forest disturbance. Although all of the indexes are able to distinguish event the subtle differences in the forest status, they have varyingly skewed distributions of values, resulting in diverse sensitivity to the different stages of forest disturbance. Thus, the NDVI index has higher variability in the zone of the healthy or slightly disturbed forest. In contrast, the SR 800/650 has higher sensitivity in the zone of the disturbed forest cover.

The study proved the good applicability of coupling the UAV imaging with multispectral sensors for analysis of the forest disturbance. The ultra-high resolution of imagery in combination with the high operability of UAV imaging is enabling to study the spatial distribution of the forest disturbance in different qualitative stages and dynamics in space and time. However, as the resolution at the level of centimetres allows distinguishing individual tree branches or trunks, it brings also new challenges for interpretation and analysis, based on the uneasy treatment of transient or mixed categories.

The narrow bands of the multispectral sensor allow using the indexes, sensitive to the area of values according to the needs of the task. As the μ-MCA sensor allows working with used defined spectral bands, the further challenge is in also in the

testing of configurations of the spectral bands, in particular in the red-edge and near-infrared zone, which might result in more accurate detection of the signal of forest disturbance.

ACKNOWLEDGEMENTS

The research was supported by the EU COST Action 1306 project LD15130 "Impact of landscape disturbance on the stream and basin connectivity".

The authors would like to thank Theodora Lendzioch for her kind help with collecting the UAV imagery and support.

REFERENCES

Adamczyk, J. and Osberger, A., 2015. Red-edge vegetation indices for detecting and assessing disturbances in Norway spruce dominated mountain forests. *International Journal of Applied Earth Observation and Geoinformation,* 37, pp. 90-99.

Barnes, E. M., Clarke, T. R., Richards, S. E., Colaizzi, P. D., Haberland, J., Kostrzewski, M., Waller, P., Choi, C. and Lascano, R. J., 2000. Coincident detection of crop water stress, nitrogen status and canopy density using ground based multispectral data. In: *Proceedings of the 5th International Conference on Precision Agriculture*, Bloomington, MN, July, pp. 16-19.

Berni, J. A., Zarco-Tejada, P. J., Suárez, L. and Fereres, E., 2009. Thermal and narrowband multispectral remote sensing for vegetation monitoring from an unmanned aerial vehicle. *Geoscience and Remote Sensing, IEEE Transactions on*, 47(3), pp. 722-738.

Blackburn, G. A., 1998. Quantifying chlorophylls and caroteniods at leaf and canopy scales: An evaluation of some hyperspectral approaches. *Remote sensing of environment,* 66(3), pp. 273-285.

Borrelli, P., Panagos, P., Langhammer, J., Apostol, B. and Schütt, B., 2016. Assessment of the cover changes and the soil loss potential in European forestland: First approach to derive indicators to capture the ecological impacts on soil-related forest ecosystems. *Ecological Indicators,* 60, pp. 1208-1220.

Buschmann, C. and Nagel, E., 1993. In vivo spectroscopy and internal optics of leaves as basis for remote sensing of vegetation. *International Journal of Remote Sensing,* 14(4), pp. 711-722.

Campbell, P. E., Rock, B. N., Martin, M. E., Neefus, C. D., Irons, J. R., Middleton, E. M. and Albrechtova, J., 2004. Detection of initial damage in Norway spruce canopies using hyperspectral airborne data. *International Journal of Remote Sensing,* 25(24), pp. 5557-5584.

Chambers, J. Q., Asner, G. P., Morton, D. C., Anderson, L. O., Saatchi, S. S., Espírito-Santo, F. D., Palace, M. and Souza, C., 2007. Regional ecosystem structure and function: ecological insights from remote sensing of tropical forests. *Trends in Ecology & Evolution,* 22(8), pp. 414-423.

Datt, B., 1998. Remote sensing of chlorophyll a, chlorophyll b, chlorophyll a+b, and total carotenoid content in eucalyptus leaves. *Remote Sensing of Environment,* 66(2), pp. 111-121.

Datt, B., 1999. Visible/near infrared reflectance and chlorophyll content in Eucalyptus leaves. *International Journal of Remote Sensing*, 20(14), pp. 2741-2759.

Frelich, L. E., 2002. *Forest dynamics and disturbance regimes, studies from temperate evergreen-deciduous forests.* Cambridge University Press, Cambridge, UK.

Gitelson, A. A. and Merzlyak, M. N., 1997. Remote estimation of chlorophyll content in higher plant leaves. *International Journal of Remote Sensing,* 18(12), pp. 2691-2697.

Gitelson, A. A., Zur, Y., Chivkunova, O. B. and Merzlyak, M. N., 2002. Assessing carotenoid content in plant leaves with reflectance spectroscopy. *Photochemistry and Photobiology,* 75(3), pp. 272-281.

Gitelson, A. A., Keydan, G. P. and Merzlyak, M. N., 2006. Three-band model for noninvasive estimation of chlorophyll, carotenoids, and anthocyanin contents in higher plant leaves. *Geophysical research letters*, 33(11), pp. 1-5.

Göthlin, E., Schroeder, L. M. and Lindelöw, A., 2000. Attacks by Ips typographus and Pityogenes chalcographus on windthrown spruces (Picea abies) during the two years following a storm felling. *Scandinavian Journal of Forest Research,* 15(5), pp. 542-549.

Hais, M., Jonášová, M., Langhammer, J. and Kučera, T., 2009. Comparison of two types of forest disturbance using multitemporal Landsat TM/ETM+ imagery and field vegetation data. *Remote Sensing of Environment*, 113(4), pp. 835-845.

Heurich, M., Ochs, T., Andresen, T. and Schneider, T., 2010. Object-orientated image analysis for the semi-automatic detection of dead trees following a spruce bark beetle (Ips typographus) outbreak. *European Journal of Forest Research*, 129(3), pp. 313-324.

Kulakowski, D. and Bebi, P., 2004. Range of Variability of unmanaged subalpine forests. In: *Conference proceedings: Forum für Wissen: Schutzwald und Naturgefahren,* Davos, Switzerland. October 28–29, pp. 47–54.

Laliberte, A. S., Goforth, M. A., Steele, C. M. and Rango, A., 2011. Multispectral remote sensing from unmanned aircraft: Image processing workflows and applications for rangeland environments. *Remote Sensing*, 3(11), pp. 2529-2551.

Langhammer, J., Su, Y. and Bernsteinová, J., 2015. Runoff Response to Climate Warming and Forest Disturbance in a Mid-Mountain Basin. *Water,* 7(7), pp. 3320-3342.

Latifi, H., Schumann, B., Kautz, M. and Dech, S., 2014. Spatial characterization of bark beetle infestations by a multidate synergy of SPOT and Landsat imagery. *Environmental monitoring and assessment*, 186(1), pp. 441-456.

Lausch, A., Heurich, M., Gordalla, D., Dobner, H. J., Gwillym-Margianto, S. and Salbach, C., 2013. Forecasting potential bark beetle outbreaks based on spruce forest vitality using hyperspectral remote-sensing techniques at different scales. *Forest Ecology and Management,* 308, pp. 76-89.

Lehmann, J. R. K., Nieberding, F., Prinz, T. and Knoth, C., 2015. Analysis of unmanned aerial system-based CIR images in forestry—A new perspective to monitor pest infestation levels. *Forests,* 6(3), pp. 594-612.

Le Maire, G., Francois, C. and Dufrene, E., 2004. Towards universal broad leaf chlorophyll indices using PROSPECT simulated database and hyperspectral reflectance measurements. *Remote sensing of environment,* 89(1), pp. 1-28.

Lindner, M., Maroschek, M., Netherer, S., Kremer, A., Barbati, A., Garcia-Gonzalo, J., Seidl, R., Delzon, S., Corona, P., Kolström, M., Lexer, M. J. and Marchetti, M., 2010. Climate change impacts, adaptive capacity, and vulnerability of European forest ecosystems. *Forest Ecology and Management,* 259(4), pp. 698-709.

Masaitis, G., Mozgeris, G. and Augustaitis, A., 2013. Spectral reflectance properties of healthy and stressed coniferous trees. *Iforest-biogeosciences and Forestry*, 6(1), pp. 30-36.

Näsi, R., Honkavaara, E., Lyytikäinen-Saarenmaa, P., Blomqvist, M., Litkey, P., Hakala, T., Viljen, N., Kantola, T., Tanhuanpää, T. and Holopainen, M., 2015. Using UAV-Based Photogrammetry and Hyperspectral Imaging for Mapping Bark Beetle Damage at Tree-Level. *Remote Sensing,* 7(11), pp. 15467-15493.

Ortiz, S. M., Breidenbach, J. and Kändler, G., 2013. Early detection of bark beetle green attack using TerraSAR-X and RapidEye data. *Remote Sensing,* 5(4), pp. 1912-1931.

Salamí, E., Barrado, C. and Pastor, E., 2014. UAV flight experiments applied to the remote sensing of vegetated areas. *Remote Sensing*, 6(11), pp. 11051-11081.

Tetracam, 2015. Tetracam µ-MCA User's Guide, Tetracam Inc., Los Angeles, CA, USA.

Topcon, 2012. HiPer SR Operator´s manual, Topcon Positioning Systems, Inc., Livermore, CA, USA.

Tucker, C. J., 1979. Red and photographic infrared linear combinations for monitoring vegetation. *Remote sensing of Environment,* 8(2), pp. 127-150.

Tuominen, J., Lipping, T., Kuosmanen, V., and Haapanen, R., 2009. Remote sensing of forest health. In: *Geoscience and Remote Sensing*, InTech, Rijeka, Croatia, pp. 29–52.

Turner, D., Lucieer, A. and Watson, C., 2011. Development of an Unmanned Aerial Vehicle (UAV) for hyper resolution vineyard mapping based on visible, multispectral, and thermal imagery. In: *Proceedings of 34th International Symposium on Remote Sensing of Environment*, Sydney, NSW, Australia, 10–15 April, pp. 1-4.

Turner, D., Lucieer, A., Malenovský, Z., King, D. H., and Robinson, S. A., 2014. Spatial co-registration of ultra-high resolution visible, multispectral and thermal images acquired with a micro-UAV over Antarctic Moss Beds. *Remote Sensing*, 6(5), pp. 4003-4024.

Verhoeven, G., 2011. Taking computer vision aloft–archaeological three-dimensional reconstructions from aerial photographs with photoscan. *Archaeological Prospection*, *18*(1), pp. 67-73.

Zhang, C. and Kovacs, J. M., 2012. The application of small unmanned aerial systems for precision agriculture: a review. *Precision agriculture, 13*(6), pp. 693-712.

Článek II

Minařík, R., Langhammer, J., & Hanuš, J. (2019). Radiometric and Atmospheric Corrections of Multispectral μMCA Camera for UAV Spectroscopy. *Remote Sensing*, *11*(20), 2428. https://doi.org/10.3390/rs11202428

remote sensing

MDPI

Article

Radiometric and Atmospheric Corrections of Multispectral μMCA Camera for UAV Spectroscopy

Robert Minařík [1], Jakub Langhammer [1,*] and Jan Hanuš [2]

[1] Department of Physical Geography and Geoecology, Faculty of Science, Charles University, Albertov 6, 128 43 Prague 2, Czech Republic; robert.minarik@natur.cuni.cz

[2] Global Change Research Institute of the Czech Academy of Sciences, Bělidla 986/4a, 603 00 Brno, Czech Republic; hanus.j@czechglobe.cz

* Correspondence: jakub.langhammer@natur.cuni.cz; Tel.: +420-221-951-364

Received: 21 August 2019; Accepted: 15 October 2019; Published: 19 October 2019

Abstract: This study presents a complex empirical image-based radiometric calibration method for a Tetracam μMCA multispectral frame camera. The workflow is based on a laboratory investigation of the camera's radiometric properties combined with vicarious atmospheric correction using an empirical line. The effect of the correction is demonstrated on out-of-laboratory field campaign data. The dark signal noise behaviour was investigated based on the exposure time and ambient temperature. The vignette effect coupled with nonuniform quantum efficiency was studied with respect to changing exposure times and illuminations to simulate field campaign conditions. The efficiency of the proposed correction workflow was validated by comparing the reflectance values that were extracted from a fully corrected image and the raw data of the reference spectroscopy measurement using three control targets. The Normalized Root Mean Square Errors (NRMSE) of all separate bands ranged from 0.24 to 2.10%, resulting in a significant improvement of the NRMSE compared to the raw data. The results of a field experiment demonstrated that the proposed correction workflow significantly improves the quality of multispectral imagery. The workflow was designed to be applicable to the out-of-laboratory conditions of UAV imaging campaigns in variable natural conditions and other types of multiarray imaging systems.

Keywords: UAV; multispectral sensor; Tetracam μMCA; radiometric corrections; atmospheric corrections; spectroscopy

1. Introduction

Unmanned Aerial Vehicles (UAVs) equipped with miniature multispectral sensors are popular spectral imaging tools for nondestructive environmental monitoring in many fields of study, such as precision agriculture, forestry and nature protection [1–5]. Compared to spaceborne multispectral sensors, UAV sensors feature substantially higher spatial resolutions, temporal resolution, especially in areas with frequent cloud cover, and greater flexibility when designing the imaging campaigns and selecting suitable payloads [6]. Compared with airborne imaging, UAV sensors have lower operational costs and better spatial resolutions, thus enabling more detailed analyses of study sites [7]. However, the high level of spatial details that is enabled by the low imaging altitudes is balanced by the limited spatial coverage of the campaigns resulting from the short flight times for most unmanned imaging platforms. In geosciences, the key role of UAV imaging is to conduct detailed mapping of spatially highly heterogeneous or dynamic phenomena in often varying natural conditions. The ability to acquire correct spectral imaging results that are unbiased by the sensor properties or the atmospheric or topographic conditions is thus vital for the reliability and reproducibility of the results.

Optical remote sensing measures the radiance that is emitted, transmitted and mainly reflected from the surface [8]. The raw spectral data are stored as discrete Digital Numbers (DNs) and are altered by a mixture of effects that include the surface conditions, atmospheric effects, adjacency effects, topographic effects and sensor characteristics [9]. These alterations of the original spectral signal limit the quality and validity of the raw data for further quantitative analysis. To enable the extraction of qualitative information about land cover status from the imagery, it is important to apply radiometric and atmospheric corrections in processing. The restoration of the at-sensor measurement values and the data calibration using the surface reflectance factors improve the data quality, guarantees proper spectral image analysis and ultimately ensures the dataset's consistency with other calibrated datasets. Moreover, the quality and unbiased data could be used in decision support systems.

Radiometric processing consists of two main phases: radiometric (sensor) corrections and atmospheric corrections [10]. The aim of radiometric corrections is to restore the normalized DNs (called relative radiometric calibration), which have uniform responses over the whole image [11], or even to transform normalized DNs to radiance (called absolute radiometric calibration) [12]. These radiometric corrections reduce the undesirable additive noise component and the changes in the amounts of incoming radiance from sensors and optics, resulting in a vignetting effect and nonuniform quantum efficiency among chip cells. Atmospheric correction further builds upon the sensor correction results by deriving the surface radiance or reflectance from the corrected DN values. The atmospheric correction methods can be based on the following approaches: (i) Radiative Transfer Models (RTM) and (ii) empirical atmospheric corrections, which could be subdivided into image based and in situ measurement (vicarious calibration) [13].

In case of satellite multi/hyperspectral remote sensing sensors, the radiometric corrections are usually known and the atmospheric corrections methods are well defined, including both empirical or RTM approaches [9,10,14]. However, some of the UAV multispectral sensors, such as Tetracam MCA or sensors based on converted cameras are implemented using only basic or no calibration protocol and the sensors' radiometric properties are not known [15–17]. The recent generation of multispectral multi-array sensors such as the MicaSense RedEdge or Parrot Sequoia enables automated calculation of the corrections based on capturing a calibration image of a single calibration target before and after the flight [18,19]. However, such approaches are usually simplified and for an accurate data collection, analysis and comparison of data across different sensors, there is a need to develop user-designed correction methods [20]. This is mainly because the satellite and airborne multi/hyperspectral sensors (e.g., Landsat and Sentinel missions) are unique devices with known parameters of the sensor. However, the UAV multispectral sensors are manufactured in large series with slight differences in parameters among the same model.

Moreover, UAV imagery is typically acquired and processed by research teams or clients themselves, and feature high variability in the imaging platform instruments, acquisition conditions and workflow controls [8]. Moreover, some of the advanced UAV multispectral cameras enable the customization of the spectral bands using interchangeable filters according the scope of the given research task, which results in highly individualized parameters for each sensor. Hence, the calibration model must be adjusted to each camera [21]. Therefore, it is essential that at least basic radiometric data calibration is included in each study on UAV spectroscopy to ensure the reliability and consistency of the imaging results.

The general sensor correction methods for UAV digital cameras can be adapted from the pioneer works on RGB cameras [22–25] and from the self-designed multispectral imaging systems [26–28]. This is enabled by the common technical solution of cameras since the typical multispectral UAV cameras are equipped with Charge-Coupled Device (CCD) or Complementary Metal Oxide Semiconductor (CMOS) sensors, which are combined with optical filters [29–31]. Due to the growing variety of multi and hyperspectral sensors, the corresponding correction methods have evolved. Lelong et al. [32] used modified RGB cameras with an NIR filter to quantitatively monitor wheat crops, and the image processing included the vignetting correction using a polynomial function. Berni et al. [33], Kelcey and

Lucieer [34,35] and Del Pozo et al. [36] proposed a workflow of the image-based sensor corrections of a Mini-MCA 6 UAV multispectral camera with a rolling shutter sensor. Nocerino et al. [37] presented the geometric and radiometric calibration workflow for an MAIA multispectral camera. Padró et al. [38] used empirical line vicarious calibration for MicaSense RedEge and for Parrot Sequoia [39], being the widely used commercial UAV multispectral sensors. Custom calibration procedures are not just for multispectral sensors. Crusiol et al. [17] suggested a semiprofessional calibration method for an RGB camera and compared the laboratory and field implementations of the method. Honkavaara et al. [40] and Hakala et al. [41] designed a calibration workflow for a Fabry-Perot interferometer-based spectral camera. Hruska et al. [42], Aasen et al. [43], Buettner and Roeser [44] and Suomalainen et al. [45] proposed preliminary results on hyperspectral sensor calibration. From the current knowledge and practice, illustrated by the above-cited studies, there is apparent that radiometric corrections are vital for the correct use of multispectral sensors in UAV imaging campaigns. Most of the studies, however, is focused on resolving the particular problems of the given sensors or to testing their properties in laboratory conditions. However, the variety of UAV multispectral sensors is quickly expanding and includes the models with customizable spectral bands. This is resulting in often limited or lacking calibration protocols and information on the key sensor's radiometric properties—the linear response, vignetting and the signal-to-noise ratio. Hence, there is emerging a need for development of a universal radiometric correction method, practically applicable in conditions of UAV field imaging campaigns.

The aim of this study was to propose and test a universal and reliable radiometric calibration workflow for a Tetracam μMCA Snap multispectral camera featuring six separated channels with customizable spectral band settings for UAV spectroscopy. The proposed workflow enabled relatively simple empirical, image-based radiometric corrections combined with vicarious atmospheric corrections using the empirical line approach for easy applicability to other sensors. Compared to the preceding studies, the applied μMCA camera model was equipped with a global shutter, the radiometric corrections were assessed in controlled laboratory conditions with varying parameters, and the correction effect was tested using the acquired real-world dataset. The use of a multispectral sensor with a global shutter in the workflow is of substantial importance for the quality and reliability of the imagery. A rolling shutter sensor is not suited for taking images from moving imaging platforms because the rolling shutter will distort the acquired moving images and also causes a strong horizontal noise banding [8,34]. The use of the out-of laboratory dataset enabled a clear quantitative assessment of the effect of the corrections which is inconsiderable and proved the practical applicability of the approach. Moreover, the dark signal noise behaviour is investigated depending on the exposure time and ambient temperature. The nonuniform quantum efficiency is studied in changing exposure time and illumination.

In the case of the Tetracam μMCA Snap sensor, the radiometric properties of the camera were not known. Therefore, first, the camera's radiometric properties were investigated using a laboratory experiment to study the effects of the sensor on the resulting image quality and to calculate the radiometric corrections. The radiometric corrections were assessed in controlled laboratory conditions with varying parameters to simulate most typical natural conditions during imaging. To validate the workflow, a single multispectral image from the imaging campaign was selected to test the efficiency of the proposed method by comparing the raw and corrected images.

2. Materials and Methods

2.1. Multispectral Camera

We used a Tetracam μ-MCA Snap 6 (Figure 1) multiple camera array system to capture the images in six independent channels. Each channel is equipped with an identical camera with a fixed focal length, a 1.3 mega-pixel (1280 × 1024 pixels) CMOS global shutter sensor and a changeable bandpass filter. The global shutter sensor μ-MCA Snap cameras were selected as the preferred solution over the rolling shutter ones since they can better capture images with faster and less stable UAV platforms.

The key feature of the µ-MCA array is the possibility to customize the configuration of the wavelength pass filters at each lens according to the needs of the research task. The data sets that were collected for this study used the following setup of optical filters: 550 nm (Band 1), 650 nm (Band 2), 700 nm (Band 3), 800 nm (Band 4), 850 nm (Band 5) and 900 nm (Band 6) optical filters with a Full-Width at Half Maximum (FWHM) of 20 nm. The nonuniform global snap sensor's relative sensitivity to light and the nonuniform filter transmittance is compensated using the relative exposure settings to the master channel (Band 4), which are set in the cameras' production and differ for each camera model. The sensor parameters are given in Table 1.

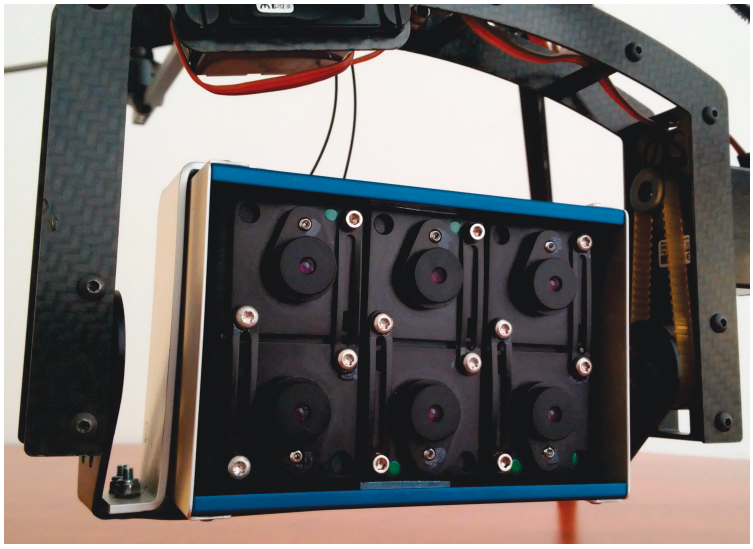

Figure 1. Multispectral 6-channel camera Tetracam uMCA Snap 6 equipped with 6 1.3 mega-pixel complementary metal oxide semiconductor (CMOS) sensors and changeable bandpass filters. This filter set includes 550 nm, 650 nm, 700 nm, 800 nm, 850 nm, 900 nm filter with FWHM 20 mm.

Table 1. The parameters of Tetracam µ-MCA Snap 6 camera.

Specification	Description/Value
Type	µMCA 6 Snap, 6 identical global shutter sensors, changeable bandpass filters
Sensor	1.3 mega-pixel CMOS sensor (1280 × 1024 pixels)
Sensitivity	~450 nm to ~1000 nm
Pixel Size	4.8 microns
Focal length	9.6 mm fixed lens
Aperture	f/3.2
Horizontal Angle of View	38.26°
Vertical Angle of View	30.97°
Default Depth of Field	~2 m to infinity
Bands	B1: 550 nm (FWHM 20 nm) B2: 650 nm (FWHM 20 nm) B3: 700 nm (FWHM 20 nm) B4: 800 nm (FWHM 20 nm) B5: 900 nm (FWHM 20 nm) B6: 950 nm (FWHM 20 nm)

2.2. Proposed Workflow

The proposed workflow is based on a laboratory investigation of the cameras' radiometric properties combined with vicarious atmospheric correction using the empirical line approach. It comprises techniques that reduce the noise, lens vignetting and nonuniform quantum efficiency

of the CMOS array, as the main source of errors [27,28,34]. Radiometric corrections were conducted using a calibrating sphere featuring an absolutely uniform light distribution, thereby ensuring the high accuracy of the corrections. The underlying assumption that the camera has a linear response to incoming light was examined. Moreover, the radiometric corrections were performed for variable laboratory conditions to simulate most typical natural conditions during imaging, thereby resulting in a radiometric correction database. The dark signal noise behaviour was investigated depending on the exposure time and ambient temperature. The nonuniform quantum efficiency was studied with respect to changing exposure times and illumination. A single multispectral image was selected from a field campaign as a practical example to demonstrate the efficiency of the proposed method by comparing the raw and corrected images. The results were validated by a field experiment using spectrally homogeneous calibration targets and consequent statistical testing. The data processing workflow is given in Figure 2.

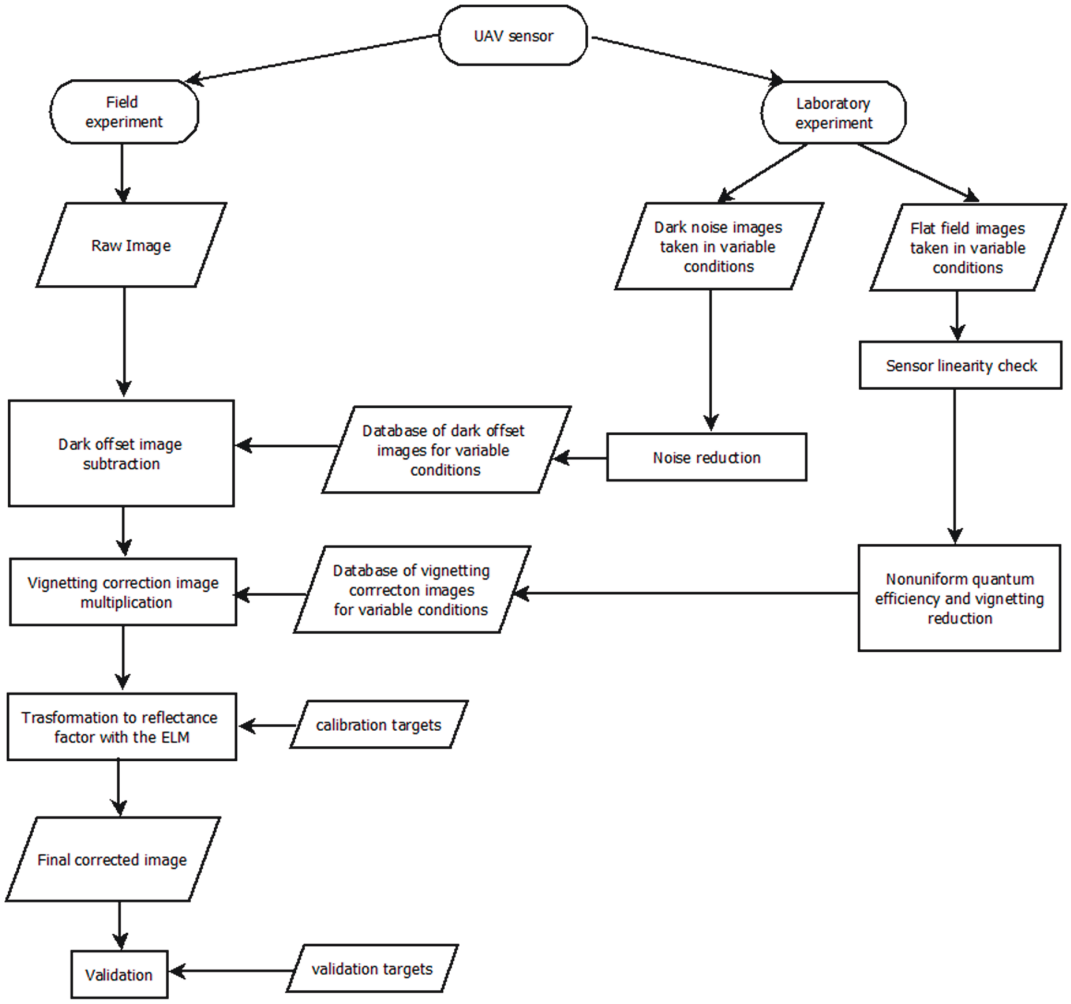

Figure 2. The full data processing workflow proposed in this study to create a reflectance data product.

2.3. Data Collection

2.3.1. Laboratory Experiment

The radiometric response of the camera was evaluated in the air-conditioned calibration laboratory of the Global Change Research Institute of the Czech Academy of Sciences featuring a CSTM-LR-20-M 1 m diameter integrating sphere (Labsphere Inc.) and ETHS 150 W light source (Figure 3). The calibration laboratory is a completely dark room that eliminates unwanted light sources and reflections. The light

source emits radiance from 300 nm to 2500 nm with a maximum radiance of approximately 900 nm. The spectral radiance curve is presented in Figure 4. The dark room itself was used to test the noise reduction methodology. The integrating sphere was used to verify the sensor's linearity, the reduction of the nonuniform quantum efficiency of the CMOS array and the reduction of the vignette effect. The primary laboratory temperature was set to 19°. However, a portable refrigerator and air condition were used to set required temperature during noise reduction experiment. The laboratory experiment was done prior to any further steps.

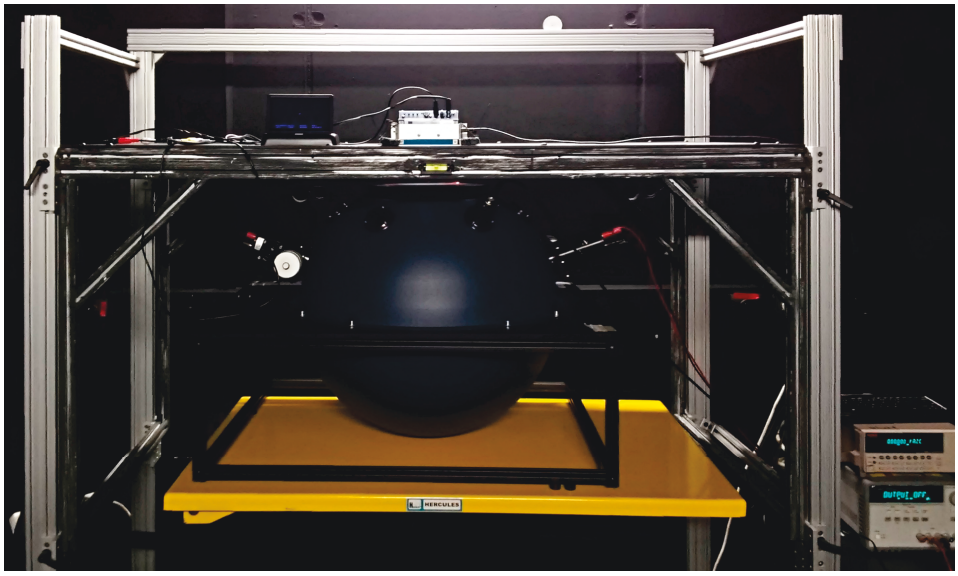

Figure 3. CSTM-LR-20-M integrating sphere with mounted multispectral camera above in the dark room.

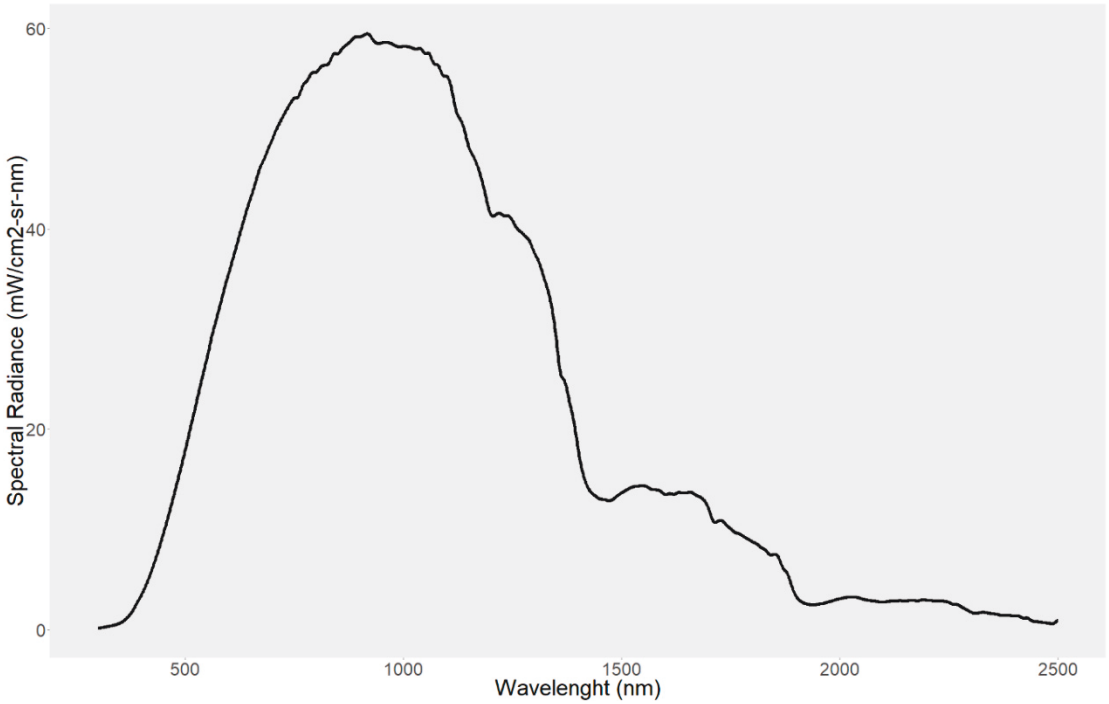

Figure 4. CSTM-LR-20-M integrating sphere spectral radiance curve from 300 nm to 2500 nm with maximum radiance around 900 nm.

2.3.2. Field Experiment

The full-resolution image was taken in March 2018 at noon (solar angle = 34.43°; solar azimuth = 175.83°) from a height of 15 m with a Ground Sampling Distance (GSD) of 0.75 cm. As a test ground, we used a beach volleyball court since the sand represents an almost lambertian surface with stable reflectance [46]. The ambient temperature was 8.3 °C. The exposure time was set to 500 µS in coherence with the illumination and a general rule of thumb that the brightest object on the surface (white target) should reach a maximum of 80% of the dynamic range.

The effect of the proposed correction workflow was first investigated using the profile (red line in Figure 5) comparing the normalized DNs of the original and corrected image. Radiometric corrections were conducted according to the proposed workflow consisting of subtracting the dark offset image from the database (T of 8 °C and exposure time of 500 µS) and multiplying that by the correction coefficient image from the database (Intensity of 0.6 mA and exposure time of 500 µS) that corresponded with the field conditions. We tested the hypothesis that the variation of the pixels along the profile that were extracted from the noncorrected raw image is greater than the variation of the pixels that were extracted from the corrected image. Since we found that normality of the raw profile data was violated, we used the robust Fligner-Killeen scale test with the *p*-value being estimated using the normal approximation.

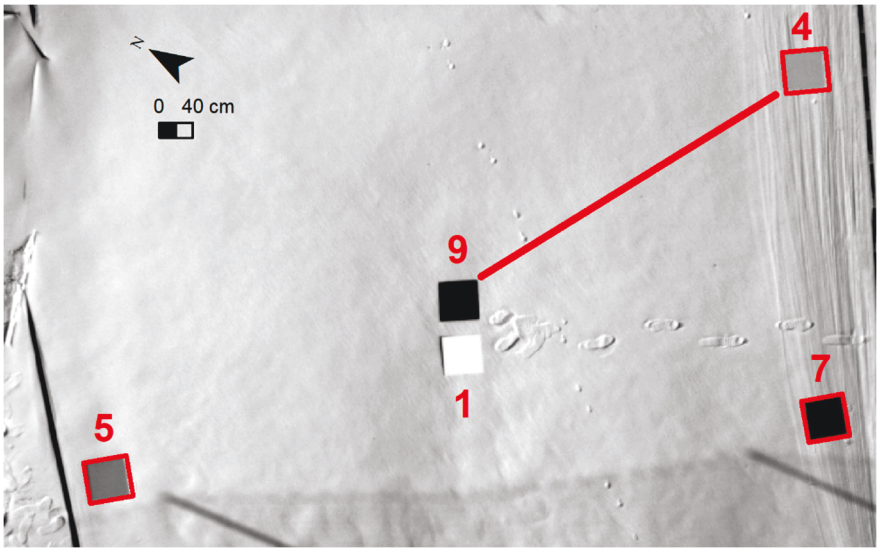

(a)

(b)

Figure 5. (**a**) The design of the field experiment. The single image in sensor geometry with the ground sampling distance (GSD) of 0.75 cm was used for the analysis. Figure shows the distribution of calibrating (1, 9) and validation (4, 5, 7) targets. Red line marks the profile to test the hypothesis that the variation of pixels along profile extracted from original non-corrected image is greater than the variation of pixels extracted from correction image. Red squares mark the validation targets; (**b**) The detailed view on targets.

The proposed correction procedure should also significantly refine the surface reflectance values, which was examined by using the validation targets. Therefore, the resulting reflectance distribution of the three verification targets that were extracted from raw and corrected images was compared with the field spectrometric measurement. The calibration targets were deliberately distributed on the beach volleyball court. The two targets (9—Anthracite and 1—Cream) were placed in the middle to reduce the vignetting effect and aid empirical line construction. Three verification targets (4—Pearl, 5—Light Gray, and 7—Medium Gray) were positioned according to the current conditions. They were not in the shadows and were placed on the edges and in the corners of the image where the vignette effect was the strongest. The targets were made of sheet metal (40 × 40 cm) that were professionally sprayed using NEXTEL colors with an absolute matt finish, resulting in the near lambertian surface properties in the visible-near infrared part of the spectrum. The properties of the targets were verified in the laboratory. The reflectance of targets was measured using StellarNet BlueWAVE field spectrometer directly before flight to achieve the maximum coherence with the image data (Figure 6).

We performed the atmospheric corrections using the two calibration targets in the middle of a scene, as inputs to computing the empirical line. The placement of the calibration targets in the middle minimized the influence of vignetting in both images. We computed the respective linear relationships for every channel of the raw and radiometrically corrected images. DN values from 500 pixels were extracted for the calibration. The median value was used to assign the reflectance value. Then, we extracted the median reflectance values and an interquartile range of the three verification targets (4, 5, and 7) from the raw and radiometrically corrected images and compared the results with the data from the spectrometer. We used 500 pixels for descriptive statistics and normalized root mean square error (NRMSE) calculations.

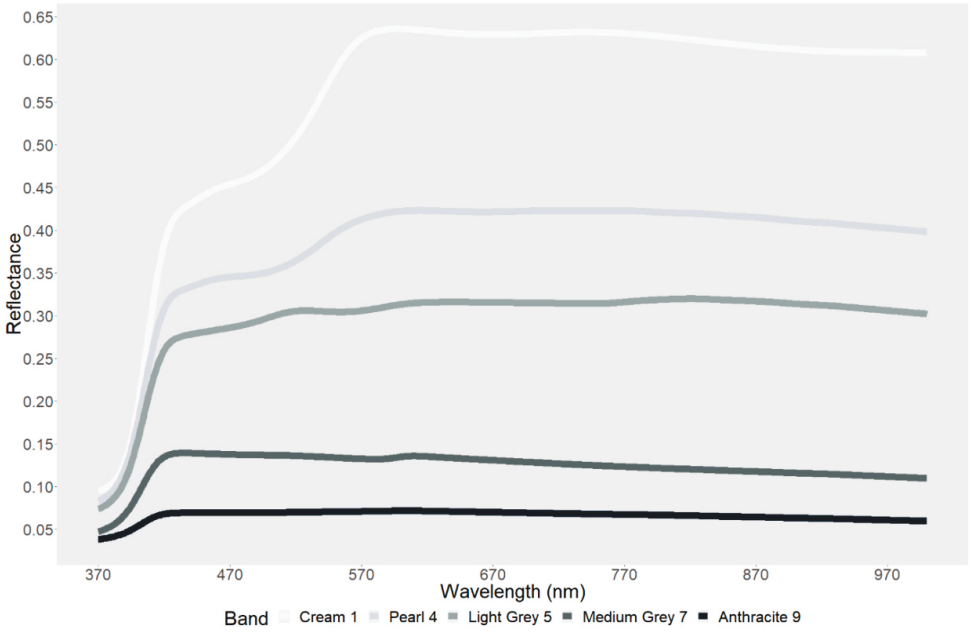

Figure 6. The reflectance of targets used in the field experiment measured by StellarNet BlueWAVE field spectrometer directly before flight.

2.4. Applied Correction Methods

2.4.1. Sensor Linearity

Sensor linearity is the underlying presumption of empirical line atmospheric correction. Here, a linear model that relates the digital level to the radiance that is captured by the sensor is established for each spectral channel of the camera. The sensor's linear response was investigated using different exposure times during the laboratory experiment. Typical exposure times used in the field and varying

light intensities were selected to simulate all spectra in natural lighting conditions. The images were taken at multiple exposure times of 50, 250, 500, and 1000 µS at a constant temperature of 19 °C. The mean DN number was computed for all channels at each exposure time at 10 levels of light intensity and plotted on a chart (Table 2). The light intensities were chosen in order to avoid the saturation of the image.

Table 2. The design of the experiment investigating the sensor linearity. Light intensity is given as a percentage of the integrating sphere source maximum light intensity. The maximum power of the source is 1 mA. Only the first 7 levels of light intensity were used in the 1000 µS experiment to avoid the image saturation.

Exposure Time (µS)	Light Intensity %
50	10, 20, 30, 40, 50, 60, 70, 80, 90, 96
250	8, 16, 24, 32, 40, 48, 56, 64, 72, 80
500	6, 12, 18, 24, 30, 36, 42, 48, 54, 60
1000	16, 20, 24, 28, 32, 36, 40

2.4.2. Noise Reduction

Noise is the unwanted additional component of a signal. In addition to the incoming radiance itself, an electrical signal can be affected by the temperature of the semiconductor devices and integrated circuits and increase as the exposure time increases [47]. It is particularly noticeable in the absence of light, especially when the radiance signal is zero and only dark signal noise is present. It consists of constant readout noise and random noise depending mainly on the sensor temperature and exposure time [11]. These can be used to reduce noise using image-based method called dark offset subtraction [23,34]. Through repetition, a sensor specific database of average dark offset images can be constructed and the characteristics of the per-pixel distribution of the noise can be extracted for the same exposure times that are used in the field. The average image is then subtracted from the field images and the standard deviation represents an approximation of the remaining noise following the dark offset subtraction. In this study, we apply dark offset subtraction to reduce the noise and study the effects of the ambient temperature and exposure time on the amount of image noise, which are the main user-controllable sources of noise, in a laboratory experiment with a factorial design. The parameters of the camera like the ISO and aperture are fixed so that there is no need to consider them.

The dark offset images were taken in a completely dark room simulating real conditions by changing ambient temperature and exposure time in the factorial design for each band (Table 3). For each combination of factors, 20 dark offset samples were taken. The average and standard deviation (SD) images were computed for each combination to characterize the distributions of the per-pixel noise. Before starting the experiment, the camera was turned on for 30 min to be properly warmed up under the chosen ambient temperature using a portable refrigerator and air conditioning in the dark room. The effects of the ambient temperature and exposure time on the amount of image noise were studied using the Repeated Measures Analysis of Variance (ANOVA). The 1000 pixels were randomly selected from the resulting average images from each combination as an input to the ANOVA. Since the normality and sphericity assumptions were violated, we used the Box-Cox parametric power transformation [48] and the Greenhouse and Geisser adjustment method for the within subject effects [49]. Finally, dark offset subtraction was applied to the corresponding UAV test image. The average image was subtracted from the test image from a field experiment.

Table 3. The factorial design of experiment studying the effects of the ambient temperature and exposure time on the amount of image noise as a main user-controllable sources of noise in laboratory.

Temperature (°C)	Exposure Time (μS)
8	50
	250
	500
	1000
19	50
	250
	500
	1000
27	50
	250
	500
	1000

2.4.3. Nonuniform Quantum Efficiency and Vignetting Reduction

The vignette effect is a well-known phenomenon that is visible in flat field images as the light intensity falloff from the center to the edge (Figure 7). It is the percentage decrease in the illumination level reaching the focal sensor that is composed of the cosine of the fourth falloff (unavoidable) and the field efficiency of the lens itself [50]. The nonuniform quantum efficiency is the small per pixel random variation of the collected charge of pixels under the same illumination that is introduced during the manufacturing process. It overlies the vignette effect trend [28] resulting in a bumpy surface in Figure 7. Also, dust could be present on the sensor. It occurs as a black stigma in dark image (Figure 7). These effects greatly bias the DNs, so they must be reduced.

The per-pixel vignette effect, nonuniform quantum efficiency effect and dust defects were corrected using a set of flat field noise corrected images under uniform illumination using the look-up-table (LUT) correction method. The LUT correction method is constructed on the assumption that the brightest pixels in the center are not affected by any error and they can serve as reference values for normalization. Then, the ratio of the normalized DNs to the DN of each pixel can be calculated as the vignetting correction coefficient. The correction coefficients were computed using Equation (1) [51]:

$$I_{LUT}(i, j) = I_{ref,\,max}/I_{ref}\,(i, j) \quad (1)$$

where $I_{LUT}(i, j)$ is the correction coefficient of the pixel at position (i, j), $I_{ref,\,max}$ is the maximum brightness value of the image and I_{ref} (i, j) is the brightness value of pixel position (i, j). The result is a raster of per-pixel correction coefficients (Figure 7b) that, after multiplying by the field images, reduces vignetting.

The effects of the exposure time and illumination intensity on the correction coefficients were studied using the same dataset, which was used for linearity testing. The flat field images were taken at multiple exposure times of 50, 250, 500, and 1000 μS at 10 levels of light intensity at a constant temperature of 19 °C (see Table 2). The average image was computed using a set of 10 images, which were taken for every combination of exposure time and intensity. After subtracting the corresponding dark offset image from the average flat field image, the correction coefficient images were computed. The appropriate correction image was then applied to the test image from a field experiment.

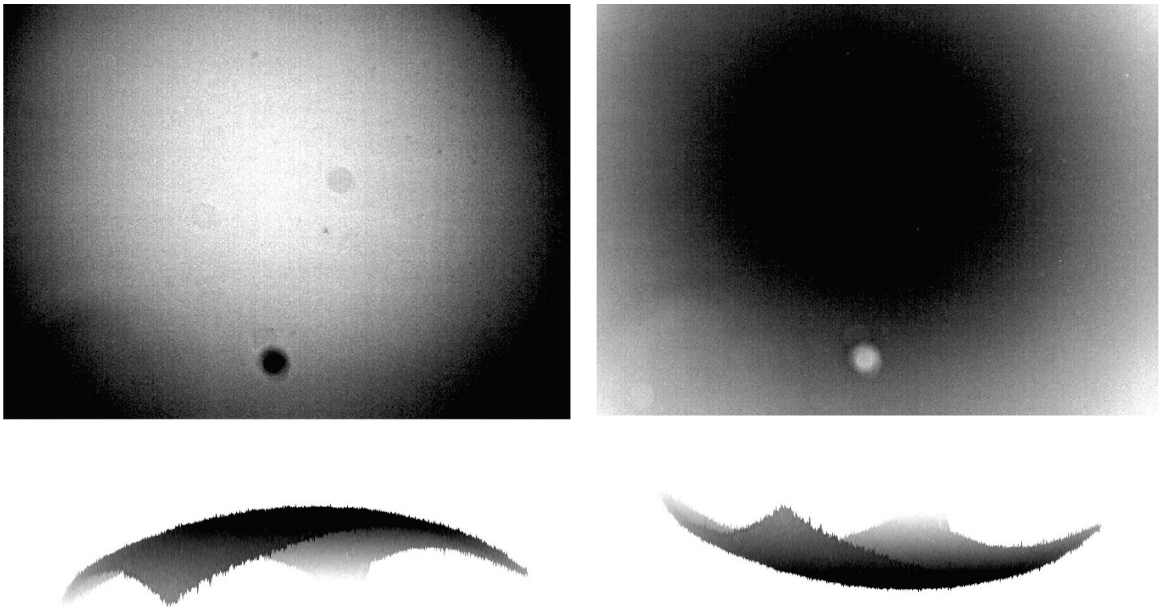

(**a**) (**b**)

Figure 7. (**a**) 3D Illustration of vignette effect and flat field image with typical light falloff and bumpy surface caused by nonuniform quantum efficiency in Channel 4; (**b**) corresponding correction coefficient image. The black stigma in (**a**) is the dust on sensor itself that could not be removed by user, but it could be corrected using look-up-table (LUT) correction method (**b**).

2.4.4. Atmospheric Correction

Once the sensor correction is applied to the calibration image, the atmospheric corrections can be processed. Among the different calibration methodologies, we chose a vicarious calibration based on the empirical line method [52], which is also used for UAV imaging [33,53]. The method assigns a reflectance value to each pixel that is based on the computed linear relationship between the known reflectance value of the light and the dark reflectance panels (see Figure 5) and their DN numbers that were extracted from images. In general, the calibration targets should be 10+ times bigger than GSD to extract at least one hundred of pixel values [16,20]. This method greatly reduces both illumination and atmospheric effects, converts the DNs to reflectance and thus allows for the comparison of datasets that were collected in different seasons and light conditions [9].

2.5. Data Processing

The analytical processing of the data from the laboratory experiment and the computation of radiometric corrections were carried out in R [54] according to the methodology that was described in the previous subsections. The radiometric corrections and radiometric calibration of the field image were conducted in R too. R was used also to create graphs, calculate the descriptive statistics and conduct hypothesis testing. Prior to any processing in R, the images mages were converted from the proprietary 10-bit RAW format to a multispectral 16-bit Single-Page Tagged Image File Format (TIFF) using PixelWrench2 [55].

3. Results

3.1. Sensor Linearity

The sensor linearity was confirmed for each channel using a regression coefficient that was higher than 0.99, regardless of the irradiance and exposure time (Figure 8; Figure 9). The experiment also

evaluated the efficiency of the relative exposure time setting that balanced the nonuniform relative sensitivity of sensors to monochromatic light. The channels with longer wavelengths in the NIR part of the spectrum have automatically longer exposure times. The channels are well balanced except for band 1 (550 nm) that has a shorter exposure time than it should have. This is because of the differences in the halogen light of the sphere and sunlight.

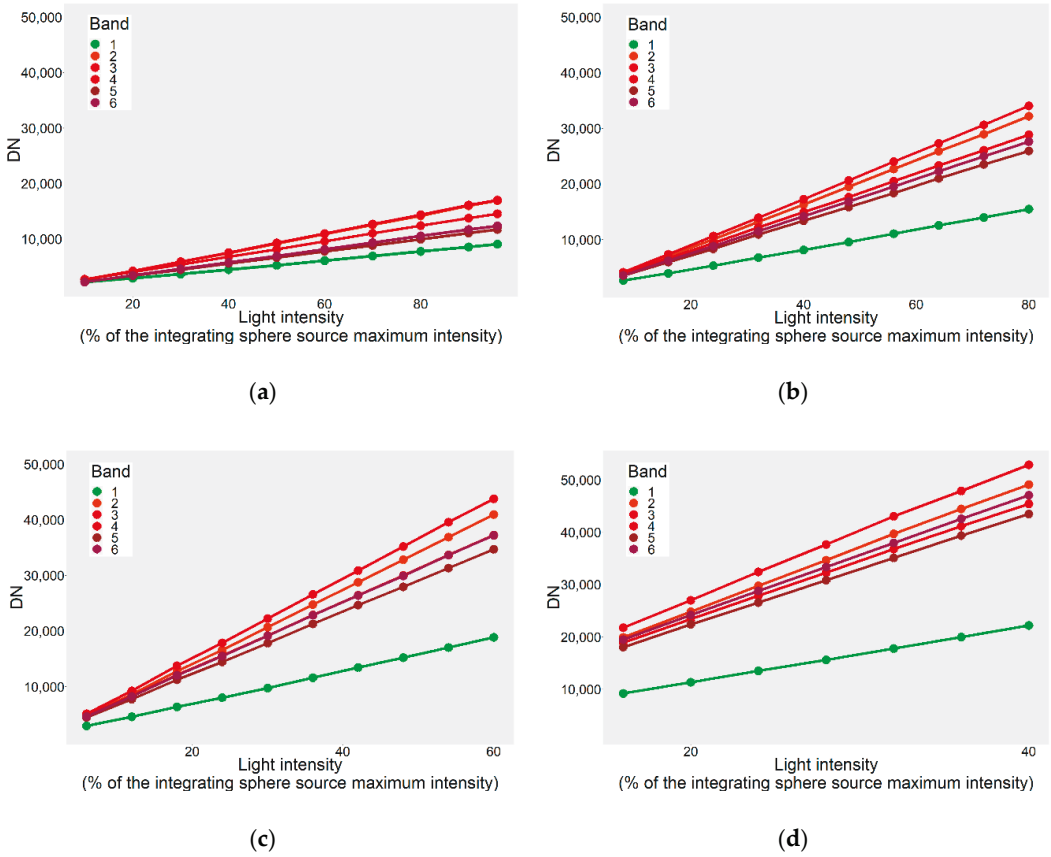

Figure 8. The linear response of the camera at different exposure times: (**a**) Exposure time 50 µS; (**b**) Exposure time 250 µS; (**c**) Exposure time 500 µS; (**d**) Exposure time 1000 µS. The sensor linearity was confirmed on each channel with a regression coefficient higher than 0.99.

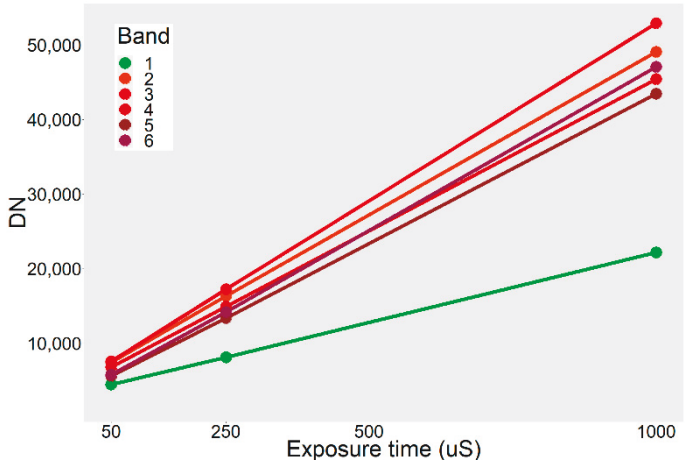

Figure 9. The linear response of the camera at 40% of the integrating sphere source maximum intensity.

3.2. Noise Reduction

The dark offset images were computed for each combination of factors and bands of the camera. A simple visual assessment of the per-pixel noise characteristics of the dark offset average images reveals checkered patterns in bands 1–3 (a–c) (Figure 10). Bands 4–6 (d–f) contain salt-and-pepper and periodic noise, which more significantly affect the longer wavelengths. The checkered pattern is more visible in SD images because it forms squares with similar values.

An examination of the per-pixel dark offset images (average of 20 samples) reveals that the highest noise is in band 1, but band 1 has the smallest variability and a left skewed distribution (Figure 11). This is due to the strong checkered pattern that is associated with similar higher noise values. A shorter relative exposure time (0.75 of the master channel´s band 4 exposure time) has also an effect on the higher noise values. A similar distribution with a higher median and smaller variability of the noise is also Band 4, but it has no skewness. Band 4 also has a short relative exposure time under 1 (0.8 of the set exposure time). The distributions of Bands 4, 5, and 6 are symmetric since no strong pattern is presented. Bands 2 and 3, which also have checkered patterns, are also skewed in accordance with the previous results. Band 2 is skewed left too. Conversely, Band 3 is skewed right, which means that the checkered pattern is formed by pixels with lower noise values. The noise variability of Bands 2, 3, and 5 is less equal but higher compared to Bands 1 and 4 because all bands have longer relative exposure times of approximately 1 of the master channel´s band 4 exposure time. The band 6 shows the highest noise variability due to highest relative exposure time (1.3 of the master channel´s band 4 exposure time). The boxplot of Band 6 (exp. time 500 µS and temp. 27 °C) is missing because of damage to the RAW images.

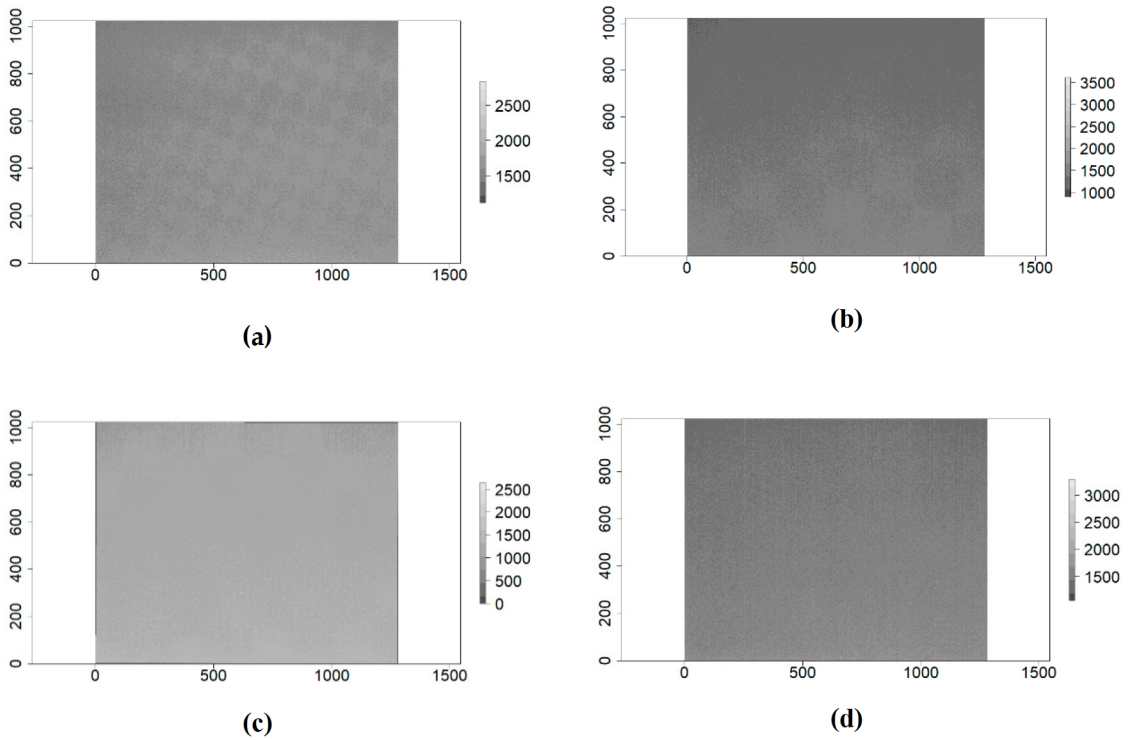

Figure 10. *Cont.*

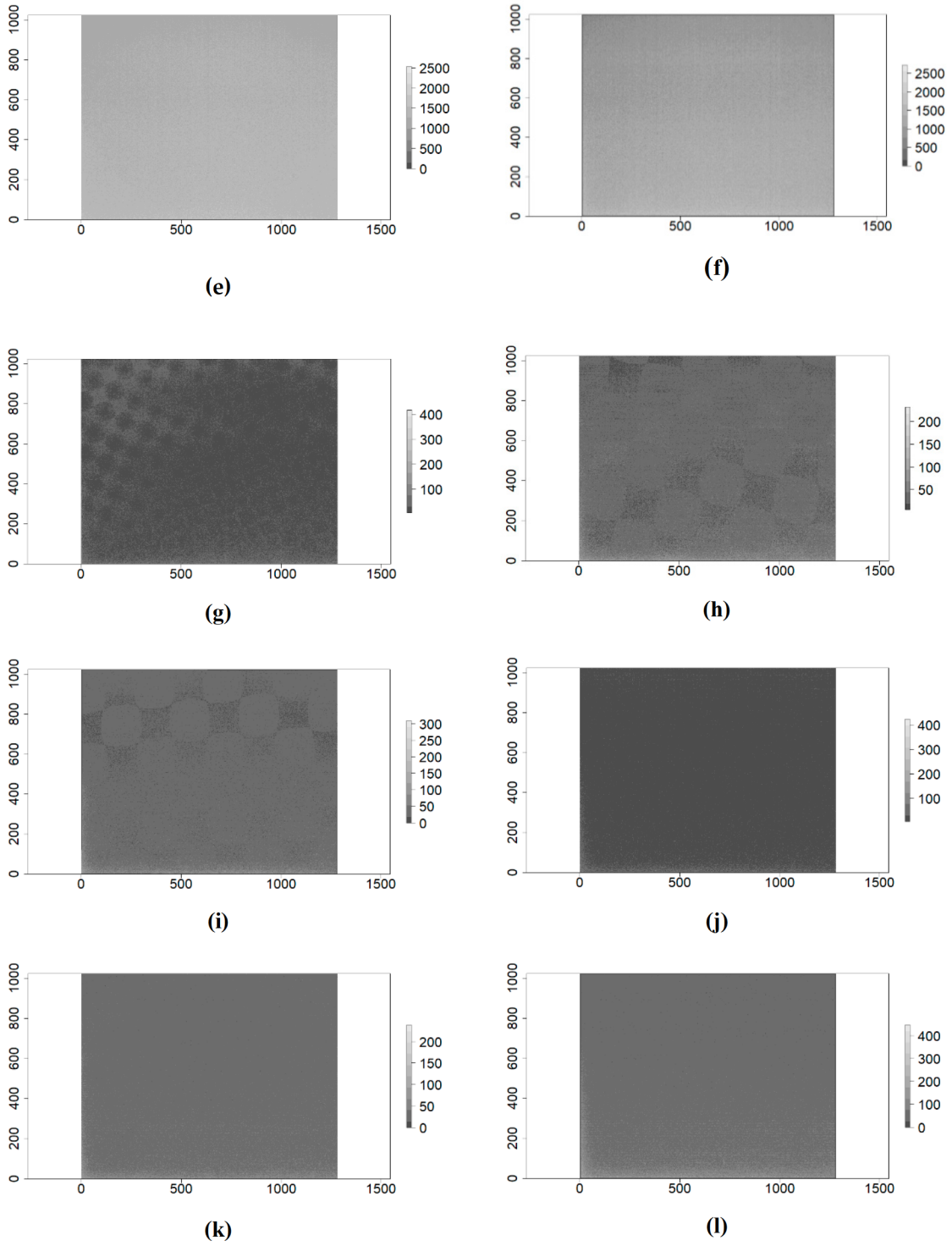

Figure 10. Dark offset imagery taken at a temperature 8 °C, exposure time 500μS of all bands: (**a**) Average image B1; (**b**) Average image B2; (**c**) Average image B3; (**d**) Average image B4; (**e**) Average image B5; (**f**) Average image B6; (**g**) Standard deviation image B1; (**h**) Standard deviation image B2; (**i**) Standard deviation image B3; (**j**) Standard deviation image B4; (**k**) Standard deviation image B5; (**l**) Standard deviation image B6. The average and standard deviation (SD) images are calculated from 20 samples.

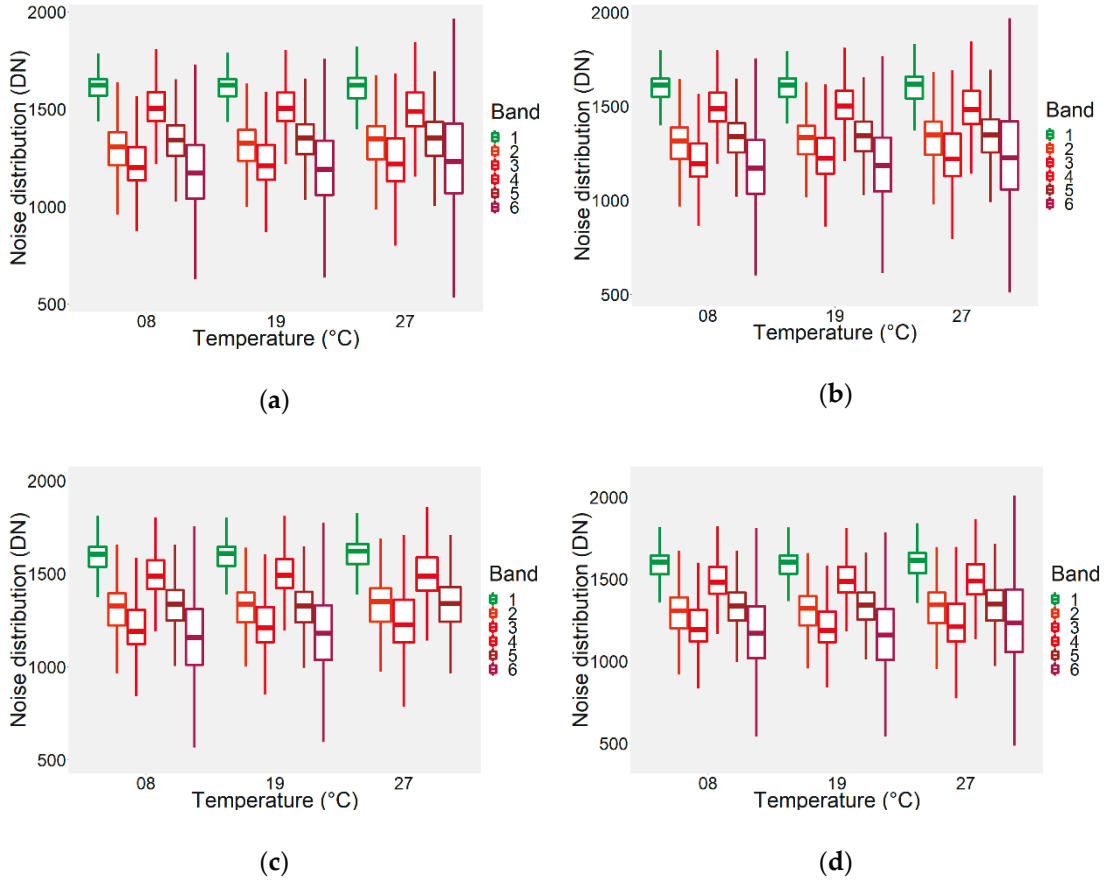

Figure 11. Comparison of the per-pixel noise distribution of dark offset images in the laboratory experiment: (**a**) Exposure time 50 µS; (**b**) Exposure time 250 µS; (**c**) Exposure time 500 µS; (**d**) Exposure time 1000 µS.

Although only the average image is used to reduce the noise by subtracting it from the field images, it makes sense to calculate and examine the SD image that is calculated from the 20 samples since it represents an approximation of the remaining noise following dark offset subtraction. An examination of Figure 12 shows that the highest variability in the per-pixel SD that also has the highest median value is band 6. Conversely, the lowest variability and noise are visible in Bands 1 and 4. This is associated with the relative exposure time. The bands with longer relative exposure times have larger noise variation in single frames, which is reflected in the higher SD. The dark offset subtraction method reduces the image noise well. The residual noise remaining after noise correction is less than 1% of the dynamic range. The boxplot of Band 6 (exp. time of 500 µS and temp. of 27 °C) is missing because of the damage to the RAW images.

If we focus on the noise depending on the changing ambient temperature and exposure time, it is especially evident in Bands 2, 5, and 6 that at the same exposure time, the noise increases as the ambient temperature increases. Therefore, we studied these effects as the main user-controllable sources of noise.

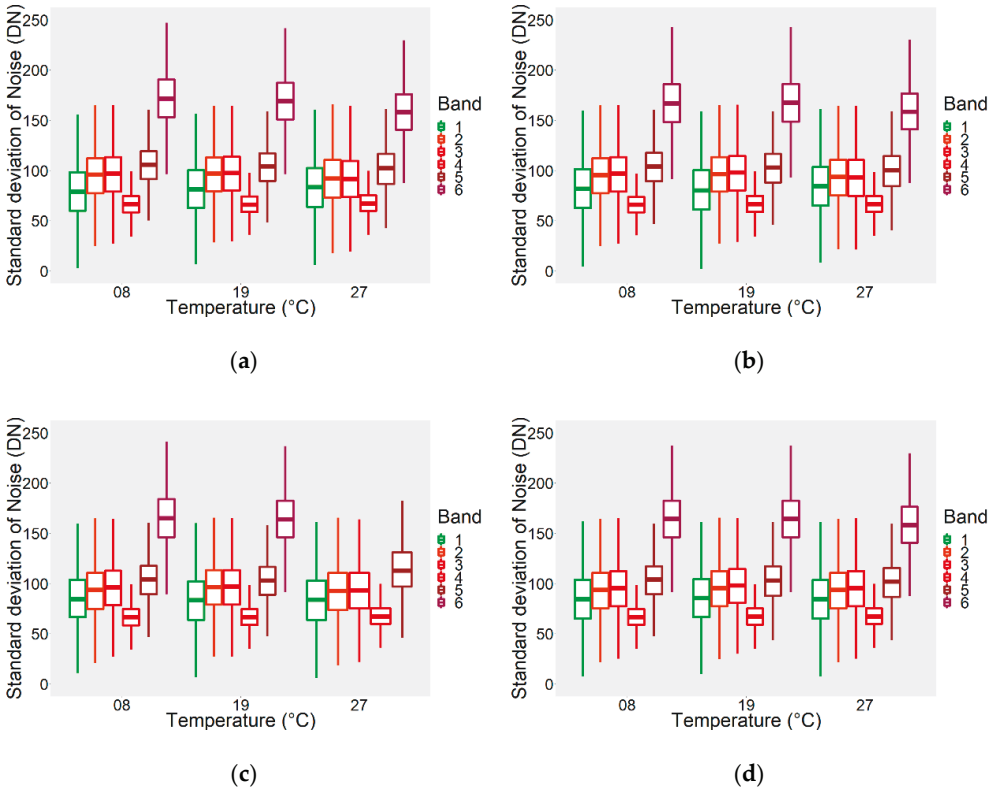

Figure 12. Comparison of the per-pixel SD noise characteristics divided by exposure time: (**a**) Exposure time 50 µS; (**b**) Exposure time 250 µS; (**c**) Exposure time 500 µS; (**d**) Exposure time 1000 µS.

We found a significant difference in the average value of the noise depending on the ambient temperature and exposure time. The ANOVA results are summarized in Table 4. Both effects were significant in every band. Therefore, it is necessary to apply a proper dark offset image that was calculated using dark images that were taken under the same conditions to the real-world image. Moreover, the interaction between factors was also significant for all bands; therefore, an interaction plot was created (Figure 13). The interactions are complicated and less significant compared to the main effects size. The positive effect of the rising ambient temperature to noise is clear and more pronounced, especially in Bands 1, 2, and 3, and in infrared Bands 5 and 6. In these bands, there has been a rapid increase of the noise in the measurements from 19° to 27° C with longer exposure times (500 and 1000 µS). The negative effect of the rising exposure time due to decreasing noise was more pronounced in Bands 1, 4 and 5. In Bands 1, 2, and 5, we could assume that the interactions were close to the additive effect of the factors.

Table 4. The repeated measures analysis of variance (ANOVA) table of ambient temperature (temp) and exposure time (exptime) upon image noise. The column statistics shows degrees of freedom after Greenhouse-Geisser correction. The F value column represents the values of test statistics for each model term, *p* value represents the test significance for this term.

Band	Expression	Statistics	F-Value	*p*-Value
B1	temp	F(1.35, 1348.41)	57.57	<0.001
	exptime	F(2.69, 2682.73	106.70	<0.001
	temp:exptime	F(5.50, 5808.43)	21.97	<0.001
B2	temp	F(1.66, 1658.68)	327.60	<0.001
	exptime	F(2.93, 2922.19)	41.31	<0.001
	temp:exptime	F(5.91, 5906.79)	8.54	<0.001

Table 4. *Cont.*

Band	Expression	Statistics	F-Value	*p*-Value
B3	temp	F(1.34, 1697.68)	163.14	<0.001
	exptime	F(2.74, 2741.60)	43.91	<0.001
	temp:exptime	F(5.87, 5868.6)	38.29	<0.001
B4	temp	F(2, 1998)	44.46	<0.001
	exptime	F(3, 2997)	150.28	<0.001
	temp:exptime	F(6, 5994)	60.26	<0.001
B5	temp	F(1.67, 1676.18)	53.26	<0.001
	exptime	F(2.89, 2888.67)	80.76	<0.001
	temp:exptime	F(5.85, 5842.95)	10.28	<0.001
B6	temp	F(1.47, 1472.17)	559.63	<0.001
	exptime	F(1.95, 1949.77)	29.87	<0.001
	temp:exptime	F(3.91, 3905,11)	37.38	<0.001

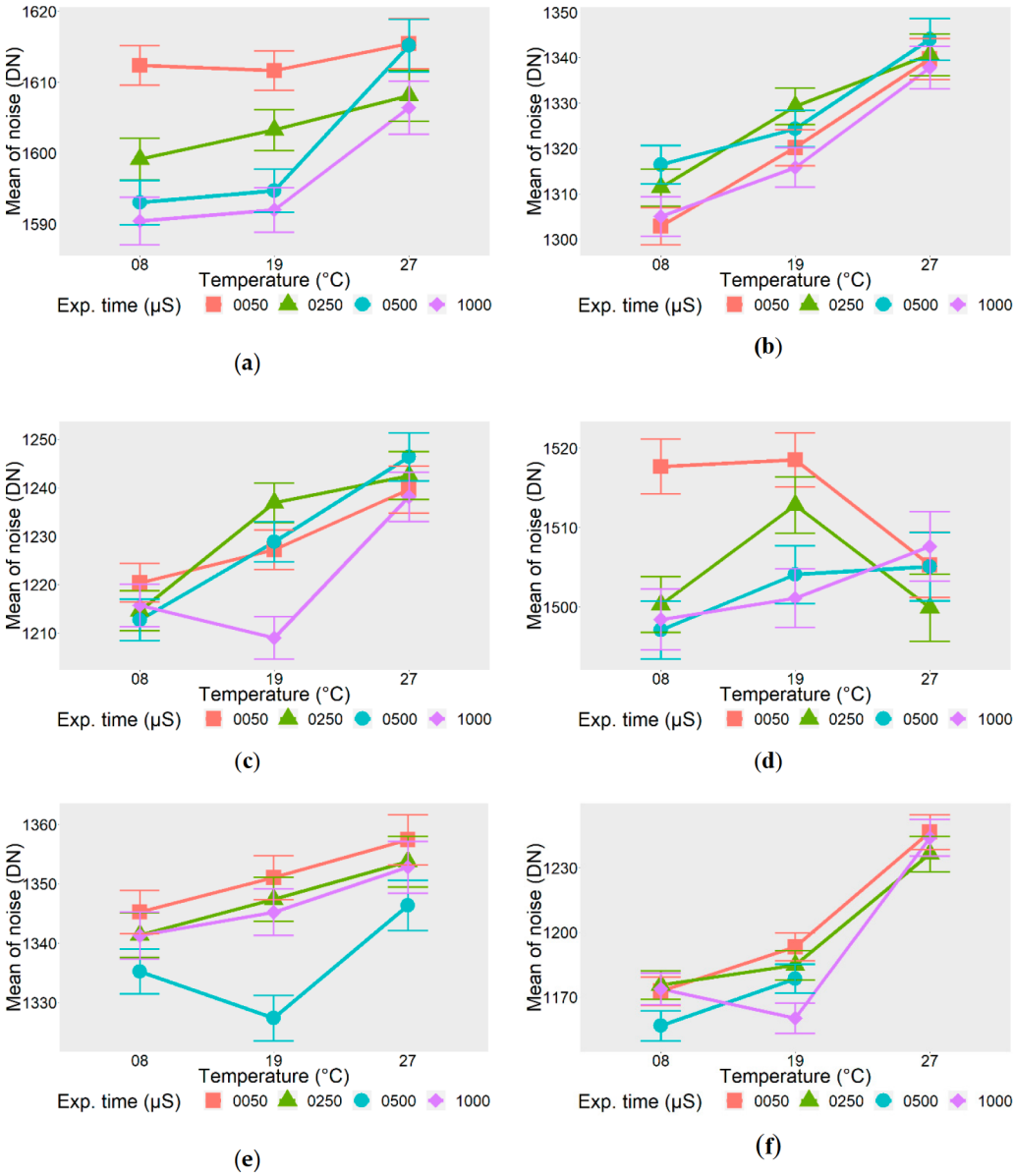

Figure 13. The interaction plot of model term temp:exptime for each band: (**a**) Band 1; (**b**) Band 2; (**c**) Band 3; (**d**) Band 4; (**e**) Band 5; (**f**) Band 6. Error bars represent 95% confidence intervals.

3.3. Nonuniform Quantum Efficiency of CMOS Array and Vignetting Reduction

A visual assessment of the vignette effect showed that the vignetting structure is different for every band (Figure 14), but it is affected by the physical location of the sensors on the camera. We can see that the middle point of the falloff circle is significantly shifted down in Band 1 (c). On the opposite side, Band 4 (f) is shifted up. The middle pairs of Bands 3 and 6 (b and e) are shifted left. The left pairs of Bands 2 and 5 (a and d) are roughly centered. There are also visible stigmas in (e and f) that are caused by dust on sensors.

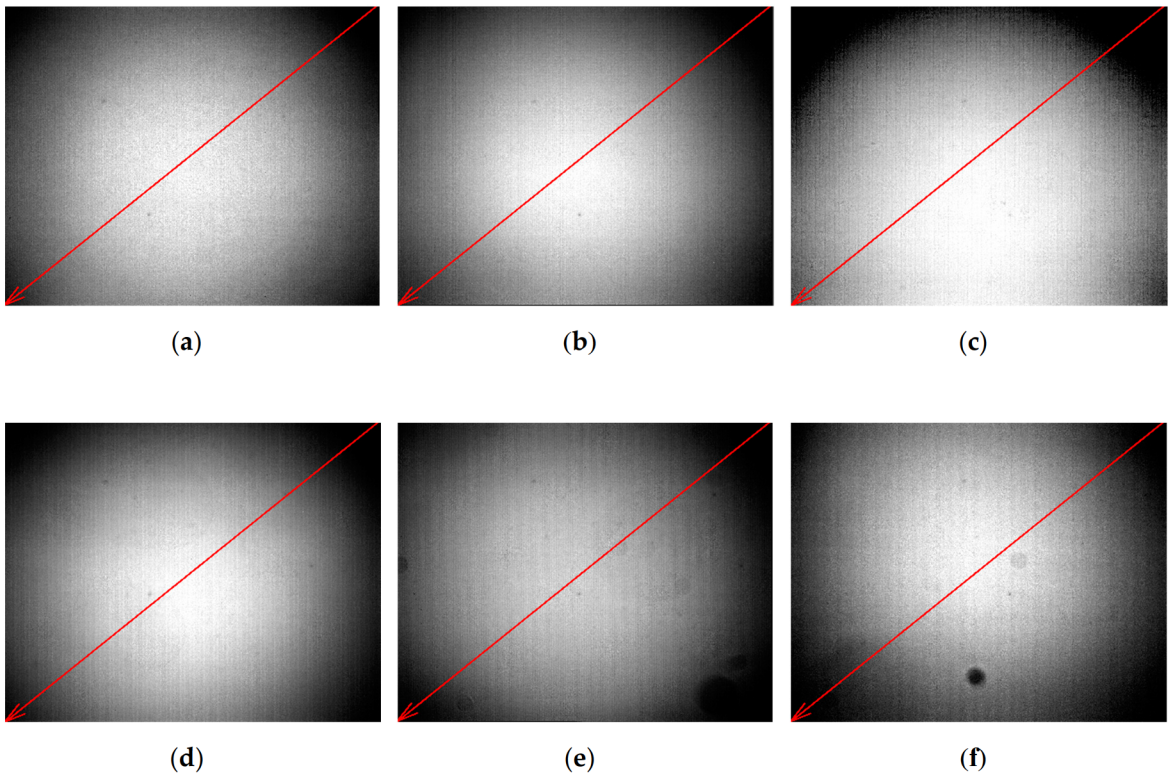

Figure 14. The vignette effect of μMCA camera channels: (**a**) Band 5; (**b**) Band 6; (**c**) Band 1; (**d**) Band 2; (**e**) Band 3; (**f**) Band 4 (Master). The order of channels is in consistent with physical location of sensors on the camera. The red arrow marks a vignetting profile where correction coefficients were subjected to further investigation for each. Profile starts in upper right corner and ends in lower left corner.

The vignetting radial falloff of each band is shown in Figure 15. The radial falloff rates (the shapes of the curves) reveal only minor variations between bands. These disparities are caused by the imperfections of the optical system of individual lenses and the different transmittance of each filter. Furthermore, there are major differences in the correction coefficient values. The strongest vignette effect results in the highest correction coefficients in Bands 1 and 4 followed by Bands 6, 5, 2 and 3. These differences are caused by the different points of origin of the vignetting (especially Bands 1 and 4, as shown in Figure 14). It is also clearly visible that the correction coefficient decreases in all bands as the exposure time increases, and that the values of the correcting factor at 50 μS significantly differ from the others in all bands. The variance of the individual pixel values also changes across the profile. The longer the exposure time that is used, the lower the variance. These disparities are caused mainly by the actual dynamic range of the flat field image.

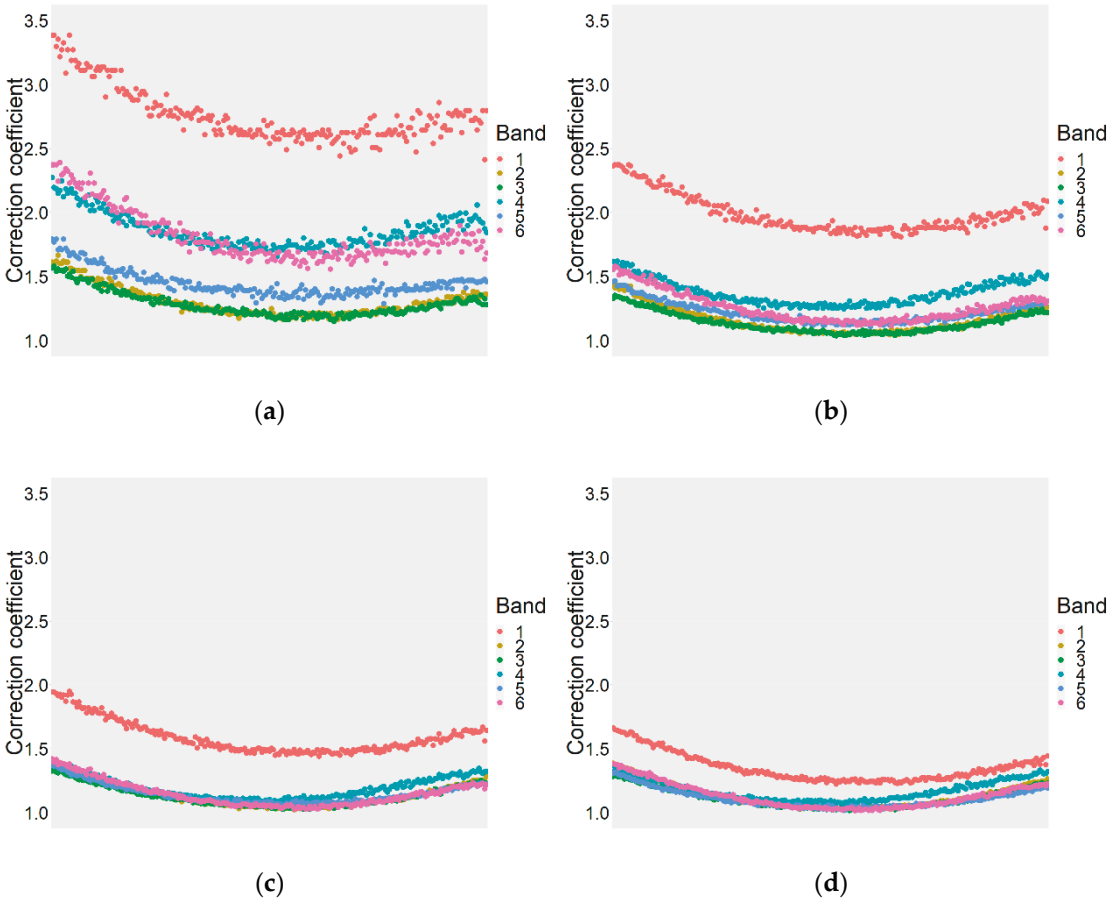

Figure 15. The vignetting radial falloff of each band at the 40% of the integrating sphere source maximum intensity: (**a**) Exposure time 50 µS; (**b**) Exposure time 250 µS; (**c**) Exposure time 500 µS; (**d**) Exposure time 1000 µS.

The dynamic range is dependent on both the exposure time and the illumination intensity (Figure 16). The interaction plot shows the effects of the exposure time and illumination intensity on the mean correction coefficient. It is clearly visible that the mean correction coefficient decreases as the exposure time increases and the illumination is stronger since both factors influence the dynamic range that is stored in the flat field. A short exposure time combined with the low light intensity limit the dynamic range, resulting in a higher mean value of the correction coefficient.

The results of the laboratory experiment show that the value of the correction factor is dependent on the selected exposure time and actual light intensity. Therefore, it is necessary to apply a proper vignetting correction coefficient array to the real-world image, which was calculated from the flat field images that were taken in the same conditions.

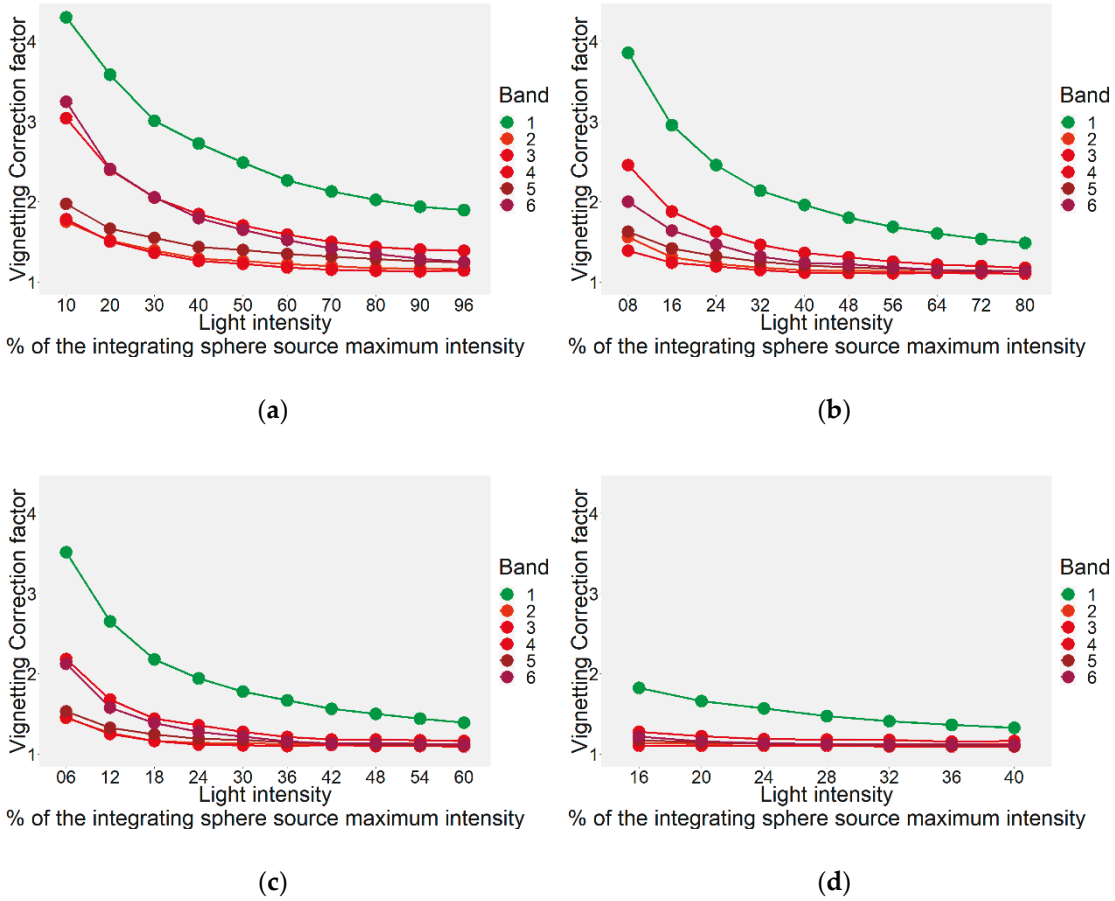

Figure 16. The interaction plot of the effect of exposure time and illumination intensity on mean correction coefficient: (**a**) Exposure time 50 µS; (**b**) Exposure time 250 µS; (**c**) Exposure time 500 µS; (**d**) Exposure time 1000 µS.

3.4. Results of Field Experiment

The effect of the proposed correction workflow was first investigated using a randomly selected profile (red line in Figure 5) to compare the normalized DNs of the raw and corrected images of the profile (Figure 17) and the distribution of the values (Figure 18). The original profile reveals a strong decrease of the DNs that is caused by the vignette effect. Conversely, the normalized DNs show no decrease or only a slight decrease. If we compare the Coefficients of Variation of the profiles, we can see that there is a significant reduction in the variation from 50% to 70% after correction occurs. To prove this hypothesis, we performed the Fligner-Killeen scale test with the null hypothesis that the variation ratio of the original and corrected DNs is less or equal than 1. I.e., the numerator (variation of the original DNs) would have to be bigger than the denominator (the variation of the normalized DNs) (Table 5). The result showed that the variation of the DNs that are extracted from the corrected image is significantly smaller than that from the original image. In addition, there is also a visible reduction in DNs errors that is caused by random nonuniform quantum efficiency (Figure 17).

Table 5. The results of Fligner-Killeen scale test. V means variation of samples extracted from original raw image and fully corrected image.

Band	Null Hypotheses	Z-Statistics	p-Value
1	$\frac{V_{(raw)}}{V_{corrected}} \leq 1$	14.347	<0.001
2	$\frac{V_{(raw)}}{V_{corrected}} \leq 1$	18.179	<0.001
3	$\frac{V_{(raw)}}{V_{corrected}} \leq 1$	13.656	<0.001
4	$\frac{V_{(raw)}}{V_{corrected}} \leq 1$	12.889	<0.001
5	$\frac{V_{(raw)}}{V_{corrected}} \leq 1$	14.641	<0.001
6	$\frac{V_{(raw)}}{V_{corrected}} \leq 1$	15.601	<0.001

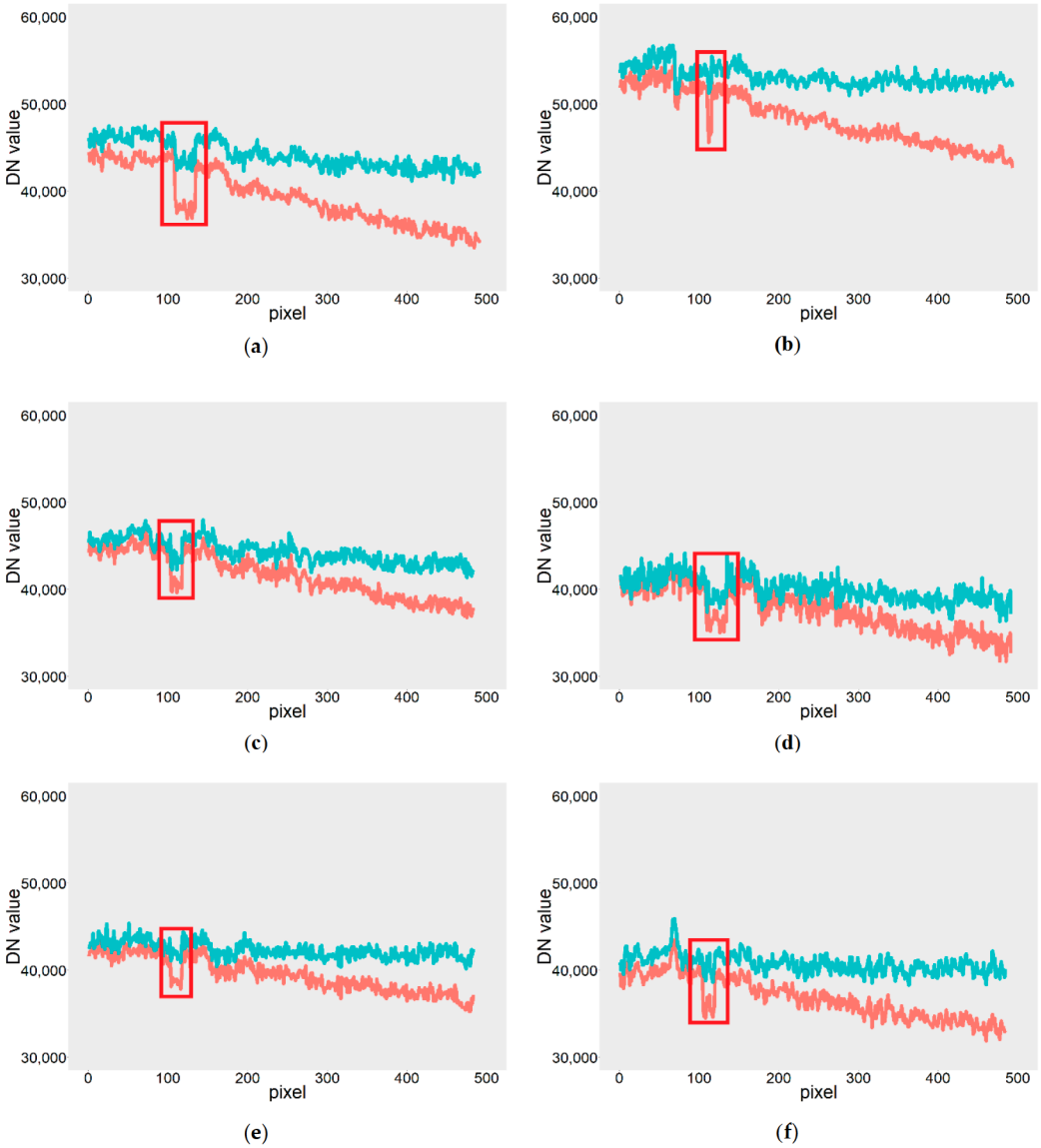

Figure 17. Digital numberss (DNs) extracted along profile from raw image (red lines) and corrected image (blue lines): (**a**) Band 1; (**b**) Band 2; (**c**) Band 3; (**d**) Band 4; (**e**) Band 5; (**f**) Band 6. The coefficient of variation was reduced from 8.14% to 3.55% in Band 1 (**a**); from 6.25% to 2.08% in Band 2 (**b**); from 6.05% to 3.09% in Band 3 (**c**); from 6.78% to 3.63% in Band 4 (**d**); from 5.04% to 2.16% in Band 5 (**e**); from 6.45% to 2.68% in Band 6 (**f**). There is also visible reduction effect of DNs errors caused by random non-uniform quantum efficiency (red boxes).

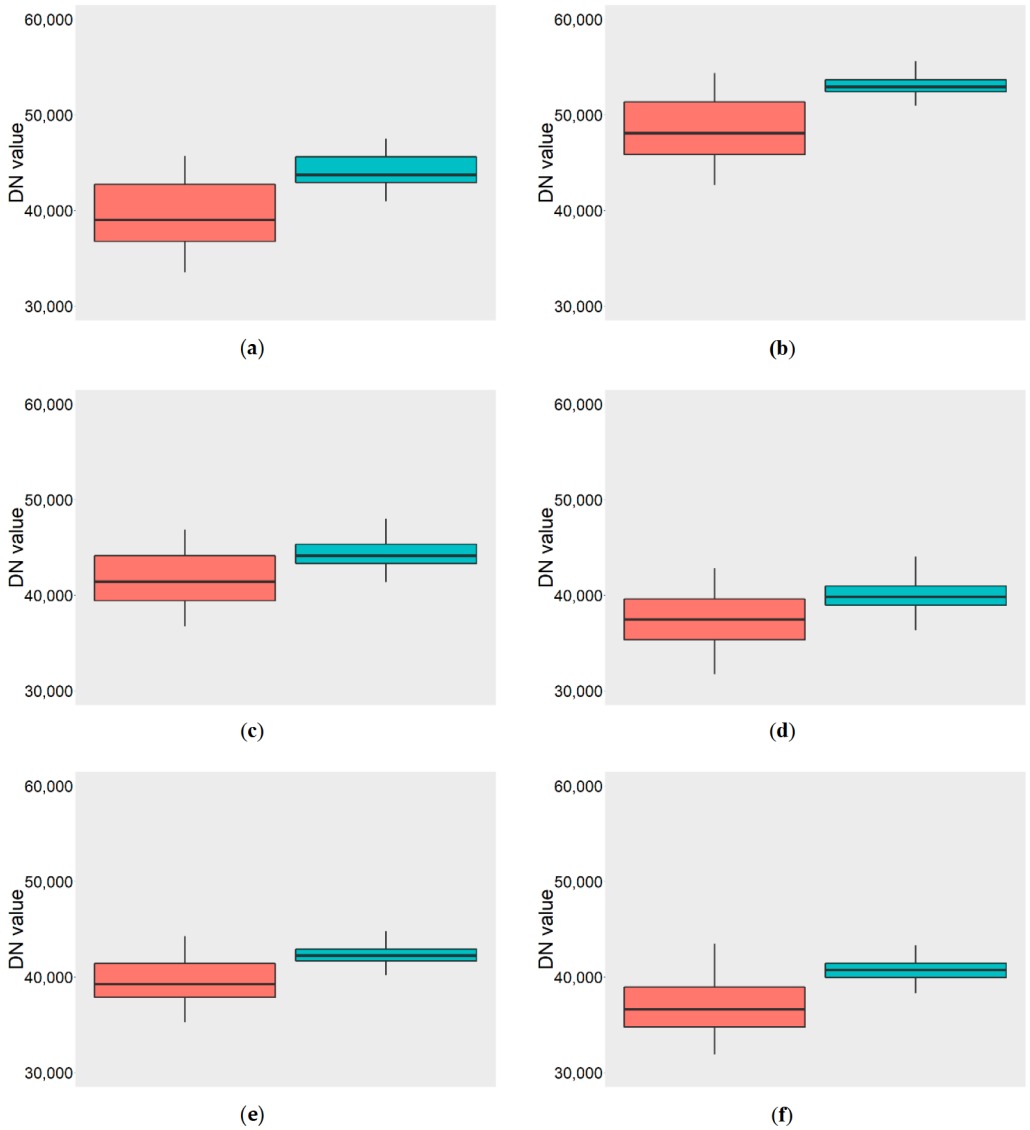

Figure 18. Variability of samples from raw image (red boxes) and corrected image (blue boxes): (**a**) Band 1; (**b**) Band 2; (**c**) Band 3; (**d**) Band 4; (**e**) Band 5; (**f**) Band 6.

The main practical result of this study is the confirmation that the proposed calibration workflow significantly restored the surface reflectance compared to a field measurement, as shown in Figure 19. Figure 19 compares the three validation target reflectance curves that are derived from the spectrometer measurement using the median reflectance values of the same targets that are extracted from the raw (red dots) and corrected (green dots) images.

The greatest improvement occurs, as expected at Target 4, due to the strongest vignette effect resulting from its location in the selected field image (see Figure 5). While the raw image reflectance values are below 0.35, the corrected reflectance values strongly respond with reflectance curve values of approximately 0.40. A similar improvement in the reflectance values after applying all corrections occurs also in the case of Target 7 with the exception that there is not such a strong vignette effect at the target as in Target 4; therefore, the reflectance improves from 0.01 to 0.03. Another reason is the dynamic range, which is lower in the case of dark targets than in the case of light ones. In the case of Target 5, the improvement is not as large because the target is closest to the center and the vignetting effect is not as pronounced.

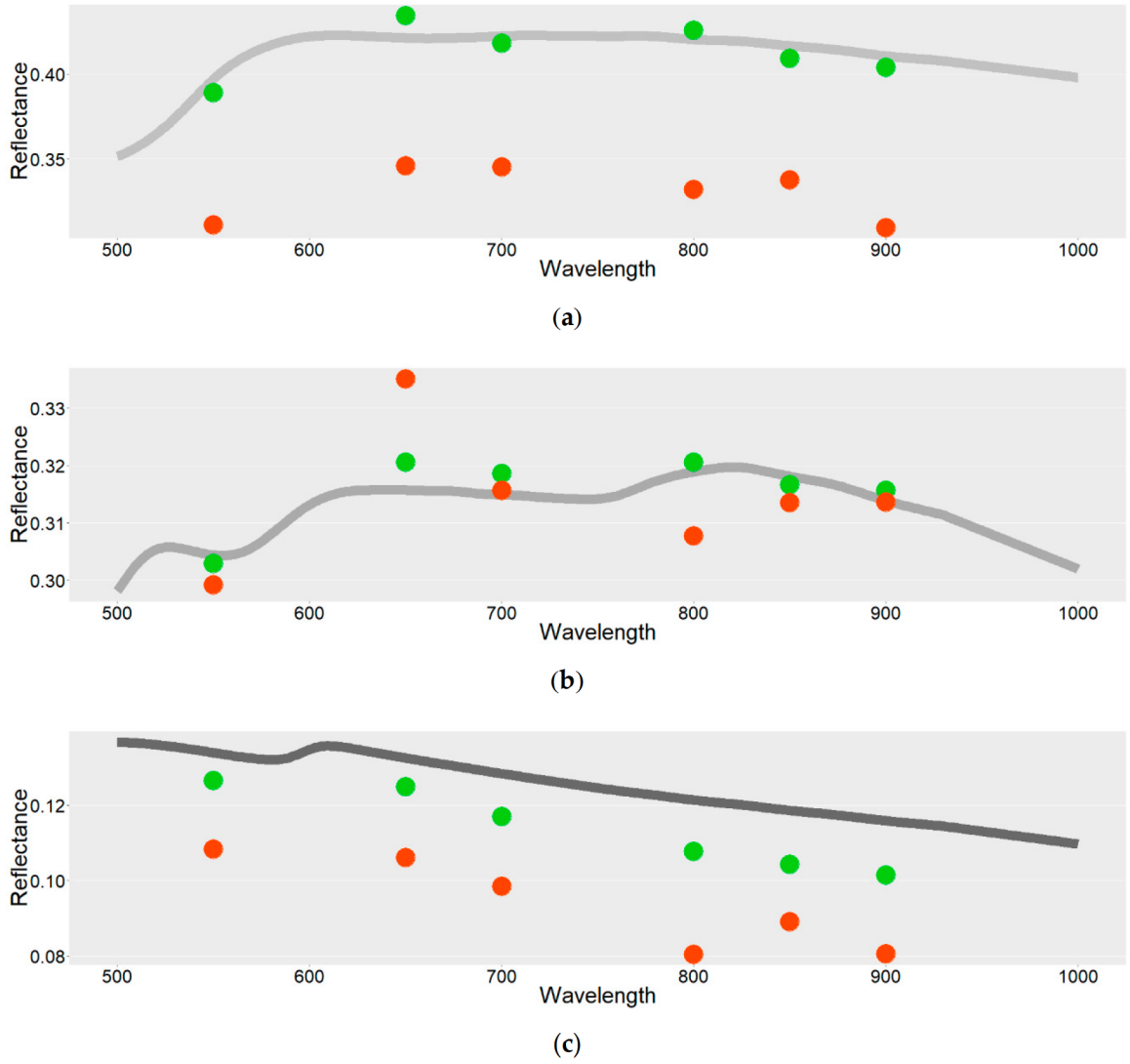

Figure 19. The comparison of thee validation target reflectance curves: (**a**) Pearl 4; (**b**) Light Grey 5; (**c**) Medium Grey 7 (see Figure 5) derived from a spectrometer measurement with median reflectance values of the same targets extracted from raw (red dots) and corrected (green dots) image.

If we compare the NRMSE values between the raw and corrected images, we can see that the values for Target 4 are ten times lower in the corrected image (Table 6). The NRMSE values of Target 7 are 2-10 times lower in the corrected image. The greatest improvement was achieved for more distant targets where the vignetting effect was the strongest. These results confirm the high efficiency of the proposed correction procedure resulting in excellent coherence between the reflectance of the verification targets between the reference field measurement and the fully radiometrically and atmospherically corrected image.

Table 6. The normalized root mean square errors of reflectance values comparing reference spectral curve of verification targets with reflectance values extracted from raw and fully corrected image. The normalization was performed by dividing the RMSE by interquartile range. The values are expressed as percentage.

Wavelength	RAW 4	Calibrated 4	RAW 5	Calibrated 5	RAW 7	Calibrated 7
550	17.60	1.40	0.94	0.69	3.29	1.73
650	13.86	2.10	2.38	0.82	5.65	1.15
700	13.30	0.91	0.87	0.94	7.15	0.24
800	8.56	0.54	1.06	0.72	4.44	0.62
850	9.80	1.07	0.80	0.77	2.52	0.95
900	11.63	0.70	0.91	0.73	3.08	0.53

4. Discussion

To achieve the proper spectral image properties and retain the consistency across multispectral UAV imaging campaigns, the application of the appropriate radiometric and atmospheric corrections is a necessary prerequisite. Due to the limited or lacking calibration protocols and information on the sensor's radiometric properties (linear response, vignetting and the signal-to-noise ratio), the growing variety of UAV sensors and the customization of their spectral bands using interchangeable filters, the development of a reliable radiometric correction method that is applicable in conditions of field imaging campaigns is important both for research and practical applications.

Increasing number of multispectral sensors and growing volumes of imagery, acquired by different sensors underlines the importance of achieving comparability across the sensors and acquisition conditions [20]. For this purpose, an open workflow for transparent calculation of radiometric corrections, enabling comparison and use of the imagery acquired by different sensors, is of growing importance and is applicable also to the sensors, featuring auto-calibration routines such as Parrot Sequoia or MicaSense RedEdge.

In this study, we have proposed and tested a reliable calibration workflow enabling straightforward empirical, image-based radiometric corrections combined with vicarious atmospheric correction using the empirical line approach. The workflow comprises techniques that reduce noise, lens vignetting and nonuniform quantum efficiency of the CMOS array. The sensor corrections (noise and vignetting reduction) should be applied prior any photogrammetric processing. The atmospheric corrections can be performed apriori to processing, or during processing using tools implemented to the photogrammetric software. This approach was tested on the Tetracam uMCA sensor with customizable spectral bands. The achieved results are related to this particular sensor, however the workflow was designed to be reproducible and applicable to the other types of multispectral multiframe systems with CCD/CMOS sensors and global shutters as well, such as Parrot Sequoia and MicaSense RedEdge. Every step of the proposed workflow can be used as it is designed for if another camera has monochrome frame sensors with global shutter and the linear response to incoming light. If the sensors have a rolling shutter, the additional source of noise should be considered [34]. The sensor linearity is also an underlying assumption of using empirical line atmospheric correction with two targets. When the camera does not have a linear response, modified empirical methods using more than two targets have to be applied. This occurs in the study of Wang and Myint [56], which used nine shades of gray to model the exponential relationship of a modified color infrared single-lens reflex camera.

The key reason for selecting Tetracam camera for our research was its relevance to our research aims, namely its ability to provide a set of relatively narrow spectral bands, configured according to the needs of our research tasks. In particular, for our research, there is beneficial ability of the sensor to split the near-infrared light into several narrow spectral bands. To the contrary, the other popular global shutter multispectral cameras, as MicaSense RedEdge or Parrot Sequoia have fixed configuration of spectral bands, not allowing customization according to the research needs.

The linear response of the camera to incoming light was examined first. It was important to carry out a complex experiment assessing various relevant exposure times and sunlight intensities to check the stability of the radiometric response due to the variation of the camera's radiometric properties [53]. In the experiment that was performed in this study, the sensor's linearity was established. This confirmed the appropriate setting of the relative exposure time compensating for the sensors' nonuniform relative sensitivity to the light and the nonuniform filter transmittance of the individual bands, except for Band 1. The reason is the radiance difference in the halogen light of the sphere and sunlight. While sunlight has a maximum radiance of approximately 500 nm, the sphere light has a maximum radiance of 900 nm. That is why exposure time of Band 1 (550 nm) is underestimated.

A visual assessment of the per-pixel noise characteristics of the dark offset samples revealed the checkered pattern on Bands 1–3, which is apparent both in all the averaged datasets and in the single images. Since there was no natural explanation for the phenomenon, we inquired with the camera's manufacturer on the occurrence of the patterns. According to the manufacturer, this moire pattern is a product of the rotation and scaling of slave images relative to master images (Band 4) and each other. The moire pattern occurred when converting images from the RAW format to TIFF in PixelWrench 2, which is the system software that was provided by the sensor manufacturer. Therefore, the moire pattern is present in each frame, as a constant noise pattern in addition to random thermal noise. The testing of the correction workflow thus disclosed the undesired and undocumented effects of the sensor array. Although Kelcey and Lucieer [34] state that dark offset subtraction is limited when reducing this effect, the camera manufacturer nevertheless considers it as an appropriate method for reducing the moire pattern.

The vignette effect analysis showed that the vignetting structure acts differently in the sensor array. The central point of the falloff circle is shifted for every band. The central point is shifted the most in Band 1, which also explains the significantly higher vignetting corrections on the selected transverse profile. In addition, it was discovered that the maximum values of the correcting factors for Bands 2, 3, and 6 were over 100. We have revealed that these values are present only on the last edge line of the pixels of each picture and are a product of the defective cells of the CMOS chip. The black stigma in master channel Band 4 (Figure 7) is the dust on sensor that could not be removed by user, but it could be corrected using LUT correction method. The filter that produces the greatest numbers of electrons in response to the radiation is then by the manufacturer selected as master filter/channel [15]. The similar spot artifacts on the imagery were, indeed, reported as dust particles on chip by Kelcey and Lucieer [34]. The potential impact of removable dust was eliminated by cleaning lenses before each use and by keeping the integration sphere tidy.

In addition to previous studies, the radiometric corrections were performed in varying controlled laboratory conditions to simulate the most typical natural conditions during imaging, and the variation of the camera's radiometric properties was assumed to be due to inexpensive sensors. The results of the laboratory experiment revealed that the noise distribution significantly varied depending on the exposure time and the ambient temperature. The exposure time should be considered to be the main interior user-controllable source of thermal noise because the aperture value is fixed (f/3.2). The ambient temperature could be considered as the main external independent source of thermal noise, which is consistent with the experiments using hyperspectral sensors in [16,43,44]. Moreover, the noise distribution's characteristics were significantly different in each band due to the relative exposure settings of the camera. If we compare the SDs, which represented approximations of the remaining noise following dark offset subtraction, we can conclude that the best results are achieved in the bands with relatively shorter exposure times resulting in less random noise.

The vignetting correction coefficient values have been shown to vary depending on the exposure time and the intensity of the incident radiation. A short exposure time and/or low light intensity reduce the dynamic range, resulting in the presence of extremely low values and their increased frequency in proportion to the maximum value. This results in an increase in both the maximum and mean values of the calculated vignetting correction coefficient (see Figure 15; Figure 16). This finding makes

the noise reduction methods for dark offset images and the vignetting correction methods for LUT tables less applicable, although the methods themselves may be suitable for reducing these undesirable effects [44,53]. The main principles of both methods are calculating a database of correction images in the laboratory and then applying the correction images that were taken in the same conditions as during flight. For this solution, however, it is necessary to build a large database of correction pictures for all combinations of relevant exposures, ambient temperatures and light intensities, resulting in hundreds of correction images and thousands of input images for calculating the corrections, which is truly time and storage consuming.

Simultaneously, it is still necessary to measure the ambient temperature using an on-board thermologger and the irradiance using an on-board or field sensor to determine the correct intensity of the calibration sphere [57,58], which requires further equipment investments. An alternative to this approach would be to acquire a set of correction pictures in the field. Dark images could be taken in a black box and vignetting correction images could be generated by capturing photos of spectrally homogeneous panels under the same illumination. However, only a few authors have addressed this. Aasen et al. [16] and Yang et al. [53] included in situ flat field vignetting calibration into the processing chain because the results were comparable with laboratory calibrations. Crusiol et al. [17] compare the laboratory and field calibrations of a modified color infrared single-lens reflex camera, but without noise removal. The results look promising with a correlation coefficient of $R^2 > 0.9$ that was found for the cross calibration (laboratory vs field).

Calibration images for the vicarious calibration can be collected before and after flight from ground, or during the flight [20]. The common practice is to take one calibration image before and after the flight from drone and sensor held manually above the target with MicaSense RedEdge or Parrot Sequoia [18,19]. However, such approaches are usually simplified, and atmospheric effects are not reduced [10]. On the other side, the in-flight calibration, where calibration targets are taken from the flight altitude, reduce the atmospheric effects

In this field experiment, the flight altitude was set to fit the size of the court that defined the distribution of the targets. The experiment was designed to demonstrate the main radiometric issues (noise and vignetting) of frame multispectral cameras, which alter the DN numbers and derived reflectance values in every single image. If these effects are not reduced in every image, the resulting reflectance mosaic used for analysis is biased. To demonstrate these effects, we used the single image, but with raw and corrected DN values to avoid additional effects of mosaicking (blending the DN values around seamlines) and to preserve the pure effect of vignetting. The similar approach was used in previous works [17,35,36].We performed the field experiment comparing the reflectance values of three validation targets distributed in the corners, where the vignette effect is the strongest.

The results of the field experiment confirmed the general assumption that the greatest impact on overall accuracy is the removal of vignetting, which is consistent with the statement of Lebourgeois et al. [59]. The vignetting correction using the LUT method, which is the most for precise application compared to the optical modeling method [51], significantly reduced the diagonal profile variance. The Coefficient of variation decreased by half in all bands and the DNs were equalized. A similar decrease of the CV was achieved by calibrating a spaceborne linear scanner using a CCD chip [28]. The application of atmospheric calibration to normalized DNs resulted in a significantly more accurate determination of the reflectance of the three validation targets compared to the raw data, thus improving the NRMSE. The NRMSEs after processing all corrections ranged from 0.24 to 2.10%, which are comparable with the results of Del Pozo et al. [36] (2%), Aasen et al. [16] (1%), and Yang et al. [53] (5%). The results, which were verified using a field experiment, demonstrated that the proposed correction workflow significantly improves the quality of multispectral imagery.

In the main field experiment, the calibration targets were placed in the field center in order to minimize the influence of vignetting in the raw and calibrated images. However, the calibration targets are not always located in the center of the calibration image during a field campaign but can be shifted to the edges. Hence, an additional experiment was conducted for this reason when

the location effect of the calibration targets on radiometric corrections was considered. We used the Pearl 4 and Medium Gray 7 targets that were located close to the outer edge as the calibration targets and the remaining Cream 1, Light Gray 5 and Anthracite 9 targets were used as validation targets. The separate linear relationship between the DN and reflectance was computed for every channel of the raw and radiometrically corrected images. The results of this experiment are shown in Figure 20. In this case, the vignetting corrections have an even greater effect on the accuracy of the radiometric calibration comparing raw and corrected images. If the calibration targets are placed on the edges without vignetting corrections, their DNs are strongly underestimated. Calculating an empirical line using these underestimated values then leads to a strong overestimation of the reflectance values for the validation targets (dark red dots in Figure 20). The more biased values are obtained from the center targets of Cream 1 (b) and Anthracite 9 (c) where the vignetting effect is low. In the case of the Light Gray 5 target (a), a comparison of the location effect can be made. Slightly more accurate results are obtained when calibration targets are placed in the center. In addition, the bias of the raw reflectance values completely degrades the data quality when the calibration targets are placed close to an edge.

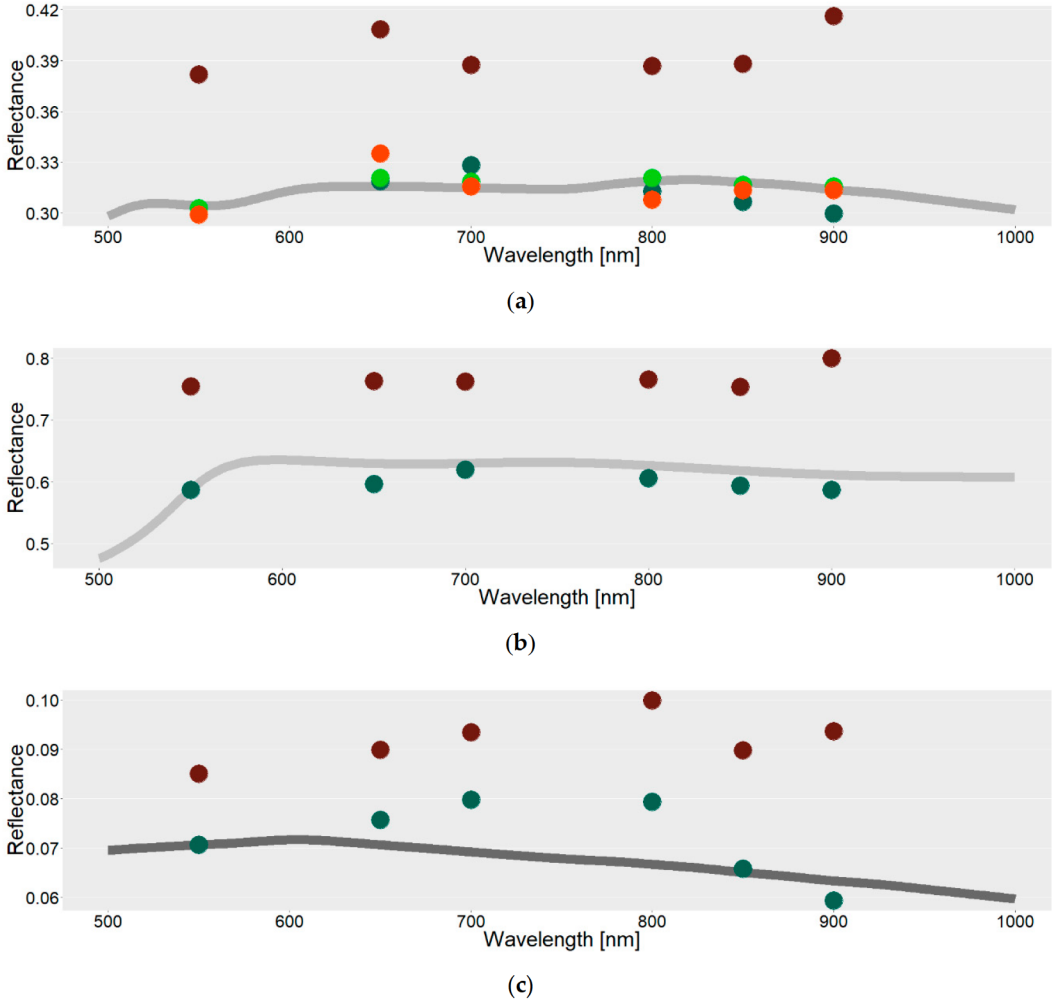

Figure 20. The location effect of calibration targets on radiometric corrections at validation target Light Grey 5 (**a**): The reflectance values are extracted from raw (red dots) and corrected (green dots) image using calibration targets 1 and 9, placed in the center. The reflectance values are extracted from raw (dark red dots) and corrected (dark green dots) image using calibration targets 4 and 7, placed near the outer edge of calibration images; The comparison of validation targets reflectance curves: (**b**) Cream 1; (**c**) Anthracite 9 (see Figure 5) derived from a spectrometer measurement with the median reflectance values of the same targets extracted from raw (dark red dots) and corrected (dark green dots) image.

5. Conclusions

This study proposed and tested a complex empirical image-based radiometric calibration and atmospheric correction method for a Tetracam μMCA multispectral frame camera with a global shutter. Our proposed correction workflow comprises techniques for reducing noise, lens vignetting, and nonuniform quantum efficiency of the CMOS array, which extends the previous works on the calibration of older camera models with rolling shutters by adopting the calibration experiments to hyperspectral sensors. The workflow is based on a laboratory investigation of the camera's radiometric properties combined with vicarious atmospheric correction using an empirical line. The effect of the corrections, which were demonstrated using out-of-laboratory field data, proved the substantial effect of the corrections.

Sensor linearity was confirmed for each channel with coefficients of correlated greater than 0.999, regardless of the irradiance and exposure time. The dark signal noise behaviour was investigated based on the exposure time and ambient temperature and the vignette effect coupled with nonuniform quantum efficiency was studied for changing exposure times and illumination to simulate real-world conditions. In both cases, there was a strong dependence on the exposure time, ambient temperature and illumination.

The results of the field experiment confirmed the general assumption that the greatest impact on the overall accuracy is the reduction of vignetting. The vignetting correction using the LUT method resulted in a significant reduction of the diagonal profile variance, thereby decreasing the Coefficient of variation by half in all bands and overall equalizing the DNs. The application of atmospheric calibration to normalized DNs led to a significantly more accurate determination of the reflectance of the three validation targets compared to the raw data and resulted in the improvement of the NRMSE by an order of magnitude. The NRMSEs after processing all corrections ranged from 0.24 to 2.10%, which demonstrates that the correction procedure is well designed to calibrate multispectral frame cameras.

The presented workflow showed the efficiency of the method by increasing the accuracy of the determination of the reflectance from UAV multispectral imagery, which is a key for the reliability and reproducibility of imaging results. Meanwhile, it demonstrated its practical applicability in conditions of field campaigns and the approach is applicable to other multiarray imaging systems that equipped with CCD/CMOS sensors and global shutters.

Author Contributions: R.M. designed the research, conducted laboratory and field experiments, collected data, analysed data and prepared the manuscript. J.L. supervised the study, contributed in field experiment, reviewed and edited the manuscript and J.H. contributed in laboratory experiment and data processing.

Funding: The study was supported by the Charles University, project GA UK No. 824217 "Analysis of disturbance and regeneration of forest vegetation using UAV multispectral photogrammetry" and COST Action CA16219—Harmonization of UAS techniques for agricultural and natural ecosystems monitoring.

Acknowledgments: The authors would like to thank Daniel Žížala for his statistical computation support and Theodora Lendzioch for her help in the field.

Conflicts of Interest: The authors declare no conflict of interest.

References

1. Salamí, E.; Barrado, C.; Pastor, E. UAV flight experiments applied to the remote sensing of vegetated areas. *Remote Sens.* **2014**, *6*, 11051–11081. [CrossRef]
2. Candiago, S.; Remondino, F.; De Giglio, M.; Dubbini, M.; Gattelli, M. Evaluating Multispectral Images and Vegetation Indices for Precision Farming Applications from UAV Images. *Remote Sens.* **2015**, *7*, 4026–4047. [CrossRef]
3. Torresan, C.; Berton, A.; Carotenuto, F.; Di Gennaro, S.F.; Gioli, B.; Matese, A.; Miglietta, F.; Vagnoli, C.; Zaldei, A.; Wallace, L. Forestry applications of UAVs in Europe: A review. *Int. J. Remote Sens.* **2017**, *38*, 2427–2447. [CrossRef]

4. Adão, T.; Hruška, J.; Pádua, L.; Bessa, J.; Peres, E.; Morais, R.; Sousa, J. Hyperspectral Imaging: A Review on UAV-Based Sensors, Data Processing and Applications for Agriculture and Forestry. *Remote Sens.* **2017**, *9*, 1110. [CrossRef]
5. Pádua, L.; Vanko, J.; Hruška, J.; Adão, T.; Sousa, J.J.; Peres, E.; Morais, R. UAS, sensors, and data processing in agroforestry: A review towards practical applications. *Int. J. Remote Sens.* **2017**, *38*, 2349–2391. [CrossRef]
6. Zhang, C.; Kovacs, J.M. The application of small unmanned aerial systems for precision agriculture: A review. *Precis. Agric.* **2012**, *13*, 693–712. [CrossRef]
7. Näsi, R.; Honkavaara, E.; Lyytikäinen-Saarenmaa, P.; Blomqvist, M.; Litkey, P.; Hakala, T.; Viljanen, N.; Kantola, T.; Tanhuanpää, T.; Holopainen, M. Using UAV-based photogrammetry and hyperspectral imaging for mapping bark beetle damage at Tree-Level. *Remote Sens.* **2015**, *7*, 15467–15493. [CrossRef]
8. Aasen, H.; Honkavaara, E.; Lucieer, A.; Zarco-Tejada, P.J. Quantitative remote sensing at Ultra-High resolution with UAV spectroscopy: A review of sensor technology, measurement procedures, and data correctionworkflows. *Remote Sens.* **2018**, *10*, 1091. [CrossRef]
9. Smith, G.M.; Milton, E.J. The use of the empirical line method to calibrate remotely sensed data to reflectance. *Int. J. Remote Sens.* **1999**, *20*, 2653–2662. [CrossRef]
10. Aspinall, R.J.; Marcus, W.A.; Boardman, J.W. Considerations in collecting, processing, and analysing high spatial resolution hyperspectral data for environmental investigations. *J. Geogr. Syst.* **2002**, *4*, 15–29. [CrossRef]
11. Sandau, R.; Beisl, U.; Braunecker, B.; Cramer, M.; Driescher, H.; Eckardt, A.; Fricker, P.; Gruber, M.; Hilbert, S.; Jacobsen, K.; et al. *Digital Airborne Camera: Introduction and Technology*; Sandau, R., Ed.; Springer: Dordrecht, The Netherlands, 2010; ISBN 9781402088773.
12. Ryan, R.E.; Pagnutti, M. Enhanced absolute and relative radiometric calibration for digital aerial cameras. In *Proceedings of the Photogrammetric Week'09*; Fritch, D., Ed.; Wichtmann Verlag: Heidelberg, Germany, 2009; pp. 81–90.
13. Gao, B.C.; Montes, M.J.; Davis, C.O.; Goetz, A.F.H. Atmospheric correction algorithms for hyperspectral remote sensing data of land and ocean. *Remote Sens. Environ.* **2009**, *113*, 16–24. [CrossRef]
14. Dinguirard, M.; Slater, P.N. Calibration of Space-Multispectral imaging sensors: A review. *Remote Sens. Environ.* **1999**, *68*, 194–205. [CrossRef]
15. Tetracam Inc. Tetracam µMCA User's Guide. Available online: http://www.tetracam.com/PDFs/u%20MCA%20Users%20Guide%20V1.1.pdf (accessed on 17 August 2019).
16. Aasen, H.; Burkart, A.; Bolten, A.; Bareth, G. Generating 3D hyperspectral information with lightweight UAV snapshot cameras for vegetation monitoring: From camera calibration to quality assurance. *ISPRS J. Photogramm. Remote Sens.* **2015**, *108*, 245–259. [CrossRef]
17. Crusiol, L.G.T.; Nanni, M.R.; Silva, G.F.C.; Furlanetto, R.H.; da Silva Gualberto, A.A.; de Carvalho Gasparotto, A.; De Paula, M.N. Semi professional digital camera calibration techniques for Vis/NIR spectral data acquisition from an unmanned aerial vehicle. *Int. J. Remote Sens.* **2017**, *38*, 2717–2736. [CrossRef]
18. Parrot. *Parrot Announcement-Release of Application Notes*. Available online: https://forum.developer.parrot.com/t/parrot-announcement-release-of-application-notes/5455 (accessed on 27 September 2019).
19. MicaSense. *Best Practices: Collecting Data with MicaSense Sensors*. Available online: http://support.micasense.com/hc/en-us/articles/224893167-Best-practices-Collecting-Data-with-MicaSense-RedEdge-and-Parrot-Sequoia (accessed on 27 September 2019).
20. Assmann, J.J.; Kerby, J.T.; Cunliffe, A.M.; Myers-Smith, I.H. Vegetation monitoring using multispectral sensors—Best practices and lessons learned from high latitudes. *J. Unmanned Veh. Syst.* **2018**, *7*, 54–75. [CrossRef]
21. Withagen, P.J.; Groen, F.C.A.; Schutte, K. CCD color camera characterization for image measurements. *IEEE Trans. Instrum. Meas.* **2007**, *56*, 199–203. [CrossRef]
22. Healey, G.E.; Kondepudy, R. Radiometric CCD camera calibration and noise estimation. *IEEE Trans. Pattern Anal. Mach. Intell.* **1994**, *16*, 267–276. [CrossRef]
23. Mullikin, J.C.; van Vliet, L.J.; Netten, H.; Boddeke, F.R.; van der Feltz, G.; Young, I.T. Methods for CCD Camera Characterization. In *Proceedings of the Image Acquisition and Scientific Imaging Systems*; Titus, H.C., Waks, A., Eds.; International Society for Optics and Photonics: San Jose, CA, USA, 1994; Volume 2173, pp. 73–84.
24. Fraser, C.S. Digital camera Self-Calibration. *ISPRS J. Photogramm. Remote Sens.* **1997**, *52*, 149–159. [CrossRef]

25. Hytti, H.T. Characterization of digital image noise properties based on RAW data. *Electron. Imaging* **2006**, *6059*, 60590A.
26. Neale, C.M.U.; Crowther, B.G. An airborne multispectral video/radiometer remote sensing system: Development and calibration. *Remote Sens. Environ.* **1994**, *49*, 187–194. [CrossRef]
27. Mansouri, A.; Marzani, F.S.; Gouton, P. Development of a Protocol for CCD Calibration: Application to a Multispectral Imaging System. *Int. J. Robot. Autom.* **2005**, *20*. [CrossRef]
28. Olsen, D.; Dou, C.; Zhang, X.; Hu, L.; Kim, H.; Hildum, E. Radiometric calibration for AgCam. *Remote Sens.* **2010**, *2*, 464–477. [CrossRef]
29. Hunt, E.R.; Dean Hively, W.; Fujikawa, S.J.; Linden, D.S.; Daughtry, C.S.T.; McCarty, G.W. Acquisition of NIR-Green-Blue digital photographs from unmanned aircraft for crop monitoring. *Remote Sens.* **2010**, *2*, 290–305. [CrossRef]
30. Lehmann, J.; Nieberding, F.; Prinz, T.; Knoth, C. Analysis of Unmanned Aerial System-Based CIR Images in Forestry—A New Perspective to Monitor Pest Infestation Levels. *Forests* **2015**, *6*, 594–612. [CrossRef]
31. Minařík, R.; Langhammer, J. Use of a multispectral UAV photogrammetry for detection and tracking of forest disturbance dynamics. In *Proceedings of the International Archives of the Photogrammetry, Remote Sensing and Spatial Information Sciences*; Halounova, L., Ed.; Copernicus GmbH: Göttingen, Gemany, 2016; Volume XLI-B8, pp. 711–718.
32. Lelong, C.C.D.; Burger, P.; Jubelin, G.; Roux, B.; Labbé, S.; Baret, F. Assessment of unmanned aerial vehicles imagery for quantitative monitoring of wheat crop in small plots. *Sensors* **2008**, *8*, 3557–3585. [CrossRef]
33. Berni, J.A.J.; Zarco-tejada, P.P.J.; Suarez, L.; Fereres, E.; Member, S.; Suárez, L. Thermal and Narrowband Multispectral Remote Sensing for Vegetation Monitoring From an Unmanned Aerial Vehicle. *IEEE Trans. Geosci. Remote Sens.* **2009**, *47*, 722–738. [CrossRef]
34. Kelcey, J.; Lucieer, A. Sensor correction of a 6-Band multispectral imaging sensor for UAV remote sensing. *Remote Sens.* **2012**, *4*, 1462–1493. [CrossRef]
35. Kelcey, J.; Lucieer, A. Sensor Correction and Radiometric Calibration of a 6-Band Multispectral Imaging Sensor for Uav Remote Sensing. *ISPRS-Int. Arch. Photogramm. Remote Sens. Spat. Inf. Sci.* **2012**, *XXXIX-B1*, 393–398. [CrossRef]
36. Del Pozo, S.; Rodríguez-Gonzálvez, P.; Hernández-López, D.; Felipe-García, B. Vicarious radiometric calibration of a multispectral camera on board an unmanned aerial system. *Remote Sens.* **2014**, *6*, 1918–1937. [CrossRef]
37. Nocerino, E.; Dubbini, M.; Menna, F.; Remondino, F.; Gattelli, M.; Covi, D. Geometric calibration and radiometric correction of the maia multispectral camera. In *Proceedings of the International Archives of the Photogrammetry, Remote Sensing and Spatial Information Sciences*; Honkavaara, E., Ed.; Copernicus GmbH: Göttingen, Germany, 2017; Volume XLII-3/W3, pp. 149–156.
38. Padró, J.-C.; Muñoz, F.-J.; Ávila, L.; Pesquer, L.; Pons, X. Radiometric Correction of Landsat-8 and Sentinel-2A Scenes Using Drone Imagery in Synergy with Field Spectroradiometry. *Remote Sens.* **2018**, *10*, 1687. [CrossRef]
39. Padró, J.-C.; Carabassa, V.; Balagué, J.; Brotons, L.; Alcañiz, J.M.; Pons, X. Monitoring opencast mine restorations using Unmanned Aerial System (UAS) imagery. *Sci. Total Environ.* **2019**, *657*, 1602–1614. [CrossRef] [PubMed]
40. Honkavaara, E.; Saari, H.; Kaivosoja, J.; Pölönen, I.; Hakala, T.; Litkey, P.; Mäkynen, J.; Pesonen, L. Processing and Assessment of Spectrometric, Stereoscopic Imagery Collected Using a Lightweight UAV Spectral Camera for Precision Agriculture. *Remote Sens.* **2013**, *5*, 5006–5039. [CrossRef]
41. Hakala, T.; Honkavaara, E.; Saari, H.; Mäkynen, J.; Kaivosoja, J.; Pesonen, L.; Pölönen, I. Spectral imaging from UAVs under varying illumination conditions. In *Proceedings of the International Archives of the Photogrammetry, Remote Sensing and Spatial Information Sciences*; Grenzdörffer, G., Bill, R., Eds.; Copernicus GmbH: Göttingen, Germany, 2013; Volume XL-1/W2, pp. 189–194.
42. Hruska, R.; Mitchell, J.; Anderson, M.; Glenn, N.F. Radiometric and geometric analysis of hyperspectral imagery acquired from an unmanned aerial vehicle. *Remote Sens.* **2012**, *4*, 2736–2752. [CrossRef]
43. Aasen, H.; Bendig, J.; Bolten, A.; Bennertz, S.; Willkomm, M.; Bareth, G. Introduction and preliminary results of a calibration for full-frame hyperspectral cameras to monitor agricultural crops with UAVs. In *Proceedings of the International Archives of the Photogrammetry, Remote Sensing and Spatial Information Sciences*; Sunar, F., Altan, O., Taberner, M., Eds.; Copernicus GmbH: Göttingen, Gemany, 2014; Volume XL–7, pp. 1–8.

44. Buettner, A.; Roeser, H.P. Hyperspectral remote sensing with the UAS "Stuttgarter adler"—Challenges, experiences and first results. In *Proceedings of the International Archives of the Photogrammetry, Remote Sensing and Spatial Information Sciences*; Grenzdörffer, G., Bill, R., Eds.; Copernicus GmbH: Göttingen, Germany, 2013; Volume XL-1/W2, pp. 61–65.
45. Suomalainen, J.; Anders, N.; Iqbal, S.; Roerink, G.; Franke, J.; Wenting, P.; Hünniger, D.; Bartholomeus, H.; Becker, R.; Kooistra, L. A lightweight hyperspectral mapping system and photogrammetric processing chain for unmanned aerial vehicles. *Remote Sens.* **2014**, *6*, 11013–11030. [CrossRef]
46. Baugh, W.M.; Groeneveld, D.P. Empirical proof of the empirical line. *Int. J. Remote Sens.* **2008**, *29*, 665–672. [CrossRef]
47. Al-Amri, S.S.; Kalyankar, N.V.; Santosh, K. A Comparative Study of Removal Noise from Remote Sensing Image. *Int. J. Comput. Sci. Issues* **2010**, *7*, 32–36.
48. Box, G.E.P.; Cox, D.R. An Analysis of Transformations. *J. R. Stat. Soc. Ser. B* **1964**, *26*, 211–252. [CrossRef]
49. Greenhouse, S.W.; Geisser, S. On methods in the analysis of profile data. *Psychometrika* **1959**, *24*, 95–112. [CrossRef]
50. Goldman, D.B. Vignette and Exposure Calibration and Compensation. *IEEE Trans. Pattern Anal. Mach. Intell.* **2010**, *32*, 2276–2288. [CrossRef]
51. Yu, W. Practical Anti-Vignetting methods for digital cameras. *IEEE Trans. Consum. Electron.* **2004**, *50*, 975–983.
52. Teillet, P.M. Image correction for radiometric effects in remote sensing. *Int. J. Remote Sens.* **1986**, *7*, 1637–1651. [CrossRef]
53. Yang, G.; Li, C.; Wang, Y.; Yuan, H.; Feng, H.; Xu, B.; Yang, X. The DOM generation and precise radiometric calibration of a UAV-Mounted miniature snapshot hyperspectral imager. *Remote Sens.* **2017**, *9*, 642. [CrossRef]
54. R Core Team. *R: A Language and Environment for Statistical Computing*; R Foundation for Statistical Computing: Vienna, Austria; Available online: http://www.R-project.org/ (accessed on 21 January 2018).
55. Tetracam Inc. *PixelWrench2 User Guide*. Available online: http://www.tetracam.com/PDFs/Tetracam_PixelWrench2_User_Guide.pdf (accessed on 21 January 2018).
56. Wang, C.; Myint, S.W. A Simplified Empirical Line Method of Radiometric Calibration for Small Unmanned Aircraft Systems-Based Remote Sensing. *IEEE J. Sel. Top. Appl. Earth Obs. Remote Sens.* **2015**, *8*, 1876–1885. [CrossRef]
57. Nevalainen, O.; Honkavaara, E.; Tuominen, S.; Viljanen, N.; Hakala, T.; Yu, X.; Hyyppä, J.; Saari, H.; Pölönen, I.; Imai, N.; et al. Individual Tree Detection and Classification with UAV-Based Photogrammetric Point Clouds and Hyperspectral Imaging. *Remote Sens.* **2017**, *9*, 185. [CrossRef]
58. Tuominen, S.; Balazs, A.; Honkavaara, E.; Pölönen, I.; Saari, H.; Hakala, T.; Viljanen, N. Hyperspectral UAV-Imagery and photogrammetric canopy height model in estimating forest stand variables. *Silva Fenn.* **2017**, *51*, 7721. [CrossRef]
59. Lebourgeois, V.; Bégué, A.; Labbé, S.; Mallavan, B.; Prévot, L.; Roux, B. Can Commercial Digital Cameras Be Used as Multispectral Sensors? A Crop Monitoring Test. *Sensors* **2008**, *8*, 7300–7322. [CrossRef]

© 2019 by the authors. Licensee MDPI, Basel, Switzerland. This article is an open access article distributed under the terms and conditions of the Creative Commons Attribution (CC BY) license (http://creativecommons.org/licenses/by/4.0/).

Článek III

Minařík, R., & Langhammer, J. (2019). Rapid Radiometric calibration of multiple camera array using in-situ data for UAV multispectral photogrammetry. *The International Archives of the Photogrammetry, Remote Sensing and Spatial Information Sciences*, *XLII-2/W17*, 209–215. https://doi.org/10.5194/isprs-archives-XLII-2-W17-209-2019

RAPID RADIOMETRIC CALIBRATION OF MULTIPLE CAMERA ARRAY USING IN-SITU DATA FOR UAV MULTISPECTRAL PHOTOGRAMMETRY

R. Minařík [1], J. Langhammer [1, *]

[1] Charles University, Faculty of Science, Dept. of Physical Geography and Geoecology, Albertov 6, Prague 2, 128 43, Czech Republic - (robert.minarik, jakub.langhammer)@natur.cuni.cz

Commission II

KEY WORDS: Radiometric Calibration, Multispectral Camera, Tetracam μMCA, Vignetting Reduction, Noise Reduction

ABSTRACT:

This study compares two possible radiometric calibration approaches of Tetracam μMCA Snap multispectral camera using the Dark offset subtraction and Look-Up Table (LUT) methods. A laboratory-based calibration using correction images taken under the controlled conditions was compared with a rapid in-situ based calibration featuring correction images taken during the field campaign. The hypothesis was that the accuracy of in-situ calibration could be comparable with the laboratory calibration, and thus could replace it and simplify the radiometric calibration process. The accuracy of calibration approaches was assessed by comparison of three validation targets reflectance values extracted from corrected UAV images based on laboratory and in-situ calibration with a reference spectroscopy measurement. The results of the field experiment showed that both calibration approaches led to significant accuracy improvement compared to raw data. The vignetting correction using resulted in a significant reduction of the Coefficient of variation by half in all bands and overall equalizing the DNs on the selected diagonal profile. The NRMSEs after processing all corrections ranged from 0.24 to 3.40%. Although the statistical testing revealed slightly better agreement of laboratory calibrated reflectance with reference data, the accuracy of in-situ calibration is sufficient, because the accuracy improvement quantified by the NRMSE is 2 – 10 times better using both calibration approaches compared to raw data than the NRMSE differences between them. These findings make the proposed in-situ approach usable for various environmental studies featuring UAV multispectral photogrammetry.

1. INTRODUCTION

Unmanned Aerial Systems (UAS) featuring multispectral sensors are popular remote sensing instruments for rapid mapping and monitoring of dynamic phenomena in geosciences, because they have lower operational costs, higher spatial resolution and flexible temporal resolution compared to conventional remote sensing (Manfreda et al., 2018; Minařík and Langhammer, 2016; Zhang and Kovacs, 2012). Moreover, UAS can be operated on demand in often varying conditions, which increases the importance of radiometric calibration in the image processing (Aasen et al., 2018).

The raw spectral data are altered by a mixture of effects that include the current surface conditions, atmospheric effects, topographic effects, and sensor characteristics (Smith and Milton, 1999). These alterations of the original digital numbers (DN) limit the quality and validity of the raw data for further photogrammetric processing and time-series analysis in environmental studies (Kelcey and Lucieer, 2012a). Some of the UAS multispectral sensors, such as multiple camera arrays form Tetracam MCA family or sensors based on converted cameras are implemented using only basic or no calibration protocol and the sensors' radiometric properties are not known (Aasen et al., 2015; Tetracam Inc., 2015). For newest multiple array systems (MicaSense RedEdge and Parrot Sequoia), the basic radiometric calibration is implemented into photogrammetric software (Parrot., 2017). However, such approaches are usually simplified, and for an accurate data collection, analysis, and comparison of data across different sensors, there is a need to develop user-designed correction methods (Assmann et al., 2018). The results of imaging should be processed quickly. Hence, the used sensor corrections and radiometric calibration of the images should be relatively simple and standardized preferably featuring empirical, image-based calibration methods. The calibration workflow for multiple array multispectral cameras (e. g. Tetracam μMCA, Parrot Sequoia and MicaSense Red-Edge) generally involves: a noise reduction, a vignette effect reduction and an atmospheric correction to surface reflectance using empirical approach (Nocerino et al., 2017; Padró et al., 2019, 2018; Pozo et al., 2014). Assmann et al. (2018) proposed workflow of vegetation monitoring with radiometric calibration using Parrot Sequoia. Iqbal et al. (2018) and Guo et al. (2019) successfully evaluated the suitability of the empirical line method for atmospheric corrections of UAS data.

The common image-based sensor correction methods are a Dark offset subtraction method for noise reduction (Kelcey and Lucieer, 2012b; Mansouri et al., 2005) and Look-Up Table (LUT) method for the vignetting correction (Yu, 2004). The main principles of both methods are calculation of a database of correction images in the laboratory and then applying the correction images that were taken under in the same conditions as during flight (Minařík et al., 2019). The large database of correction pictures for all combinations of relevant exposures, ambient temperatures and light intensities under laboratory conditions should be built, which is time and storage consuming. An alternative to this approach is to acquire a set of correction pictures in the field. Dark images could be taken in a portable black box and vignetting correction images could be generated by capturing photos of spectrally homogeneous panels under the same illumination in the field. However, only a few authors have addressed this for hyperspectral sensors. Aasen et al. (2015) and

* Corresponding author

Yang et al. (2017) included in-situ LUT flat field calibration into their processing workflows.
The aim of this study is to compare two possible radiometric calibration approaches of Tetracam μMCA Snap multispectral camera using the Dark offset subtraction and LUT methods. We compared a laboratory-based calibration using correction images taken in the laboratory under the controlled conditions with a rapid in-situ based calibration featuring correction images taken during the field campaign. The hypothesis was that the accuracy of in-situ calibration could be comparable with the laboratory calibration, and thus could replace it and simplify the radiometric calibration process. This study stems on and extends the previous study (Minařík et al., 2019) which proposes the calibration workflow for multiple array camera arrays based on laboratory experiments.

2. METHODS

2.1 Multispectral camera array

We used a Tetracam μ-MCA Snap 6 (Figure 1) multiple camera array system to capture the images in six independent channels with changeable bandpass filters. The nonuniform global snap sensor's relative sensitivity to light and the nonuniform filter transmittance is compensated using the relative exposure settings to the master channel (Band 4), which are set in the cameras' production and differ for each camera model. The sensor parameters are given in Table 1.

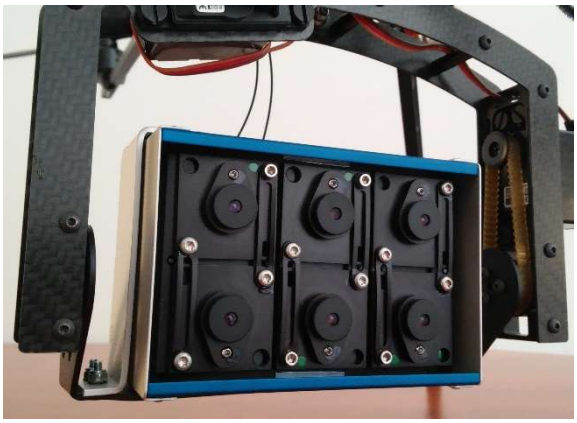

Figure 1. Multiple camera array Tetracam μ-MCA Snap 6.

Specification	Description/Value
Type	μMCA 6 Snap, 6 identical global shutter sensors, changeable bandpass filters
Sensor	1.3 mega-pixel CMOS sensor (1280 x 1024 pixels)
Sensitivity	~450 nm to ~1000 nm
Pixel Size	4.8 microns
Focal length	9.6 mm fixed lens
Aperture	f/3.2
Horizontal Angle of View	38.26°
Vertical Angle of View	30.97°
Default Depth of Field	~2 meters to infinity
Bands	B1: 550 nm (FWHM 20 nm) B2: 650 nm (FWHM 20 nm) B3: 700 nm (FWHM 20 nm) B4: 800 nm (FWHM 20 nm) B5: 900 nm (FWHM 20 nm) B6: 950 nm (FWHM 20 nm)

Table 1. Technical parameters and the band composition of the used camera model.

2.2 Applied correction methods

2.2.1 Noise reduction

We used dark offset subtraction method (Kelcey and Lucieer, 2012b; Mansouri et al., 2005) for noise reduction. This method estimates the noise of sensor from dark images in the absence of light when no signal is generated, and only noise is present. Through averaging, the characteristics of the sensor-specific per-pixel distribution of the noise can be extracted for the same exposure times that are used in the field. The Standard Deviation (SD) is the approximation of the remaining noise following the dark offset subtraction.

2.2.2 Vignetting reduction

We used look-up table (LUT) correction method (Yu, 2004) for the per-pixel vignette effect, nonuniform quantum efficiency effect, and dust defects reduction. The LUT was calculated from a set of flat field noise corrected images under uniform illumination. The LUT correction method is constructed on the assumption that the brightest pixels in the center are not affected by any error and they can serve as reference values for normalization (Minařík et al., 2019). The correction coefficients were computed as the ratio of the central DN to the DN of each pixel using equation 1 (Yu, 2004):

$$I_{LUT}(i, j) = I_{ref,\,max}/I_{ref}(i, j) \quad (1)$$

where $I_{LUT}(i, j)$ is the correction coefficient of the pixel at position (i,j), $I_{ref,\,max}$ is the maximum brightness value of the image and I_{ref} (i, j) is the brightness value of pixel position (i,j).

2.2.3 Atmospheric corrections method

We chose the empirical line method (Teillet, 1986), which is widely used for UAV imaging (Iqbal et al., 2018). The method assigns a reflectance value to each pixel that is based on the computed linear relationship between the known reflectance value of the light and the dark reflectance panels (see Figure 2) and their DN numbers that were extracted from images.

2.3 Laboratory calibration

The laboratory sensor calibration of the camera was conducted in the air-conditioned calibration laboratory of the Global Change Research Institute of the Czech Academy of Sciences featuring a CSTM-LR-20-M optical integrating sphere (Labsphere Inc.).
Firstly, the sensor´s linear response was investigated in the integrating sphere as a presumption of using an empirical line method for different exposure times (50, 250, 500 and 1000 μS) typically used in the field. The linearity was confirmed using a regression coefficient that was higher than 0.99 regardless the exposure time and light intensity.
The dark offset images were taken in a completely dark room using the same exposure times (50, 250, 500 and 1000 μS). Twenty dark offset samples were taken to eliminate a random noise. The average images were calculated. The appropriate dark offset (500 μS) image was subtracted from a field image.
The per-pixel vignette effect was corrected using a set of flat field noise corrected images. In the laboratory, the integrating sphere

served as the flat field surface. The same datasets were used for calculating vignetting correction coefficients as for linearity testing to be consistent. The average image was computed using the set of 20 images with the same exposure time. After subtracting the corresponding dark offset image from the average flat field image, the correction coefficient images were computed. The appropriate correction image (500 µS) was then applied to the test image from a field experiment.
The noise corrected average flat field image with exposure time 500µS was used for Signal-to-Noise Ratio (SNR) estimation. SNR was estimated as the ratio of average DN value extracted from flat field image to the SD of the corresponding dark offset imagery.

2.4 Rapid in-situ calibration and field experiment

The field experiment was conducted in March 2018 at noon from a height of 15 m with a Ground Sampling Distance of 0.75 cm (Figure 2). As a test field, we used a beach volleyball court since the sand represents an almost lambertian surface with stable reflectance (Baugh and Groeneveld, 2008).

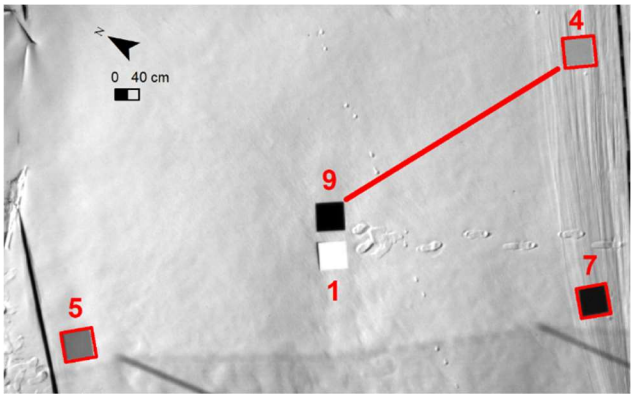

Figure 2. The design of the field experiment. Figure shows the distribution of calibrating (1, 9) and validation (4, 5, 7) targets. Red squares mark the validation targets.

The exposure time was set to 500 µS in coherence with the illumination and a general rule of thumb that the brightest object on the surface (white target) should reach a maximum of 80% of the radiometric resolution.
The rapid in-situ calibration was performed during a field experiment. The portable black box was used for taking the dark images. Twenty dark offset samples were taken to eliminate a random noise. The same exposure time 500 µS was used. The average image was calculated and subtracted from the field image. The calibration target Cream 1 served as the flat field surface for in-situ vignetting corrections. The average image was computed using a set of 20 calibration images from a near-ground level (1 m). After subtracting the corresponding dark offset image from the average flat field image, the correction coefficient image was computed. The field image was multiplied by the correction coefficient image then.
Before the accuracy of in-situ and laboratory calibration comparison using validation targets, the effect of vignetting correction method was investigated at selected profile (see Figure 2), because both the vignette effect reduction and non-uniform quantum efficiency of the chip cells have the most significant impact on sensor calibration overall accuracy (Lebourgeois et al., 2008). We compared Coefficients of Variation (CV) of DN extracted from the raw image and corrected image using two proposed calibrating approaches.

The accuracy of laboratory and in-situ radiometric calibration was assessed by comparison of three validation targets reflectance values extracted from corrected UAV images based on laboratory and in-situ calibration with a reference spectroscopy measurement. The calibration targets were placed in the middle to reduce the vignette effect and aid empirical line construction. Three verification targets were placed on the edges and in the corners of the image where the vignette effect was the strongest.
The targets were made of metal plates (40 × 40 cm) that were professionally painted using NEXTEL colours. We computed the empirical line for every channel of the laboratory and in-situ calibrated images extracting values from 500 pixels. The median value was used to assign the reflectance value. We used 500 reflectance values from each validation target for descriptive statistics, Normalized Root Square Error (NRMSE) calculation and statistical testing.

3. RESULTS AND DISCUSSION

3.1 Signal to noise ratio

The results of signal-to-noise analysis are in Table 2. Band 6 records the worst response to dark offset subtraction resulting in the highest remaining noise (SD) and the lowest SNR. This may be due to fact that band 6 has the longest relative exposure time and the lowest filter transmittance. Both properties increase the image noise (Al-Amri et al., 2010). Band 1 records the lowest remaining noise, but the SNR is relatively low. This is due to relatively low dynamic range of flat field image caused by short relative exposure time of band 1. The relative exposure time of band 1 may seems underestimated, but the reason is the radiance difference in the halogen light of the sphere and sunlight. While sunlight has a maximum radiance of approximately 500 nm, the sphere light has a maximum radiance of 900 nm (Minařík et al., 2019).
On the other side, the band 4 (master channel) and band 2 generate the highest quality data. It confirms the appropriate master channel selection by manufacturer. The manufacturer selects master channel individually according to the featured set of bandpass filters. The filter that produces the greatest numbers of electrons in response to the radiation is then by the manufacturer selected as master channel (Tetracam Inc., 2015). The other bands reveal balanced SNR.

Band	Avg. flat field DN	SD of dark offset image	SNR
B1	18864.84	133.57	141.33
B2	40944.57	174.36	234.81
B3	43762.72	217.46	201.24
B4	37239.93	166.86	223.17
B5	34695.04	162.56	213.41
B6	37215.58	376.30	100.22

Table 2. The results of signal-to-noise analysis.

The resulting SNR are higher to values presented by Kelcey and Lucieer (2012a), but it can be caused by different type of surface (artist´s canvas). Hruska et al. (2012) calculated in-flight SNR values around 120 compared to SNR around 250 reported by the manufacturer for hyperspectral sensor PIKA II. This decrease of SNR can occur, because the true SNR is obtained only when calculating a uniform image, as in an integrating sphere or an otherwise uniformly lit featureless image. When the calculation is applied to an image with significant features and luminance variations it reflects only the variability or complexity of the image (Heinold, 2017).

3.2 Rapid in-situ and laboratory calibration comparison

The effect of vignette effect reduction was first investigated using the randomly selected sand profile to compare the normalized DNs of the raw and corrected images (Figure 3). The original profile (red lines) reveals a substantial decrease of the DNs that is caused by the vignette effect. Conversely, the normalized DNs show no decrease or only a slight decrease. Moreover, the green in-situ line is almost identical to blue laboratory line. It indicates that both averaged flat field images of integrating and target Cream 1 provide relatively equal options for vignetting correction by LUT method. If we compare the CV of the profiles, we can see that there is a significant reduction in the variation from 50% to 70% after correction occurs in both cases (Table 3).

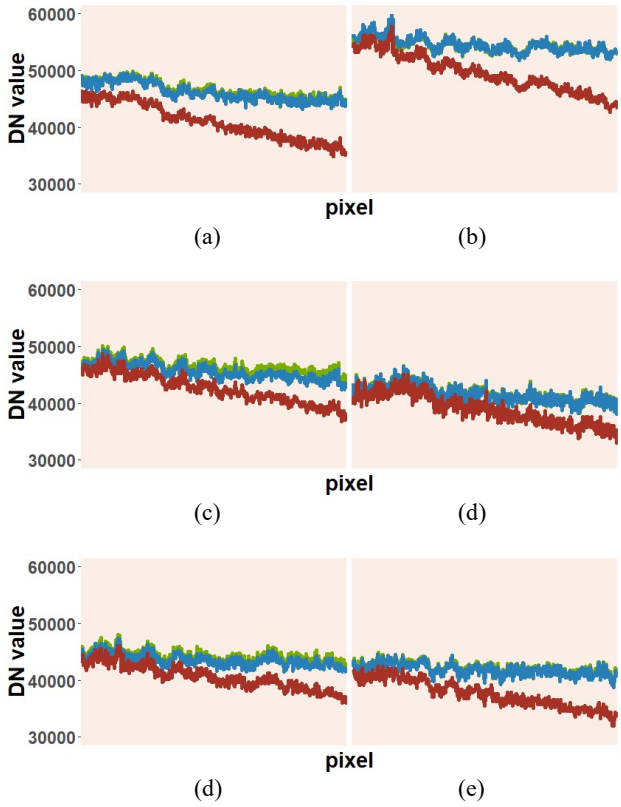

Figure 3. DNs extracted along profile from raw image (red lines), laboratory corrected image (blue lines) and in-situ corrected image (green lines): (**a**) Band 1; (**b**) Band 2; (**c**) Band 3; (**d**) Band 4; (**e**) Band 5; (**f**) Band 6.

Band	raw CV %	Laboratory cal. CV %	In-situ cal. CV %
B1	7.69	3.36	3.16
B2	6.71	2.50	2.24
B3	6.02	3.09	2.54
B4	6.49	3.45	3.42
B5	5.22	2.44	2.29
B6	6.33	2.42	2.39

Table 3. Coefficients of variation at selected profile.

The vignetting correction using the LUT method, which is the most for precise application compared to the optical modelling method (Yu, 2004), significantly reduced the diagonal profile variance. The CV decreased by half in all bands and the DNs were equalized. The similar results were achieved in the study by (Olsen et al., 2010), who presented a calibration of a spaceborne linear scanner using a CCD chip. Moreover, we obtained equal CV values for laboratory and in-situ calibration, which can be considered a simple form of validation.

Figure 4 compares the three validation target reflectance curves that are derived from the spectrometer measurement using the median reflectance values of the same targets that are extracted from the raw (red dots) and corrected data using correction images taken in the laboratory (green dots) and in-situ (dark green dots). The most significant improvement occurs as expected at target 4 (a) due to the strongest vignette effect resulting from its location in the selected field image. The raw values are strongly underestimated (~0.35) compared to the reference and corrected values (~0.42). Lower, but still inconsiderable, improvement of the conformity with reference data was obtained at target 7 (c), because of the vignette effect reduction. On the contrary, target 5 (b) reveals only minor improvement, because the target is placed closer to the image center and the vignette effect is not so strong.

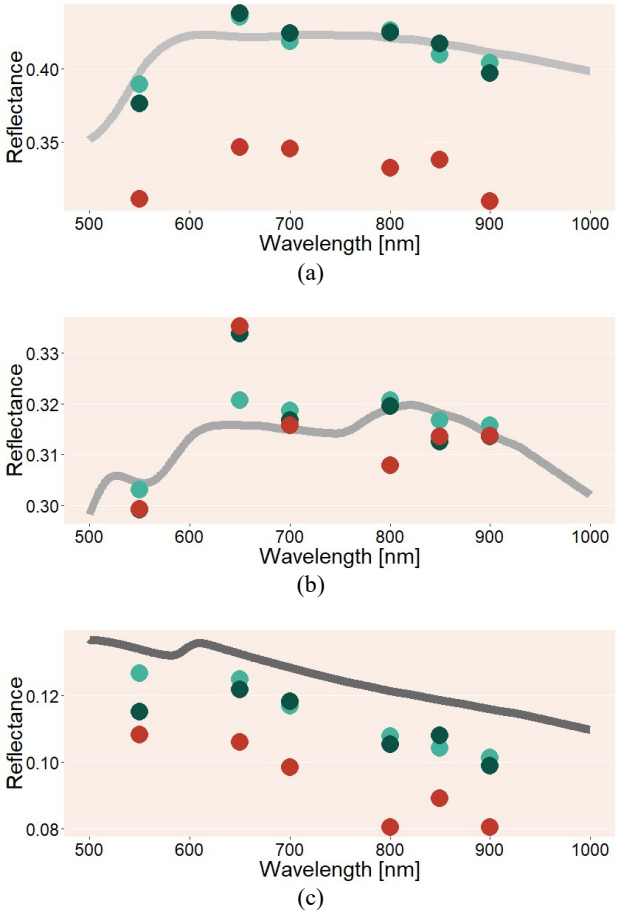

Figure 4. The comparison of three validation target reflectance curves: (a) Pearl 4; (b) Light Grey 5; (c) Medium Grey 7 derived from a spectrometer measurement with median reflectance values of the same targets extracted from raw (red dots), laboratory corrected (green dots) and in-situ corrected image (dark green dots).

If we compare the normalized root mean square errors (NRMSEs) between raw data, laboratory and in-situ corrected images (Table 4). We see the similar accuracy improvement of using both calibration approaches. The NRMSE values for target 4 are ten times lower in the corrected images. The NRMSE values of target 7 are 2-10 times lower in the corrected images. The calibration accuracy improvement at target 5 is only minor, because the local vignette effect is relatively minor resulting in low vignetting correction coefficient.

WL	R4	L4	S4	R5	L5	S5	R7	L7	S7
550	17.6	1.4 *	3.4	0.9	0.7 *	1.2	3.3	1.7 *	1.9
650	13.9	2.1 *	2.8	2.4	0.8 *	2.9	5.7	1.2	0.8 *
700	13.3	0.9 *	1.2	0.9	0.9	0.8 *	7.2	0.2	0.2
800	8.6	0.5	0.5	1.1	0.7 *	0.8	4.4	0.6 *	0.7
850	9.8	1.1 *	0.8	0.8	0.8 *	0.9	2.5	1.0	0.7 *
900	11.6	0.7 *	1.4	0.9	0.7	0.7	3.1	0.5 *	0.9

Table 4. The normalized root mean square errors of reflectance values comparing the reference spectral curve of verification targets with reflectance values extracted from the raw and fully corrected images. The normalization was performed by dividing the RMSE by interquartile range. The values are expressed as percentage. WL is wavelength in nanometres, R is raw data, L is laboratory calibrated data and S is in-situ calibrated data. The numbers define the calibration target. * marks lower NRMSE value in the corresponding pair of L and S.

The lower values of laboratory-based calibration NRMSE indicate less residual variance. Hence, we used a Mann-Whitney U test to test the hypothesis that the resulting reflectance values of three validation targets extracted from the laboratory calibrated and in-situ calibrated image are from the same distribution (Table 5). The resulting p-values show significant differences in most cases. The result shows that the calculated reflectance estimates based on laboratory calibration are slightly more accurate because of the controlled illumination conditions resulting in more balanced flat field correction image. Moreover, the result shows that the null hypothesis cannot be rejected three times (Band 1,3,4) in the case of the darkest target 7 compared to one case of targets 4 and 5. This relates to the reflectance values distribution of the targets. The dark target reveals the lower variance of reflectance values no matter of illumination conditions in general.

Band	p-value		
	Pearl 4	Light Grey 5	Medium Grey 7
550 nm	< 0.001	< 0.001	0.2466
650 nm	< 0.001	< 0.001	< 0.001
700 nm	< 0.001	< 0.001	0.2879
800 nm	0.3407	0.2294	0.2238
850 nm	< 0.001	< 0.001	< 0.001
900 nm	< 0.001	0.005	0.006

Table 5. The results of Mann-Whitney U test. The null hypothesis was: Resulting reflectance values of three validation targets extracted from the laboratory calibrated and in-situ calibrated image are from the same distribution

The resulting NRMSE values are comparable with the results of previous works of Pozo et al. (2014) (2%), Aasen et al. (2014) (1%) and Yang et al. (2017) (5%) focused on calibration of hyperspectral sensors. In general, Richter and Schläpfer (2002) consider NRMSE values under 2% as a very good agreement with reference data and NRMSE values under 5% as a sufficient match. Moreover, Aasen et al. (2015) implemented in-situ calibration into main image processing chain, because the results were comparable with laboratory calibrations and in-field calibrations perform better for the systematic pattern removal.

These findings make the proposed in-situ approach usable for various environmental studies featuring UAV multispectral photogrammetry. To achieve the proper spectral image properties and retain the consistency across multispectral UAV imaging campaigns, the radiometric calibration procedure should be included into every processing chain (Aasen et al., 2018; Kelcey and Lucieer, 2012a). In the case of multispectral frame cameras, the vignette effect removal has the greatest impact on calibration accuracy (see Figures 3,4 and Table 4), which is consistent with the findings of Lebourgeois et al. (2008). Although the statistical testing revealed slightly better agreement of laboratory calibrated reflectance with reference data, the authors consider the proposed rapid in-situ calibration approach as an alternative to classic laboratory radiometric calibration. The differences between the accuracy of both calibration approaches are minor compared to the raw data. A similar agreement between laboratory and field calibration of a modified colour infrared single-lens reflex camera, but without noise removal. was achieved by Crusiol et al. (2017). The correlation coefficient of $r > 0.9$ was found for the cross calibration.

The main advantage of the proposed in-situ calibration method is that there is no need to additional equipment investment like the integrating sphere and building and maintaining the database of noise and vignetting reduction images apriori, which is the basic principle of dark offset subtraction and LUT correction methods. The calibration images are taken during the filed experiment under the same weather conditions and the database can be built "on the fly". Every step of the proposed workflow can be used as it is designed for another multiple array multispectral cameras systems with monochrome frame global shutter sensors and linear response to radiation e.g. Parrot Sequoia and MicaSense Red-Edge.

In addition to simplifying the radiometric correction approach as is proposed here, the empirical line method could be simplified. Moran et al. (2001) refined an empirical line approach using only one within-scene calibration target for factor retrieval from Landsat-5 TM and Landsat-7 ETM+. A similar approach has been tested by Iqbal et al. (2018) for UAV sensor. If the UAV multispectral camera has a linear relationship between raw DN values and reflectance with intercept close to zero, the empirical line can be constructed using only one light target and zero as dark target. Or a universal empirical equation can be used after performing the corresponding experiment (Guo et al., 2019). However, the universal empirical line is model specific, because of the selected set of filters and cannot be applied to a different set (Assmann et al., 2018).

4. CONCLUSIONS

This study aimed to test and compare two possible radiometric calibration approaches of Tetracam μMCA Snap multispectral camera using the Dark offset subtraction and LUT methods. We compared the standard laboratory-based calibration using correction images from the prepared database with a rapid in-situ based calibration featuring correction images taken during the field campaign. The hypothesis was that the accuracy of in-situ calibration could be comparable with the laboratory calibration, and thus could replace it and simplify the radiometric calibration process by eliminating the main drawbacks of building the large database correction pictures for all combinations of relevant exposures, ambient temperatures and light intensities apriori.

The results of the field experiment showed that both calibration approaches led to significant accuracy improvement compared to raw data. The vignetting correction using resulted in a significant

reduction of the Coefficient of variation by half in all bands and overall equalizing the DNs on the diagonal profile. The NRMSEs after processing all corrections ranged from 0.24 to 3.40%. The results show that the calculated reflectance estimates based on laboratory calibration are slightly more accurate, because of the controlled illumination conditions resulting in more balanced flat field correction image.
Although the statistical resting revealed slightly better agreement of laboratory calibrated reflectance with reference data, it can be concluded that the accuracy of in-situ calibrated approach is sufficient and can be used as an alternative to classic laboratory approach, because the accuracy improvement quantified by the NRMSE is 2 – 10 times better using both calibration approaches compared to raw data than the NRMSE differences between them.

ACKNOWLEDGEMENTS

The study was supported by the Charles University, project GA UK No. 824217 “Analysis of disturbance and regeneration of forest vegetation using UAV multispectral photogrammetry” and COST Action CA16219 - Harmonization of UAS techniques for agricultural and natural ecosystems monitoring.

REFERENCES

Aasen, H., Bendig, J., Bolten, A., Bennertz, S., Willkomm, M., Bareth, G., 2014. Introduction and preliminary results of a calibration for full-frame hyperspectral cameras to monitor agricultural crops with UAVs. *Int. Arch. Photogramm. Remote Sens. Spatial Inf. Sci.*, XL-7, 1-8.

Aasen, H., Burkart, A., Bolten, A., Bareth, G., 2015. Generating 3D hyperspectral information with lightweight UAV snapshot cameras for vegetation monitoring: From camera calibration to quality assurance. *ISPRS J. Photogramm. Remote Sens.,* 108, 245–259.

Aasen, H., Honkavaara, E., Lucieer, A., Zarco-Tejada, P.J., 2018. Quantitative remote sensing at ultra-high resolution with UAV spectroscopy: A review of sensor technology, measurement procedures, and data correctionworkflows. *Remote Sens.*, 10(7), 1091.

Al-Amri, S.S., Kalyankar, N. V., Santosh, K., 2010. A Comparative Study of Removal Noise from Remote Sensing Image. *Int. J. Comput. Sci. Issues,* 7(1), 32–36.

Assmann, J.J., Kerby, J.T., Cunliffe, A.M., Myers-Smith, I.H., 2018. Vegetation monitoring using multispectral sensors — best practices and lessons learned from high latitudes. *J. Unmanned Veh. Syst.,* 7(1), 54–75.

Baugh, W.M., Groeneveld, D.P., 2008. Empirical proof of the empirical line. *Int. J. Remote Sens.,* 29(3), 665–672.

Crusiol, L.G.T., Nanni, M.R., Silva, G.F.C., Furlanetto, R.H., da Silva Gualberto, A.A., Gasparotto, A. de C., De Paula, M.N., 2017. Semi professional digital camera calibration techniques for Vis/NIR spectral data acquisition from an unmanned aerial vehicle. *Int. J. Remote Sens*., 38(8-10), 2717–2736.

Guo, Y., Senthilnath, J., Wu, W., Zhang, X., Zeng, Z., Huang, H., 2019. Radiometric calibration for multispectral camera of different imaging conditions mounted on a UAV platform. *Sustain.,* 11(4), 978.

Heinold, S., 2017. Personal communication, Tetracam Inc.

Hruska, R., Mitchell, J., Anderson, M., Glenn, N.F., 2012. Radiometric and geometric analysis of hyperspectral imagery acquired from an unmanned aerial vehicle. *Remote Sens.,* 4(9), 2736–2752.

Iqbal, F., Lucieer, A., Barry, K., 2018. Simplified radiometric calibration for UAS-mounted multispectral sensor. *Eur. J. Remote Sens.,* 51(1), 301–313.

Kelcey, J., Lucieer, A., 2012a. Sensor correction and radiometric calibration of a 6-band multispectral imaging sensor for UAV remote sensing. *Int. Arch. Photogramm. Remote Sens. Spat. Inf. Sci.,* XXXIX-B1, 393–398.

Kelcey, J., Lucieer, A., 2012b. Sensor correction of a 6-band multispectral imaging sensor for UAV remote sensing. *Remote Sens.,* 4(5), 1462-1493.

Lebourgeois, V., Bégué, A., Labbé, S., Mallavan, B., Prévot, L., Roux, B., 2008. Can Commercial Digital Cameras Be Used as Multispectral Sensors? A Crop Monitoring Test. *Sensors,* 8(11), 7300–7322.

Manfreda, S., McCabe, M.F., Miller, P.E., Lucas, R., Madrigal, V.P., Mallinis, G., Dor, E. Ben, Helman, D., Estes, L., Ciraolo, G., Müllerová, J., Tauro, F., de Lima, M.I., de Lima, J.L.M.P., Maltese, A., Frances, F., Caylor, K., Kohv, M., Perks, M., Ruiz-Pérez, G., Su, Z., Vico, G., Toth, B., 2018. On the use of unmanned aerial systems for environmental monitoring. *Remote Sens.,* 10(4), 641.

Mansouri, A., Marzani, F.S., Gouton, P., 2005. Development of a Protocol for CCD Calibration: Application to a Multispectral Imaging System. *Int. J. Robot. Autom.,* 20(2), 94-100.

Minařík, R., Langhammer, J., 2016. Use of a multispectral UAV photogrammetry for detection and tracking of forest disturbance dynamics. *Int. Arch. Photogramm. Remote Sens. Spat. Inf. Sci.*, XLI-B8, 711-718.

Minařík, R., Langhammer, J., Hanuš, J., 2019. Radiometric and Atmospheric Corrections of Multispectral μMCA Camera for UAV Spectroscopy. *Remote Sens.,* 11(20), 2428.

Moran, M.S., Bryant, R., Thome, K., Ni, W., Nouvellon, Y., Gonzalez-Dugo, M.P., Qi, J., Clarke, T.R., 2001. A refined empirical line approach for reflectance factor retrieval from Landsat-5 TM and Landsat-7 ETM+. *Remote Sens. Environ.*, 78(1-2), 71–82.

Nocerino, E., Dubbini, M., Menna, F., Remondino, F., Gattelli, M., Covi, D., 2017. Geometric calibration and radiometric correction of the maia multispectral camera. *Int. Arch. Photogramm. Remote Sens. Spat. Inf. Sci.*, XLII-3/W3, 149–156.

Olsen, D., Dou, C., Zhang, X., Hu, L., Kim, H., Hildum, E., 2010. Radiometric calibration for AgCam. *Remote Sens*., 2(2), 464-477.

Padró, J.-C., Carabassa, V., Balagué, J., Brotons, L., Alcañiz, J.M., Pons, X., 2019. Monitoring opencast mine restorations using Unmanned Aerial System (UAS) imagery. *Sci. Total Environ.,* 657, 1602–1614.

Padró, J.-C., Muñoz, F.-J., Ávila, L., Pesquer, L., Pons, X., 2018. Radiometric Correction of Landsat-8 and Sentinel-2A Scenes Using Drone Imagery in Synergy with Field Spectroradiometry. *Remote Sens.*, 10(11), 1687.

Parrot., 2017. Parrot Announcement - Release of application notes. https://forum.developer.parrot.com/t/parrot-announcement-release-of-application-notes/5455 (27 September 2019).

Pozo, S. Del, Rodríguez-Gonzálvez, P., Hernández-López, D., Felipe-García, B., 2014. Vicarious radiometric calibration of a multispectral camera on board an unmanned aerial system. *Remote Sens.,* 6(3), 1918–1937.

Richter, R., Schläpfer, D., 2002. Geo-atmospheric processing of airborne imaging spectrometry data. Part 2: Atmospheric/topographic correction. *Int. J. Remote Sens.,* 23(13), 2631–2649.

Smith, G.M., Milton, E.J., 1999. The use of the empirical line method to calibrate remotely sensed data to reflectance. *Int. J. Remote Sens.,* 20(13), 2653–2662.

Teillet, P.M., 1986. Image correction for radiometric effects in remote sensing. *Int. J. Remote Sens.*, 7(12), 1637–1651.

Tetracam Inc., 2015. Tetracam µMCA User´s Guide.http://www.tetracam.com/PDFs/u%20MCA% 20Users%20Guide%20V1.1.pdf (17 August 2019).

Yang, G., Li, C., Wang, Y., Yuan, H., Feng, H., Xu, B., Yang, X., 2017. The DOM generation and precise radiometric calibration of a UAV-mounted miniature snapshot hyperspectral imager. *Remote Sens.,* 9(7), 642.

Yu, W., 2004. Practical anti-vignetting methods for digital cameras. *IEEE Trans. Consum. Electron.,* 50(4), 975–983.

Zhang, C., Kovacs, J.M., 2012. The application of small unmanned aerial systems for precision agriculture: A review. *Precis. Agric.,* 13(6), 693-712.

Článek IV

Minařík, R., Langhammer, J., & Lendzioch, T. (2020). Automatic Tree Crown Extraction from UAS Multispectral Imagery for the Detection of Bark Beetle Disturbance in Mixed Forests. *Remote Sensing*, *12*(24), 4081. https://doi.org/10.3390/rs12244081

remote sensing

MDPI

Article

Automatic Tree Crown Extraction from UAS Multispectral Imagery for the Detection of Bark Beetle Disturbance in Mixed Forests

Robert Minařík, Jakub Langhammer * and Theodora Lendzioch

Department of Physical Geography and Geoecology, Faculty of Science, Charles University, Albertov 6, 128 43 Prague, Czech Republic; robert.minarik@natur.cuni.cz (R.M.); theodora.lendzioch@natur.cuni.cz (T.L.)
* Correspondence: jakub.langhammer@natur.cuni.cz; Tel.: +420-221-951-364

Received: 1 November 2020; Accepted: 11 December 2020; Published: 13 December 2020

Abstract: Multispectral imaging using unmanned aerial systems (UAS) enables rapid and accurate detection of pest insect infestations, which are an increasing threat to midlatitude natural forests. Pest detection at the level of an individual tree is of particular importance in mixed forests, where it enables a sensible forest management approach. In this study, we propose a method for individual tree crown delineation (ITCD) followed by feature extraction to detect a bark beetle disturbance in a mixed urban forest using a photogrammetric point cloud (PPC) and a multispectral orthomosaic. An excess green index (ExG) threshold mask was applied before the ITCD to separate targeted coniferous trees from deciduous trees and backgrounds. The individual crowns of conifer trees were automatically delineated as (i) a full tree crown using marker-controlled watershed segmentation (MCWS), Dalponte2016 (DAL), and Li 2012 (LI) region growing algorithms or (ii) a buffer (BUFFER) around a treetop from the masked PPC. We statistically compared selected spectral and elevation features extracted from automatically delineated crowns (ADCs) of each method to reference tree crowns (RTC) to distinguish between the forest disturbance classes and two tree species. Moreover, the effect of PPC density on the ITCD accuracy and feature extraction was investigated. The ExG threshold mask application resulted in the excellent separability of targeted conifer trees and the increasing shape similarity of ADCs compared to RTC. The results revealed a strong effect of PPC density on treetop detection and ITCD. If the PPC density is sufficient (>10 points/m^2), the ADCs produced by DAL, MCWS, and LI methods are comparable, and the extracted feature statistics of ADCs insignificantly differ from RTC. The BUFFER method is less suitable for detecting a bark beetle disturbance in the mixed forest because of the simplicity of crown delineation. It caused significant differences in extracted feature statistics compared to RTC. Therefore, the point density was found to be more significant than the algorithm used. We conclude that automatic ITCD methods may constitute a substitute for the time-consuming manual tree crown delineation in tree-based bark beetle disturbance detection and sanitation of individual infested trees using the suggested methodology and high-density (>20 points/m^2, 10 points/m^2 minimum) PPC.

Keywords: bark beetle; forest disturbance detection; unmanned aircraft systems (UAS); photogrammetric point cloud (PPC); individual tree crown delineation (ITCD)

1. Introduction

Insect disturbances are natural processes in forest ecosystems to maintain healthy and heterogeneous forests [1]. However, forest ecosystems can experience increased magnitude and frequency insect disturbances due to interaction from increasing temperatures and drought [2,3]. One of the most significant threats to the temperate forests of Central Europe are climate-change driven

bark beetle Ips typographus L. (hereafter bark beetle) outbreaks [4]. Prolonged periods of warmth, longer vegetation seasons, and drought combined with an increased frequency of windstorms allow for the establishment of additional generations of the Ips typographus and a population overgrowth [4,5]. Moreover, urban forests may be affected more seriously because an urban environment produces additional stressors [6]. The stressors include changes in forest soil properties, tree species diversity, higher temperatures, and carbon dioxide content [7,8]. The stressed trees are then optimal material for a bark beetle feeding. Therefore, pest insect infestation is a serious threat to urban forests that can affect forest health and economic losses [9]. On the other hand, urban forests are under active forest management, which allows rapid individual tree sanitation. Therefore, it is necessary to use an appropriate method for the detection of individual infested trees.

A terrestrial survey of symptoms on the trunk and foliage discoloration or defoliation is traditionally used for bark beetle disturbance detection and assessment on a single tree level [10,11]. The infested tree goes through three-needle discoloration [5,12,13]. These stages are commonly known as green, red, and grey attacks. In the green attack stage, the infested trees have not shown distinct symptoms visible to the human eye, and therefore, infestation is not easy to detect at this stage at leaf and canopy levels [5,14]. However, the green attack can be better seen by remote sensing in the shortwave and thermal infrared spectra because of the changes in water content [15]. A field survey is also relatively time-consuming and costly, making this approach suitable only for a plot scale. Therefore, forest management has widely used conventional multi- or hyperspectral remote sensing to detect bark beetle infestation's spectral symptoms.

Medium resolution satellites, especially Landsat data employing subpixel analysis, are more frequently used in the of study bark beetle disturbances compared to coarser resolution sensors, i.e., MODIS or AVHRR, indicating that spatial resolution is crucial feature for mapping such infestations [16]. However, the spatial resolution (>10 m) of these satellites is not suitable for the detection of bark beetle infestation at the individual tree level because the pixel size is more extensive than the mapping unit (a single tree crown). This decametric spectral resolution is more appropriate for mapping larger infestations at an epidemic population scale using an area-based (pixel-based) approach only, because of the pixel size [17]. High-resolution imagery (spaceborne or airborne) with a metric resolution (1–9 m) is very suitable for mapping spatially dispersed infestations of small groups of trees [17]. However, the area-based approach is still applied in recent studies using metric imagery to detect the bark beetle damage [11,18,19]. Nevertheless, for targeted individual tree sanitation of infested trees, it is essential to use imagery with a submeter (<1 m) spatial resolution and a tree-based approach based on automatic individual tree crown delineation (ITCD) from a submetric imagery to substitute the traditional terrestrial survey [6,17,20,21]. These prerequisites have been met only by airborne remote sensing.

Three main methods (Valley following, Region growing, and Watershed segmentation) have been developed for an automatic ITCD from aerial imagery [22]. These methods worked only with image brightness values. The algorithms searched for regions surrounded by local minima (shaded gaps between tree crowns), spectral similarity to the seed pixels, or local minima within inverted grayscale imagery [23–25]. However, automatic ITCD is difficult to perform with no vertical canopy structure [16,22].

Modern remote sensing technologies are now available for providing information about vertical canopy structure, enabling the tree-based approach. Airborne laser scanning (ALS) or stereophotogrammetry is now a standard operational tool for forest inventory and producing 3D canopy models [26,27]. The most used strategy for ITCD from airborne laser scanning is currently searching for local maxima (LM) for treetops detection followed by more common watershed segmentation or a more advanced region growing algorithm for crown delineation [28]. These methods are applicable either to photogrammetrically derived point clouds (PPCs) or from light detection and ranging (LiDAR) [22]. Despite this, the area-based approach is still more frequently used for bark beetle disturbance detection [6,29]. Only two recent studies that are focused on the pest insect disturbance

detection, Nasi et al. [6] and Windrim et al. [30], have applied an essential individual treetop detection using image brightness or a canopy height model (CHM) from RGB data.

A disadvantage of airborne sensing is the high operational costs, weather conditions, and extensive mission planning. This is problematic for bark beetle disturbance management and, in general, for all pest insect infestations in the small-scale urban forest because these applications require an elevated level of spatial detail, frequent, intra-annual monitoring, and rapid processing. Nevertheless, recent developments in remote sensing and robotics have enabled the production of unmanned aircraft systems (UAS) featuring miniature multi- or hyperspectral sensors. In addition to ultra-high spatial resolution, the main advantages of employing UAS for insect disturbance detection are low operational costs (≤2000 Euro), the ability to undertake repeated image acquisition, when pest insects start to attack the trees, or when the damage is most likely visible and high operability under varying weather conditions, e.g., drizzling and moderate wind. Moreover, thanks to modern photogrammetric techniques based on Structure from Motion (SfM), it is possible to produce more cost-effective 3D photogrammetric canopy PPC and orthomosaics from UAS data as an alternative to airborne LiDAR to perform ITCD [31,32]. This enables processing precision, which cannot be achieved using LiDAR. Widespread practice involves applying an automatic ITCD from CHM derived from RGB or UAS LiDAR data [33]. Local maxima are used for raster-based treetop detection, while for tree crown delineation, watershed segmentation is commonly used [34].

The current state of the art in the UAS literature is to apply a tree-based approach for deriving individual tree parameters, such as tree height [35,36] or crown diameter [37], using an automatic ITCD from CHM. Studies focused on bark beetle driven disturbance detection have used the pixel-based approach [38]. Only two studies, Näsi et al. [39] and Klouček et al. [40], have been applied to a basic ITCD based on an automatic treetop identification combined with a buffer zone around the treetops for a bark beetle damage classification in the mature even-aged spruce forest. Both studies used the CHM derived photometrically. All of these studies implemented only spectral based features (original spectral bands and vegetation indices) to classification, which is sufficient to detect infested trees within a monoculture. Nonetheless, this is problematic in a highly diverse mixed forest when spectral response of different species is similar. For example, Sothe et al. [41] implemented UAS PPC-derived elevation tree metrics to tree species classification of tropical forests resulting in an overall accuracy increase of 15% compared to classification-based only on spectral features.

Despite this, studies combining spectral and elevation features for bark beetle damage detection are rare [42]. Little research has examined the segmentation of tree crowns directly from a PPC, especially in terms of multispectral analysis, because the accuracy of the LM method is linked intricately to point density, and multispectral cameras have been characterized by lower resolution [43]. Moreover, minimal investigations have performed ITCD within an uneven-aged, mixed forest [44]. Canopies of a distinct size may cause problems to set the correct spatial resolution when using CHM for ITCD, because smaller crowns may disappear in a coarser raster [22]. Therefore, it would be beneficial to use an original dense PPC to perform ITCD in a mixed forest.

This study focuses on the detection of individual spruce trees infested with bark beetles. We investigated whether it is possible to substitute laborious and commonly used manual ITCD with automatic ITCD without increasing extracted feature uncertainty of disturbance classes due to inaccurate ITCD. This aspect has not been thoroughly investigated in the scientific literature. The objectives of this study are (1) to examine and compare current methods for an individual tree crown spectral and elevation feature extractions from UAS multispectral data to clearly distinguish between the forest disturbance classes, (2) to statistically compare extracted features among reference crowns and automatically delineated tree crowns and (3) to discuss the uncertainties of the automatic crown delineations based on a used method and the extracted feature statistics for the bark beetle disturbance at individual tree level.

The methodology of this study was designed to address the abovementioned limitations. We use a multispectral PPC with a high point density to ensure accurate treetop identifications and ITCD

in an uneven-aged mixed forest. The CHMs were derived from the high point density PPCs to guarantee a sufficient spatial resolution for ITCD. Moreover, we hypothesized that individual tree-based extraction of spectral and elevation features from a multispectral PPC and orthomosaic would improve the detection of individual bark beetle infested trees in a heterogeneous urban mixed forest. Hence, the suggested methodology for detecting bark beetle infestation in the urban forest aims to introduce a more efficient approach to forest health monitoring and damage reduction.

2. Materials and Methods

2.1. Study Area

Klánovice Forest represents the largest suburban forest complex in the Prague metropolitan area (Figure 1). Until the mid -19th century, the area was a vast, deep, and unmanaged forest without a regular settlement. Human activities started after 1845, following the construction of a railway and new residential complex of Klánovice. Since 1982, the almost whole forest complex has been protected as a natural reserve with several valuable parts, featuring a higher protection status under Natura 2000. Currently, the Klánovice forest has an extent of 1030 ha and features a mixed structure of broadleaved and coniferous tree species, dominated by 33% oak, 31% pine, 11% birch, and 6% Norway spruce [45].

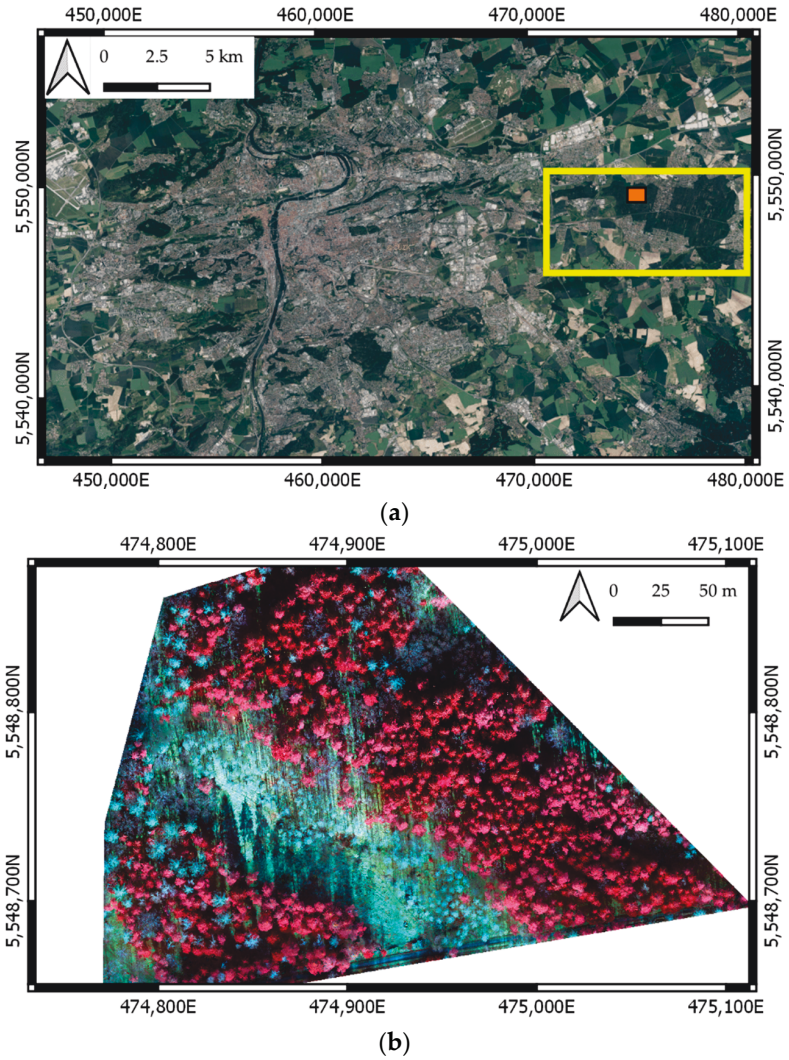

Figure 1. Study area. (**a**) Location of Klánovice forest (yellow rectangle) and study area (orange rectangle) in Prague metropolitan area, (**b**) Study area on a multispectral image. The coordinate reference system is WGS 84/UTM zone 33N.

Since 2015, the forest complex has experienced repeated disturbance by insect infestation and windstorms. The forest health status was deteriorated by a five-year-long period of droughts and summer heatwaves, leading to rapid bark beetle infestation and forest disturbance. In October 2017, the region was hit by the windstorm Herwart and in February 2000, the windstorm Sabine [46].

Compared to the midlatitude montane regions, which experiencing severe bark beetle disturbance, the Klánovice forest's infestation was more intense. For example, in Šumava Mts., severely hit by the insect disturbance, two generations of bark beetles are typically recorded per year [47]. The forests in the Prague metropolitan region with a warmer climate resulting from the lowland position and vicinity of urban heat island, experience four insect generations in a year [48].

However, the rapid progress of disturbance led to a limited hybrid structure of tree species with only limited homogeneous areas. The second aspect that prevented extensive forest damage was selective forest management, aimed at rapid detection and cutting the individual infested trees. However, since 2017, the forest disturbance resulted in several glades being subsequently replanted. Hence, the ability to identify the disturbance and detect early stages of disturbance, allowing for a selective response, is vital for managing mixed forests with limitations set by the protected area's status.

2.2. UAS Data Acquisition

The UAS imaging campaign was performed on 24 February 2020, using DJI Matrice 210 RTK featuring a multispectral camera MicaSense RedEdge-M. A flight altitude was 100 m above ground level resulting in a ground sample distance (GSD) of 6.8 cm. The flight covered 5.5 ha of the urban forest. The high values of frontlap (90%) and sidelap (80%) were set to secure the adequate number of initial points needed for dense PPC extraction in forest scenes during photogrammetric processing. The point cloud density, driven by the parameters of flight height, focal length, and spatial resolution and the frontlap and sidelap values in our study were calculated in Agisoft Metashape. The weather conditions were mostly sunny, and the flight was conducted around noon (solar angle = 30.37°; sun azimuth = 179.82°) to minimize shadows. Twenty white ground control points were sprayed on the ground to get accurate image orientations. The WGS 84/UTM zone 33N coordinates of GCPs were measured by geodetic global navigation satellite system (GNSS) receiver Topcon. A real-time kinematic (RTK) GNSS method was used with the position accuracy of 1–2 cm employing a virtual reference station. We used this method to calculate precise image orientations and for orthorectification, because we needed precise positioning of individual trees on the orthomosaic to join the disturbance class from the ground truth points. If the position of the trees is not precise in the dense forest, the true disturbance class would be altered among neighboring trees. The flight was conducted deliberately just before vegetation season to distinguish spruce trees and conifers from broadleaves and use ground truth data for targeted tree sanitation of the most damaged trees before pioneer bark beetles started to swarm [49].

Five discrete identical cameras equip the MicaSense RedEdge-M camera with a fixed focal length of 5.4 mm, global shutter sensors with a resolution of 1280 × 980 pixels, and different bandpass filters. The set of bandpass filters is shown in Table 1. The camera is bundled with a downwelling light sensor (DLS), which records the current ambient light in the same wavelengths as the camera and stores it in the image metadata. This metainformation automatically corrects the raw imagery for light changes during the photogrammetric processing flight. Additionally, we took photos of the MicaSense calibration panel under the open sky to perform a calibration to reflectance factors. The calibration was performed using the recommended procedure in the Agisoft Metashape [50].

Table 1. Spectral resolution of the MicaSense RedEdge-M camera used in the study.

Band Number	Band Name	Center Wavelength (nm)	Bandwidth FWHM * (nm)
1	Blue	475	20
2	Green	560	20
3	Red	668	10
4	Red edge	717	10
5	Near infrared (NIR)	840	40

* FWHM: full width at half maximum.

2.3. Ground Truth Data

A field inventory was conducted at five randomly selected stands at the beginning of March 2020, where the spruce trees were newly attacked in the summer or autumn of 2019. The stands' coordinates were measured by GNSS receiver Topcon using an RTK method. Coordinates of visible individual trees were measured around the stands by total station due to multipath the of GNSS signal under the canopy. Regarding the study's focus, the field inventory was primarily focused on mature spruces mapping and the health assessment. Nevertheless, pines were also mapped to compare their spectral and elevation features with spruce disturbance classes to suggest the best features for distinguishing these two species. A total of 122 mature spruce trees (*Picea abies*) and 23 pines (*Pinus sylvestris*) were mapped. All reference tree crowns (RTC) were manually digitized into a polygon shapefile using QGIS 3.10.2. The reference polygons served for the evaluation of automatic ITCD and treetops detection. The descriptive statistics of the reference tree crowns are given in Table 2.

Table 2. Descriptive statistics of reference tree crowns.

Statistics	Crown Area (sq. m)
Mean	15.79
St. dev.	7.80
Minimum	1.90 *
Maximum	50.15
Q1	9.95
Median	13.84
Q3	19.90
IQR	9.95

* The second smallest crown area was 4.61 m^2.

The health status of spruce trees was assessed relative to each other based on crown discoloration and defoliation. These symptoms are typically used for indicating the infestation status of Ips typographus [6]. Moreover, resin ducts were observed as a symptom of a fresh attack of pioneer beetles [51]. Spruce trees were classified into three classes (Table 3). The spruce tree classes and the type of pine trees are referred to as disturbance classes hereafter.

2.4. Photogrammetric Processing

Photogrammetric processing was performed using Agisoft Metashape Professional 1.6.2., which implements recent photogrammetric techniques of structure from motion and semiglobal matching [52]. Moreover, Metashape sensor database contains the Red-Edge M camera model, including distortion parameters and vignetting [53]. Metashape also automatically extracts the information about DLS from image metadata so no additional corrections are necessary.

The multispectral images were aligned using high accuracy settings and generic preselection. Band 5 was set as a master channel for processing. After initial image alignment, the GCP were displayed in images, and image orientations were calculated and transformed into WGS 84/UTM zone 33N using GCPs. The original MicaSense reflectance panel and an empirical line method implemented

in the software were used for radiometric calibration. The dense point cloud was generated using ultra-high settings and aggressive depth filtering. Ground points were automatically classified in Metashape. Based on the PPC, the digital surface model (DSM) was computed and used to derive the multispectral orthomosaic (10 cm/pixel). The resulting ultra-high-quality PPC and multispectral orthomosaic were further used for analysis. All vegetation indices (VIs) maps used in this study (Sections 2.5.1 and 2.5.4) were calculated using a raster calculator in Metashape to keep the consistency with the orthomosaic.

Table 3. The classification of mature spruce trees based on the field investigation. N/A indicates that resin ducts were not used to classify the tree into sbbd class.

Code	Tree Status	Canopy	Resin Ducts	N. of Trees	False Color Image *
sh	Live and not infested	needles green	absent	12	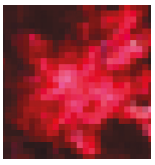
sbbg	green attack	needles green or light green	present	69	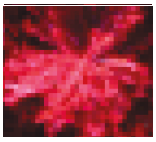
sbbd	damaged tree ("yellow attack")	needles light green or yellow, light green needles dropped; bark flaked away by woodpeckers	N/A	41	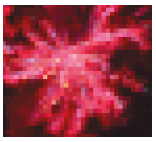

* Band combination 5–3–1.

2.5. Individual Tree Crown Delineation Workflow

We have proposed and tested an innovative workflow for the detection of individual tree crowns, enabling further classification of the forest health status. The workflow is wrapped around current ITCD methods that were primarily designed to ALS point cloud to the UAS-based photogrammetric PPC [54]. It is based on masking target tree species in the ITCD process, which was necessary for automizing the process.

The suggested workflow included several steps. Firstly, we prepared green vegetation masks (Section 2.5.1) to separate the conifers from the ground, shadows, and broadleaves (i.e., the background). Then, we tested three current automatic ITCD methods and simple buffer zones around the detected treetops (Section 2.5.2). We investigated the effect of PPC density, and the ITCD method performing a standard accuracy assessment of segmentation comparing automatically delineated tree crowns to manually digitized reference tree crowns (Section 2.5.3). The selected tree crown segmentation datasets of each method were used for feature extraction (Section 2.5.4). The testing methodology suggested in this subsection was designed to investigate the separability of disturbance classes within the reference dataset and test the treatments (automatically delineated tree crowns) versus control (reference tree crowns) equality of selected features' distributions. The testing results were then used to make conclusions about the usability of automatic ITCD for the detection of bark beetle disturbance using the individual-tree-based approach. The flowchart of the data processing workflow is presented in Figure 2.

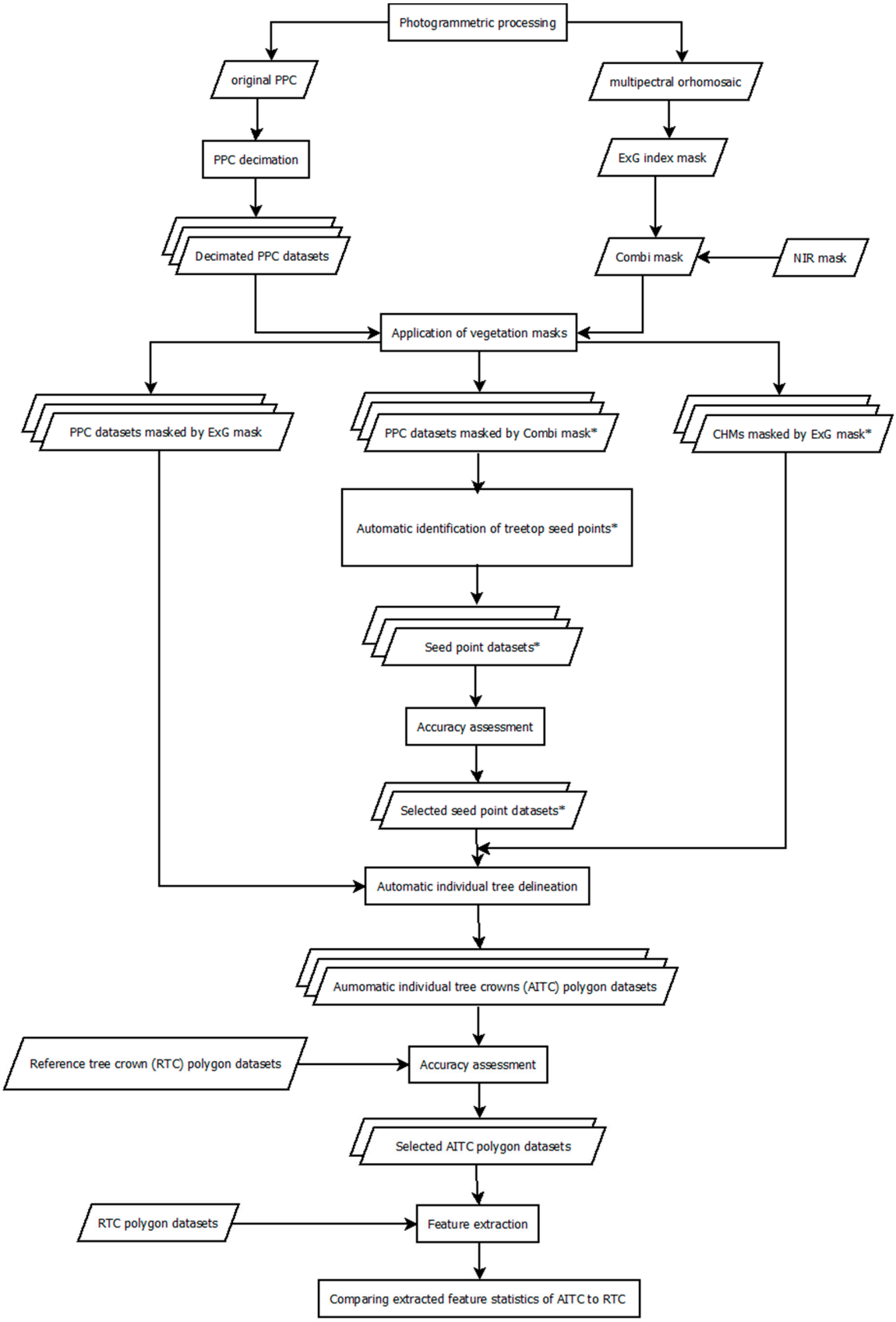

Figure 2. The processing workflow suggested in this study. Steps marked with * are optional regarding to used ITCD method. These steps are necessary for Dalponte2016 and Marker controlled watershed segmentation methods in this study.

2.5.1. Vegetation Masks

To separate the conifers from the ground, shadows, and broadleaves (i.e., =the background), we applied the excess green index (ExG) index threshold mask [55]. The ExG index map was computed from the multispectral orthomosaic (Equation (1)). The original ExG map was resampled to raster with a 30 cm spatial resolution to eliminate isolated pixels.

$$ExG = 2[G/(R + G + B)] - [R/(R + G + B)] - [B/(R + G + B)], \quad (1)$$

where R is the red band, G is the green band, and B is the blue band of the camera

The threshold for conifer trees was set according to histogram analysis of the resampled ExG map. An automatic unsupervised k-means classification of the ExG map into two classes (conifers and the background) was performed to detect a threshold value [56]. The final ExG threshold (ExG = 0.20) value was selected after a visual interpretation of the classified image. All pixels under the threshold value (ExG < 0.20) were set to NA within the mask. The final ExG mask was smoothed by a 3X3 modal filter (including NAs) to eliminate isolated pixels. The ExG mask was applied to the PPC before ITCD. In addition to the ExG mask, we applied a near infrared (NIR) shadow mask to remove shadowed gaps between treetops for the treetop's detection routine.

The NIR shadow mask has been traditionally used to reduce false positive treetops formed by small local maxima of lower shadowed branches of large crowns) [22]. In this step, we used the NIR band (Band 5) of the original orthomosaic. The processing workflow was like ExG mask creation. The NIR map was resampled to a spatial resolution of 30 cm. An automatic unsupervised k-means classification of NIR map into five classes was performed to detect a shadows' potential threshold value. The final NIR threshold (DN = 2670) value was selected after a visual interpretation of the classified image. Shadows formed a separate class. All pixels above the threshold value (DN > 2670) were set to NA within the mask. These two masks were combined for treetops detection (hereafter referred to as a combi mask). The combi mask was finally smoothed by a 3X3 modal filter (including NAs) to eliminate isolated pixels. The resulting mask was formed only by pixels of illuminated coniferous crowns.

2.5.2. Automatic Tree Crown Delineation

We tested three automatic ITCD methods to the UAS-based photogrammetric PPC (Table 4). We selected the Dalponte2016 region growing algorithm [57], marker-controlled watershed segmentation [58], and Li2012 [59] methods for comparison because they have been highly rated in previous comparative studies of Xiao et al. [60] and Hastings et al. [61]. These methods can be divided into two groups. Dalponte2016 (DAL) and marker-controlled watershed segmentation (MCWS) are CHM-based algorithms that rely on antecedent seed map of treetops. Li2012 (LI) is a 3D region growing algorithm applied directly to a PPC using a built-in function for treetops detection. These methods are available in the R package lidR [54] within *lastrees* function for the direct ITCD from the PPC. In the case of DAL and MCWS, this function automatically segments the PPC according to CHM-based segmentation results.

Table 4. Four automatic ITCD methods investigated in this study.

Crow Delineation Method	Application to	Priority Seed Points	Reference
Dalponte2016 (DAL)	CHM	Y	[57]
Marker-control. watershed (MCWS)	CHM	Y	[58]
Li 2012 (LI)	Point cloud	N	[59]

CHM: Canopy height model.

Treetop seed points used in DAL and MCWS were created using a local maximum filter (*lmf*) algorithm with variable circular window size [62]. The algorithm is implemented in the lidR package. The variable window size is calculated as a user-defined function of the local height extracted from the PPC. The function takes a height of a given point or pixel and returns the desired window size centered on that point or pixel. The *lmf* algorithm is highly dependent on crown size [63]. For this reason, we designed two functions (hereafter referred as f1 and f2) to return the moving window diameter equal to the minimum (f1 ≅ 2.75 m) or median diameter (f2 ≅ 4.01 m) of the reference crowns using the median reference tree height (25.14 m) extracted from the CHM. Because bark beetle prefers the mature spruce trees that provide a plentiful source of phloem [64], we set the height threshold to ignore all points under the 14 m local maxima search.

$$\text{f1} = \text{tree height} \times 0.07 + 1, \tag{2}$$

$$\text{f2} = \text{tree height} \times 0.08 + 2. \tag{3}$$

We tested the *lmf* algorithm with two variable moving windows first on the masked (combi mask) PPC with the original point density. However, we discovered that treetops were formed by multiple identical but well-located seed points due to extreme point density. This resulted in many false-positive treetop detections. Moreover, in the context of work by Eysn et al. [65], which stated that the accurate treetops detection is of equal or greater importance than the choice of segmentation method, we decided to decimate the original PPC and investigate the effect of the point density to the treetop seed points detection and subsequent ITCD. Therefore, the original PPC without applied mask was decimated using the *lasfilterdecimate* function from the lidR package. This function applied a decimating algorithm that created a grid with a given resolution and filtered the PPC by selecting the highest point within each cell. The overview of decimated datasets is shown in Table 5.

Table 5. Overview of the UAS PPC datasets and their parameters used for the creation of treetop seed points dataset, CHM rasterization and ITCD. The original PPC was used only for preliminary treetop seed points creation.

Dataset	Decim. Grid (m)	*lmf* Function
las	N/A	f1/f2
las01	0.1	f1/f2
las02	0.2	f1/f2
las03	0.3	f1/f2
las05	0.5	f1/f2
las1	1	f1/f2

These datasets were masked by combi mask for treetop seed points detection. The *lmf* algorithm was applied to the datasets in two versions using either f1 or f2 functions.

CHMs needed for DAL, and MCWS segmentation methods were calculated for every decimated PPC with no mask using a *pitfree* algorithm [66]. The spatial resolutions of CHMs were set to be equal to the decimation grid. The ExG mask then masked the CHMs before automatic tree segmentation within *lastrees* function. In the case of the LI method, the ExG mask was applied directly to the PPC, because there was no seed points map and CHM were required.

All three delineation methods were applied to the selected decimated PPCs. Parameters of the automatic delineation algorithms were set by tuning of default parameters using the trial-and-error method (Appendix A). Individual polygons of the tree crowns were generated by *tree_hulls* function. This function created 2D concave hulls around delineated tree crowns of the segmented PPC.

2.5.3. Accuracy Assessment

After running the automatic treetops detection routine within all datasets, we compared the resulting treetops with the reference crowns in terms of true positive (TP), false-negative (FN, omission error), and false positive (FP, commission error) treetops. If more than one point fell within the crown, only one TP point was counted. The rest was assessed as FP. To evaluate the effect of point density to the accuracy of treetops detection, we calculated recall (r), precision (p), and F-score (F) statistics, according to Li et al. [59].

$$r = TP/(TP + FN), \tag{4}$$

$$p = TP/(TP + FP), \tag{5}$$

$$F = (2 \times r \times p)/(r + p). \tag{6}$$

For further automatic ITCD using DAL and MCWS methods, we employed only the more accurate treetop seed points dataset from the f1 or f2 alternatives of the given decimated PPC. These statistics were not calculated for ITCD using the LI method because the treetop detection is not a primary task for ITCD. Therefore, only the accuracy of the final automatic individual tree polygons was assessed.

The accuracy of delineation methods and the effect of PPC decimation to the ITCD were assessed by comparing the generated automatic individual tree crown (AITC) polygons to the reference tree crowns (RTC). A detection accuracy score (DA) was calculated for each delineation method and decimated PPC:

$$DA = nTP/N, \tag{7}$$

where nTP is the number of correctly segmented (true positive) AITC, and N is the number of RTC [67]. AITC polygon was considered correctly segmented if ≥ 50% of the area of both AITC and RTC intersect [68,69]. Moreover, the incorrectly segmented AITC were classified to one of three categories. In total, each AITC polygon was assigned to one of four categories [61]:

1. Oversegmentation: The intersection area of given AITC and RTC is ≥50% of AITC but <50% of the area of RTC. This indicates that AITC is smaller than RTC.
2. True positive: The intersection area of given AITC and RTC is ≥50% of the area, both for AITC and RTC.
3. Undersegmentation: The intersection area of given AITC and RTC is <50% of AITC, but ≥50% of the area of RTC. It indicates that AITC is larger than RTC.
4. False-positive: The intersection area of given AITC and RTC is <50% of the area, both for AITC and RTC.

When multiple AITC polygons fell within one RTC, only one AITC polygon that had the highest intersection area was used for the accuracy assessment.

Moreover, the quality rate (QR) index was applied to consider the geometrical similarity [70]:

$$QR = \frac{1}{n}\sum_{i=1}^{n}\left(1 - \frac{\text{area}\,(r_i \cap s_i)}{\text{area}\,(r_i \cup s_i)}\right), \tag{8}$$

where r_i is the reference RTC and s_i is the best corresponding AITC. If the intersection area between a reference polygon r_i and its candidate s_i equals the union area, the AITC segment coincides entirely [71]. The QR ranges from [0, 1]. The lower value indicates the better geometrical similarity of the AITC segment to the reference crown. Furthermore, we tested the QR's obtained accuracy values with a Kruskal–Wallis test followed by nonparametric post hoc comparisons after Siegel and Castellan [72] to detect significant accuracy variances among selected delineation methods and decimated datasets. The statistical testing was performed in R [73].

2.5.4. Feature Extraction

In addition, to the standard geometrical accuracy assessment of segmentation methods described in the Section 2.5.3, the extracted spectral and elevation features using AITC segments of DAL, MCWS, and LI were statistically compared to the extracted statistics of RTC (treatments versus control). The feature extraction was performed only for the most accurate las02 and the most inaccurate las1. Moreover, we added for comparison a simple buffer (BUFFER) method designed by authors that created buffer zones around the respective treetops. To consider the effect of different tree sizes, we applied circular buffers covering 3.14 m^2 (1 m perimeter) or 12.56 m^2 (2 m perimeter) for small and large trees, respectively. The buffer's size was set according to the descriptive statistics for the height threshold of 27 m used in LI to distinguish between small and large trees. For all selected features, we applied a Kruskal–Wallis test followed by treatment (DAL, MCWS, LI, and BUFFER) versus control (RTC) multiple comparisons test of extracted statistics to investigate the effect of different segmentation methods and PPC decimation to the purity of crown delineation and the presence of mixels [72].

According to previous studies, spectral features were represented by selected VIs, which have been shown to be sensitive to changes in the spectral response of the infested trees in the earlier stages (Table 6). We extracted mean values of spectral features per tree (AITC polygon) for the statistical analysis due to the applied individual tree-based approach. Moreover, we investigated the correlations between the indices and the number of pixels forming the crown. We found no significant correlations. Therefore, the simple mean was used regardless of the crown size. The spectral features were extracted from the index maps calculated from the original orthomosaic.

Table 6. Vegetation indices used in this study. The band names correspond with Table 1.

Vegetation Index	Equation	Ref.
Normalized Difference Vegetation Index (NDVI)	$\mathrm{NDVI} = \frac{\mathrm{NIR} - \mathrm{Red}}{\mathrm{NIR}+\mathrm{Red}}$	[74]
Normalized Difference Red-Edge index (NDRE)	$\mathrm{NDRE} = \frac{\mathrm{NIR} - \mathrm{Red\ edge}}{\mathrm{NIR}+\mathrm{Red\ edge}}$	[75]
Enhanced Normalized Difference Vegetation Index (ENDVI)	$\mathrm{ENDVI} = \frac{((\mathrm{NIR}+\mathrm{Green})-(2\times\mathrm{Blue}))}{((\mathrm{NIR}+\mathrm{Green})+(2\times\mathrm{Blue}))}$	[76]

Four elevation metrics (Table 7) were extracted to explore the additive value of 3D information for tree species recognition because preliminary results showed a similar spectral response of infested spruce trees and pines. Therefore, the differences between pines and spruces, regardless of the disturbance class, were investigated.

Table 7. Elevation features extracted from the high-density photogrammetric PPC or CHM used in this study.

Feature	Description
crownarea	crown area of each delineated tree in sq. m
zq25	25th percentile of height distribution within each delineated tree
median	50th percentile of height distribution within each delineated tree
zq75	75th percentile of height distribution within each delineated tree

We selected the metrics from Sothe et al. [41] which reflect the different crown shapes of spruce trees and pines. Pines have larger and flat spreading crowns compared to pyramidal spruce crowns. As in the case of spectral features, the mean elevation metrics were calculated per tree polygon. The elevation metrics were calculated within *tree_hulls* function (DAL, MCWS, and LI) or extracted from appropriate CHM (RTC and BUFFER). The crown area was calculated from the polygon's geometry for RTC and BUFFER.

Before treatment versus control multiple comparisons, we tested the difference in the spectral features among the disturbance classes within the RTC to investigate the ability of selected features

to detect the infested trees in the mixed forest. We used a Kruskal–Wallis test with the following nonparametric post hoc comparison after Siegel and Castellan [72]. To test the differences in elevation metrics between two tree species, we applied a Mann–Whitney U test, with the *p*-value estimated by normal approximation with continuity correction. Statistical testing was performed in R.

3. Results

3.1. Vegetation Masks

The effect of vegetation mask application before the LI segmentation technique to the PPC is illustrated in Figure 3. The mask's application resulted in a perfect reduction in deciduous tree crown segments and the better delineation of the disturbed trees.

The effect of vegetation mask applications before the MCWS and DAL treetop's detection to the PPC is illustrated in Figure 3b,c. When no mask was applied, it resulted in many false-positive treetop identifications because all trees of distinct species (larches and deciduous trees) were included in the *lmf* searching algorithm. Moreover, the larger the decimation grid that was applied, the more false-positive treetops were detected regardless of the variable size window function. The reason for this was that deciduous trees and larches had been shed due to the time of imaging. This resulted in multiple false-positive treetop detections in the crowns because the larger decimation grid formed the false local maxima from their main branches. These local maxima were more likely to be detected within the less dense PPC by the *lmf* algorithm.

Nevertheless, these false-positive treetops were strongly reduced by applied masks to the PPC. The ExG threshold mask separated the conifers from the ground, grass, deciduous trees, and partial shadows. The main proportion of the points was removed using the ExG mask. The additional NIR mask completely reduced the shadowed pixels. All the reduced points represented false positive multiple treetops of deciduous trees and larches.

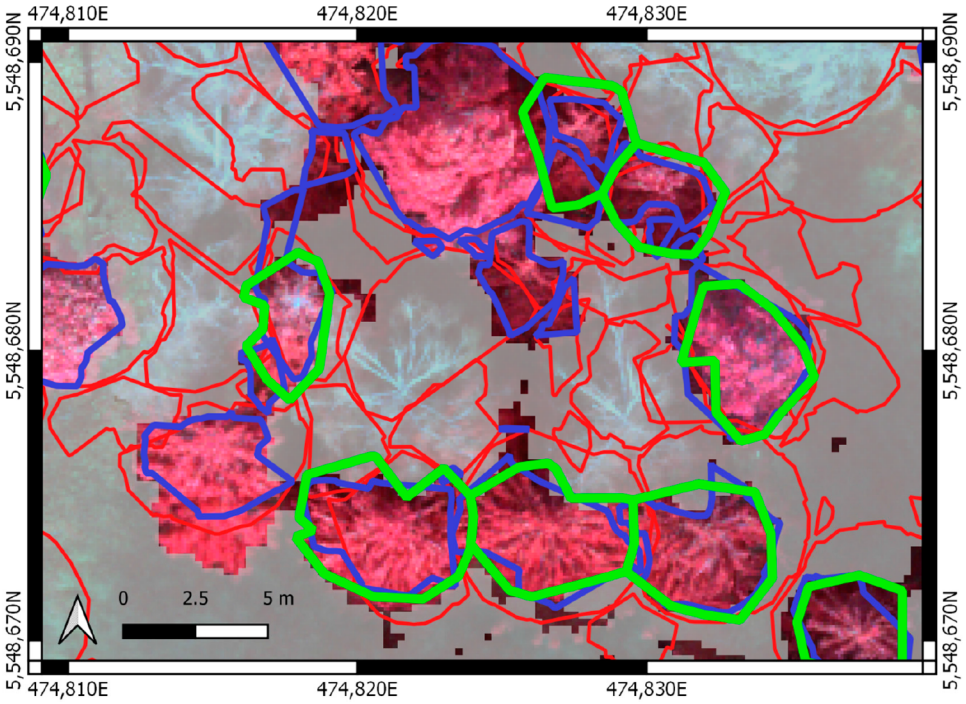

(**a**)

Figure 3. *Cont.*

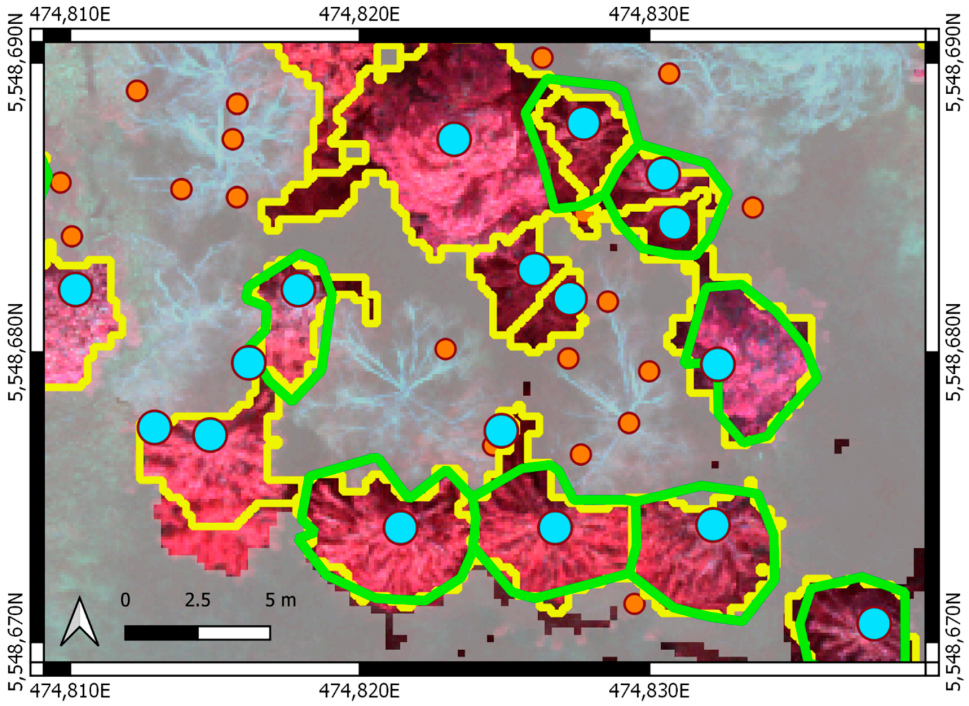

(**b**)

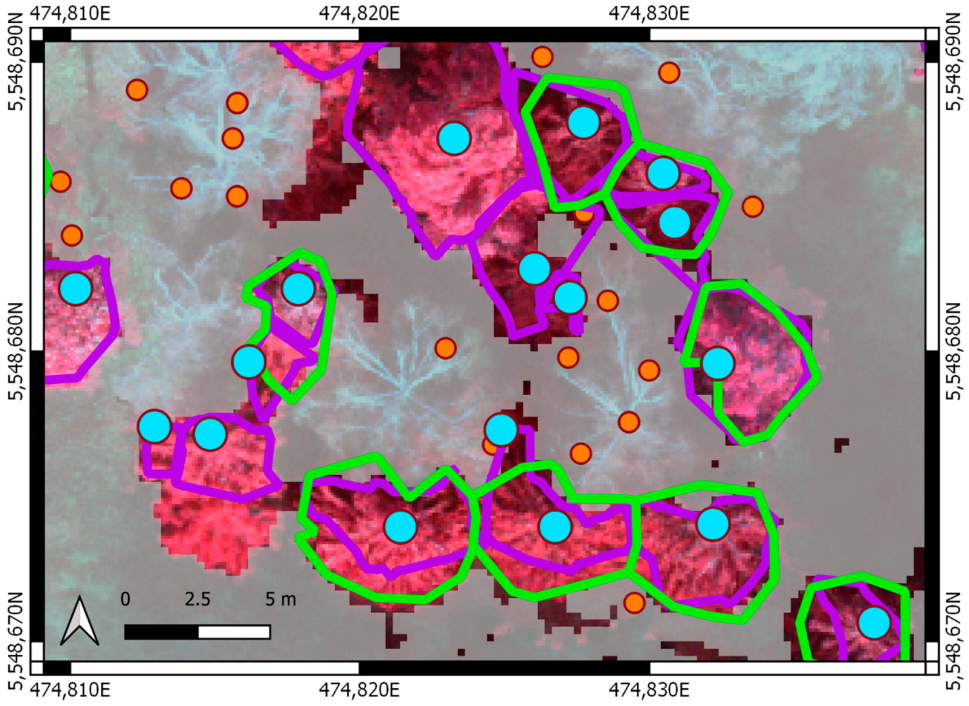

(**c**)

Figure 3. The results of vegetation masks application before the ITCD in the detail: (**a**) The LI segmentation method applied to point cloud directly. Segmented crowns using the ExG mask are highlighted in blue. Segmented crowns using no mask are highlighted in red. Reference crowns are highlighted in green; (**b**) The MCWS segmentation method using seed points. The seed points are segmented in light blue. The identified treetops from PPC with no mask are highlighted in orange. Segmented crowns are highlighted in yellow. Reference crowns are highlighted in green; (**c**) The DAL segmentation method using seed points. The seed used points masked by combi mask in light blue. The identified treetops from PPC with no mask are highlighted in orange. Segmented crowns are highlighted in purple. Reference crowns are highlighted in green.

3.2. Automatic Treetops Detection Accuracy

The resulting accuracies of treetop detections are presented in Table 8. The lowest accuracy was obtained using the original PPC with the extreme point density of 701 points/m^2 regardless of the applied variable window size function. The accuracy was decreased due to many FN treetop identifications formed by multiple seed points. Therefore, the PPC with original point density was not use for further analysis. However, the detection accuracy was enormously improved using the decimated PPCs.

Table 8. The accuracy of treetop detections using a local maxima filter algorithm applied to tested PPCs with the different point density. The number of reference treetops is 145.

Dataset	Mask	Point Density (points/m^2)	Auto Treetops	TP	FP	FN	r	*p*	F-Score
lasmtopsf1	combi	701	263	137	126	8	0.94	0.52	0.67
lasmtopsf2	combi	701	226	129	126	25	0.83	0.49	0.61
las01mtopsf1 †	combi	85	142	137	5	8	0.94	0.96	0.95 *
las01mtopsf2	combi	85	121	120	1	25	0.83	0.99	0.90
las02mtopsf1 †	combi	22	143	138	5	7	0.95	0.97	0.96 *
las02mtopsf2	combi	22	123	122	1	23	0.84	0.99	0.91
las03mtopsf1 †	combi	10	148	140	8	5	0.97	0.95	0.96 *
las03mtopsf2	combi	10	124	123	1	22	0.85	0.99	0.91
las05mtopsf1 †	combi	4	156	140	16	5	0.90	0.90	0.93
las05mtopsf2	combi	4	125	124	1	21	0.86	0.99	0.92
las1mtopsf1	combi	1	200	143	57	2	0.99	0.72	0.83
las1mtopsf2 †	combi	1	133	129	4	16	0.89	0.97	0.93

* The three most accurate seed points datasets. † The seed points datasets used for further ITCD.

These results have shown that the density of the PPC affects the accuracy of treetops detection. The larger decimation grid was applied, the more FP and the fewer FN treetops were detected regardless of the variable size window function. These trends were caused by keeping the highest point in each decimation cell and the principle of the implemented *lmf* algorithm. The larger crown's FP treetops were formed because the more extensive decimation grid selected more than one highest point within the crown. These more isolated points were more likely to have been selected as the false local maxima because there were no higher points in the search radius of the *lmf* algorithm after the combi mask application.

The moving window size function also affected the accuracy of treetops detection. The application of larger moving windows (function f2) resulted in fewer FP but more FN detections than function f1, because the reference crown area data are positively skewed. Therefore, the smaller trees were not detected by the variable moving window fitted to median crown size. These two features had a common effect on the treetop detection accuracy. The larger decimation grid increased FP detections, while the larger moving window increased FN detections.

The three most accurate datasets had a dense cloud with a point density from 10 to 85 points/m^2 and a search window size function corresponding to the minimum diameter of the reference tree crowns. However, the accuracy between these three dense PPCs showed only minor variance. The more dense or sparse PPC affects the accuracy of treetop detections negatively. Therefore, the density from 10 points/m^2 to 85 points/m^2 can be considered sufficient for treetop detections using the *lmf* algorithm.

3.3. Automatic Individual Tree Crown Delineation Accuracy

The resulting accuracies of automatic ITCD methods are presented in Table 9. The accuracy of all methods showed a minor variance between methods within one PPC, confirmed by subsequent statistical testing. Statistical tests revealed insignificant differences among delineation methods in the densest PPCs las01 and las02. In the case of more decimated PPCs, the accuracies varied significantly.

The results of statistical testing were expressed by accuracy ranking within each dataset in Table 9. Tied ranks expressed insignificant differences. Higher overall accuracy was obtained by applying traditional MCWS, followed by the LI method regardless of the PPC density. The accuracy of the DAL method was slightly lower compared to MCWS and, sometimes, LI.

Table 9. The accuracy of automatic ITCD applied to tested PPCs with the different point density.

Dataset	Mask	Method	Seed Points	OS	TP	US	FP	DA	QR	Rank
las01	ExG	MCWS	las01mtopsf1	5	119	18	1	0.82	0.40	1–3
		LI	N/A	10	117	13	4	0.81	0.42	1–3
		DAL	las01mtopsf1	9	110	19	4	0.76	0.43	1–3
las02 †	ExG	MCWS	las02mtopsf1	6	120	16	2	0.83	0.40	1–3
		LI	N/A	9	117	14	4	0.81	0.42	1–3
		DAL	las02mtopsf1	12	114	16	2	0.79	0.43	1–3
		BUFFER	las02mtopsf1	100	37	2	0	0.27	0.65	4
las03	ExG	MCWS	las03mtopsf1	5	117	18	2	0.81	0.40	1–2
		LI	N/A	11	117	11	5	0.81	0.43	1–2
		DAL	las03mtopsf1	12	111	15	4	0.77	0.44	3
las05	ExG	MCWS	las05mtopsf1	7	119	17	0	0.82	0.40	1
		LI	N/A	20	109	7	8	0.75	0.45	2–3
		DAL	las05mtopsf1	23	106	11	2	0.73	0.47	2–3
las1 *,†	ExG	MCWS	las1mtopsf2	2	100	39	3	0.69	0.47	1
		LI	N/A	67	65	3	7	0.45	0.57	2
		DAL	las1mtopsf2	57	53	15	14	0.37	0.62	3
		BUFFER	las1mtopsf02	94	34	2	4	0.23	0.65	4

OS: oversegmentation; TP: true positive; US: undersegmentation; FP: False positive; DA: detection accuracy score; QR: quality rate index. * The dataset with a significant decrease in segmentation accuracy of each applied method. † The selected datasets used for feature extraction and comparison. The BUFFER method was applied only to the selected las02 and las1 dataset for feature extraction comparison with the other automatic delineation methods.

Moreover, the statistical testing revealed insignificant differences in each method's accuracy among decimated datasets, except for the las1 datasets with the point density 1 point/m^2, because the low point density reduced detailed crown shapes in a dense forest. It resulted in significantly less accurate oversegmentation (DAL and LI) or undersegmentation (MCWS) of the automatically delineated crowns.

The oversegmentation or undersegmentation is caused by the low point density and the type of the algorithm. In the case of DAL and LI oversegmentation, the region-growing algorithm selected only a few topmost points around the treetop that met the height conditions. The MCWS algorithm also included points of the neighboring crowns because the height gradient magnitudes between the crowns were reduced due to the low point density. That resulted in undersegmentation. The same effect of starting oversegmentation was also detectable in another sparse las05 PPC (4 points/m^2) using DAL and LI methods, but the accuracy decrease was not significant within this dataset.

It appears that the main effect of automatic ITCD accuracy is the density of the PPC because the significant decrease in accuracy was obtained using the most decimated PPC (1 point/m^2). A point density greater than 10 points/m^2 can be considered sufficient with the margin of our results. If the point density is sufficient, the selection of the segmentation method is a minor issue. Every recent ITCD method based on point cloud or CHM segmentation can be used. However, the MCWS was the most accurate method, even in the case of too little point density.

Because statistical tests revealed significantly lower accuracy of all delineation methods using the most decimated las1 dataset compared with other datasets, we decided to compare extracted feature statistics of the reference dataset only with extracted statistics of las02 and las1.

3.4. Feature Extraction

The statistical testing revealed significant differences among disturbance classes within the reference dataset (Table 10). Therefore, the distinguishing of disturbance classes and bark beetle disturbance detection is possible. Multiple comparisons using spectral features exposed problematic distinguishing between pines and seriously infested trees (sbbd) using NDVI and ENDVI indices, consistent with the preliminary results. However, these two classes were well separated, employing the NDRE index. Another problematic distinction was revealed between noninfested trees (sh) and the trees under the green attack using NDRE, but significant differences between classes were detected applying NDVI and ENDVI indices. This makes the NDRE index less suitable for detection of infested spruce trees.

Table 10. The multiple comparisons test between information (disturbance) classes within the reference dataset (RTC). True (T) or False (F) marks statistically significant/insignificant differences between pairs.

Feature	Multiple Comparisons *	Ref. Crowns
NDRE	pine-sbbd	T
	pine-sbbg	T
	pine-sh	T
	sbbd-sbbg	T
	sbbd-sh	T
	sbbg-sh	F
NDVI	pine-sbbd	F
	pine-sbbg	T
	pine-sh	T
	sbbd-sbbg	T
	sbbd-sh	T
	sbbg-sh	T
ENDVI	pine-sbbd	F
	pine-sbbg	T
	pine-sh	T
	sbbd-sbbg	T
	sbbd-sh	T
	sbbg-sh	T
crown area	pine-spruce	T
zq25	pine-spruce	T
median	pine-spruce	T
zq75	pine-spruce	T
Number of FALSE		3+0

* We used Mann–Whitney U test to test the elevation features differences of two tree species.

The excellent separability of pines was reached using elevation features and the Mann–Whitney U test. That is consistent with the study's hypotheses documenting the supporting role of elevation features for tree species separation. However, the crown area's application could be limiting for tree species separation if the crown area of these species were equal. This makes the feature less applicable. On the other hand, the quartile features are universally applicable because the different crown shapes of these tree species are more likely to remain stable regardless of crown size.

The Kruskal–Wallis test revealed some significant differences among extracted feature statistics of RTC and automatically delineated crowns of las02 and las1 within disturbance classes (Figure 4). The statistical testing results were similar, although the delineated crowns of las1 showed a higher variance of extracted statistics within the group and also between groups. These variations are visible mainly for spectral features that are key to separate disturbance classes of spruce trees (Figure 4b,d,f). They are caused by less accurate ITCD of las1 and they increase the uncertainty of disturbance classes separation.

Figure 4 also illustrates the result presented in Table 10. If the RTC classes' boxplots highly overlap (NDVI and ENDVI boxplots of pine-sbbd NDRE boxplots of sbbg and sh), there is no significant difference. Moreover, the NDRE and crown area features are less resistant to inaccurate ITCD than NDVI, ENDVI and quartile elevation features resulting in higher variance. This lack of robustness may potentially limit these features for bark beetle disturbance detection. These findings are consistent with the results of statistical testing presented in Table 10. All disturbance classes were separable using at least one of the selected spectral or elevation features. However, no VI was able to distinguish between all disturbance classes by itself. The NDVI and ENDVI indices were able to separate all stages of bark beetle attack which makes them more appropriate for bark beetle disturbance detection. However, these indices are not able to separate pines from spruces. Nevertheless, the application of elevation features alone is barely relevant for bark beetle infestation detection. Therefore, we recommend the mixture of spectral and elevation features. This set of features can serve as a starting point for similar studies.

The significant differences among delineation methods were revealed only within sbbd and sbbg class of spectral features. The significant variances among delineation methods were obtained within each tree species class of all elevation features. These significant differences were further investigated using post-hoc treatment (BUFFER, DAL, LI, MCWS) versus control (RTC) multiple comparisons tests of each dataset for spectral (Table 11) and elevation (Table 12) features.

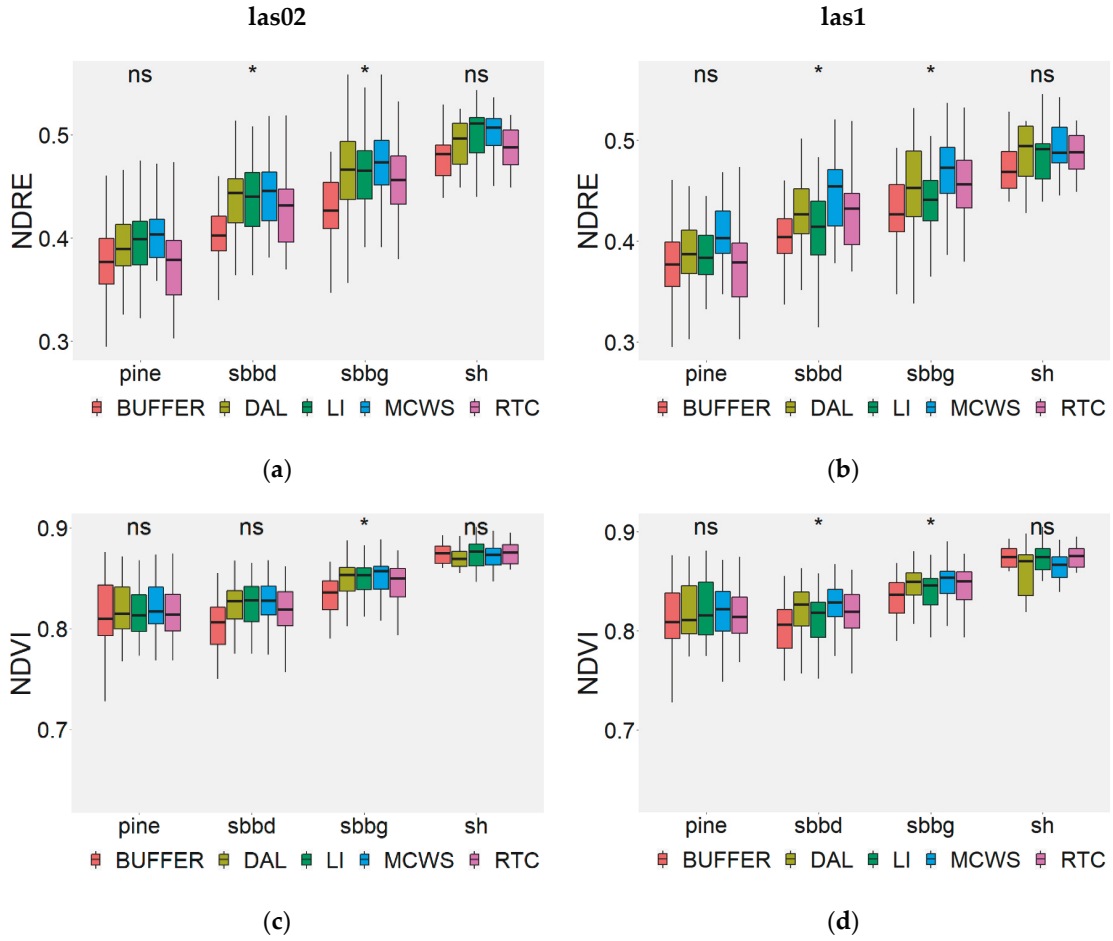

Figure 4. *Cont.*

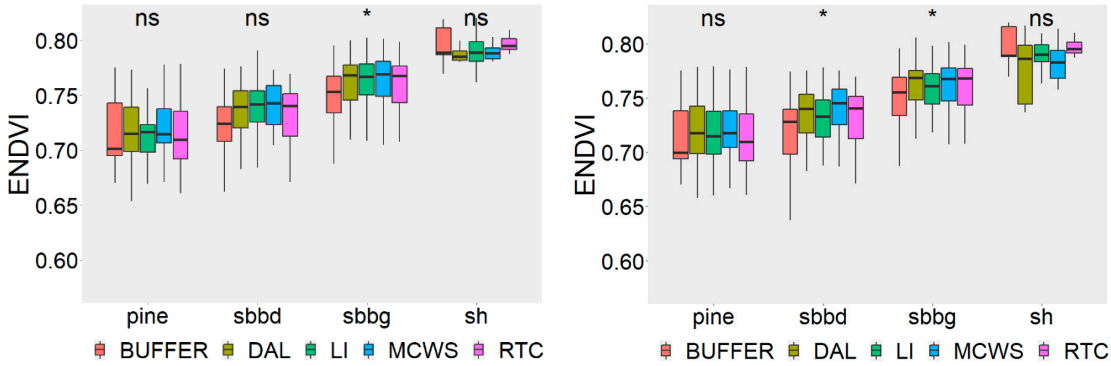

(**e**)

(**f**)

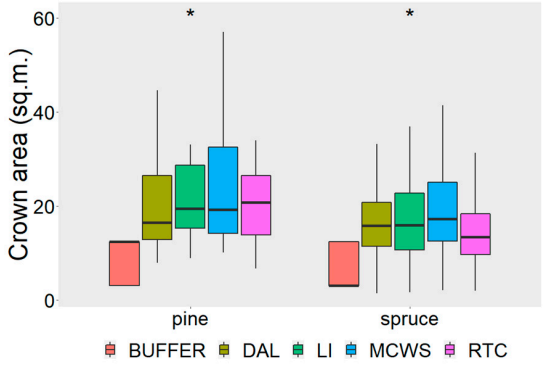

(**g**)

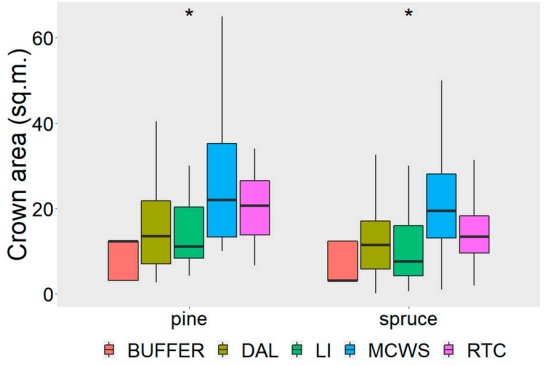

(**h**)

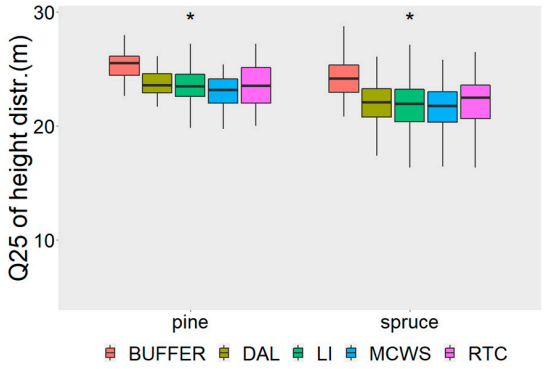

(**i**)

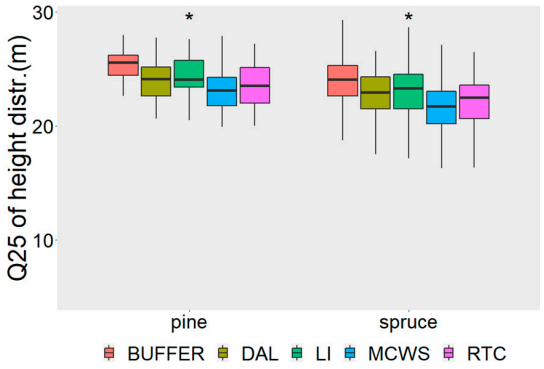

(**j**)

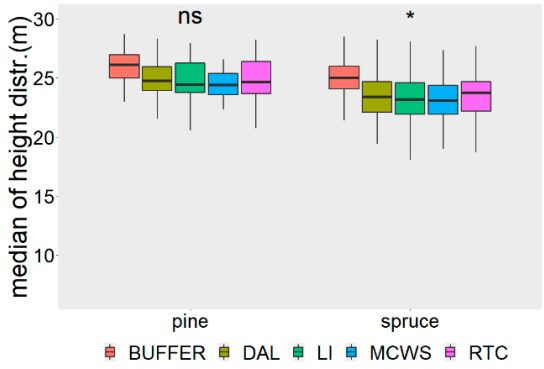

(**k**)

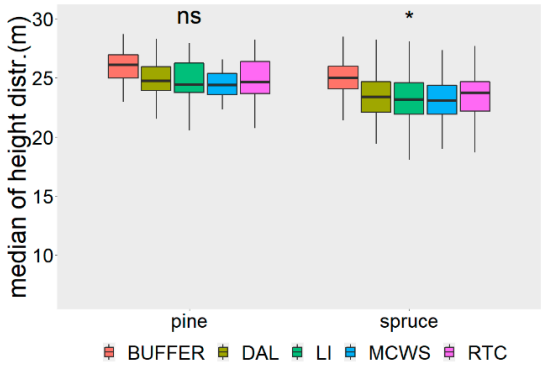

(**l**)

Figure 4. *Cont.*

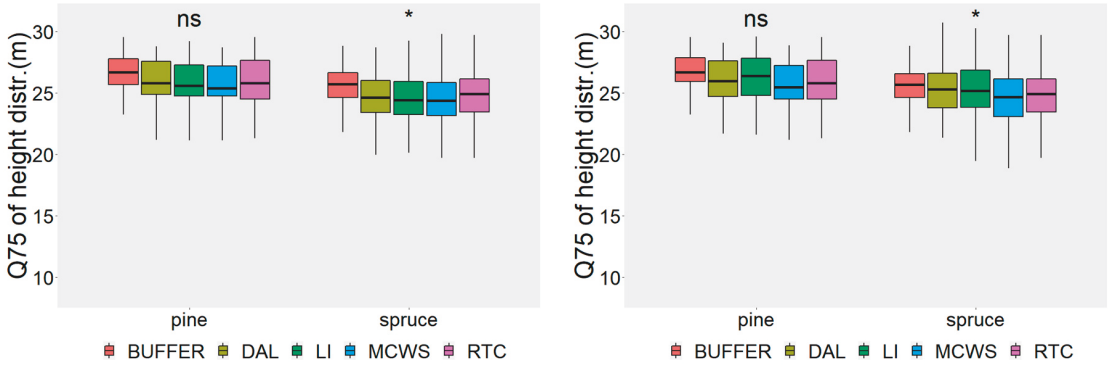

Figure 4. The distribution of extracted individual tree crown features and significant differences among RTC and automatically delineated crowns within disturbance classes of the las02 dataset (left column) and las1 dataset (right column): (**a**) NDRE boxplots of las02; (**b**) NDRE boxplots of las1; (**c**) NDVI boxplots of las02; (**d**) NDVI boxplots of las1; (**e**) ENDVI boxplots of las02; (**f**) ENDVI boxplots of las1; (**g**) Crown area boxplots of las02; (**h**) Crown area boxplots of las1; (**i**) Q25 of height distribution boxplots of las02; (**j**) Q25 of height distribution boxplots of las1; (**k**) median of height distribution boxplots of las02; (**l**) median of height distribution boxplots of las1; (**m**) Q75 of height distribution boxplots of las02; (**n**) Q75 of height distribution boxplots of las1. * marks the significant differences (the significance level $\alpha = 0.05$) among applied delineation methods within each feature's class.

Table 11. The treatment versus control multiple comparison test after the Kruskal–Wallis test of spectral features. True (T) or False (F) marks statistically significant/insignificant differences between pairs. Significant differences among las02 and las1 within treatment versus control tests caused by significantly lower segmentation accuracy of las1 are highlighted in yellow.

Class	Multiple Comparisons	NDRE		NDVI		ENDVI	
		las02	las1	las02	las1	las02	las1
sbbd	RTC-DAL	F	F	F	F	F	F
	RTC-MCWS	F	F	F	F	F	F
	RTC-LI	F	F	F	F	F	F
	RTC-BUFFER	T	T	F	F	F	F
sbbg	RTC-DAL	F	F	F	F	F	F
	RTC-MCWS	F	F	F	F	F	F
	RTC-LI	F	T	F	F	F	F
	RTC-BUFFER	T	T	T	T	T	T

The results showed that extracted features from AITC polygons of the BUFFER method significantly differed from RTC in both PPCs because the polygon buffers covered only the crowns' parts. BUFFER's extracted spectral feature statistics differed significantly from RTC within sbbd and sbbg classes (Figure 4 and Table 11).

The limited extent of buffer polygons was more significant for elevation features than spectral features, especially in more massive crowns. It resulted in a much lower crown area compared to RTC and other delineation methods (Figure 4g–h). Moreover, the BUFFER method's application resulted in higher quartile values of the tree heights because the buffer covered the topmost part of the trees. This, in fact, was more evident in the case of zq25 and median quartiles of spruce trees because no lower parts of tree crowns were present (Figure 4i–n, Table 12), increasing the quartile values.

In contrast, the automatic delineation methods based on PPC segmentation (DAL, MCWS, and LI) were more accurate than the BUFFER method. This resulted in almost no significant differences between the extracted spectral features of RTC and AITC polygons within disturbance classes, regardless of

PPC density. The results revealed only the significant differences among RTC and LI NDRE values of more decimated las1 inside the sbbg class.

Table 12. The treatment versus control multiple comparison test after the Kruskal–Wallis test of elevation features. True (T) or False (F) marks statistically significant/insignificant differences between pairs. Significant differences among las02 and las1 within treatment versus control tests caused by significantly lower segmentation accuracy of las1 are highlighted in yellow.

Class	Multiple Comparisons	Crown Area		zq25		Median		zq75	
		las02	las1	las02	las1	las02	las1	las02	las1
pine	RTC-DAL	F	F	F	F	F	F	F	F
	RTC-MCWS	F	F	F	F	F	F	F	F
	RTC-LI	F	F	F	F	F	F	F	F
	RTC-BUFFER	T	T	T	T	F	F	F	F
spruce	RTC-DAL	F	T	F	F	F	F	F	F
	RTC-MCWS	T	T	F	F	F	F	F	F
	RTC-LI	F	T	F	T	F	T	F	F
	RTC-BUFFER	T	T	T	T	T	T	T	T

Due to the lower ITCD accuracy of the las1 dataset, there were significant differences among crown areas causally related to delineation's geometrical accuracy. The MCWS method tended to slightly undersegment the crowns. The undersegmentation was more evident in las1 (Table 9), but it was also significant using las02. The undersegmentation resulted in significantly different (larger) crown areas compared to RTC (Table 12). In contrast, DAL and especially LI tended to oversegment the crowns in the case of strongly decimated las1 PPCs (see Table 9). This led to significant differences in these methods' elevation features in the case of las1 because the AITC was oversegmented (smaller) compared to RTC (Figure 4h and Table 12). However, there were almost no significant differences in extracted elevation statistics among RTC and AITC of las02 regardless of the applied delineation method.

To fully understand the effect of PPC decimation on feature extraction and consequent differences between las02 and las1 within treatment versus control tests (Tables 11 and 12, highlighted in yellow), we additionally performed a Kruskal–Wallis test between treatments (RTC, las02, and las02) of each method within each class for all features. The results were entirely in line with the changes presented in Tables 11 and 12. The changes in treatments versus control test results of las02 and las1 within the same disturbance class and feature were caused by significant differences between the tested statistics of las02 and las1. Therefore, the lower PPC density negatively and significantly affected the feature extraction in these cases. Moreover, it could be concluded that the method most sensitive to the decimation of the PPC is the LI method, because the ITCD was performed directly using a decimated PPC instead of CHM.

Based on the experimental results of this subsection, several conclusions were made. The selected spectral and elevation features are suitable for bark beetle disturbance detection documented by excellent disturbance class separability of RTC. The BUFFER method is less suitable for detecting bark beetle disturbance in the mixed forest using the individual tree-based approach because of the simplicity of crown delineation around treetop. The buffers' application led to significant differences in extracted feature statistics compared to RTC using the Kruskal–Wallis test and post hoc treatment versus control multiple comparisons tests. Therefore, these significant dissimilarities reduce the separability of disturbance classes, especially tree species, using the BUFFER method. The other methods (DAL, MCWS, and LI), which delineated the full crown based on PPC or subsequently derived CHM, led to insignificant differences of extracted feature statistics compared to RTC. However, these methods are affected by PPC density. The more decimated PPC las1 revealed significant differences in extracted feature statistics (especially elevation features) compared to RTC due to significantly lower crown delineation accuracy caused by low point density. If the PPC is sparse (less than 4 points/m^2), it results in undersegmentation (MCWS) or oversegmentation (DAL and LI) of delineated crows, which negatively

affect the feature extraction. The PPC-based delineation method (LI) is more sensitive to the cloud's point density than CHM-based methods. Therefore, we assume that the most accurate and the most robust to point density is the watershed segmentation for detecting bark beetle infestation using the individual tree-based approach. Moreover, the spectral features are more robust to the ITCD variability of applied methods and the lower PPC density because the significant differences between RTC and delineated crowns were less frequent than for elevation features. It is an advantage for bark beetle infestation detection.

4. Discussion

4.1. The Effect of Vegetation Mask

The excellent separability of targeted conifer trees from the background was obtained using simple spectral threshold masks. Traditionally, thresholding has been used for shadow detection [77,78], but it can be used for any classification problem when a clear separation is observed in bimodal distribution [79]. The idea of applying vegetation masks before the ITCD was inspired by previous studies using vegetation threshold masks for classification problems. The ExG index threshold mask was successfully applied to separate green crops from bare soil using object-based image analysis in Torres-Sanchéz et al. [55]. Otsu et al. [80] conducted per pixel classification of tree crown defoliation using nested histogram thresholding. The authors suggested to include a CHM model to automatically delineate individual tree crowns and classify only the pixels forming the crowns. This nested histogram threshold classification was improved by Cardil et al. [56], who classified pine processionary moth defoliation per pixel in automatically segmented crowns. Compared to above mentioned forestry studies that applied thresholding for per-pixel classification after ITCD or with no ITCD, we applied vegetation threshold mask to PPC before the ITCD. Therefore, only the targeted conifer tree crowns were delineated for bark beetle disturbance detection in the mixed urban forest using the individual tree-based approach. This saves computation time because only the targeted trees are delineated. Moreover, the vegetation mask application significantly increased the similarity of AITC compared to RTC, which is documented in Figure 3. Therefore, we suggest applying a proper vegetation mask to PPCs before the ITCD. To our knowledge, this approach is novel, and it has benefits for specific tree species disturbance detection because of the findings mentioned earlier.

The suitability of combined vegetation threshold masks to separate targeted conifer trees was confirmed in this study. We took advantage of imaging time when conifers were the only green vegetation on the orthomosaic to apply a "green" threshold mask using the ExG index that has accentuated the green vegetation in the remotely sensed images [81,82]. Moreover, the application of a mask before the ITCD reduced the imaging time's adverse side effects. The imaging time allowed the distinction between evergreen conifers and deciduous trees, and deciduous tree crowns resulted in multiple false-positive treetops detection in their crowns. Therefore, the separation of conifers could be problematic using this approach if the imaging is conducted when deciduous trees are not shed. In this case, the nested histogram threshold method [80] or unsupervised classification [83,84] could be tested for a conifer tree or directly spruce tree PPC masking.

4.2. The Effect of Point Density to ITCD Accuracy

The results revealed the strong effect of PPC density on treetops detection and ITCD. According to our experimental results, overly dense original photogrammetric PPC (701 points/m^2) resulted in many FP treetops using local maxima filtering. These FP treetops could cause subsequent oversegmentation, but they were reduced by applying the combi mask. We discovered that multiple seed points formed these FN treetops. Due to the extreme point density of the original photogrammetric PPC, the treetop was formed by multiple points of equal height overlapping each other selected by the local maxima filter. In contrast, the ITCD delineation accuracy of the most decimated PPC las1 (1 point/m^2) was significantly lower compared to las03, las02, and las01 (10–85 points/m^2). Although the significantly lower ITCD

accuracy of las 05 (4 points/m^2) was not confirmed, the result showed starting undersegmentation of DAL and LI methods. Therefore, it seems optimal to reduce the point density of photogrammetric PPCs to high-density ALS data because too dense or too sparse PPCs negatively affect the treetop identifications and ITCD accuracy.

These findings are novel because very little research has investigated the effect of photogrammetric PPC density on ITCD up to date, even though this effect is examined in studies using ALS and the performance of ITCD is primarily limited by the availability of high-density LiDAR data [85]. Nevertheless, our findings are consistent with the previous studies focusing on the ALS PPC density affecting ITCD accuracy. Reitberger et al. [86] and Yao et al. [87] concluded that a point density higher than 10 points/m^2 did not significantly lead to the ITCD accuracy improvement. Kandare et al. [88] discovered that the PPC density from 6 to 50 points/m^2 did not improve the ITCD accuracy, but lower values (<6 points/m^2) were significantly less accurate using the same delineation method. However, Wallace et al. [43] examined that the increase in point density from 5 to 50 points/m^2 led to a significant improvement in the omission error rate. Moreover, the recent study of Guerra-Hernández et al. [89] comparing the UAS-derived PPC (48.85 or 96.63 points/m^2) to ALS (44.33 points/m^2) concluded that they are comparable at the plot level.

The ITCD accuracy is likely to vary depending on the tree species composition in the forest. Therefore, it is hard to find the strict minimum point density for ITCD [43]. Nevertheless, the ITCD accuracy achieved in this study is superior compared to two recent comparative studies focused on ITCD in a mixed forest. Hastings et al. [61] reached the best DA accuracy score of 0.69 for conifer trees in a mixed temperate forest using the airborne LiDAR data with a density of 26.98 points/m^2. Gu et al. [44] obtained an average QR accuracy from 0.70 to 0.87 for CHM-based ITCD derived from UAS images using MCWS in a dense mixed forest during vegetation season which decreased the accuracy.

This paper showed that the point density was found to be more significant than the algorithm used. If the point density was high, the accuracy of the methods was comparable, resulting in the tied ranks (see Table 9). This finding is consistent with Wallace et al. [43], who showed that the increase of point density from 5 to 50 points/m^2 was more significant than the algorithm used for ITCD. However, this is contrary to previous findings of Kaartinen et al. [90] and Reitberger et al. [86]. This is because these studies compared only relatively sparse PPCs using 2–5points/m^2 per tree. Therefore, they are comparable only to las05 and las01 used in this study, which reveals significant accuracy differences among ITCD methods.

Concerning our experimental results and previous findings, we suggest decimating the photogrammetric PPC to the point spacing of high-dense LiDAR PPC (~20–60 points/m^2, 10 points/m^2 minimum) for ITCD of conifer trees in a mixed urban forest. An additional argument for decimation is that state-of-the-art algorithms are designed for airborne or UAS LiDAR data with a density of around 50 points/m^2 [91]. However, modern photogrammetric software allows users to control the PPC density during the processing. Therefore, further research may be directed to comparing differently dense PPCs exported from photogrammetric software to ultra-dense PPC decimation for ITCD.

4.3. The Effect Segmentation Methods to ITCD Accuracy and Feature Extraction

The results showed that the BUFFER method's application led to significantly different extracted feature statistics than RTC because the polygon buffers covered only the crowns' topmost parts, which also resulted in low ITCD accuracy. The BUFFER method was not superior in feature extraction compared to methods delineating the full crown (DAL, MCWS, and LI). This finding contrasts with the preliminary assumption that automatic ITCD methods would lead to significant differences in extracted feature statistics due to the presence of mixels. This assumption was not confirmed because ITCD techniques could delineate the crowns more precisely than we expected. The results showed the superior performance of automated ITCD methods. Moreover, the ITCD methods applied to the same PPC are comparable, revealing only minor variation in feature extraction which are consistent with Hastings et al. [61] This resulted in almost no significant differences among extracted feature statistics

of these methods and RTC. Therefore, they could substitute the time-consuming manual tree crown delineation for detecting bark beetle disturbance using an individual tree-based approach.

Concerning our experimental results, the superior ITCD accuracy was obtained using the CHM-based MCWS method when the method was applied to more decimated PPCs (las05 and las1). In the study of Hastings et al. [61] using ALS, the LI PPC segmentation method marginally outperformed the CHM-based delineation methods using a high-density PPC. Even if this seems to be in contrast with our results, it is not. We investigated that the LI method is the most sensitive to the decimation of the PPC, because the ITCD was performed directly using a decimated PPC instead of CHM. Therefore, we documented the same effect in an opposite way in this study. The LI method performs well only when applied to a high-density PPC. This finding is consistent with Wallace et al. [43]. They found that the most significant improvement of tree crown delineation after increasing the point density from 5 to 50 points/m^2 was for algorithms using PPC directly for ITCD (including LI). The other reason for this inconsistency (except for the point density) is that the photogrammetric PPC does not penetrate the crowns compared to LiDAR, and we have not assessed the understory vegetation. According to Aubry-Kientz et al. [92], PPC-based methods outperform CHM-based methods in detecting and delineating understory and suppressed crowns, but there is less of an advantage for delineation of canopy trees. Therefore, it was investigated that the point density affects the feature extraction more significantly than the algorithm used in this study (see Tables 11 and 12).

4.4. Application of Tree-Based Approach to the Detection of Forest Disturbance

A pixel-based approach is problematic at submetric imagery because the pixel size is much smaller than the mapping unit [21]. Branches and branches' shadows cause spectral variation within the tree crown, the spatial context of individual tree crowns, and the distinction between the crown area and the background disappears [22]. These issues can limit an image interpretation using a pixel-based approach for the detection of bark beetle driven forest disturbance, especially in a mixed forest because other conifer tree species (e.g., pines) may show a similar spectral response to infested trees. Our study detected the spectral similarity among disturbance classes of pines and sbbd using common NDVI and ENDVI indices and sbbg and sh using NDRE index. One way to overcome this issue is to test more vegetation indices to distinguish between disturbance classes [93–95]. Another option is state-of-the-art object-based segmentation to detect forest disturbance [80,96,97]. A more advanced approach also adds CHM to segmentation, e.g., [98]. However, this approach still does not include precise ITCD. Tree crowns are usually formed from more segments because generated segments are delineated using spectral, spatial contextual information [99], but no information about individual trees (e.g., treetop seed points) is included. Therefore, the most advanced approach entirely substituting traditional forest survey of bark beetle disturbance is an individual tree-based approach.

The ITCD using the BUFFER method can be considered as a fundamental individual tree-based approach. Our experimental results revealed significant differences in the extracted feature statistics among BUFFER crowns and RTC due to the limited and simplified crown delineation. The median index values extracted from buffers were equal to or lower than the values of reference crowns because the buffers covered only the topmost part of the tree crowns, where the index values of infested classes (sbbd and sbbg) were lower due to discoloration caused by bark beetle infestation. This is an advantage for bark beetle infestation detection, but here we considered the statistically significant differences of extracted feature statistics between RTCs and automatically delineated crowns. Nevertheless, we additionally performed a statistical test (see Appendix B) to investigate the disturbance class separability using extracted spectral feature statistics from the BUFFER crows within las02. The results showed that infested trees are not separable from pines based only on spectral features. However, they are separable from each other. This finding is consistent with Klouček et al. [40], who successfully applied ITCD using buffers to detect the bark-beetle disturbance in a spruce tree monoculture. Therefore, the BUFFER method is sufficient for bark-beetle detection in monocultures.

However, it is not appropriate for bark beetle disturbance detection in a mixed forest to the limited and simplified crown delineation.

For the separation of other tree species showing similar spectral responses, it is beneficial to employ a full crown delineation using a photogrammetric PPC and a combination of spectral and elevation features. These findings are consistent with a previous study of Kampen et al. [42], who first implemented elevation metrics extracted from a CHM to the object-based classification of spruce tree vitality status. However, the ITCD was performed manually in this study, which would be time-consuming for practical usage. Nevertheless, based on our findings, we conclude that automatic ITCD methods can constitute a substitute for the time-consuming manual tree crown delineation for individual tree-based image analysis using the methodology suggested in this study.

5. Conclusions

This study aimed to compare current ITCD methods for individual tree crown feature extractions from UAS multispectral data to distinguish between the forest disturbance classes in a mixed urban forest. The extracted spectral and elevation feature statistics from automatically delineated tree crowns were compared to feature statistics of RTC. Moreover, the effect of vegetation mask and PPC density on the ITCD accuracy was investigated.

The BUFFER method is less suitable for detecting a bark beetle disturbance in a mixed forest using the individual tree-based approach because of the simplicity of crown delineation around a treetop. This caused significant differences in extracted feature statistics compared to RTC. In contrast, the extracted feature statistics of automatically delineated crowns produced by DAL, MCWS, and LI segmentation methods insignificantly differed from RTC. The delineation accuracy of these methods and subsequent feature extraction is affected more by PPC density than the method used. The ITCD methods applied to the same PPC are comparable, revealing only minor accuracy variation in feature extraction. A PPC density less than 4 points/m2 resulted in undersegmentation (MCWS) or oversegmentation (DAL and LI) of delineated crows, which negatively affected the feature extraction. The PPC-based delineation method (LI) is more sensitive to the cloud's point density than CHM-based methods.

Based on our findings, we conclude that automatic ITCD methods may constitute a substitute for the time-consuming manual tree crown delineation method for individual tree-based bark beetle disturbance detection using the suggested methodology and high-density (>20 points/m^2, 10 points/m^2 minimum) photogrammetric PPC.

Author Contributions: Conceptualization, R.M. and J.L.; methodology, R.M.; software, R.M.; validation, R.M. and J.L.; formal analysis, R.M.; investigation, R.M., J.L. and T.L.; resources, R.M. and J.L.; data curation, R.M.; writing—original draft preparation, R.M., J.L. and T.L.; writing—review and editing, R.M., J.L. and T.L.; visualization, R.M.; supervision, J.L.; project administration, J.L. and R.M.; funding acquisition, J.L. and R.M. All authors have read and agreed to the published version of the manuscript.

Funding: This research was supported by the COST Action CA16219, project "Harmonization of UAS techniques for agricultural and natural ecosystems monitoring", by the Prague Environment grant, project MHMP 54/12/013649 "Monitoring of bark beetle spread in Prague forests", by the Charles University, project GA UK No. 824217 "Analysis of disturbance and regeneration of forest vegetation using UAV multispectral photogrammetry" and by the Czech Science Foundation project 19-05011S.

Conflicts of Interest: The authors declare no conflict of interest. The funders had no role in the design of the study; in the collection, analyses, or interpretation of data; in the writing of the manuscript, or in the decision to publish the results.

Appendix A

Parameters of automatic delineation algorithms in the structure of R command finally used in the study:

1. lastrees(*pointcloud*, dalponte2016(*chm*, *seed_point_dataset*, th_tree = 10, th_seed = 0.65, th_cr = 0.75, max_cr = 14))
2. lastrees(*pointcloud*, mcwatershed(*chm*, *seed_point_dataset*, th_tree = 10))

3. lastrees(*pointcloud*, li2012(dt1 = 1.5, dt2 = 4, R = 0, Zu = 27, hmin = 10, speed_up = 3.5))

Appendix B

Table A1. Investigation of the disturbance class separability using extracted spectral feature statistics from BUFFER crows within las02. The table shows a post-hoc multiple comparison test after Kruskal–Wallis test.

Multiple Comparisons	NDRE	NDVI	ENDVI
pine-sbbd	F	F	F
pine-sbbg	T	F	T
pine-sh	T	T	T
sbbd-sbbg	T	T	T
sbbd-sh	T	T	T
sbbg-sh	F	T	T

References

1. Raffa, K.F.; Aukema, B.; Bentz, B.J.; Carroll, A.; Erbilgin, N.; Herms, D.A.; Hicke, J.A.; Hofstetter, R.W.; Katovich, S.; Lindgren, B.S.; et al. A Literal Use of "Forest Health" Safeguards against Misuse and Misapplication. *J. For.* **2009**, *107*, 276–277. [CrossRef]
2. Millar, C.I.; Stephenson, N.L. Temperate forest health in an era of emerging megadisturbance. *Science* **2015**, *349*, 823–826. [CrossRef] [PubMed]
3. Seidl, R.; Thom, D.; Kautz, M.; Martin-Benito, D.; Peltoniemi, M.; Vacchiano, G.; Wild, J.; Ascoli, D.; Petr, M.; Honkaniemi, J.; et al. Forest disturbances under climate change. *Nat. Clim. Chang.* **2017**, *7*, 395–402. [CrossRef] [PubMed]
4. Lindner, M.; Maroschek, M.; Netherer, S.; Kremer, A.; Barbati, A.; Garcia-Gonzalo, J.; Seidl, R.; Delzon, S.; Corona, P.; Kolström, M.; et al. Climate change impacts, adaptive capacity, and vulnerability of European forest ecosystems. *For. Ecol. Manag.* **2010**, *259*, 698–709. [CrossRef]
5. Wermelinger, B. Ecology and management of the spruce bark beetle Ips typographus—A review of recent research. *For. Ecol. Manag.* **2004**, *202*, 67–82. [CrossRef]
6. Näsi, R.; Honkavaara, E.; Blomqvist, M.; Lyytikäinen-Saarenmaa, P.; Hakala, T.; Viljanen, N.; Kantola, T.; Holopainen, M. Remote sensing of bark beetle damage in urban forests at individual tree level using a novel hyperspectral camera from UAV and aircraft. *Urban For. Urban Green.* **2018**, *30*, 72–83. [CrossRef]
7. Alvey, A.A. Promoting and preserving biodiversity in the urban forest. *Urban For. Urban Green.* **2006**, *5*, 195–201. [CrossRef]
8. Tubby, K.V.; Webber, J.F. Pests and diseases threatening urban trees under a changing climate. *Forestry* **2010**, *83*, 451–459. [CrossRef]
9. Aukema, J.E.; Leung, B.; Kovacs, K.; Chivers, C.; Britton, K.O.; Englin, J.; Frankel, S.J.; Haight, R.G.; Holmes, T.P.; Liebhold, A.M.; et al. Economic impacts of Non-Native forest insects in the continental United States. *PLoS ONE* **2011**, *6*, e24587. [CrossRef]
10. Göthlin, E.; Schroeder, L.M.; Lindelöw, A. Attacks by Ips typographus and Pityogenes chalcographus on Windthrown Spruces (Picea abies) During the Two Years Following a Storm Felling. *Scand. J. For. Res.* **2000**, *15*, 542–549. [CrossRef]
11. Lausch, A.; Heurich, M.; Gordalla, D.; Dobner, H.J.; Gwillym-Margianto, S.; Salbach, C. Forecasting potential bark beetle outbreaks based on spruce forest vitality using hyperspectral remote-sensing techniques at different scales. *For. Ecol. Manag.* **2013**, *308*, 76–89. [CrossRef]
12. Coulson, R.N.; Amman, G.D.; Dahlsten, D.L.; DeMars Jr, C.J.; Stephen, F.M. *Forest-Bark Beetle Interactions: Bark Beetle Population Dynamics. Integrated Pest Management in Pine-Bark Beetle Ecosystems*; John Wiley & Sons: New York, NY, USA, 1985.
13. Sprintsin, M. Combining land surface temperature and shortwave infrared reflectance for early detection of mountain pine beetle infestations in western Canada. *J. Appl. Remote Sens.* **2011**, *5*, 053566. [CrossRef]

14. Niemann, K.O.; Visintini, F. *Assessment of Potential for Remote Sensing Detection of Bark Beetle-Infested Areas during Green Attack*; Natural Resources Canada, Canadian Forest Service, Pacific Forestry Centre: Victoria, BC, Canada, 2005.
15. Cheng, T.; Rivard, B.; Sánchez-Azofeifa, G.A.; Feng, J.; Calvo-Polanco, M. Continuous wavelet analysis for the detection of green attack damage due to mountain pine beetle infestation. *Remote Sens. Environ.* **2010**, *114*, 899–910. [CrossRef]
16. Senf, C.; Seidl, R.; Hostert, P. Remote sensing of forest insect disturbances: Current state and future directions. *Int. J. Appl. Earth Obs. Geoinf.* **2017**, *60*, 49–60. [CrossRef] [PubMed]
17. Hall, R.J.; Castilla, G.; White, J.C.; Cooke, B.J.; Skakun, R.S. Remote sensing of forest pest damage: A review and lessons learned from a Canadian perspective. *Can. Entomol.* **2016**, *148*, S296–S356. [CrossRef]
18. Fassnacht, F.E.; Latifi, H.; Ghosh, A.; Joshi, P.K.; Koch, B. Assessing the potential of hyperspectral imagery to map bark beetle-induced tree mortality. *Remote Sens. Environ.* **2014**, *140*, 533–548. [CrossRef]
19. Foster, A.C.; Walter, J.A.; Shugart, H.H.; Sibold, J.; Negron, J. Spectral evidence of early-stage spruce beetle infestation in Engelmann spruce. *For. Ecol. Manag.* **2017**, *384*, 347–357. [CrossRef]
20. Bater, C.W.; Wulder, M.A.; White, J.C.; Coops, N.C. Integration of LIDAR and Digital Aerial Imagery for Detailed Estimates of Lodgepole Pine (Pinus contorta) Volume Killed by Mountain Pine Beetle (Dendroctonus ponderosae). *J. For.* **2010**, *108*, 111–119.
21. Wulder, M.A.; White, J.C.; Ortlepp, S.M.; Mora, B.; Coggins, S.; Coops, N.C.; Heath, J. Digital high spatial resolution aerial imagery to support forest health monitoring: The mountain pine beetle context. *J. Appl. Remote Sens.* **2012**, *6*, 062527. [CrossRef]
22. Ke, Y.; Quackenbush, L.J. A review of methods for automatic individual tree-crown detection and delineation from passive remote sensing. *Int. J. Remote Sens.* **2011**, *32*, 4725–4747. [CrossRef]
23. Gougeon, F.A. Comparison of possible multispectral classification schemes for tree crowns individually delineatedon high spatial resolution meis images. *Can. J. Remote Sens.* **1995**, *21*, 1–9. [CrossRef]
24. Culvenor, D.S. TIDA: An algorithm for the delineation of tree crowns in high spatial resolution remotely sensed imagery. *Comput. Geosci.* **2002**, *28*, 33–44. [CrossRef]
25. Wang, L.; Gong, P.; Biging, G.S. Individual Tree-Crown Delineation and Treetop Detection in High-Spatial-Resolution Aerial Imagery. *Photogramm. Eng. Remote Sens.* **2004**, *70*, 351–357. [CrossRef]
26. Næsset, E. Airborne laser scanning as a method in operational forest inventory: Status of accuracy assessments accomplished in Scandinavia. *Scand. J. For. Res.* **2007**, *22*, 433–442. [CrossRef]
27. White, J.C.; Coops, N.C.; Wulder, M.A.; Vastaranta, M.; Hilker, T.; Tompalski, P. Remote Sensing Technologies for Enhancing Forest Inventories: A Review. *Can. J. Remote Sens.* **2016**, *42*, 619–641. [CrossRef]
28. Koch, B.; Heyder, U.; Welnacker, H. Detection of individual tree crowns in airborne lidar data. *Photogramm. Eng. Remote Sens.* **2006**, *72*, 357–363. [CrossRef]
29. Meddens, A.J.H.; Hicke, J.A.; Vierling, L.A. Evaluating the potential of multispectral imagery to map multiple stages of tree mortality. *Remote Sens. Environ.* **2011**, *115*, 1632–1642. [CrossRef]
30. Windrim, L.; Carnegie, A.J.; Webster, M.; Bryson, M. Tree Detection and Health Monitoring in Multispectral Aerial Imagery and Photogrammetric Pointclouds Using Machine Learning. *IEEE J. Sel. Top. Appl. Earth Obs. Remote Sens.* **2020**, *13*, 2554–2572. [CrossRef]
31. Lisein, J.; Pierrot-Deseilligny, M.; Bonnet, S.; Lejeune, P. A photogrammetric workflow for the creation of a forest canopy height model from small unmanned aerial system imagery. *Forests* **2013**, *4*, 922–944. [CrossRef]
32. Puliti, S.; Ørka, H.O.; Gobakken, T.; Næsset, E. Inventory of small forest areas using an unmanned aerial system. *Remote Sens.* **2015**, *7*, 9632–9654. [CrossRef]
33. Fernández-álvarez, M.; Armesto, J.; Picos, J. LiDAR-based wildfire prevention in WUI: The automatic detection, measurement and evaluation of forest fuels. *Forests* **2019**, *10*, 148. [CrossRef]
34. Guimarães, N.; Pádua, L.; Marques, P.; Silva, N.; Peres, E.; Sousa, J.J. Forestry Remote Sensing from Unmanned Aerial Vehicles: A Review Focusing on the Data, Processing and Potentialities. *Remote Sens.* **2020**, *12*, 1046. [CrossRef]
35. Wallace, L.; Lucieer, A.; Malenovský, Z.; Turner, D.; Vopěnka, P. Assessment of Forest Structure Using Two UAV Techniques: A Comparison of Airborne Laser Scanning and Structure from Motion (SfM) Point Clouds. *Forests* **2016**, *7*, 62. [CrossRef]

36. Guerra-Hernández, J.; González-Ferreiro, E.; Monleón, V.J.; Faias, S.P.; Tomé, M.; Díaz-Varela, R.A. Use of multi-temporal UAV-derived imagery for estimating individual tree growth in Pinus pinea stands. *Forests* **2017**, *8*, 300. [CrossRef]
37. Panagiotidis, D.; Abdollahnejad, A.; Surový, P.; Chiteculo, V. Determining tree height and crown diameter from high-resolution UAV imagery. *Int. J. Remote Sens.* **2017**, *38*, 2392–2410. [CrossRef]
38. Hussain, M.; Chen, D.; Cheng, A.; Wei, H.; Stanley, D. Change detection from remotely sensed images: From pixel-based to object-based approaches. *ISPRS J. Photogramm. Remote Sens.* **2013**, *80*, 91–106. [CrossRef]
39. Näsi, R.; Honkavaara, E.; Lyytikäinen-Saarenmaa, P.; Blomqvist, M.; Litkey, P.; Hakala, T.; Viljanen, N.; Kantola, T.; Tanhuanpää, T.; Holopainen, M. Using UAV-based photogrammetry and hyperspectral imaging for mapping bark beetle damage at tree-level. *Remote Sens.* **2015**, *7*, 15467–15493. [CrossRef]
40. Klouček, T.; Komárek, J.; Surový, P.; Hrach, K.; Janata, P.; Vašíček, B. The Use of UAV Mounted Sensors for Precise Detection of Bark Beetle Infestation. *Remote Sens.* **2019**, *11*, 1561. [CrossRef]
41. Sothe, C.; Dalponte, M.; de Almeida, C.M.; Schimalski, M.B.; Lima, C.L.; Liesenberg, V.; Miyoshi, G.T.; Tommaselli, A.M.G. Tree species classification in a highly diverse subtropical forest integrating UAV-based photogrammetric point cloud and hyperspectral data. *Remote Sens.* **2019**, *11*, 1338. [CrossRef]
42. Kampen, M.; Vienna, L.S.; Immitzer, M.; Vienna, L.S. UAV-Based Multispectral Data for Tree Species Classification and Tree Vitality Analysis. In Proceedings of the Dreiländertagung OVG—DGPF—SGPF, Wien, Austria, 28 August 2018–22 February 2019; pp. 623–639.
43. Wallace, L.; Lucieer, A.; Watson, C.S. Evaluating tree detection and segmentation routines on very high resolution UAV LiDAR ata. *IEEE Trans. Geosci. Remote Sens.* **2014**, *52*, 7619–7628. [CrossRef]
44. Gu, J.; Grybas, H.; Congalton, R.G. A Comparison of Forest Tree Crown Delineation from Unmanned Aerial Imagery Using Canopy Height Models vs. Spectral Lightness. *Forests* **2020**, *11*, 605. [CrossRef]
45. MHMP. Klanovice Forest. In *Prague Environment Yearbook Online*; MHMP: Prague, Czech Republic. Available online: http://www.praha-priroda.cz/lesy/klanovicky-les/ (accessed on 15 September 2020).
46. Hujslova, J.; Simandl, P. Windstorm Herwart in Czechia. *Meteorol. Bull.* **2018**, *71*, 61–63.
47. Berec, L.; Doležal, P.; Hais, M. Population dynamics of Ips typographus in the Bohemian Forest (Czech Republic): Validation of the phenology model PHENIPS and impacts of climate change. *For. Ecol. Manag.* **2013**, *292*, 1–9. [CrossRef]
48. Hlásny, T.; Krokene, P.; Liebhold, A.; Montagné-Huck, C.; Müller, J.; Qin, H.; Raffa, K.; Schelhaas, M.; Seidl, R.; Svoboda, M.; et al. *Living with Bark Beetles: Impacts, Outlook and Management Options*; European Forest Institute: Joensuu, Finland, 2019.
49. Toffin, E.; Gabriel, E.; Louis, M.; Deneubourg, J.L.; Grégoire, J.C. Colonization of weakened trees by mass-attacking bark beetles: No penalty for pioneers, scattered initial distributions and final regular patterns. *R. Soc. Open Sci.* **2018**, *5*, 170454. [CrossRef] [PubMed]
50. Agisoft LLC. MicaSense RedEdge MX Processing Workflow (including Reflectance Calibration) in Agisoft Metashape Professional. Available online: https://agisoft.freshdesk.com/support/solutions/articles/31000148780-micasense-rededge-mx-processing-workflow-including-reflectance-calibration-in-agisoft-metashape-pro (accessed on 5 September 2020).
51. Christiansen, E.; Franceshi, V.R.; Nagy, N.E.; Krekling, T.; Berryman, A.A.; Krokene, P.; Solheim, H. *Traumatic Resin Duct Formation in Norway Spruce (Picea abies (L.) Karst.) after Wounding or Infection with a Bark Beetle-Associated Blue-Stain Fungus, Ceratocystis Polonica Siem*; Colloq. l'INRA: Paris, France, 1999.
52. Verhoeven, G. Taking computer vision aloft - archaeological three-dimensional reconstructions from aerial photographs with photoscan. *Archaeol. Prospect.* **2011**, *18*, 67–73. [CrossRef]
53. Agisoft LLC. Agisoft Metashape. Available online: https://www.agisoft.com (accessed on 23 September 2020).
54. Roussel, J.R.; Auty, D.; Coops, N.C.; Tompalski, P.; Goodbody, T.R.H.; Meador, A.S.; Bourdon, J.F.; de Boissieu, F.; Achim, A. lidR: An R package for analysis of Airborne Laser Scanning (ALS) data. *Remote Sens. Environ.* **2020**, *251*, 112061. [CrossRef]
55. Torres-Sánchez, J.; López-Granados, F.; Peña, J.M. An automatic object-based method for optimal thresholding in UAV images: Application for vegetation detection in herbaceous crops. *Comput. Electron. Agric.* **2015**, *114*, 43–52. [CrossRef]
56. Cardil, A.; Otsu, K.; Pla, M.; Silva, C.A.; Brotons, L. Quantifying pine processionary moth defoliation in a pine-oak mixed forest using unmanned aerial systems and multispectral imagery. *PLoS ONE* **2019**, *14*, e0213027. [CrossRef]

57. Dalponte, M.; Coomes, D.A. Tree-centric mapping of forest carbon density from airborne laser scanning and hyperspectral data. *Methods Ecol. Evol.* **2016**, *7*, 1236–1245. [CrossRef]
58. Meyer, F.; Beucher, S. Morphological segmentation. *J. Vis. Commun. Image Represent.* **1990**, *1*, 21–46. [CrossRef]
59. Li, W.; Guo, Q.; Jakubowski, M.K.; Kelly, M. A New Method for Segmenting Individual Trees from the Lidar Point Cloud. *Photogramm. Eng. Remote Sens.* **2012**, *78*, 75–84. [CrossRef]
60. Xiao, W.; Zaforemska, A.; Smigaj, M.; Wang, Y.; Gaulton, R. Mean shift segmentation assessment for individual forest tree delineation from airborne lidar data. *Remote Sens.* **2019**, *11*, 1263. [CrossRef]
61. Hastings, J.H.; Ollinger, S.V.; Ouimette, A.P.; Sanders-DeMott, R.; Palace, M.W.; Ducey, M.J.; Sullivan, F.B.; Basler, D.; Orwig, D.A. Tree species traits determine the success of LiDAR-based crown mapping in a mixed temperate forest. *Remote Sens.* **2020**, *12*, 309. [CrossRef]
62. Popescu, S.C.; Wynne, R.H. Seeing the Trees in the Forest. *Photogramm. Eng. Remote Sens.* **2004**, *70*, 589–604. [CrossRef]
63. Wulder, M.; Niemann, K.O.; Goodenough, D.G. Local maximum filtering for the extraction of tree locations and basal area from high spatial resolution imagery. *Remote Sens. Environ.* **2000**, *73*, 103–114. [CrossRef]
64. Hais, M.; Wild, J.; Berec, L.; Brůna, J.; Kennedy, R.; Braaten, J.; Brož, Z. Landsat Imagery Spectral Trajectories—Important Variables for Spatially Predicting the Risks of Bark Beetle Disturbance. *Remote Sens.* **2016**, *8*, 687. [CrossRef]
65. Eysn, L.; Hollaus, M.; Lindberg, E.; Berger, F.; Monnet, J.M.; Dalponte, M.; Kobal, M.; Pellegrini, M.; Lingua, E.; Mongus, D.; et al. A benchmark of lidar-based single tree detection methods using heterogeneous forest data from the Alpine Space. *Forests* **2015**, *6*, 1721–1747. [CrossRef]
66. Khosravipour, A.; Skidmore, A.K.; Isenburg, M.; Wang, T.; Hussin, Y.A. Generating pit-free canopy height models from airborne lidar. *Photogramm. Eng. Remote Sen.* **2014**, *80*, 863–872. [CrossRef]
67. Yin, D.; Wang, L. How to assess the accuracy of the individual tree-based forest inventory derived from remotely sensed data: A review. *Int. J. Remote Sens.* **2016**, *37*, 4521–4553. [CrossRef]
68. Leckie, D.G.; Jay, C.; Gougeon, F.A.; Sturrock, R.N.; Paradine, D. Detection and assessment of trees with Phellinus weirii (laminated root rot) using high resolution multi-spectral imagery. *Int. J. Remote Sens.* **2004**, *25*, 793–818. [CrossRef]
69. Lamar, W.R.; McGraw, J.B.; Warner, T.A. Multitemporal censusing of a population of eastern hemlock (*Tsuga canadensis* L.) from remotely sensed imagery using an automated segmentation and reconciliation procedure. *Remote Sens. Environ.* **2005**, *94*, 133–143. [CrossRef]
70. Weidner, U. Contribution to the assessment of segmentation quality for remote sensing applications. *Int. Arch. Photogramm. Remote Sens. Spat. Inf. Sci.* **2008**, *37*, 479–484.
71. Chen, Y.; Ming, D.; Zhao, L.; Lv, B.; Zhou, K.; Qing, Y. Review on high spatial resolution remote sensing image segmentation evaluation. *Photogramm. Eng. Remote Sen.* **2018**, *84*, 629–646. [CrossRef]
72. Siegel, S.; Castellan, N.J.J. *Non-Parametric Statistics for the Behavioural Sciences*; McGraw-Hill: New York, NY, USA, 1988.
73. R core team. R: A Language and Environment for Statistical Computing. Available online: https://www.r-project.org/ (accessed on 21 September 2020).
74. Tucker, C.J. Red and photographic infrared linear combinations for monitoring vegetation. *Remote Sens. Environ.* **1979**, *8*, 127–150. [CrossRef]
75. Barnes, E.M.; Clarke, T.R.; Richards, S.E.; Colaizzi, P.D.; Haberland, J.; Kostrzewski, M.; Waller, P.; Choi, C.; Riley, E.; Thompson, T.; et al. Coincident detection of crop water stress, nitrogen status and canopy density using ground based multispectral data. In Proceedings of the Fifth International Conference on Precision Agriculture, Bloomington, MN, USA, 16–19 July 2000.
76. Strong, C.J.; Burnside, N.G.; Llewellyn, D. The potential of small-Unmanned Aircraft Systems for the rapid detection of threatened unimproved grassland communities using an Enhanced Normalized Difference Vegetation Index. *PLoS ONE* **2017**, *12*, e0186193. [CrossRef]
77. Chen, Y.; Wen, D.; Jing, L.; Shi, P. Shadow information recovery in urban areas from very high resolution satellite imagery. *Int. J. Remote Sens.* **2007**, *28*, 3249–3254. [CrossRef]

78. Adeline, K.R.M.; Chen, M.; Briottet, X.; Pang, S.K.; Paparoditis, N. Shadow detection in very high spatial resolution aerial images: A comparative study. *ISPRS J. Photogramm. Remote Sens.* **2013**, *80*, 21–38. [CrossRef]
79. Aasen, H.; Honkavaara, E.; Lucieer, A.; Zarco-Tejada, P.J. Quantitative remote sensing at ultra-high resolution with UAV spectroscopy: A review of sensor technology, measurement procedures, and data correctionworkflows. *Remote Sens.* **2018**, *10*, 1091. [CrossRef]
80. Otsu, K.; Pla, M.; Duane, A.; Cardil, A.; Brotons, L. Estimating the Threshold of Detection on Tree Crown Defoliation Using Vegetation Indices from UAS Multispectral Imagery. *Drones* **2019**, *3*, 80. [CrossRef]
81. Peña, J.M.; Torres-Sánchez, J.; de Castro, A.I.; Kelly, M.; López-Granados, F. Weed Mapping in Early-Season Maize Fields Using Object-Based Analysis of Unmanned Aerial Vehicle (UAV) Images. *PLoS ONE* **2013**, *8*, e77151. [CrossRef]
82. Torres-Sánchez, J.; Peña, J.M.; de Castro, A.I.; López-Granados, F. Multi-temporal mapping of the vegetation fraction in early-season wheat fields using images from UAV. *Comput. Electron. Agric.* **2014**, *103*, 104–113. [CrossRef]
83. Schäfer, E.; Heiskanen, J.; Heikinheimo, V.; Pellikka, P. Mapping tree species diversity of a tropical montane forest by unsupervised clustering of airborne imaging spectroscopy data. *Ecol. Indic.* **2016**, *64*, 49–58. [CrossRef]
84. Franklin, S.E. Pixel- and object-based multispectral classification of forest tree species from small unmanned aerial vehicles. *J. Unmanned Veh. Syst.* **2018**, *6*, 195–211. [CrossRef]
85. Lindberg, E.; Holmgren, J. Individual Tree Crown Methods for 3D Data from Remote Sensing. *Curr. For. Rep.* **2017**, *3*, 19–31. [CrossRef]
86. Reitberger, J.; Schnörr, C.; Krzystek, P.; Stilla, U. 3D segmentation of single trees exploiting full waveform LIDAR data. *ISPRS J. Photogramm. Remote Sens.* **2009**, *64*, 561–574. [CrossRef]
87. Yao, W.; Krull, J.; Krzystek, P.; Heurich, M. Sensitivity analysis of 3D individual tree detection from LiDAR point clouds of temperate forests. *Forests* **2014**, *5*, 1122–1142. [CrossRef]
88. Kandare, K.; Ørka, H.O.; Chan, J.C.W.; Dalponte, M. Effects of forest structure and airborne laser scanning point cloud density on 3D delineation of individual tree crowns. *Eur. J. Remote Sens.* **2016**, *49*, 337–359. [CrossRef]
89. Guerra-Hernández, J.; Cosenza, D.N.; Rodriguez, L.C.E.; Silva, M.; Tomé, M.; Díaz-Varela, R.A.; González-Ferreiro, E. Comparison of ALS- and UAV(SfM)-derived high-density point clouds for individual tree detection in Eucalyptus plantations. *Int. J. Remote Sens.* **2018**, *39*, 5211–5235. [CrossRef]
90. Kaartinen, H.; Hyyppä, J.; Yu, X.; Vastaranta, M.; Hyyppä, H.; Kukko, A.; Holopainen, M.; Heipke, C.; Hirschmugl, M.; Morsdorf, F.; et al. An International Comparison of Individual Tree Detection and Extraction Using Airborne Laser Scanning. *Remote Sens.* **2012**, *4*, 950–974. [CrossRef]
91. Yan, W.; Guan, H.; Cao, L.; Yu, Y.; Li, C.; Lu, J.Y. A self-adaptive mean shift tree-segmentation method using UAV LiDAR data. *Remote Sens.* **2020**, *12*, 515. [CrossRef]
92. Aubry-Kientz, M.; Dutrieux, R.; Ferraz, A.; Saatchi, S.; Hamraz, H.; Williams, J.; Coomes, D.; Piboule, A.; Vincent, G. A comparative assessment of the performance of individual tree crowns delineation algorithms from ALS data in tropical forests. *Remote Sens.* **2019**, *11*, 1086. [CrossRef]
93. Adamczyk, J.; Osberger, A. Red-edge vegetation indices for detecting and assessing disturbances in Norway spruce dominated mountain forests. *Int. J. Appl. Earth Obs. Geoinf.* **2015**, *37*, 90–99. [CrossRef]
94. Minařík, R.; Langhammer, J. Use of a multispectral uav photogrammetry for detection and tracking of forest disturbance dynamics. *ISPRS—Int. Arch. Photogramm. Remote Sens. Spat. Inf. Sci.* **2016**, *XLI-B8*, 711–718. [CrossRef]
95. Abdullah, H.; Darvishzadeh, R.; Skidmore, A.K.; Groen, T.A.; Heurich, M. European spruce bark beetle (*Ips typographus*, L.) green attack affects foliar reflectance and biochemical properties. *Int. J. Appl. Earth Obs. Geoinf.* **2018**, *64*, 199–209. [CrossRef]
96. Lehmann, J.; Nieberding, F.; Prinz, T.; Knoth, C. Analysis of Unmanned Aerial System-Based CIR Images in Forestry—A New Perspective to Monitor Pest Infestation Levels. *Forests* **2015**, *6*, 594–612. [CrossRef]
97. Brovkina, O.; Cienciala, E.; Surový, P.; Janata, P. Unmanned aerial vehicles (UAV) for assessment of qualitative classification of Norway spruce in temperate forest stands. *Geo-Spat. Inf. Sci.* **2018**, *21*, 12–20. [CrossRef]

98. Hentz, A.M.K.; Strager, M.P. Cicada damage detection based on UAV spectral and 3D data. *Silvilaser* **2017**, *10*, 95–96.
99. Blaschke, T. Object based image analysis for remote sensing. *ISPRS J. Photogramm. Remote Sens.* **2010**, *65*, 2–16. [CrossRef]

Publisher's Note: MDPI stays neutral with regard to jurisdictional claims in published maps and institutional affiliations.

© 2020 by the authors. Licensee MDPI, Basel, Switzerland. This article is an open access article distributed under the terms and conditions of the Creative Commons Attribution (CC BY) license (http://creativecommons.org/licenses/by/4.0/).

Článek V

Minařík, R., Langhammer, J., & Lendzioch, T. (2021). Detection of Bark Beetle Disturbance at Tree Level Using UAS Multispectral Imagery and Deep Learning. *Remote Sensing*, *13*(23), 4768. https://doi.org/10.3390/rs13234768

remote sensing

MDPI

Article

Detection of Bark Beetle Disturbance at Tree Level Using UAS Multispectral Imagery and Deep Learning

Robert Minařík, Jakub Langhammer * and Theodora Lendzioch

Department of Physical Geography and Geoecology, Faculty of Science, Charles University, Albertov 6, 128 43 Prague 2, Czech Republic; robert.minarik@natur.cuni.cz (R.M.); theodora.lendzioch@natur.cuni.cz (T.L.)
* Correspondence: jakub.langhammer@natur.cuni.cz; Tel.: +420-221-951-364

Abstract: This study aimed to examine the potential of convolutional neural networks (CNNs) for the detection of individual trees infested by bark beetles in a multispectral high-resolution dataset acquired by an unmanned aerial system (UAS). We compared the performance of three CNN architectures and the random forest (RF) model to classify the trees into four categories: pines, sbbd (longer infested trees when needles turn yellow), sbbg (trees under green attack) and non-infested trees (sh). The best performance was achieved by the Nez4c3b CNN (kappa 0.80) and Safaugu4c3b CNN (kappa 0.76) using only RGB bands. The main misclassifications were between sbbd and sbbg because of the similar spectral responses. Merging sbbd and sbbg into a more general class of infested trees made the selection of model type less important. All tested model types, including RF, were able to detect infested trees with an F-score of the class over 0.90. Nevertheless, the best overall metrics were achieved again by the Safaugu3c3b model (kappa 0.92) and Nez3cb model (kappa 0.87) using only RGB bands. The performance of both models is comparable, but the Nez model has a higher learning rate for this task. Based on our findings, we conclude that the Nez and Safaugu CNN models are superior to the RF models and transfer learning models for the identification of infested trees and for distinguishing between different infestation stages. Therefore, these models can be used not only for basic identification of infested trees but also for monitoring the development of bark beetle disturbance.

Keywords: bark beetle; forest disturbance detection; individual tree-based classification (ITBC); deep learning; machine learning

Citation: Minařík, R.; Langhammer, J.; Lendzioch, T. Detection of Bark Beetle Disturbance at Tree Level Using UAS Multispectral Imagery and Deep Learning. *Remote Sens.* **2021**, *13*, 4768. https://doi.org/10.3390/rs13234768

Academic Editors: Flor Alvarez Taboada and Miro Govedarica

Received: 13 October 2021
Accepted: 22 November 2021
Published: 24 November 2021

Publisher's Note: MDPI stays neutral with regard to jurisdictional claims in published maps and institutional affiliations.

Copyright: © 2021 by the authors. Licensee MDPI, Basel, Switzerland. This article is an open access article distributed under the terms and conditions of the Creative Commons Attribution (CC BY) license (http://creativecommons.org/licenses/by/4.0/).

1. Introduction

Pest insect disturbances are a natural part of the structural development process of temperate and boreal forests [1,2]. However, ongoing climate change has increased the frequency and severity of pest insect outbreaks in these biomes worldwide, including Europe [3–5]. In Central Europe, recent outbreaks of bark beetles, especially Ips typographus (Linnaeus, 1758), have contributed significantly to the doubling in canopy mortality, generating serious concerns about the effects on the environment, timber markets and human wellbeing [6–8]. Although bark beetle outbreaks have been intensifying in Central Europe for the last three decades [6], the most recent outbreaks in Czechia since 2015 exceeded the frequency and severity of outbreaks observed in the last two decades [9]. Moreover, the predictions expect the increase of bark beetle disturbances seven times more up to 2030 compared to the period 1971–1980 in Europe [6]. Therefore, the relatively fast, inexpensive and (if possible) automated methodology for the detection of single infested trees would help to reduce damage in a timely manner.

A terrestrial survey of discoloration symptoms has traditionally been used to detect Ips typographus (Linnaeus, 1758) (hereafter bark beetle) infestation on a single tree level [10,11]. However, the terrestrial method is time-consuming and therefore suitable only at

the plot scale. Nevertheless, discoloration symptoms can be detected relatively easily from a bird's-eye perspective over a large area. Consequently, conventional optical remote sensing and area-based (pixel-based) classification approaches have been used for pest insect disturbance detection at regional, national and global scales [12–17]. However, for the detection of individual infested trees and their timely sanitation, an individual tree-based classification (ITBC) approach is essential [18,19]. The area-based approach is not suitable because the mapping unit is not a single crown, but one pixel whose size reflects the spatial resolution of the data [20], often resulting in a few (spaceborne sensors) or too many pixels (airborne or drone-borne sensors) forming a crown that enters a classification. The spatial resolution of freely available satellite data from Sentinel-2 and Landsat missions (>10 m) is too coarse for the detection of single infested trees [16]. Although the ultrahigh resolution (in cm) may seem beneficial, the artificial mapping unit (the pixel) is much smaller than a crown, making the interpretation of the classified map more complicated and limiting its usage for in situ forest management decision making. Therefore, recent studies classifying bark beetle disturbance at the single tree level from ultrahigh-resolution images (airborne or drone-borne data) employed ITBC.

Previous work can be separated into a few groups according to the process of crown delineation. The basic approach is a time consuming manual delineation and labeling of the crowns followed by classification of the crowns [21–23]. These authors apply generalized linear models [21], maximum entropy [21], or random forest classifiers [21–23] to multispectral images. However, manual delineation and labeling are time-consuming and impractical for forest management. Other studies apply classic object-based classification to multispectral images [24–26]. However, this approach still does not delineate crowns but only segments based on spectral and spatial contextual information. Therefore, the most advanced approach combines automatic delineation of individual tree crowns with a subsequent classification of the crowns. Nevertheless, this approach is uncommon, and only a few studies have been published. Näsi et al. [19,27] detected individual spruce trees infested by the bark beetle in an urban forest classifying spectral features of identified treetops into three classes (healthy, infested and dead). Treetops were automatically detected as dead according to the highest brightness value. They used a support vector machine classifier, and the resulting kappa coefficient value was 0.61. Klouček et al. [28] identified individual infested, healthy and dead trees in a natural spruce monoculture combining local maxima filtering for tree identification and a maximum likelihood classifier, with a kappa coefficient of 0.78.

All of the abovementioned studies implemented statistical or machine learning algorithms. These algorithms usually require heuristic selection of appropriate transformations and hand-crafted latent variables such as vegetation indices [29] and texture metrics [30] calculated from the data prior to modeling [31,32]. Therefore, the selection of the best predictors demands user knowledge about interactions between biochemical and structural tree properties and electromagnetic signals detected by the sensor [32]. This requirement is a potential drawback for forest management applications. However, the drawback is addressed by deep learning, especially convolutional neural networks (CNNs), for image analysis [33,34]. CNNs are superior to the previous parametric and machine learning algorithms used in remote sensing, including vegetation and forest applications, because they can learn the best data transformations (convolutions) on different spatial scales (pooling) by iterative optimization of layers during training with no addition of handcrafted feature layers [32,34–36].

This advantage is documented by current forestry studies on forestry using CNNs for image analysis at the single tree level from ultrahigh-resolution RGB images. CNNs have been used for individual tree crown delineation in a tropical forest (synthetic dataset) [37] or in a temperate forest [38]. Much effort has been devoted to developing CNNs for tree species classification using manually delineated crowns [39,40], automatically delineated crowns [41,42], or CNN architectures, including crown segmentation [43,44]. However, studies detecting pest insect infestation are not still common. Safonova et al. [31]

detected infested clusters (no single trees) of Abies sibirica Ledeb. in boreal forests using CNN and RGB images. Nguyen et al. [45] identified individual sick *Abies mariesii Mast.* by means of RGB images and deep learning trained on a large dataset. Little research has also been conducted on classification or segmentation of multi-/hyperspectral images due to the lower resolution of the images. Only Miyoshi et al. [46] and Nezami et al. [47] classified tree species using drone hyperspectral images. Therefore, previous research raised the question of when it is possible to perform the successful detection of individual infested trees by applying CNN on a small multispectral dataset.

The aim of this study is to examine the potential of CNNs for the detection of individual trees infested by bark beetles on a dataset from multispectral images acquired by an unmanned aircraft system (UAS) with very high spatial resolution. We compare the classification accuracy of the different CNN architectures with the well-established random forest (RF) classifier. The research questions addressed in the study are as follows: (1) Is it possible to reach acceptable accuracy of the model trained from scratch? (2) Does transfer learning improve the detection of infested trees? (3) What CNN architecture performs for the identification of infested trees? (4) Are CNNs superior to machine learning algorithms for the classification of bark beetle disturbances on small multispectral datasets? In a broader context, the study aims to design a relatively simple, semiautomated and efficient workflow for the detection of infested individual trees that can be adopted by forest management in the country.

2. Materials and Methods

2.1. Study Site and Remote Sensing Data

The study site (approximately 50.090°N and 14.650°E) is in Klánovice Forest. Klánovice Forest is a typical suburban temperate forest located in the Prague metropolitan area, Czechia. Klánovice Forest has suffered from massive bark beetle outbreaks since 2015 (up to four generations per year) due to urban heat islands [48]. The dominant tree species are Norway spruce, pine, oak and birch at the study site (Figure 1).

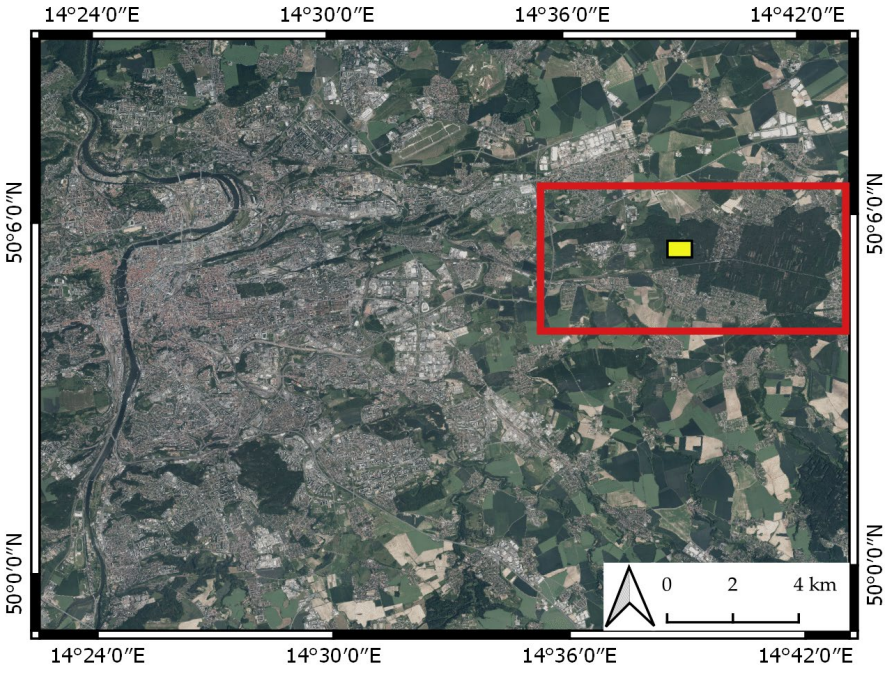

(**a**)

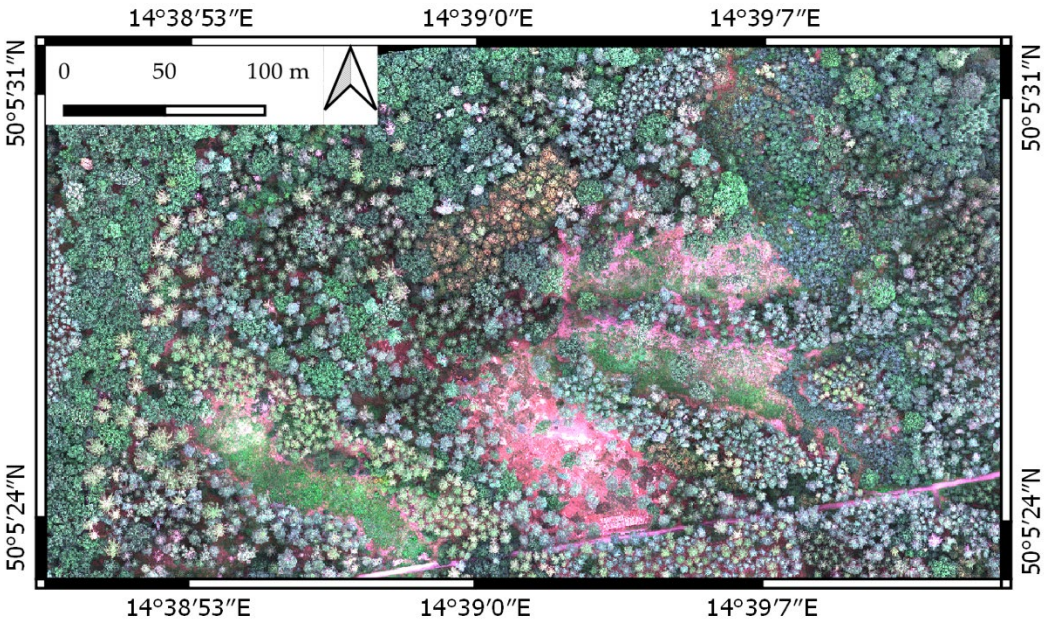

(**b**)

Figure 1. RGB imagery of the study site: (**a**) Klánovice forest (red rectangle) and study site (yellow rectangle) located near Prague; (**b**) RGB orthomosaic of the study site.

UAS imaging was conducted on 4 September 2020 using a DJI Matrice 210 RTK featuring a MicaSense RedEdge-M multispectral camera. The weather conditions were sunny, and flight was performed at approximately noon to minimize shadows. We set the flight altitude to 100 m above ground, frontlap 90% and sidelap 80% to be identical to previous flights conducted at the study site. The calibrating images of the reflectance panel were taken prior to and after flight to be used for radiometric calibration of images during photogrammetric processing.

Photogrammetric processing was performed in Agisoft Metashape Professional 1.6.2. using the standard procedure for multispectral images, including reflectance calibration [49]. Onboard real-time kinematics (RTK) global navigation satellite system (GNSS) data were used for image alignment using high accuracy settings. After the alignment, the dense cloud was generated using high-quality and aggressive depth filtering. Based on dense clouds, the digital surface model (DSM) was computed and projected into WGS84/UTM zone 33N. A multispectral mosaic was orthorectified based on images and DSM with a spatial resolution of 6 cm/pixel. The dense cloud was decimated to preserve only the highest point in each cell (0.2 m) of the grid that was virtually placed over the dense cloud. For a detailed description of the Klánovice forest, camera parameters and photogrammetric processing, we refer to Minařík et al. [50].

2.2. Ground Truth Data

A terrestrial survey of the health status of *Picea abies* (L.) *H. Karst*. (hereafter, Norway spruce or spruce) was conducted one day prior to the flight. The health status of mature Norway spruces was assessed relative to each other based on foliage discoloration, defoliation and trunk symptoms (resin ducts) that are typical for bark infestation [51]. The spruce trees were classified into three groups: live and not infested (sh), green attack (sbbg) and longer infested trees when needles turned yellow (sbbd) (Figure 2). Among spruce trees, pines (*Pinus sylvestris* L.) were also mapped because their spectral response is similar to the spectral response of infested trees.

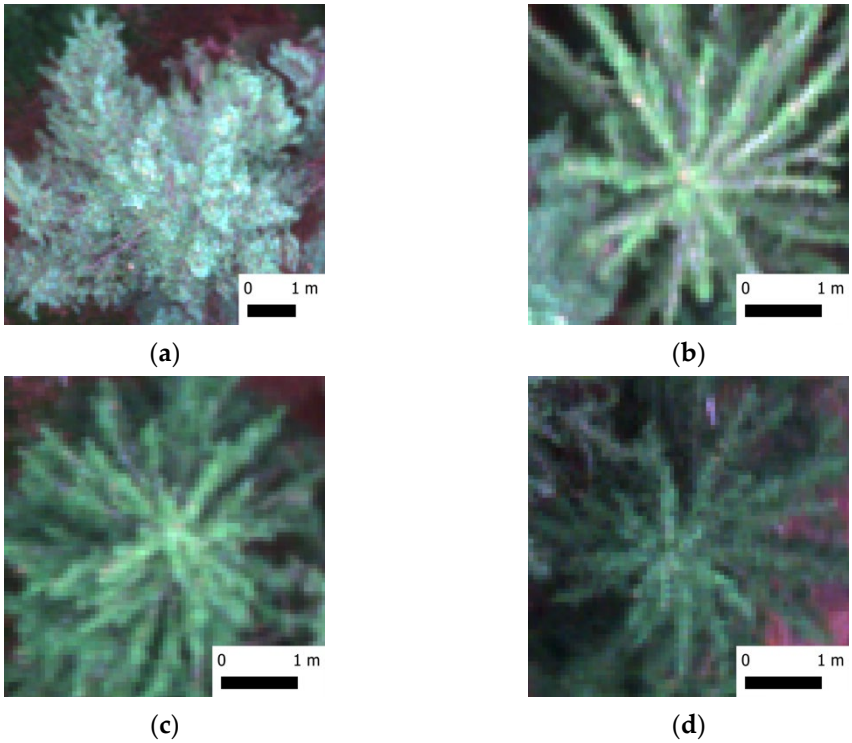

Figure 2. Disturbance classes used in the study: (**a**) pine; (**b**) sbbd—damaged spruce tree (longer infested spruce tree when needles turn to yellow, light green needles dropped, bark flaked away by woodpeckers); (**c**) sbbg—spruce tree under green attack (needles green or light green, resin ducts present); (**d**) sh—live and not infested spruce tree (needles green).

The survey of the infestation symptoms extended the previous one carried out in March 2020 using the same methodology [50]. We checked the previously mapped trees and reclassified them if necessary. Some of the trees had already been cut down. Moreover, we located and classified new trees. The ground truth dataset was extended from 122 mature spruce trees to 429 by the survey. The position of each tree was measured by the total station due to the multipath GNSS signal. The number of pines in the ground truth dataset was increased from 23 to 243 using visual interpretation from the orthomosaic.

2.3. Tree Crown Segmentation and Spectral Separability Analysis

Even if we located the position of every tree as a point during the field survey or visual interpretation, and tree crowns could be extracted manually, we decided to perform a simple automatic tree crown delineation to be consistent with the objectives of the study concerning the semiautomated ITBC workflow design. The crown delineation methodology was partially based on the delineation workflow designed in a previous study [50]. We describe here only the basic principle and methods.

We applied the identical excess green index vegetation mask calculated in a previous study [50] to separate the conifers from the surface and broadleaves. Therefore, only targeted spruces and pines were considered in the tree delineation routine. Then, treetops were identified from the normalized dense point cloud using a local maxima filter with the adaptive circular moving window size according to the tree height function f1 [50].

$$f1 = \text{tree height} \times 0.07 + 1 \quad (1)$$

Around each identified treetop, a square bounding box (buffer) was automatically constructed. The size of the buffer was set according to the height distribution of identified treetops. The trees under the median height received bounding boxes (BBs) of 2 m size, those lower than quantile 0.75 received 3.2 m BB, and those higher than quantile 0.75 received 4 m BB centered on the treetops. The bounding box sizes were selected to cover at

least the upper 50% of the crown where bark beetle infestation was the most significant [28].

We applied no spectral transformation of the original bands, such as vegetation index calculations, because previous studies stated that the original data were already sufficient [39,52]. Moreover, we analyzed the spectral separability of disturbance classes to reduce the dimensionality of inputs.

The spectral separability of disturbance classes was investigated using all spectral bands of the multispectral camera. MicaSense RedEdge-M is sensible to Blue (475 nm), Green (560 nm), Red (668 nm) Red-edge, (717 nm) and near infrared (NIR) (840 nm) parts of the spectrum [50]. Central wavelengths are in brackets. The bounding boxes were used for extracting the reflectance values of tree crowns of individual disturbance classes. We used a Kruskal–Wallis test with the following nonparametric post hoc comparison after Siegel and Castellan [53] to test the spectral separability of the disturbance classes. Only bands with high separability of disturbance classes were used for classification.

The bounding boxes were primarily used for cutting the individual tree crowns from the original orthomosaic. Every tree was represented by a small multispectral image of 33/53/66 × 33/53/66 × 4(3) pixels of size stored on the hard drive (see Figure 2). According to the results of spectral separability analysis, we tested two band subsets consisting of Red, Green, Blue bands and Red, Green, Blue and Red-edge bands for classification. The reflectance values were multiplied by 200 and stored as integers. Data preprocessing was performed in R [54].

2.4. Classification Models

2.4.1. Convolutional Neural Networks

In this study, we tested three types of CNN architectures applicable to tree classification using a small dataset selected based on a literature search. We decided to test a fairly simple and fast network trained from scratch with no data augmentation, CNN designed directly for pest insect detection with data augmentation trained from scratch and pretrained CNN using transfer learning.

As a fairly simple network, we modified the CNN published in [47] (hereafter, Nez), which quickly reduced dimensionality and ultimately performed the classification of the tree species (Table 1). For a quick decrease in the loss function, we applied batch size 1 for this network as theoretically recommended by Chollet and Allaire [55].

Table 1. Configuration of Nez CNN model. (i) is the number of input bands. We classified into 4 or 3 disturbance classes.

Layer	Kernel Size	Kernel Number	Stride	Output Size
Input		-	-	32 × 32 × (i)
Conv1	5 × 5	4	1	28 × 28 × 4
Maxpool1	3 × 3	1	3	9 × 9 × 4
Conv2	5 × 5	16	1	5 × 5 × 16
Maxpool1	3 × 3	1	3	1 × 1 × 16
ReLU		-	-	
Conv3	1 × 1	4	1	1 × 1 × 4
Dense (softmax)		-	-	4 (3)

Second, we were inspired by the CNN previously published in [31] that was superior to state-of-art pretrained CNN in the classification of damaged firs from RGB data. However, we designed our own architecture with respect to the spatial resolution of our data (Table 2). We trained the network in two instances, without (Saf) or with (SafAugu) data augmentation.

Table 2. Configuration of Saf/Safaugu CNN model. (i) is the number of input bands. We classified into 4 or 3 disturbance classes.

Layer	Kernel Size	Kernel Number	Stride	Output Size
Input		-	-	32 × 32 × (i)
Conv1	3 × 3	8	1	32 × 32 × 8
Max Pool1	2 × 2	1	2	16 × 16 × 8
Conv2	5 × 5	16	1	16 × 16 × 16
Conv3	3 × 3	16	1	16 × 16 × 16
Max Pool2	2 × 2	1	2	8 × 8 × 16
Conv4	3 × 3	16	1	8 × 8 × 16
Conv5	5 × 5	16	1	8 × 8 × 16
Dropout1		-	-	0.15
Conv6	5 × 5	64	-	8 × 8 × 64
Glob Avg Pool		-	-	64
Dense1 (ReLU)		-	-	64
Dropout2		-	-	0.25
Dense2 (ReLU)		-	-	16
Dense3 (softmax)		-	-	4 (3)

Moreover, we applied transfer learning (specifically feature extraction) because of the small data problem. We selected DenseNet169 [56] because it showed good performance in previous studies [31,57]. The network weights were pretrained on the ImageNet dataset. We adopted the whole convolutional base, and we only wrote and trained the classifier on the top (Table 3). DenseNet169 was trained only with data augmentation.

Table 3. Configuration of Dense169 CNN model. (i) is the number of input bands. We classified into 4 or 3 disturbance classes.

Layer	Output Size
Input	32 × 32 × (i)
DenseNet169 (convolutional base)	1664
Dense1 (ReLU)	128
Dense2 (ReLU)	16
Dense3 (softmax)	4 (3)

2.4.2. Random Forest

RF is a well-established machine learning algorithm [58]. Several benchmark studies consider the algorithm to be one of the best data-driven algorithms currently available [59–61]. RF is a robust algorithm because the classification is made an ensemble estimate from a high number of decision trees based on bagging and random selection of covariates. The final classification is a majority vote of all predicted classes over trees [58]. We applied the implementation from the caret [62] package in R. The algorithm was applied only to the basic training dataset using original spectral bands and no data augmentation. We applied no feature engineering because of comparison to CNNs.

2.5. Training and Validation

The original dataset consisting of 672 tree crowns was split randomly into training, validation, and test folders at a rate of 70:10:20. The relative frequency of elements in the classes was preserved in data splitting. Each model was trained using the same 70% of the tree crows.

The tree crown images were read as a multidimensional tensor (arrays) from the hard drive. Every image was converted back to reflectance values, and crowns were resampled

to 32 × 32 × i using the nearest neighborhood prior to training. The weights of the CNN models were randomly set at the beginning. The weights were optimized iteratively to minimize the loss function. We used a categorical cross-entropy loss function for all CNN models because we had a typical multiclass classification problem. We selected the adaptive moment estimation optimizer (Adam) [63].

For the RF, the median reflectance values of each crown were extracted from the orthomosaic in R to perform tree-based classification (one tree, one object). Therefore, each tree was represented by one row in the attribute table of buffer polygons with median reflectance values of all bands. Buffer polygons were used for the classification. The default number of decision trees (500) suggested in the original paper was preserved.

The validation dataset was used during training to detect overfitting of the models. For CNN models, the validation dataset was used to empirically set the appropriate batch size, number of epochs and steps per epoch to prevent overfitting using trial and error methods (Table 4). For RF, we used a validation dataset to check the overfitting of the models for the selected number of decision trees.

Table 4. The overview of finally selected batch size, number of epochs and steps per epoch for every CNN model to prevent overfitting.

Model	Batch Size T	Batch Size V	Epochs	Steps per Epoch T	Steps per Epoch V
Nez	1	1	40	-	-
Saf	27	26	160	18	2
SafAugu	27	26	400	18	2
DenseNet 169	27	26	160	18	2

T: training dataset; V: validation dataset.

All code was written in R v. 4.0.5 using the packages keras, tensorflow and caret [55,62]. We used the R interface to Keras with the TensorFlow backend ver. 2.4.0 for computation. Nez, Saf and Safaugu CNNs were written in R by the authors according to the description in the original articles using the Keras package. DenseNet convolution was already available in the keras package. The models were trained on CUDA-compatible NVIDIA GeForce MX250 graphic card with 2 GB RAM installed in a notebook.

2.6. Accuracy Assesment

The test dataset was used to assess the performance of the classification models. The test dataset had no contact with the test samples during training and validation; therefore, the results showed unbiased model effectiveness [64]. The confusion matrix was calculated based on comparing the predicted disturbance classes of the test dataset to ground truth classes. From the confusion matrix, several indices of agreement were calculated for each model and for each disturbance class. For the between-class comparison, we calculated precision (p), recall (r) and F-score [32]. These metrics were also applied to the accuracy assessment of automatic tree identification.

The general performance of the model was assessed using the mean F-score of the model and Cohen´s kappa index. The kappa index is objective because it gives the agreement to the true class considering the random chance of correct classification [65].

3. Results

3.1. Tree Indentification

Tree identification was assessed compared to ground truth in terms of true-positive (TP), false-negative (FN, omission error), and false-positive (FP, commission error) trees. The results of automatic tree identification are presented in Table 5. The recall was lower than the precision, showing that the algorithm had a problem identifying smaller and lower crowns in dense forests that were partially shaded by larger trees, especially pines. Therefore, the adaptive moving window included more than one tree and identified only the highest tree. In contrast, the very high precision score shows that the algorithm detected almost no multiple treetops. The wrongly identified or unidentified trees were corrected according to the ground truth dataset prior to ITBC.

Table 5. The results of automatic tree identification.

Point Density (points/m²)	TP	FP	FN	r	p	F-Score
22	585	14	87	0.87	0.98	0.92

TP: true positive, FP: false positive; FN: false negative; r: recall; p: precision.

3.2. Spectral Separability of Disturbance Classes

The results of spectral separability analysis are presented in Figure 3. The null hypothesis of no spectral separability of disturbance classes was rejected for all bands because there were significant reflectance differences between pines and spruces. However, the following multiple comparisons showed some separability issues between disturbance categories of spruce trees that were the most important. The best spectral separability of spruce disturbance classes was in the blue and red bands (Figure 4a,c). The interquartile range of sbbd, sbbg and sh revealed only small overlap between sbbd and sbbg categories, and the multiple comparison test showed significant differences among reflectance values. These disturbance classes were also separable in the green- and red-edge parts of the spectrum. The results showed increased overlap among sbbd and sbbg trees within these two bands, but there were still significant differences. However, the sbbd, sbbg and sh categories were not spectrally separable in the NIR band, and the boxplots highly overlapped with each other. Therefore, the NIR band was skipped for the ITBC. Based on the results, we decided to perform classification with two datasets composed of bands 1–4 (4b) and 1–3 (3b) and to investigate the effect of band selection on the classification results.

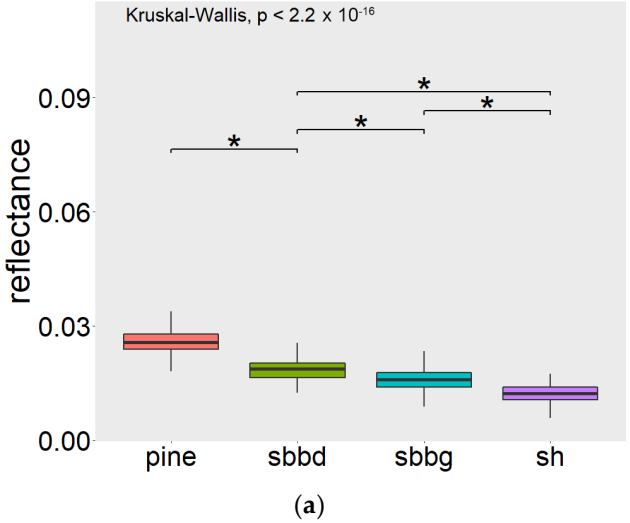

(**a**)

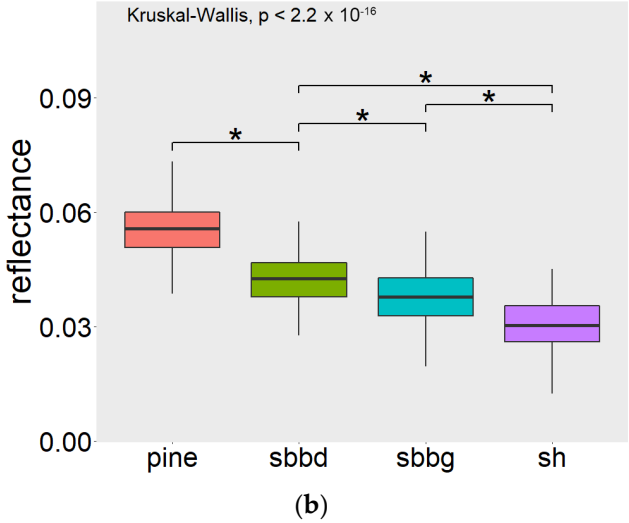

(**b**)

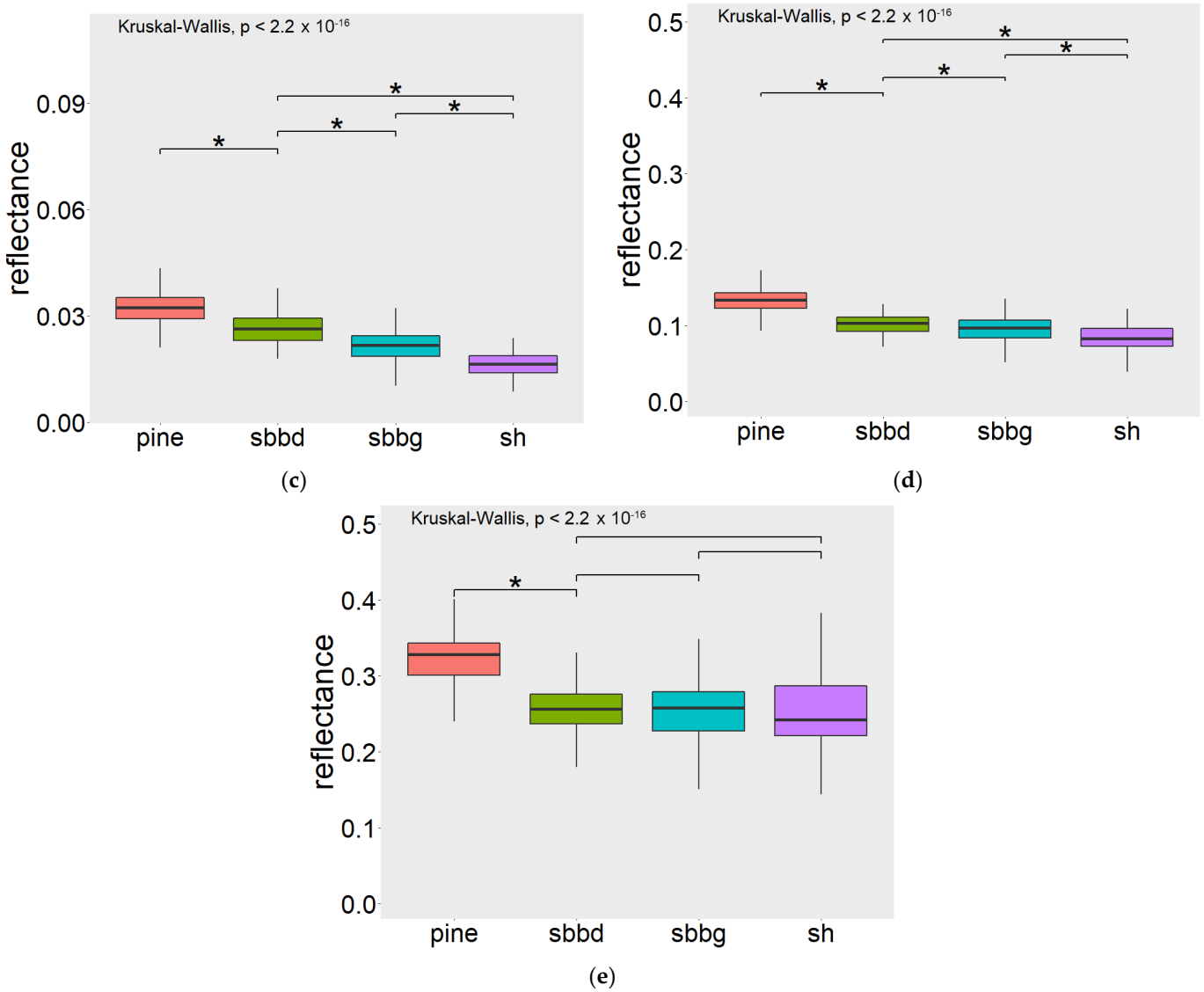

Figure 3. Spectral separability of disturbance classes: (**a**) Band 1—Blue, 475 nm; (**b**) Band 2—Green 560 nm; (**c**) Band 3—Red, 668 nm; (**d**) Band 4—Red-edge, 717 nm; (**e**) Band 5—NIR, 840nm. * Marks the significant spectral differences (the significance level $\alpha = 0.05$) among disturbance classes. The results of multiple comparisons are presented only for the most important disturbance classes reflecting the bark beetle infestation.

3.3. Classification Results

The ITBC results employing different models and model types are presented in Table 5. Basically, each model classified the trees using the four (model version 4c4b) or three (model version 4c3b) most informative bands (Section 3.2) into all four disturbance classes. The comparison of class-specific F-scores showed the strong connection to spectral separability of the disturbance classes. The highest mean F-score was obtained for pines (0.93) regardless of the model version because of their spectral and textural responses that were different from spruces. However, the more important spruce disturbance classes reached lower mean F-Scores of 0.68, 0.65 and 0.72 for sbbd, sbbg and sh, respectively, because of their more similar spectral and textural responses, resulting in misclassifications of the trees of these classes (Figure 4, left column). Nevertheless, previous studies used coarser classification for infested/healthy (not infested) categories. Therefore, we decided to experimentally merge the sbbd and sbbg classes into a more general class of infested trees (sbb) and train the classification models for three output categories using the four (model version 3c4b) or three (model version 3c3b) most informative spectral bands

(Figure 4, right column). Finally, each model was trained and assessed in four versions (Table 6).

Table 6. Evaluation metrics of bark beetle disturbance classification at the tree level. For the pair of models of the same architecture and the same number of output classes but the different number of input bands, the more accurate model is highlighted in bold. For each model, the most accurate model version is highlighted in green. The model showing the general poorest performance is highlighted in orange.

Model	Model Version	F-Score by Class				Mean F-Score	Model's Kappa	Mean Kappa
		pine	sbbd	sbbg	sh			
Nez	4c4b	0.93	0.72	0.77	0.80	0.80	0.74	0.81
	4c3b	0.95	0.79	0.83	0.78	**0.84**	**0.80**	
	3c4b	0.93	0.91		0.81	0.88	0.84	
	3c3b	0.92	0.94		0.86	**0.91**	**0.87**	
Saf	4c4b	0.91	0.71	0.68	0.69	0.75	0.69	0.79
	4c3b	0.96	0.78	0.77	0.75	**0.82**	**0.77**	
	3c4b	0.95	0.90		0.73	0.86	0.82	
	3c3b	0.95	0.93		0.78	**0.89**	**0.86**	
Safaugu	4c4b	0.95	0.69	0.72	0.79	0.79	0.72	0.81
	4c3b	0.93	0.80	0.77	0.75	**0.81**	**0.76**	
	3c4b	0.95	0.93		0.73	0.87	0.85	
	3c3b	0.98	0.96		0.83	**0.92**	**0.92**	
Dense169	4c4b	0.94	0.65	0.60	0.67	0.72	0.64	0.77
	4c3b	0.93	0.68	0.72	0.73	**0.77**	**0.70**	
	3c4b	0.95	0.95		0.76	**0.89**	**0.87**	
	3c3b	0.93	0.94		0.73	0.87	0.85	
RF	**4c4b**	0.93	0.49	0.63	0.76	**0.70**	**0.60**	0.69
	4c3b	0.92	0.50	0.60	0.45	0.62	0.55	
	3c4b	0.94	0.92		0.76	**0.87**	**0.85**	
	3c3b	0.94	0.88		0.45	0.76	0.75	
Class's F-score	4c	0.93	0.68	0.65	0.72	-	-	-
	3c	0.94	0.92		0.74	-	-	

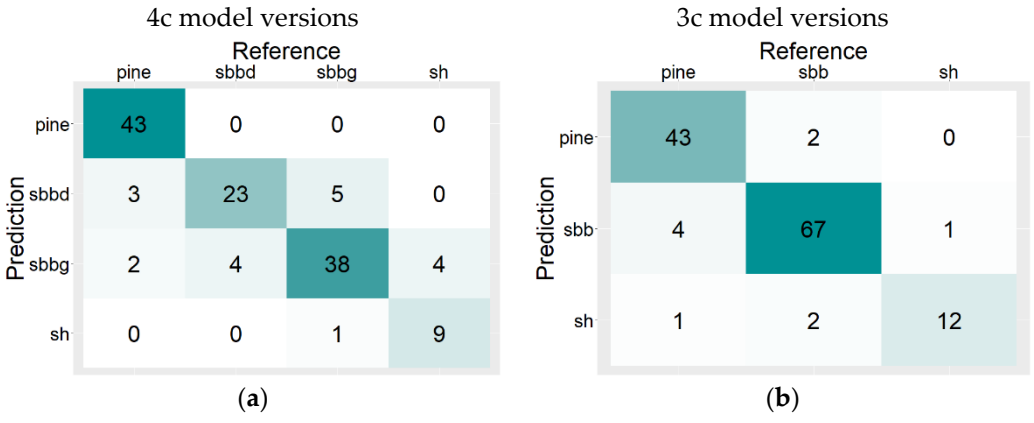

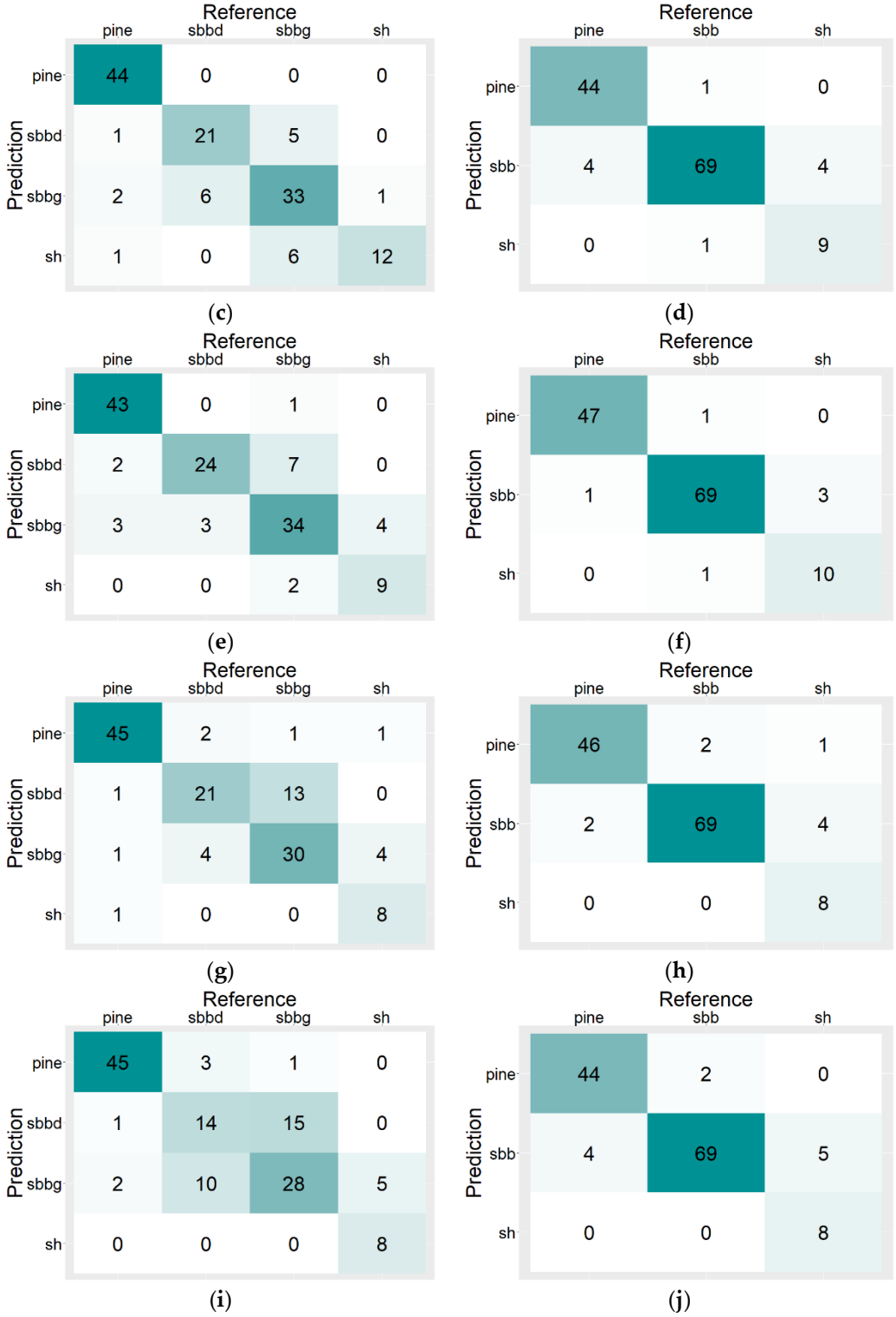

Figure 4. Confusion matrices of the best performing models classifying trees into four classes (left column) or three classes (right column) according to Table 5: (**a**) Nez 4c3b; (**b**) Nez 3c3b; (**c**) Saf 4c3b; (**d**) Saf 3c3b; (**e**) Safaugu 4c3b; (**f**) Safaugu 3c3b; (**g**) Dense169 4c3b; (**h**) Dense 3c4b; (**i**) RF 4c4b; (**j**) RF 3c4b.

The results showed that the model types using only the three most informative RGB bands (4c3b) were superior to the 4c4b types of CNNs. The best classification performance was reached using Nez4c3b, showing only a few misclassifications between the sbbd and sbbg categories (Figure 4a). The second-best classification performance was achieved by Saf4c3b/Safaugu4c3b. However, the model misclassified the largest number of sbbg trees

(13%) to sh, which could be a problem despite the highest number of correctly classified sh trees (Figure 4c). Nevertheless, featuring data augmentation in the Saf4c3b model reduced the misclassifications of sbbg trees to sh class (Figure 4e), even if the overall accuracy metrics remained similar. All three CNNs were trained from scratch. The relatively lower overall performance among CNN classifiers was achieved using the adapted Dense169 4c3b model. The Dense169 4c3b model misclassified 30% of sbbg trees into the sbbd category (Figure 4g). All 4c CNN classifiers achieved higher mean F-scores and kappa metrics than the 4c RF models. The confusion matrices of RF models revealed the issue of distinguishing sbbd from sbbg, resulting in misclassification of 37% of sbbd trees to sbbg and 34% of sbbg trees to sbbd (Figure 4i). Nevertheless, 4c RF models reached F-scores comparable to the F-scores of CNNs for pines and sh classes.

Merging two related classes of the infested trees (sbbg and sbbd) prior to classification resulted in an increase in classification accuracy (Figure 4, right column). The mean F-scores increased by 7–17%, and kappa increased by 7–25% comparing the best 3c models to their 4c versions. The lowest increase was for Nez and Saf models. The highest increase was for the Safaugu, Dense169 and RF models. However, the classification accuracy of pine sh trees was similar regardless of the number of input classes. The evaluation metrics of the models increased only by merging the classes.

The 3c3b model versions were mostly superior to the 3c4b versions of the models again. Only the RF3c4b model reached 10% higher evaluation metrics than the 3c3b version. The best classification accuracy was obtained using Safaugu3c3b, achieving a mean F-score of 0.92 and kappa. Nevertheless, the accuracy metrics were comparable for all 3c3c CNN models and even for RF3c4b. The rest of the models achieved a mean F-score of 0.86–0.91 and kappa of 0.82–0.87.

Based on the experimental results of this subsection, several conclusions were drawn concerning the identification of infested trees from the small multispectral dataset. The more important is the selection of representative features with high separability of disturbance classes than the number of features for the classification using CNNs. To distinguish between newly infested trees (sbbg), non-infested trees (sh) and longer infested trees (sbbd), the CNN classifiers developed for forest applications (Nez and Saf/Safaugu) (Figure 5a) are more accurate than RF (Figure 5b) and pretrained DenseNet169. Data augmentation has a positive effect on the classification accuracy of the deeper Saf model, but the number of epochs must be increased. However, misclassifications between the sbbd and sbbg classes up to 20% can occur because of spectral overlaps. Therefore, it should be considered when the classification results serve decision making. If the complexity of the problem decreases by merging the related information classes (sbbd and sbbg) to a more general infested tree (sbb) category, the selection of model type is less important. All tested model types, including RF, were able to detect the most important class of infested trees with an F-score of the class over 0.90.

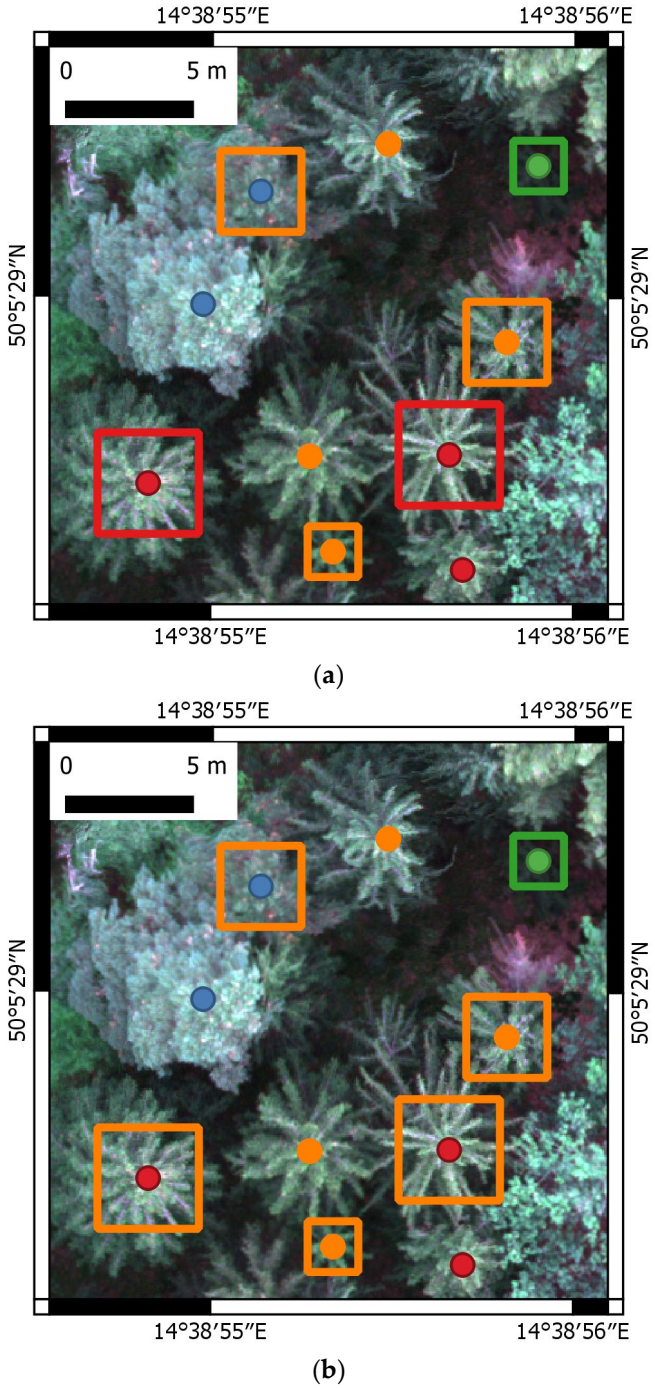

Figure 5. Illustration of classification results using test dataset: (**a**) Safaugu 4c3b; (**b**) RF 4c3b. Ground truth data are represented by points. Model predictions are represented by squares. Pines are highlighted in blue. Sbbd spruces are highlighted in red. Sbbg spruces are highlighted in orange. Sh spruces are highlighted in green.

4. Discussion

4.1. Tree Delineation

The accuracy of individual tree detection is comparable or superior to other studies focused on the identification of conifers in an uneven-aged mixed forest using local maxima filtering [66,67]. Although the recall score (0.87) of automatic tree identification points to the omission of small trees in the dense part of the mixed forest, the method is more efficient and less time-consuming than the manual identification of all trees because only the unidentified trees must be detected manually by visual interpretation. The recall of

treetop identification is lower than that recall in a previous study [50] using the same methodology because the previous study focused only on mature spruce trees over 60 years that are primarily infested by the bark beetle [13]. In this study, conifer trees over 5 m were considered.

The issue of small tree omissions could be reduced using another algorithm of treetop detection, e.g., a deep-learning method based on 2D confidence map estimation from hyperspectral data [46]. The authors reached F-score, precision and recall values of 0.959, 0.973 and 0.945, respectively. Another option is to apply instance segmentation. However, this approach requires very sophisticated reference data, including both the identification of individuals and delineation of their explicit spatial extent [32,44]. Therefore, the approach was tested only on synthetic data [37,68]. Moreover, the approach requires very high computational power (workstation, server or cloud computing) [68] that can limit the usage in a common practice. For these reasons, we segmented the trees prior to classification using the simple representation of the crown by bounding box instead of more advanced tree crown delineations. This practice is common because CNNs require basically rectangular inputs, and it has been verified by previous studies [31,42,47,57]. In this study, we did not investigate the other algorithms because they are beyond the scope of the study.

4.2. The Effect of Feature Layer Selection on Classification Results

We applied no spectral transformation of the original bands, such as vegetation index calculations, because according to previous studies, the addition of spectral transformations may even introduce information loss and decrease the model accuracy [47,69,70]. Concerning the addition of elevation features such as the canopy height model, the results of previous studies focused on three species classifications revealed no significant improvement in CNN models [47,69,70]. Therefore, we decided to test only a basic pipeline with the original bands to preserve high automation and easy reproducibility of the workflow.

Spectral separability analysis can be understood in a broader context as feature layer selection for classification. Feature layer selection is not investigated much for CNNs because CNNs provide end-to-end learning, including feature extraction, and CNNs are mostly applied only to RGB images [32]. The basic principle is to select all bands of multi-/hyperspectral images or select combinations and retrospectively verify the effect on the accuracy of classification of the trees [47,69]. However, this approach requires running the classification multiple times, which is counterproductive if the goal is to reduce the dimensionality of the inputs to save computation time. One way to overcome this issue is to analyze the spectral differences between disturbance classes using descriptive statistics and statistical inference prior to classification, as suggested in this study. We found that CNN models using only RGB bands (Xc3b) were superior to models using red edges (Xc4b) because the red-edge band had higher spectral overlaps of spruce disturbance classes, which resulted in lower classification accuracy metrics. The results are consistent with a previous study focused on conifer tree species classification using hyperspectral data [47]. The best results of the study were achieved using only RGB bands. However, the explanation remains unclear because separability analysis was not performed. Moreover, Miyoshi et al. [46] implemented a band selection module in a CNN classifier, resulting in the reduction of 25 original bands into a linear combination of 5 bands, including RGB. Therefore, there is no evidence to date that adding more bands into the CNN model improves the classification of conifer species or the infestation status compared to the RGB-based model. In contrast, the higher accuracy of RF models was reached by Xc4b versions, and the poorest performance was achieved using the 4c3b RF model because the RF algorithm generally benefits from more feature layers [32,71].

4.3. Considerations about Bark-Beetle Disturbance Classification Using CNN

The differences between model performances were higher when the trees were classified into four categories (pine, sbbd, sbbg, sh). The best performance was achieved by the Nez4c3b model and Safaugu 4c3b model. The overall scores of Nez4c3b had a mean F-score of 0.84 and kappa of 0.80. The F-scores of the sbbd, sbbg and sh classes were 0.79, 0.83 and 0.78, respectively. The overall scores of Safaugu 4c3b had a mean F-score of 0.81 and kappa of 0.76. The F-scores of the sbbd, sbbg and sh classes were 0.80, 0.77 and 0.75, respectively. Nez4c3b reached the highest learning rate and high accuracy for our task within 40 epochs because of batch size 1 and model architecture. Nez CNN was originally designed to quickly decrease the dimensionality of the hyperspectral inputs with similar spatial resolution and ultimately perform classification tasks [47]. The small batch size intensified the learning process. Data augmentation had a positive effect on the classification metrics of the Saf model, consistent with the original paper [31]. In the original paper, the F-scores increased by 0.24 and 0.15 for two infested classes of firs corresponding to our mixed sh + sbbg class and sbbd class after data augmentation. In our study, the data augmentation resulted in almost no improvement of F-scores, but it reduced the dangerous misclassification of sbbg trees to sh class. Nevertheless, both CNNs achieved performance superior to pretrained convnets and transfer learning in the original papers, similar to our results [31,47]. Moreover, both 4c CNN models outperformed the 4c RF models for the detection of bark beetle disturbance at the tree level, which is consistent with previous findings of Sothe et al. [69,70]. This result reflects the main advantage of deep learning methods. CNNs perform effective automatic feature extraction learning of hierarchical features during training from the original images [72,73]. Therefore, they can learn hidden features from the original spectral bands, resulting in better classification accuracy compared to RF.

The main classification problem was to separate the transitional category of sbbg (trees under green attack) from sbbd (longer infested trees when needles turn yellow) and marginally sh because of the similar spectral responses. However, the most important aspect of forest management is the identification and destruction of infested trees before the new generation of bark beetles starts swarming [74]. The first (spring) swarming occurs in the green attack stage [75]. Nevertheless, cutting trees at the beginning of yellow stage prevents summer swarming [74,76]. Moreover, previous studies used coarser classification into infested (up to red needles) and healthy (not infested) categories. For this reason, we decided to merge the sbbd and sbbg classes into the infested tree class (sbb) and performed the classification with three classes (pine, sbb, sh).

The decreasing complexity of the problem caused by merging sbbd and sbbg classes made the selection of model type less important. The best classification metrics were achieved by the Safaugu3c3b model (mean F-score 0.92, kappa 0.92) followed by the Nez3cb classifier (mean F-score 0.91, kappa 0.87). The F-scores of pines, sbb and sh classes reached 0.95, 0.93 and 0.78 for Safaugu3c3b and 0.92, 0.94 and 0.86 for Nez3cb. However, all tested model types, including 3c RF, were able to detect the most important class of infested trees with an F-score of the class over 0.90. The evaluation metrics of pine and sh classes remained the same. Merging affected only the concerned classes.

The evaluation metrics of the best performing 3c models were higher or comparable to previous studies focused on the detection of individual not infested/infested (up to red needles, including green attack) trees. Ortiz et al. [21] and Kampen et al. [23] reached kappa coefficients of classification of 0.74 and 0.73, respectively, using machine learning classifiers. Brovkina et al. [26] reached a kappa of 0.75 using object-oriented image analysis in eCognition software. Dash et al. [22] reached kappa 0.69 using a machine learning algorithm and time-series analysis. Nguyen et al. [45] reached a kappa of 0.73, and Qin et al. [77] achieved a mean F-score of 0.88 for infested trees using a deep learning algorithm but using a large dataset of approximately 5000 samples. In contrast, we reached higher or comparable evaluation metrics of models using ten times fewer samples. Safonova et al. [31] achieved F-scores over approximately 0.90 for infested tree categories.

The more detailed classification of infested trees to different stages of infestation, such as sbbg and sbbd, is rare and less accurate (published only by [17,31]), because it is challenging to separate trees under green attack. The common approach is to detect green attack retrospectively from time series of multispectral imagery [17,22,28]. This approach requires repeated flights during season, and the infestation is detected retrospectively, which could be a drawback for rapid calamity mapping. Moreover, these studies classified the trees only into infested/not infested categories for simplification of classification task. In our study, we propose the workflow that detect the green attack and provide information about disturbance dynamics by classifying to different stages of infestation at once based on precise timing and CNN. We conducted the imaging after summer swarming in the study, because vegetation stress caused by bark beetle is detectable from multispectral images after 14 days since infestation [22,78]. Therefore, it is possible to detect and eliminate infested trees early after infestation using timed UAS imaging. However, it demands the knowledge of approximate dates of swarming in the area during season. This is the potential limitation of our approach. To overcome the limitation, it is possible to use terrestrial methods of swarming detection like pheromone slit traps [74]. Nevertheless, the proposed workflow can be used to automatically monitor bark beetle disturbance development, because the performance of the Nez4c3b and Safaugu4c3b models is comparable or superior to previous work employing machine learning focused on green attack phase detection even if they used coarser classification and time series [17,19,21,22,28,79].

Another challenge of our workflow is to collect more training samples for classification. We hypothesize that using more training samples would improve the distinction between categories of infestation status (sbbd and sbbg) similarly to distinction between tree species that was documented by Natesan [41]. In addition to increasing the number of experimental sites, another possibility is to extract more training samples from repeated imaging of multiple swarming within one season or from different seasons. It could improve the generalization of disturbance class-specific patterns found by CNN classifier thanks to slightly different spectral response of the trees resulting in possible accuracy improvement. For now, high generalization of class-specific patterns is guaranteed by CNN architecture itself that iteratively optimize the transformations of feature space during training process [32,55]. We plan to combine our classification methodology with time-series analysis for monitoring bark beetle disturbance, detecting hotspots and predicting infestation spreading in our future work.

5. Conclusions

This study examined the potential of CNN for the detection of individual trees infested by the bark beetle on a very high-resolution dataset from multispectral images. We compared the performance of three CNN architectures and the random forest (RF) model to classify the trees into four categories: pines, sbbd (longer infested trees when needles turn yellow), sbbg (trees under green attack) and non-infested trees (sh).

The best performance was achieved by the Nez4c3b model (mean F-score 0.84, kappa 0.80) and Safaugu 4c3b model (mean F-score 0.81, kappa 0.76) using only RGB bands. The main misclassifications were between sbbd and sbbg because of the similar spectral responses. We decided to merge sbbd and sbbg into a more general class of infested trees because both classes described the relatively early infestation stage. Merging sbbd and sbbg made the selection of model type less important. All tested model types, including RF, were able to detect the most important class of infested trees with an F-score of the class over 0.90. Nevertheless, the best classification metrics were achieved by the Safaugu3c3b model (mean F-score 0.92, kappa 0.92) followed by the Nez3cb classifier (mean F-score 0.91, kappa 0.87) using only RGB bands.

Better performance was achieved by the RGB models because the best spectral separability of these classes was in the blue and red bands. Therefore, the usage of the raw RGB spectral band is sufficient for the basic identification of infested trees using these

CNNs, which makes data preprocessing more straightforward. We found no evidence that adding more bands into the CNN model improves the detection of infested trees.

Based on our findings, we conclude that the Nez and Safaugu models are superior to the RF models and transfer learning models for the identification of infested trees and for distinguishing between different infestation stages. The performance of both models is comparable, but the Nez model has a higher learning rate for this task. The performance of the Nez and Safaugu models is comparable to previous work employing machine learning classifiers and some deep learning studies classifying trees into healthy/infested categories, even if the finer classification of tree infestation status is used. Therefore, CNNs are suitable for the automated identification of infested individual trees, as well as for monitoring bark beetle disturbance dynamics.

We see the potential application of the proposed workflow in combination with multitemporal analysis for monitoring bark beetle disturbance, detecting hotspots and predicting infestation spreading. Getting more training samples from appropriately timed repeated imaging could also improve the generalization of disturbance class-specific patterns found by CNN classifier and distinction between infestation stages thanks to variable spectral response of the disturbed trees under different seasonal conditions.

Author Contributions: Conceptualization, R.M. and J.L.; methodology, R.M.; software, R.M.; validation, R.M.; formal analysis, R.M.; investigation, R.M., J.L. and T.L.; resources, R.M. and J.L.; data curation, R.M.; writing—original draft preparation, R.M.; writing—review and editing, R.M., J.L. and T.L.; visualization, R.M.; supervision, J.L.; project administration, J.L. and R.M.; funding acquisition, J.L. and R.M. All authors have read and agreed to the published version of the manuscript.

Funding: This research was supported by the COST Action CA16219, project "Harmonization of UAS techniques for agricultural and natural ecosystems monitoring", by the Prague Environment grant; project MHMP 54/12/013649 "Monitoring of bark beetle spread in Prague forests", by the Charles University; project GA UK No. 824217 "Analysis of disturbance and regeneration of forest vegetation using UAV multispectral photogrammetry"; and by the Czech Science Foundation project 19-05011S.

Institutional Review Board Statement: Not applicable.

Informed Consent Statement: Not applicable.

Data Availability Statement: Data available on request from the authors.

Conflicts of Interest: The authors declare no conflict of interest. The funders had no role in the design of the study; in the collection, analyses, or interpretation of data; in the writing of the manuscript, or in the decision to publish the results.

References

1. Franklin, J.F.; Spies, T.A.; Van Pelt, R.; Carey, A.B.; Thornburgh, D.A.; Berg, D.R.; Lindenmayer, D.B.; Harmon, M.E.; Keeton, W.S.; Shaw, D.C.; et al. Disturbances and structural development of natural forest ecosystems with silvicultural implications, using Douglas-fir forests as an example. *For. Ecol. Manag.* **2002**, *155*, 399–423, doi:10.1016/s0378-1127(01)00575-8.
2. Senf, C.; Pflugmacher, D.; Wulder, M.A.; Hostert, P. Characterizing spectral–temporal patterns of defoliator and bark beetle disturbances using Landsat time series. *Remote Sens. Environ.* **2015**, *170*, 166–177, doi:10.1016/j.rse.2015.09.019.
3. Paritsis, J.; Veblen, T.T. Dendroecological analysis of defoliator outbreaks on Nothofagus pumilio and their relation to climate variability in the Patagonian Andes. *Glob. Chang. Biol.* **2011**, *17*, 239–253, doi:10.1111/j.1365-2486.2010.02255.x.
4. Kautz, M.; Meddens, A.J.H.; Hall, R.J.; Arneth, A. Biotic disturbances in Northern Hemisphere forests—A synthesis of recent data, uncertainties and implications for forest monitoring and modelling. *Glob. Ecol. Biogeogr.* **2017**, *26*, 533–552, doi:10.1111/geb.12558.
5. Seidl, R.; Thom, D.; Kautz, M.; Martin-Benito, D.; Peltoniemi, M.; Vacchiano, G.; Wild, J.; Ascoli, D.; Petr, M.; Honkaniemi, J.; et al. Forest disturbances under climate change. *Nat. Clim. Chang.* **2017**, *7*, 395–402, doi:10.1038/nclimate3303.
6. Seidl, R.; Schelhaas, M.-J.; Rammer, W.; Verkerk, P.J. Increasing forest disturbances in Europe and their impact on carbon storage. *Nat. Clim. Chang.* **2014**, *4*, 806–810, doi:10.1038/nclimate2318.
7. Senf, C.; Pflugmacher, D.; Zhiqiang, Y.; Sebald, J.; Knorn, J.; Neumann, M.; Hostert, P.; Seidl, R. Canopy mortality has doubled in Europe's temperate forests over the last three decades. *Nat. Commun.* **2018**, *9*, 1–8, doi:10.1038/s41467-018-07539-6.
8. Morris, J.L.; Cottrell, S.; Fettig, C.J.; Hansen, W.D.; Sherriff, R.L.; Carter, V.A.; Clear, J.L.; Clement, J.; Derose, R.J.; Hicke, J.A.; et al. Managing bark beetle impacts on ecosystems and society: Priority questions to motivate future research. *J. Appl. Ecol.* **2017**, *54*, 750–760, doi:10.1111/1365-2664.12782.

9. Hlásny, T.; Zimová, S.; Merganičová, K.; Štěpánek, P.; Modlinger, R.; Turčáni, M. Devastating outbreak of bark beetles in the Czech Republic: Drivers, impacts, and management implications. *For. Ecol. Manag.* **2021**, *490*, 119075, doi:10.1016/j.foreco.2021.119075.
10. Göthlin, E.; Schroeder, L.M.; Lindelöw, A. Attacks by Ips typographus and Pityogenes chalcographus on Windthrown Spruces (Picea abies) During the Two Years Following a Storm Felling. *Scand. J. For. Res.* **2000**, *15*, 542–549, doi:10.1080/028275800750173492.
11. Lausch, A.; Heurich, M.; Gordalla, D.; Dobner, H.-J.; Gwillym-Margianto, S.; Salbach, C. Forecasting potential bark beetle outbreaks based on spruce forest vitality using hyperspectral remote-sensing techniques at different scales. *For. Ecol. Manag.* **2013**, *308*, 76–89, doi:10.1016/j.foreco.2013.07.043.
12. Wulder, M.A.; Dymond, C.C.; White, J.C.; Leckie, D.G.; Carroll, A.L. Surveying mountain pine beetle damage of forests: A review of remote sensing opportunities. *For. Ecol. Manag.* **2006**, *221*, 27–41, doi:10.1016/j.foreco.2005.09.021.
13. Hais, M.; Wild, J.; Berec, L.; Brůna, J.; Kennedy, R.; Braaten, J.; Brož, Z. Landsat Imagery Spectral Trajectories—Important Variables for Spatially Predicting the Risks of Bark Beetle Disturbance. *Remote Sens.* **2016**, *8*, 687, doi:10.3390/rs8080687.
14. Hall, R.J.; Castilla, G.; White, J.C.; Cooke, B.J.; Skakun, R.S. Remote sensing of forest pest damage: A review and lessons learned from a Canadian perspective. *Can. Èntomol.* **2016**, *148*, S296–S356, doi:10.4039/tce.2016.11.
15. Foster, A.C.; Walter, J.A.; Shugart, H.H.; Sibold, J.; Negron, J. Spectral evidence of early-stage spruce beetle infestation in Engelmann spruce. *For. Ecol. Manag.* **2017**, *384*, 347–357, doi:10.1016/j.foreco.2016.11.004.
16. Senf, C.; Seidl, R.; Hostert, P. Remote sensing of forest insect disturbances: Current state and future directions. *Int. J. Appl. Earth Obs. Geoinf.* **2017**, *60*, 49–60, doi:10.1016/j.jag.2017.04.004.
17. Bárta, V.; Lukeš, P.; Homolová, L. Early detection of bark beetle infestation in Norway spruce forests of Central Europe using Sentinel-2. *Int. J. Appl. Earth Obs. Geoinf.* **2021**, *100*, 102335, doi:10.1016/j.jag.2021.102335.
18. Bater, C.W.; Wulder, M.A.; White, J.C.; Coops, N.C. Integration of LIDAR and Digital Aerial Imagery for Detailed Estimates of Lodgepole Pine (Pinus contorta) Volume Killed by Mountain Pine Beetle (*Dendroctonus ponderosae*). *J. For.* **2010**, *108*, 111–119.
19. Näsi, R.; Honkavaara, E.; Blomqvist, M.; Lyytikäinen-Saarenmaa, P.; Hakala, T.; Viljanen, N.; Kantola, T.; Holopainen, M. Remote sensing of bark beetle damage in urban forests at individual tree level using a novel hyperspectral camera from UAV and aircraft. *Urban For. Urban Green.* **2018**, *30*, 72–83, doi:10.1016/j.ufug.2018.01.010.
20. Wulder, M.A.; White, J.C.; Ortlepp, S.M.; Mora, B.; Coggins, S.; Coops, N.C.; Heath, J. Digital high spatial resolution aerial imagery to support forest health monitoring: The mountain pine beetle context. *J. Appl. Remote Sens.* **2012**, *6*, 062527, doi:10.1117/1.jrs.6.062527.
21. Ortiz, S.M.; Breidenbach, J.; Kändler, G. Early Detection of Bark Beetle Green Attack Using TerraSAR-X and RapidEye Data. *Remote Sens.* **2013**, *5*, 1912–1931, doi:10.3390/rs5041912.
22. Dash, J.P.; Watt, M.S.; Pearse, G.D.; Heaphy, M.; Dungey, H.S. Assessing very high resolution UAV imagery for monitoring forest health during a simulated disease outbreak. *ISPRS J. Photogramm. Remote Sens.* **2017**, *131*, 1–14, doi:10.1016/j.isprsjprs.2017.07.007.
23. Kampen, M.; Ledebauer, S.; Mund, J.-P.; Immitzer, M. UAV-Based Multispectral Data for Tree Species Classification and Tree Vitality UAV-Based Multispectral Data for Tree Species Classification and Tree Vitality Analysis. In Proceedings of the Dreilandertagung der DGPF, der OVG und der SGPF, Vienna, Austria, 20–22 February 2019; pp. 623–639.
24. Heurich, M.; Ochs, T.; Andresen, T.; Schneider, T. Object-orientated image analysis for the semi-automatic detection of dead trees following a spruce bark beetle (Ips typographus) outbreak. *Eur. J. For. Res.* **2010**, *129*, 313–324, doi:10.1007/s10342-009-0331-1.
25. Adamczyk, J.; Osberger, A. Red-edge vegetation indices for detecting and assessing disturbances in Norway spruce dominated mountain forests. *Int. J. Appl. Earth Obs. Geoinf.* **2015**, *37*, 90–99, doi:10.1016/j.jag.2014.10.013.
26. Brovkina, O.; Cienciala, E.; Surový, P.; Janata, P. Unmanned aerial vehicles (UAV) for assessment of qualitative classification of Norway spruce in temperate forest stands. *Geo-Spat. Inf. Sci.* **2018**, *21*, 12–20, doi:10.1080/10095020.2017.1416994.
27. Näsi, R.; Honkavaara, E.; Lyytikäinen-Saarenmaa, P.; Blomqvist, M.; Litkey, P.; Hakala, T.; Viljanen, N.; Kantola, T.; Tanhuanpää, T.; Holopainen, M. Using UAV-Based Photogrammetry and Hyperspectral Imaging for Mapping Bark Beetle Damage at Tree-Level. *Remote Sens.* **2015**, *7*, 15467–15493, doi:10.3390/rs71115467.
28. Klouček, T.; Komárek, J.; Surový, P.; Hrach, K.; Janata, P.; Vašíček, B. The Use of UAV Mounted Sensors for Precise Detection of Bark Beetle Infestation. *Remote Sens.* **2019**, *11*, 1561, doi:10.3390/rs11131561.
29. Guimarães, N.; Pádua, L.; Marques, P.; Silva, N.; Peres, E.; Sousa, J.J. Forestry Remote Sensing from Unmanned Aerial Vehicles: A Review Focusing on the Data, Processing and Potentialities. *Remote Sens.* **2020**, *12*, 1046, doi:10.3390/rs12061046.
30. Haralick, R.M. Statistical and structural approaches to texture. *Proc. IEEE* **1979**, *67*, 786–804, doi:10.1109/PROC.1979.11328.
31. Safonova, A.; Tabik, S.; Alcaraz-Segura, D.; Rubtsov, A.; Maglinets, Y.; Herrera, F. Detection of Fir Trees (*Abies sibirica*) Damaged by the Bark Beetle in Unmanned Aerial Vehicle Images with Deep Learning. *Remote Sens.* **2019**, *11*, 643, doi:10.3390/rs11060643.
32. Kattenborn, T.; Leitloff, J.; Schiefer, F.; Hinz, S. Review on Convolutional Neural Networks (CNN) in vegetation remote sensing. *ISPRS J. Photogramm. Remote Sens.* **2021**, *173*, 24–49, doi:10.1016/j.isprsjprs.2020.12.010.
33. Chollet, F. Xception: Deep Learning with Depthwise Separable Convolutions. In Proceedings of the 30th IEEE Conference on Computer Vision and Pattern Recognition (CVPR), Honolulu, HI, USA, 21–26 July 2017; pp. 1800–1807. doi:10.1109/CVPR.2017.195.
34. Zhu, X.X.; Tuia, D.; Mou, L.; Xia, G.-S.; Zhang, L.; Xu, F.; Fraundorfer, F. Deep Learning in Remote Sensing: A Comprehensive Review and List of Resources. *IEEE Geosci. Remote Sens. Mag.* **2017**, *5*, 8–36, doi:10.1109/mgrs.2017.2762307.

35. Reichstein, M.; Camps-Valls, G.; Stevens, B.; Jung, M.; Denzler, J.; Carvalhais, N.; Prabhat. Deep learning and process understanding for data-driven Earth system science. *Nature* **2019**, *566*, 195–204, doi:10.1038/s41586-019-0912-1.
36. Hoeser, T.; Kuenzer, C. Object Detection and Image Segmentation with Deep Learning on Earth Observation Data: A Review-Part I: Evolution and Recent Trends. *Remote Sens.* **2020**, *12*, 1667, doi:10.3390/rs12101667.
37. Braga, J.R.G.; Peripato, V.; Dalagnol, R.; Ferreira, M.P.; Tarabalka, Y.; Aragão, L.E.O.C.; Velho, H.F.D.C.; Shiguemori, E.H.; Wagner, F.H. Tree Crown Delineation Algorithm Based on a Convolutional Neural Network. *Remote Sens.* **2020**, *12*, 1288, doi:10.3390/rs12081288.
38. Weinstein, B.G.; Marconi, S.; Bohlman, S.; Zare, A.; White, E. Individual Tree-Crown Detection in RGB Imagery Using Semi-Supervised Deep Learning Neural Networks. *Remote Sens.* **2019**, *11*, 1309, doi:10.3390/rs11111309.
39. Hartling, S.; Sagan, V.; Sidike, P.; Maimaitijiang, M.; Carron, J. Urban Tree Species Classification Using a WorldView-2/3 and LiDAR Data Fusion Approach and Deep Learning. *Sensors* **2019**, *19*, 1284, doi:10.3390/s19061284.
40. Dos Santos, A.A.; Marcato Junior, J.; Araújo, M.S.; Di Martini, D.R.; Tetila, E.C.; Siqueira, H.L.; Aoki, C.; Eltner, A.; Matsubara, E.T.; Pistori, H.; et al. Assessment of CNN-Based Methods for Individual Tree Detection on Images Captured by RGB Cameras Attached to UAVs. *Sensors* **2019**, *19*, 3595, doi:10.3390/s19163595.
41. Natesan, S.; Armenakis, C.; Vepakomma, U. Resnet-Based Tree Species Classification Using UAV Images. *Int. Arch. Photogramm. Remote Sens. Spat. Inf. Sci.* **2019**, *42*, 475–481, doi:10.5194/isprs-archives-xlii-2-w13-475-2019.
42. Onishi, M.; Ise, T. Explainable identification and mapping of trees using UAV RGB image and deep learning. *Sci. Rep.* **2021**, *11*, 1–15, doi:10.1038/s41598-020-79653-9.
43. Lobo Torres, D.; Queiroz Feitosa, R.; Nigri Happ, P.; Elena Cue La Rosa, L.; Marcato Junior, J.; Martins, J.; Ola Bressan, P.; Gonçalves, W.N.; Liesenberg, V. Applying Fully Convolutional Architectures for Semantic Segmentation of a Single Tree Species in Urban Environment on High Resolution UAV Optical Imagery. *Sensors* **2020**, *20*, 563, doi:10.3390/s20020563.
44. Schiefer, F.; Kattenborn, T.; Frick, A.; Frey, J.; Schall, P.; Koch, B.; Schmidtlein, S. Mapping forest tree species in high resolution UAV-based RGB-imagery by means of convolutional neural networks. *ISPRS J. Photogramm. Remote Sens.* **2020**, *170*, 205–215, doi:10.1016/j.isprsjprs.2020.10.015.
45. Nguyen, H.T.; Caceres, M.L.L.; Moritake, K.; Kentsch, S.; Shu, H.; Diez, Y. Individual Sick Fir Tree (*Abies mariesii*) Identification in Insect Infested Forests by Means of UAV Images and Deep Learning. *Remote Sens.* **2021**, *13*, 260, doi:10.3390/rs13020260.
46. Miyoshi, G.T.; Arruda, M.d.S.; Osco, L.P.; Marcato Junior, J.; Gonçalves, D.N.; Imai, N.N.; Tommaselli, A.M.G.; Honkavaara, E.; Gonçalves, W.N. A Novel Deep Learning Method to Identify Single Tree Species in UAV-Based Hyperspectral Images. *Remote Sens.* **2020**, *12*, 1294, doi:10.3390/rs12081294.
47. Nezami, S.; Khoramshahi, E.; Nevalainen, O.; Pölönen, I.; Honkavaara, E. Tree Species Classification of Drone Hyperspectral and RGB Imagery with Deep Learning Convolutional Neural Networks. *Remote Sens.* **2020**, *12*, 1070, doi:10.3390/rs12071070.
48. Hlásny, T.; Krokene, P.; Liebhold, A.; Montagné-Huck, C.; Müller, J.; Qin, H.; Raffa, K.; Schelhaas, M.; Seidl, R.; Svoboda, M.; et al. *Living with Bark Beetles: Impacts, Outlook and Management Options*; European Forest Institute: Joensuu, Finland, 2019.
49. Agisoft LLC. MicaSense RedEdge MX Processing Workflow (Including Reflectance Calibration) in Agisoft Metashape Professional. Available online: https://agisoft.freshdesk.com/support/solutions/articles/31000148780-micasense-rededge-mx-processing-workflow-including-reflectance-calibration-in-agisoft-metashape-pro (accessed on 5 September 2020).
50. Minařík, R.; Langhammer, J.; Lendzioch, T. Automatic Tree Crown Extraction from UAS Multispectral Imagery for the Detection of Bark Beetle Disturbance in Mixed Forests. *Remote Sens.* **2020**, *12*, 4081, doi:10.3390/rs12244081.
51. Coulson, R.N.; Amman, G.D.; Dahlsten, D.L.; DeMars, C.J., Jr.; Stephen, F.M. *Forest-Bark Beetle Interactions: Bark Beetle Population Dynamics*; Integrated pest management in pine-bark beetle ecosystem; John Wiley & Sons: New York, NY, USA, 1985; pp. 61–80.
52. Geng, J.; Wang, H.; Fan, J.; Ma, X. Deep Supervised and Contractive Neural Network for SAR Image Classification. *IEEE Trans. Geosci. Remote Sens.* **2017**, *55*, 2442–2459, doi:10.1109/tgrs.2016.2645226.
53. Siegel, S.; Castellan, N.J.J. *Non-Parametric Statistics for the Behavioural Sciences*; McGraw-Hill: New York, NY, USA, 1988.
54. R Core Team. *R: A Language and Environment for Statistical Computing*; R Foundation for Statistical Computing: Vienna, Austria, 2020; Available online: https://www.R-project.org/ (accessed on 26 May 2021).
55. Chollet, F.; Allaire, J.J. *Deep Learning with R*; Simon and Schuster: New York, NY, USA, 2018; ISBN 9781617295546.
56. Huang, G.; Liu, Z.; Van Der Maaten, L.; Weinberger, K.Q. Densely connected convolutional networks. In Proceedings of the 30th IEEE Conference on Computer Vision and Pattern Recognition (CVPR), Honolulu, HI, USA, 21–26 July 2017; pp. 2261–2269.
57. Natesan, S.; Armenakis, C.; Vepakomma, U. Individual tree species identification using Dense Convolutional Network (DenseNet) on multitemporal RGB images from UAV. *J. Unmanned Veh. Syst.* **2020**, *8*, 310–333, doi:10.1139/juvs-2020-0014.
58. Breiman, L. Random forests. *Mach. Learn.* **2001**, *45*, 5–32, doi:10.1023/A:1010933404324.
59. Cutler, D.R.; Edwards, T.C., Jr.; Beard, K.H.; Cutler, A.; Hess, K.T.; Gibson, J.; Lawler, J.J. Random Forests for Classification in Ecology. *Ecology* **2007**, *88*, 2783–2792, doi:10.1890/07-0539.1.
60. Boulesteix, A.-L.; Janitza, S.; Kruppa, J.; König, I.R. Overview of random forest methodology and practical guidance with emphasis on computational biology and bioinformatics. *Wiley Interdiscip. Rev. Data Min. Knowl. Discov.* **2012**, *2*, 493–507, doi:10.1002/widm.1072.
61. Olson, R.S.; La Cava, W.; Mustahsan, Z.; Varik, A.; Moore, J.H. Data-driven advice for applying machine learning to bioinformatics problems. *Pac. Symp. Biocomput.* **2018**, *23*, 192–203, doi:10.1142/9789813235533_0018.
62. Kuhn, M. Building Predictive Models in R Using the caret Package. *J. Stat. Softw.* **2008**, *28*, 1–26, doi:10.18637/jss.v028.i05.

63. Kingma, D.P.; Ba, J. Adam: A Method for Stochastic Optimization. In Proceedings of the 3rd International Conference on Learning Representations, ICLR 2015, San Diego, CA, USA, 7–9 May 2015.
64. Russell, S.; Norvig, P. *Artificial Intelligence: A Modern Approach*, 3rd ed.; Pearson: New York, NY, USA, 2010; ISBN 9780136042594.
65. Cohen, J. A Coefficient of Agreement for Nominal Scales. *Educ. Psychol. Meas.* **1960**, *20*, 37–46, doi:10.1177/001316446002000104.
66. Hastings, J.H.; Ollinger, S.V.; Ouimette, A.P.; Sanders-DeMott, R.; Palace, M.W.; Ducey, M.J.; Sullivan, F.B.; Basler, D.; Orwig, D.A. Tree Species Traits Determine the Success of LiDAR-Based Crown Mapping in a Mixed Temperate Forest. *Remote Sens.* **2020**, *12*, 309, doi:10.3390/rs12020309.
67. Windrim, L.; Carnegie, A.J.; Webster, M.; Bryson, M. Tree Detection and Health Monitoring in Multispectral Aerial Imagery and Photogrammetric Pointclouds Using Machine Learning. *IEEE J. Sel. Top. Appl. Earth Obs. Remote Sens.* **2020**, *13*, 2554–2572, doi:10.1109/jstars.2020.2995391.
68. Chiang, C.-Y.; Barnes, C.; Angelov, P.; Jiang, R. Deep Learning-Based Automated Forest Health Diagnosis from Aerial Images. *IEEE Access* **2020**, *8*, 144064–144076, doi:10.1109/access.2020.3012417.
69. Sothe, C.; De Almeida, C.M.; Schimalski, M.B.; La Rosa, L.E.C.; Castro, J.D.B.; Feitosa, R.Q.; Dalponte, M.; Lima, C.L.; Liesenberg, V.; Miyoshi, G.T.; et al. Comparative performance of convolutional neural network, weighted and conventional support vector machine and random forest for classifying tree species using hyperspectral and photogrammetric data. *GISci. Remote Sens.* **2020**, *57*, 369–394, doi:10.1080/15481603.2020.1712102.
70. Sothe, C.; Almeida, C.; Schimalski, M.B.; Liesenberg, V.; La Rosa, L.E.C.; Castro, J.D.B.; Feitosa, R.Q. A comparison of machine and deep-learning algorithms applied to multisource data for a subtropical forest area classification. *Int. J. Remote Sens.* **2020**, *41*, 1943–1969, doi:10.1080/01431161.2019.1681600.
71. Kuhn, M.; Johnson, K. *Applied Predictive Modeling*; Springer: New York, NY, USA, 2013; Volume 26, pp. 419–443, ISBN 978-1-4614-6848-6.
72. Gao, Q.; Lim, S.; Jia, X. Hyperspectral Image Classification Using Convolutional Neural Networks and Multiple Feature Learning. *Remote Sens.* **2018**, *10*, 299, doi:10.3390/rs10020299.
73. Li, Y.; Zhang, H.; Shen, Q. Spectral–Spatial Classification of Hyperspectral Imagery with 3D Convolutional Neural Network. *Remote Sens.* **2017**, *9*, 67, doi:10.3390/rs9010067.
74. Wermelinger, B. Ecology and management of the spruce bark beetle Ips typographus—A review of recent research. *For. Ecol. Manag.* **2004**, *202*, 67–82, doi:10.1016/j.foreco.2004.07.018.
75. Fahse, L.; Heurich, M. Simulation and analysis of outbreaks of bark beetle infestations and their management at the stand level. *Ecol. Model.* **2011**, *222*, 1833–1846, doi:10.1016/j.ecolmodel.2011.03.014.
76. Wulder, M.A.; White, J.C.; Carroll, A.L.; Coops, N.C. Challenges for the operational detection of mountain pine beetle green attack with remote sensing. *For. Chron.* **2009**, *85*, 32–38, doi:10.5558/tfc85032-1.
77. Qin, J.; Wang, B.; Wu, Y.; Lu, Q.; Zhu, H. Identifying Pine Wood Nematode Disease Using UAV Images and Deep Learning Algorithms. *Remote Sens.* **2021**, *13*, 162, doi:10.3390/rs13020162.
78. Eitel, J.U.H.; Vierling, L.A.; Litvak, M.E.; Long, D.S.; Schulthess, U.; Ager, A.A.; Krofcheck, D.J.; Stoscheck, L. Broadband, red-edge information from satellites improves early stress detection in a New Mexico conifer woodland. *Remote Sens. Environ.* **2011**, *115*, 3640–3646, doi:10.1016/j.rse.2011.09.002.
79. Immitzer, M.; Atzberger, C. Early Detection of Bark Beetle Infestation in Norway Spruce (*Picea abies*, L.) using WorldView-2 Data. *Photogramm. Fernerkund. Geoinf.* **2014**, *5*, 351–367, doi:10.1127/1432-8364/2014/0229.